

DEEP CCD PHOTOMETRY OF THE RICH GALAXY CLUSTER ABELL 1656
CHARACTERISTICS OF THE DWARF ELLIPTICAL GALAXY POPULATION
IN THE CLUSTER CORE

JEFF SECKER, B.SC., M.SC.

A Thesis

Submitted to the School of Graduate Studies

in Partial Fulfilment of the Requirements for the Degree

Doctor of Philosophy

McMaster University

August 1995

(c) Copyright by Jeff Secker, 1995.

DOCTOR OF PHILOSOPHY (1995) MCMASTER UNIVERSITY
(ASTROPHYSICS) Department of Physics and Astronomy
Hamilton, Ontario

TITLE: Deep CCD Photometry Of The Rich Galaxy Cluster Abell 1656:
Characteristics Of The Dwarf Elliptical Galaxy Population In
The Cluster Core

AUTHOR: Jeff Secker
B.Sc. (University of Waterloo)
M.Sc. (McMaster University)

ADVISOR: Professor William E. Harris

PAGES: xiii, 234

DWARF ELLIPTICAL GALAXIES IN THE COMA CLUSTER

Abstract

We have developed a statistically rigorous and automated method to implement the detection, photometry and classification of faint objects on digital images. We use these methods to analyze deep R - and B -band CCD images of the central ~ 700 arcmin² of the Coma cluster core, and an associated control field. We have detected and measured total R magnitudes and $(B - R)$ colors for a sample of 3741 objects on the galaxy cluster fields, and 1164 objects on a remote control field, complete to a limiting magnitude of $R = 22.5$ mag. The typical uncertainties are ± 0.06 and ± 0.12 mag in total magnitude and color respectively. The dwarf elliptical (dE) galaxies are confined to a well-defined sequence in the color range given by $0.7 \leq (B - R) \leq 1.9$ mag; within this interval there are 2535 dE candidates on our fields in the cluster core, and 694 objects on the control field. With an image scale of 0.53 arcsec/pixel and seeing near 1.2 arcsec, a large fraction of the dE galaxy candidates are resolved.

We find a significant metallicity gradient in the radial distribution of the dwarf elliptical galaxies, which goes as $Z \propto R^{-0.32}$ outwards from the cluster center at NGC 4874. As well, there is a strong color-luminosity correlation, in the sense that more luminous dE galaxies are redder in the mean. These effects give rise to a radial variation in the cluster luminosity function. The spatial distribution of the faint dE galaxies is well fit by a standard King model with a central surface density of $\Sigma_0 = 1.44$ dEs arcmin⁻², a core radius $R_c = 18.7$ arcmin ($\simeq 0.44$ Mpc), and a tidal

radius of 1.44 deg ($\simeq 2.05$ Mpc). This core is significantly larger than $R_c = 12.3$ arcmin ($\simeq 0.29$ Mpc) found for the bright cluster galaxies. The composite luminosity function for Coma galaxies is modeled as the sum of a log-normal distribution for the giant galaxies and a Schechter function for the dwarf elliptical galaxies, with a faint-end slope of $\alpha = -1.41$, consistent with known faint-end slopes for the Virgo and Fornax clusters. The early-type dwarf-to-giant ratio for the Coma cluster core is consistent with that of the Virgo cluster, and thus with the rich Coma cluster being formed as the merger of multiple less-rich galaxy clusters.

Acknowledgements

This thesis forms a significant part of the research I have done while at McMaster, and it has benefited greatly from the experience and wisdom of my advisor, Bill Harris. The research atmosphere which he helped to create is one of enthusiasm and productivity, resulting from his eagerness to discuss and explore new ideas, and from his generous support, most memorably for conference travel and observing runs. Most of all, I appreciate the freedom his supervision has allowed.

I would like to thank Paul Wesson, friend and mentor extraordinaire, for kindling my interest in extragalactic astronomy. I thank my colleagues and fellow graduate students for their friendship and assistance over the last five years, especially those I shared an office with: Steve Butterworth, Pat Côté, Pat Durrell, Phil Fischer, David Fleming, Steve Holland, Nina Jensen-Troelsgaard, Denise Kaisler, Jennifer Larking, Dean McLaughlin, Kanan Patel and Mark Walker. And a special thanks to Phil Fischer and Pat Côté for lighting the path and showing it can be done, and helping to provide such a quick “start-up” time.

I would like to thank all of the McMaster astronomy faculty members - Bill Harris, Ralph Pudritz, Peter Sutherland, Doug Welch and Christine Wilson - for their assistance, for their friendship, for providing a strong foundation in fundamental astronomy, and for their dedication to building an excellent network of SPARC stations. I would also like to thank: John Benjamins and Patricia Monger, for their over-

whelming knowledge and excellent support of the computer network; Simon Lilly, for discussions, and for suggesting that I look into photometry methods in more detail; the Department of Physics and Astronomy, for the opportunity of graduate school and for financial support; the Natural Sciences and Engineering Research Council of Canada (for an operating grant to W.E. Harris); the Ontario Ministry of Colleges and Universities, for a 1994/95 Ontario Graduate Scholarship; and Jackie Collin, Wendy Malarek, Rosemary McNeice, Cheryl Johnston and Margaret Wilby for their friendship and administrative assistance.

To all members of both my families - Aline Bergeron, Arnold de Villiers, Louise Bergeron-de Villiers, Tim Hawkins, Dan Lefebvre, Julie Lefebvre, Marie Lefebvre, Pat Lefebvre, Sue O'Bomsawin, Bill Parsons, Barb Secker, Lori Secker, Paul Secker, Jeremy Todd, Joshua Todd, Larry Todd, Lois Todd, George Young, Susan Young - and to my friends, a general yet inexpressible thanks. For my Morn, a special thanks for her love, friendship, encouragement and unquestioning support. Julie, thank you in every way, but especially for sharing life and the experience of graduate school with me: *Jai bhagwan!*

Ma chère Julie,

With you beside me, happiness bubbles,
a touch of your hand, loneliness vanishes,
the sound of your laugh, I come alive!
Toujours ensemble, we walk through life.

Contents

Abstract	iii
List Of Figures	xi
List Of Tables	xiii
1 Introduction	1
2 An Accurate Method for Galaxy Photometry	11
1 Introduction	11
2 Estimation Of A Mean Sky Intensity For Object Detection And Photometry	15
2.1 Global Modal Sky And Object Detection	18
2.2 Annulus Selection For Local Modal Sky	22
3 Tests With Artificial CCD Images	24
4 Image Analysis And Moment Definitions	28
4.1 Limiting Radius R_ℓ For Summations	29
4.2 Intensity-Weighted Averages For Object Centers	32
4.3 The Intensity-Weighted Radial Moments	33
4.4 Other Moments Of The Intensity Distribution	41
4.5 Interactive Verification For Difficult Objects	44
5 Faint Galaxy Photometry	45
5.1 Total Magnitude Estimation	46
5.2 Colors Derived From Standard Apertures	52
5.3 Calibration Of Instrumental Magnitudes	57
5.4 Uncertainties For Aperture Magnitudes	60
5.5 Measures Of Surface Brightness	61
5.6 An Estimate Of The Number Of Overlapping Apertures And Edge Objects	64
6 Summary	65
3 The Ring Median Filter	68

1	Motivation	69
2	Filter Definition And Properties	69
3	Sample Results	70
4	Appendix	74
5	References	74
4	Photometry of the Coma Cluster Core	75
1	Introduction	75
2	Observations And Data Reduction	76
2.1	Field Placement And Cluster Coverage	76
2.2	Pre-DYNAMO Processing	81
2.3	DYNAMO Image Analysis	86
3	Calibration, Completeness And Photometric Errors	91
3.1	Calibration Procedure	91
3.2	A Magnitude (And Color) Completeness Level	94
3.3	Photometric Uncertainties	101
3.4	Photometry Comparison For Objects Matched In Overlap Regions	101
4	Image Moments For Star/Galaxy Discrimination	105
4.1	The Radial Moment r_{-2} And Object Discrimination	105
4.2	Quantization Of The Radial Moments	109
5	Color Constraints And The Dwarf Elliptical Galaxy Sequence	111
5.1	Details Of The Control Field Analysis	111
5.2	Color-Magnitude Diagram Analysis	118
5.3	Final Sample of Probably Cluster Galaxies	122
6	Summary	132
5	The Dwarf Elliptical Galaxy Population	134
1	Introduction	134
2	$(B - R)$ Color Distribution Functions	135
2.1	The Color-Magnitude Relation	136
2.2	A Radial Color Gradient	141
3	The Galaxy Luminosity Function	149
3.1	The Faint-End Slope	153
3.2	Radial Dependence	158
4	Galaxy Spatial Distributions	161
4.1	The Radial Profile For Cluster Galaxies	164
5	The Dwarf-To-Giant Ratio	173
5.1	The EDGR For The Coma Cluster Core	175
6	Discussion	185
6.1	The Effects Of Cluster Substructure On The EDGR	185

6.2	A Reduced EDGR In The Coma Core	187
6.3	Diffuse Intracluster Light	188
6.4	An Increased Density Of dE Galaxies Between The Supergiant Galaxies	191
7	Summary	193
6	The Emphasis of Future Research	195
7	References	198
A	Estimates Of The Mode And Variance	205
B	DYNAMO User's Manual	210
C	Photometry Of The Bright Sample Of Dwarf Elliptical Galaxies	228

List of Figures

2.1	The Distribution Of Pixel Intensity Values	16
2.2	Poisson Sky Noise And The Detection Threshold	20
2.3	One Of The Artificial CCD Images	26
2.4	The Input Luminosity Functions For The Artificial Images	27
2.5	Determination Of The Intensity Weighted Object Centers	34
2.6	Radial Moments For Star/Galaxy Discrimination	37
2.7	Correlation Of The Radial Moments	39
2.8	The Half-flux Radius Of Exponential Profile Galaxies	42
2.9	Estimates Of An Object's Total Magnitude	50
2.10	Central Surface Brightnesses Versus Total Magnitude	63
3.1	A Ring Median Filter Template For Starlike Objects	69
3.2	Effect Of A Ring Filter On Objects Of Various Sizes	70
3.3	Dwarf Galaxies Within The Rich Galaxy Cluster Abell 2199	71
3.4	An Extreme Test For The Ring Median Filter	72
3.5	A 16-pixel Ring Median Filter With A 6-pixel Characteristic Radius	73
4.1	Placement Of The Three Coma Cluster CCD Fields	79
4.2	A 16-pixel Ring Median Filter Template	85
4.3	A High Resolution Image Northeast Of NGC 4889	89
4.4	A High Resolution Image North Of NGC 4874 And NGC 4889	90
4.5	The Magnitude Completeness Function	97
4.6	Photometry Errors	102
4.7	Total Magnitude Comparison For Overlap Regions	104
4.8	Color Comparison For Objects Detected In Overlap Regions	106
4.9	Parameter Space Plot Of r_{-2} Versus R_{2r_1}	107
4.10	Quantization Of The First Radial Moment	110
4.11	Color Distribution For Objects On The CONTROL Field	114
4.12	The KS Statistic For Color Distributions On The CONTROL Field	116
4.13	Color-magnitude Diagrams For All Fields	119
4.14	Composite CMD For The Coma Cluster Core	125
4.15	Central Surface Brightness Versus The Total Magnitude	128

4.16	Variation Of The r_1 Radius With R Magnitude	130
5.1	An Analysis Of The Bright CMD Sequence	138
5.2	The Radial Color Distribution For Dwarf Galaxies	142
5.3	The Calibration Of Metallicity With $(B - R)$ Color	145
5.4	Program And Control Field Luminosity Functions	155
5.5	The Net Luminosity Function For Coma Cluster Galaxies	156
5.6	Radial Variation Of The Median dE Galaxy Luminosity	159
5.7	The Spatial Distribution Of E And Bright dE Cluster Galaxies	163
5.8	The Spatial Distribution Of Dwarf Ellipticals In The Cluster Core . .	165
5.9	Radial Number Density Profiles For Cluster Galaxies	168
5.10	$\text{Log}(N/\text{arcmin}^2)$ Versus $\text{Log}(R_{cc}/\text{arcmin})$ For Cluster Galaxies	169
5.11	Fit Of The Gaussian Plus Schechter Model To The Coma LF	182
5.12	The Early-type Dwarf-to-giant Ratio For The Coma Cluster	183

List of Tables

4.1	Telescope Coordinates Of The <i>R</i> -band CCD Fields	77
4.2	Properties Of The Master CCD Images	78
4.3	Summary Of The April 1991 KPNO 4m Standard Star Fields	80
4.4	Calibration Summary For The April 1991 KPNO KPNO 4m Run . .	93
5.1	Radial Distributions For Bright dE Candidates	143
5.2	Luminosity Function For Coma Cluster Galaxies	157
5.3	Radial Number Densities For Cluster Galaxies.	166
5.4	Fits Of The Gaussian Plus Schechter Model To The Coma LF	180
5.5	The Early-type Dwarf-To-Giant Ratio For The Coma Cluster	181

Chapter 1

Introduction

An understanding of the properties of individual dwarf galaxies, as well as their formation and evolution with the giant galaxies in the confines of rich galaxy clusters, is beginning to emerge. For our purposes, dwarf elliptical (dE) galaxies are defined as low luminosity, low surface brightness galaxies in the range $-18 \lesssim M_B \lesssim -8$ mag, which corresponds to a B -band luminosity of $2.5 \times 10^5 \lesssim L_B/L_\odot \lesssim 2.5 \times 10^9$. These dE galaxies typically have a color of $(B-R) \simeq 1.4$ mag, which represent the difference between B - and R -band apparent magnitudes (i.e., as measured through broadband photometric filters). The majority (i.e., $\gtrsim 90$ percent) of dwarf elliptical galaxies are located in the environment of rich clusters of galaxies, and these are thought to be composed of a metal-poor stellar population similar in age to globular clusters (Ferguson & Binggeli 1994). This appears to differ from Local Group dwarfs, many of which show evidence for more than one episode of star formation (e.g., Caldwell & Bothun 1987; Sarajedini & Layden 1995; Smecker-Hane, Stetson & Hesser 1995). Like the giant galaxies, dwarf galaxies are divided into “early”- and “late”-types. Late-

type dwarfs (irregulars showing no overall optical structure, often with evidence for recent star formation) are found predominately in the field or the less dense regions of galaxy clusters, and are dominated in number by the dwarf irregular (dIr) galaxies, with a small contribution from dwarf spirals (Schombert et al. 1995). In this thesis I am concerned primarily with the early-type (elliptical) dwarf (and giant) galaxies, as these compose the vast majority of galaxies in cluster cores.

Dwarf elliptical galaxies form a population which is fundamentally different from regular elliptical galaxies. First, dwarf elliptical galaxies in general become fainter in magnitude via a *decrease* in central surface brightness. This differs fundamentally from the class of regular elliptical galaxies, for which the central surface brightness *increases* with fainter magnitude, and the decrease in magnitude is a result of a decrease in core radius (see Kormendy 1977; Caldwell & Bothun 1987; Ferguson & Binggeli 1994; Chapter 4). This is the basis for visual discrimination between dE and E galaxies near the same total magnitude: the dE galaxies are those with the lower surface brightness. Second, dwarf elliptical galaxies are characterized by smooth (as compared to dwarf irregular) surface brightness profiles, with the non-nucleated dwarfs being well fit by a single exponential (e.g., Ichikawa et al. 1986; Ferguson & Binggeli 1994) or a modified-exponential profile (e.g., Cellone, Forte & Geisler 1994). This differs from regular elliptical galaxies whose light distribution is well described by a de Vaucouleurs $R^{1/4}$ -law. A third difference is discussed in Chapter 2 (Section 5.2.1). Briefly, while color gradients are observed in some dE galaxies, there does

not appear to be any preference for red or blue color gradients. This differs from the giant ellipticals, which become redder (a metallicity effect) at *decreasing* radius. The metallicity, denoted here as $[\text{Fe}/\text{H}]$, is defined with respect to the Solar value (i.e., Z/Z_{\odot}), as the logarithmic mass fraction of elements heavier than Hydrogen and Helium.

Dwarf galaxies also appear to be dominated by extensive, extremely massive dark-matter halos. This is quantified in terms of the mass-to-light ratio M/L , for which a larger value indicates that more low-luminosity objects are present. Measurements of the central stellar velocity dispersions in E and dE galaxies indicate that the $M/L \propto L^{0.2}$ for regular ellipticals, but that $M/L \propto L^{-0.4}$ for the dwarfs (Ferguson & Binggeli 1994). Typical values seem to range from $M/L = 4$ or $5 M_{\odot}/L_{\odot}$ for bright dEs in Virgo, up to $M/L \simeq 100$ for Draco, a faint dwarf spheroidal (essentially a very faint dE) in the Local Group (e.g., Bender, Paquet & Nieto 1991; Peterson & Caldwell 1993). This observed trend in M/L for dwarf galaxies is consistent with the models of Dekel & Silk (1986): for the case of dominant dark-matter halos, they predict a mass-to-light ratio which varies as $L^{-0.37}$. This is because the efficiency in which gas is converted into stars decreases with luminosity for dwarf galaxies, as the lower-mass dwarfs lose a larger fraction of their gas.

One similarity between dwarf elliptical galaxies and the regular elliptical galaxies is that they both have an associated globular cluster system (GCS). As in the Local Group dwarfs, dwarf elliptical galaxies in the Virgo cluster possess their own globular

star clusters, with specific frequencies (the number of globular clusters normalized by the host galaxy's luminosity; Harris & van den Bergh 1981) equal to that (in general) of regular ellipticals (Durrell et al. 1995). Since the GCS and the specific-frequency are thought to be artifacts of the galaxy formation, this similarity in specific-frequency provides evidence that at least one aspect of their formation mechanism is similar.

At the present time, the formation of dwarf galaxies is not well understood (see the review by Ferguson & Binggeli 1994 for a summary of the current scenarios). However, with a typical mass on the order of $10^9 M_\odot$, dwarf galaxies have often been considered to be the evolved state of the primeval protogalactic fragments (the first self-gravitating systems formed in a cold dark matter - CDM - cosmology) postulated by (for example) Searle and Zinn (1978) and by Larson (1985). Formation scenarios relevant to dwarf galaxies in a cluster environment attribute their observed characteristics to an interdependence between external factors such as the confinement pressure exerted by the intergalactic medium, and the dominant internal factors: large dark-matter halos, and an expulsion of residual gas, globally, via supernovae-driven winds (e.g. Wyse & Silk 1985; Dekel & Silk 1986; Silk, Wyse & Shields 1987; Babul & Rees 1992; see also Marlowe et al. 1995). The combined result is expected to be a single major star formation epoch, a galaxy mass and metallicity dependent upon location with respect to the cluster center, with a stellar population similar in age and integrated light to globular clusters.

The ensemble of early-type dwarf galaxies, represented here as dE galaxies, are

distinguished from faint regular elliptical galaxies on the basis of the physical differences (especially surface brightness) described above. Once isolated though, this dwarf elliptical galaxy population consists of several distinct morphological types occurring as deviations from the prototypical dE: a smooth, centrally concentrated, low surface brightness galaxy. Many bright dwarf elliptical galaxies are nucleated (dE,N), for which a central spike contains up to 20 percent of the total luminosity of the dwarf galaxy (van den Bergh 1986; Ferguson & Binggeli 1994). These nuclei are most likely supermassive star clusters with typical radii $\lesssim 50$ kpc (hence unresolved at distances of Virgo and Coma), for which the integrated colors are usually indistinguishable from the surrounding galaxy (Caldwell & Bothun 1987). For about 25 dwarf members of the Virgo cluster, Sandage & Binggeli (1994) introduced the dS0 class. These rare objects are intended to be analogous to the regular S0 galaxies, and show evidence for a two-component structure (i.e., a core plus flattened disk). The dwarf spheroidal (dSph) galaxy is essentially a very faint dwarf elliptical, with a less than average central concentration. The dividing lines between these classes are flexible and approximate, and for the dE galaxy population there will always be objects intermediate between classes. In our analysis to follow, I make no effort to separate our sample of dE galaxies into their morphological groups, simply because of the insufficient spatial resolution (see the next chapters).

The Coma galaxy cluster is a regular (spherically symmetric and centrally concentrated) galaxy cluster, and the nearest of the very-rich Abell clusters (Abell 1656,

richness-class 2). For a mean recession velocity of $v = 7000$ km/s, and a Hubble parameter of $H_0 = 86$ km/s/Mpc (Pierce et al. 1994), it is at a distance of 81.4 Mpc. As in all rich clusters, the early-type dwarf elliptical galaxies are by far the most numerous galaxies in the dense environment of the cluster core (Dressler 1980; Ferguson & Sandage 1991; Ferguson & Binggeli 1994; however, the contribution by dE galaxies to the total mass is not expected to be significant, Bernstein et al. 1995). In terms of luminosity, the cluster core is dominated by two supergiants, the elliptical NGC 4889 and the cD NGC 4874 (refer to Figure 4.1). These supergiants have mean total magnitudes (de Vaucouleurs et al. 1991; RC3) and colors of $B_T = 12.53 \pm 0.11$, $(B - V) = 1.04 \pm 0.01$ and $B_T = 12.63 \pm 0.11$, $(B - V) = 0.95 \pm 0.02$ respectively, making NGC 4889 the brightest cluster member, about 1.3 times more luminous than NGC 4874.

Dynamics in the core of the Coma cluster, like many other Abell clusters, are governed by the significant substructure (see, for example, Fitchett & Webster 1987; Escalera, Slezak & Mazure 1992; Davis & Mushotzky 1993; Mohr et al. 1993; White, Briel & Henry 1993; West 1994). In terms of optical observations, Coma is a Rood & Sastry (1971) B-type (binary) with NGC 4889 and NGC 4874 both obvious centers of galaxy concentration in the core (see Chapter 4), just two of the subclusters currently merging to form the Coma cluster. However, NGC 4874 differs in (at least) two significant ways from NGC 4889. First, from ROSAT X-ray observations of the Coma cluster, White, Briel & Henry (1993) place NGC 4874 at the peak of the diffuse X-

ray emission, and in this manner NGC 4874 defines a “center” for the Coma cluster. Second, while both of these supergiants have a measurable GCS, only NGC 4874 has a high (M87-like) specific-frequency GCS (Harris 1987). This is generally believed to support the argument that NGC 4874, like the other high specific-frequency cD galaxies (e.g. M87 in Virgo, NGC 3311 in Hydra, NGC 1399 in Fornax, etc.), derives its populous GCS from its special location at the center of a rich galaxy cluster. In addition to observing the expected GCS, high-resolution CCD imaging by Thompson & Valdes (1987) discovered a population of dwarf galaxies, also associated with the halo of NGC 4874. Accepting the X-ray and GCS observations of NGC 4874 as evidence for its special nature, *I adopt the position of NGC 4874 as the center of the Coma cluster.* This center location is used in the analysis of distributions such as mean galaxy color and number density, and their variation with clustercentric radius.

In addition to the analysis described in this thesis, there have been three recent studies of the Coma cluster, each which have a significant overlap with this one: (1) The photographic study of Thompson & Gregory (1993; extending the study of Thompson & Gregory 1980) is based upon m_b magnitudes and $(b - r)$ colors, complete to a limiting magnitude of $m_b = 20.0$ mag. Their survey covers an area of approximately four square degrees, and they provide a very thorough analysis of many aspects of the Coma dwarf galaxy population. (2) Biviano et al. (1995) utilize a combination of redshifts and $(b - r)$ colors, together with photographic magnitudes, to obtain a sample of cluster members complete to a limit of $m_b = 20.0$ mag. With

this data set they complete a statistical analysis of the galaxy luminosity function for an area of the cluster core 45×28 arcmin², centered upon NGC 4878 and NGC 4889. (3) Most recently, Bernstein et al. (1995) analyze deep *R*-band CCD images taken with the KPNO 4-meter telescope in 1.3'' seeing. Their single field is 7.5×7.5 arcmin², located to the south of both NGC 4889 and NGC 4874. They perform number counts of all objects to a limit of $R = 25.5$ mag, with an excellent job of statistical number correction using five randomly selected control fields. Among other results, they obtain an accurate value of the faint-end slope of the galaxy luminosity function.

The primary difference between these studies of the Coma cluster and this thesis is that I combine (i) a moderately large spatial coverage ($\simeq 700$ arcmin²), with (ii) accurate *R*- and *B*-band CCD photometry, (iii) a deep limiting magnitude, and (iv) nonstellar objects are reasonably well resolved. As described in Chapter 4, our CCD images are centered on the core environment of the Coma cluster. These include both NGC 4874 and NGC 4889, and extend south, radially outwards 23 arcmin from NGC 4874. The analysis of these images provides an extremely large sample of dwarf galaxies, the vast majority of which are the early-type dwarf ellipticals. Our cluster membership is based upon the object's ($B - R$) color, and as illustrated by Biviano et al. (1995; a comparison of redshift-selected and color-selected cluster definitions), this technique results in a minimal contamination from background galaxies. In this thesis, the analysis of our dE sample yields significant correlations relevant to their formation and subsequent dynamical evolution in this ultradense environment. Thus,

our analysis is complementary to the work completed by the groups discussed above, and to other groups looking at different areas of this observational parameter space (e.g. de Propriis et al. 1995, Lopez & Yee 1995, and others).

The characteristics of dwarf galaxies in all types of clusters represent a vast parameter space in terms of cluster richness, morphology, redshift range, etc., and its eventual coverage will involve many observational teams and techniques. The purpose of this thesis has been to use our unique data set to push observations and analysis one step further in one particular direction; *that is, to survey the present day (low-redshift) dE population deeply in the richest local cluster, and to define their various distributions (in radius, luminosity, metallicity) with high statistical certainty.*

In Chapter 2 I describe in detail the techniques and methods which have been developed specifically to detect, measure and classify faint objects on digital images, and the testing of these methods using artificial images. Appendix A and B are relevant to Chapter 2, with the latter containing a description of my (public domain) photometry package. Chapter 3 is a reprint of my paper, entitled “A Ring Median Filter For Digital Images”. This paper describes the technique which I implemented to remove global light gradients on CCD images. This, combined with the techniques described in Chapter 2, provide the only new tools necessary to analyze the Coma cluster CCD images.

In Chapter 4, I apply the image analysis methods formulated in the previous chapters to the CCD images of the Coma galaxy cluster and a control (non-cluster)

field. The result is a sample of dwarf galaxy candidates, complete in color and in magnitude to $R = 22.5$ mag, which populate the central 700 arcmin^2 near the two supergiant galaxies, NGC 4874 and NGC 4889. Appendix C contains Table 4.5, which provides photometry for a bright subsample of these dE galaxy candidates.

In Chapter 5, I analyze this sample, and address four significant aspects of the dwarf elliptical galaxy population: (a) color-luminosity and color-clustercentric radius correlations, (b) the faint-end slope of the galaxy luminosity function, (c) the radial surface density profiles of the cluster galaxies, and (d) the early-type dwarf-to-giant ratio. Finally, in Chapter 6, I briefly mention the direction in which I think future research should concentrate, both related to this thesis and for new observations.

At this point I must mention that the images of the Coma cluster, the analysis of which forms the basis for Chapters 4 and 5, were obtained by W. E. Harris and S. Holland; I was not part of this observing run. As well, the basic image preprocessing (i.e., that described in the last paragraph of Section 2.2 and the first two paragraphs of Section 3.2; Chapter 4) was completed by W. E. Harris during the observing run. An essential aspect of a Ph.D. degree in observational astronomy is knowledge of observational techniques. During the fall of 1992, I wrote an observing proposal for the CTIO Schmidt telescope, to image the dwarf galaxy population in the Hydra I galaxy cluster, and in April 1993, W.E. Harris and I successfully completed 5 nights of observing. These observations do not constitute part of this thesis.

Chapter 2

An Automated Approach To The Detection, Photometry And Classification Of Faint Objects On CCD Images

1. INTRODUCTION

In the context of data analysis, deep optical CCD (i.e., digital) images of rich galaxy clusters present a formidable challenge. The range in variables such as CCD characteristics, galaxy morphology, luminosity and surface brightness span an incredibly large parameter space. As an example, consider that for a deep wide field image of an arbitrary galaxy cluster, the detected objects would typically number in the thousands. Couple to this typical ranges of the parameters just mentioned: (1) Starlike versus non-stellar object type, with the latter subdivided into morphological classes for each of the giant cluster galaxies, dwarf galaxies, and background galaxies; (2) Extreme variations in luminosity, spanning a range of at least 10 in absolute magnitude, equivalently a range of 10^4 in luminosity; (3) Central surface brightness ranging from

globular cluster and galaxy nuclei, down to the low surface brightness values of faint dwarf elliptical galaxies, typically often less than one percent of the night sky; (4) Typical apparent diameters ranging from two to three pixels for unresolved (starlike) objects, on the order of 2-20 pixels for dwarf galaxies, and upwards of 60-100 pixels for the largest cluster members. In addition, consider the variation in noise levels, CCD pixel resolution, field crowding, and the presence of slowly varying global light gradients. This is a difficult problem indeed, so large that any single data analysis technique will be strained and unable to measure all types of objects.

The method of analysis presented here is necessarily restricted to one aspect of this overall problem, specifically *a semi-automated approach to the detection, photometry and classification of faint objects* on CCD images. Specifically, I describe the implementation of my computer code DYNAMO, which I use to measure accurate total magnitudes, integrated colors, dimensions and positions, and discriminate between contaminating objects and the cluster galaxies which we are interested in. Once measured, I use this accurate photometry to construct color-magnitude diagrams, spatial distributions and luminosity functions; that is, I address the nature of the abundant dwarf elliptical galaxy population (Chapters 4 and 5). When used in conjunction with other preexisting tools and techniques (e.g., profile-fitting photometry for crowded fields, isophote-fitting tools for large-diameter giant cluster galaxies, and median-filtering techniques for slowly varying light gradients; Chapter 3), we have a sophisticated set of computer codes implementing a statistically rigorous method-

ology, sufficient for a complete and thorough analysis of CCD images of rich galaxy clusters.

Throughout this and the next Chapter, I repeatedly refer to our set of B - and R -band CCD images of the Coma cluster core and of a background field. Characteristic of early-type galaxies such as dwarf ellipticals is the red color of their old stellar populations. For such objects, the R -band image has a higher signal-to-noise ratio (S/N) for similar exposure times than the B image. That is, there are more objects detected on the deeper R -image than would be detected on the corresponding B image. We refer to this R image as the *primary*, since it will be the image from which the primary sample of objects is detected. The B image is referred to as *secondary*, and it provides the photometry necessary to construct a $(B - R)$ color for the primary sample of objects. Throughout this chapter I use R and B as examples of primary and secondary images, though these could equally well be any two band passes (e.g. $(B - V)$, $(V - I)$, etc.).

Fundamental to the application of the techniques developed in this Chapter is the assumption that the image(s) to be analyzed are suitable for photometry. In regard to this assumption, there are four preliminary steps to keep in mind. First, all images must have had the usual and required preprocessing done to remove the instrumental signature; for our Coma CCD images, this is described in Chapter 4. Second, all images of the same field (and the same bandpass) are averaged together in some manner to yield a single, higher-S/N image for each field. Third, all secondary (B) images

are registered with fractional pixel accuracy to the reference frame of the primary image of the field. Finally, the image quality (as measured by the width of the stellar profiles; i.e., the *seeing*) of the primary and secondary images must be the same. If these differ, the highest quality image must be degraded to match the lower quality image. In our case we completed these four steps within the IRAF¹ environment, using the tasks *noao.imred.ccdred.ccdproc*, *images.imcombine*, *images.geomap/geotran*, and *images.gauss*. Refer to Chapter 4 for further details and comments on color estimation.

In the following Sections we describe in detail the astronomical and statistical principles fundamental to our calculation of total magnitudes, colors and intensity-weighted moments for faint objects on large-format CCD images. Note, however, that this methodology is not limited to galaxy photometry. It may be applied successfully in a wide variety of instances, with the proviso that the images to be analyzed are uncrowded (i.e. the separation between the objects being studied exceeds their characteristic dimensions). We begin in Section 2 with the statistical arguments leading to the estimation of accurate and unbiased mean sky values, applied to object detection and photometry. In Section 3 we discuss our generation of artificial images for use in testing our code. These images are realistic in the sense that they match well the faint galaxy population that we observe in the Coma cluster. Section 4 discusses

¹IRAF is distributed by the National Optical Astronomy Observatories, which are operated by the Association of Universities for Research in Astronomy, Inc., under contract to the National Science Foundation.

image analysis and classification via intensity-weighted radial moments. In Section 5 we describe the calculation and calibration of instrumental total magnitudes, fixed-aperture colors and measures of surface brightnesses. In Appendix B, I provide a brief User's Manual for DYNAMO, which contains a description of how to obtain the FORTRAN source code electronically. Note that the IRAF IMFORT interface (Tody 1986) is used in all instances to access IRAF images (i.e., a file extension of *.imh*).

2. ESTIMATION OF A MEAN SKY INTENSITY FOR OBJECT DETECTION AND PHOTOMETRY

For all but the most crowded fields, the set of pixels composing a CCD image is dominated by *sky pixels*, those which do not contain flux from objects such as stars or galaxies. These sky pixels have a mean value and a scatter about this mean, governed by Poisson statistics (Section 2.1). Typically in our applications, the images are only sparsely covered by objects, such that the total number of *object pixels* (i.e. the fractional area) is $\lesssim 4$ percent. Thus in general, the probability distribution function of pixel intensity values is dominated by a Gaussian distribution for the sky pixels, skewed towards brighter intensities, with a bright-side tail extending to the highest object intensity values (Figure 2.1). While the contamination by number is small, the contamination arising from the large intensity values of these object pixels is extreme, and therefore the estimates of a mean sky value are not trivial. In our approach to faint galaxy photometry, there are two separate instances in which we depend upon

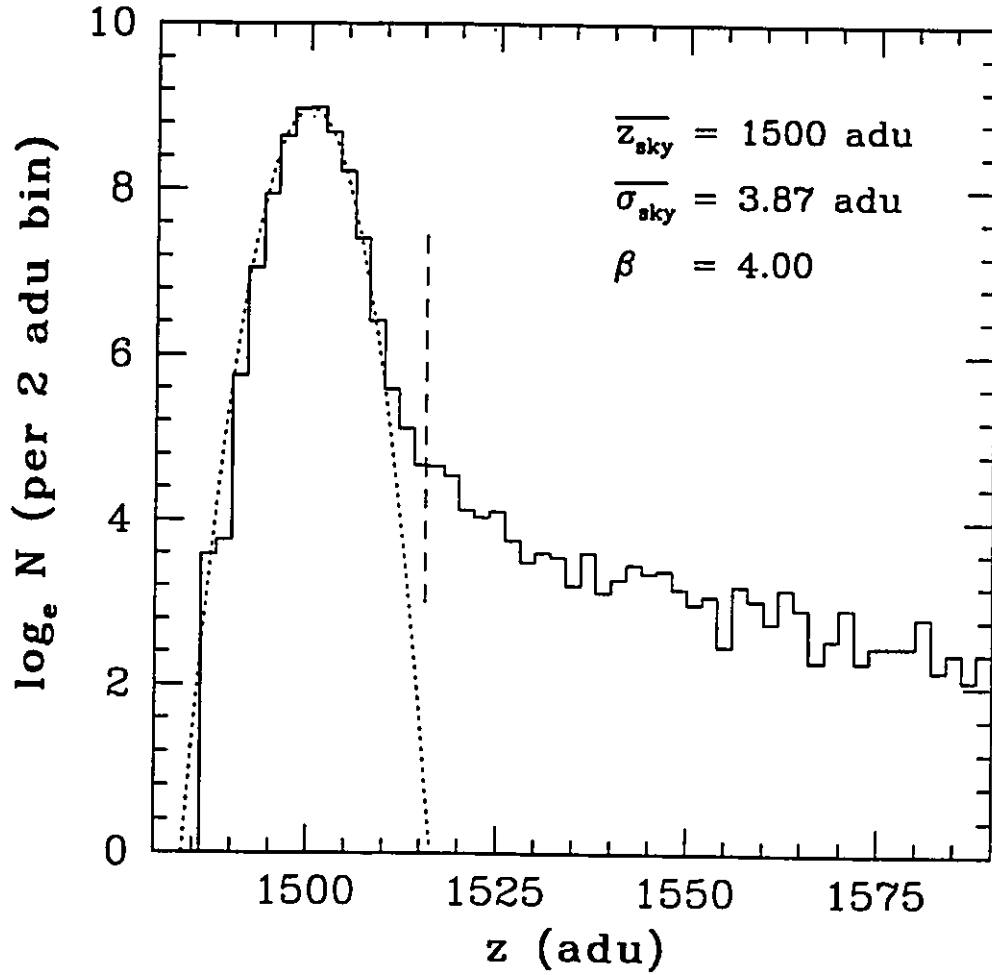


Figure 2.1: A randomly-selected sample of 40 000 pixels was chosen from an artificially-generated CCD image (Section 3). The dotted line illustrates our Gaussian solution for the sky; the mode sky is given by $\overline{z}_{\text{sky}}$, and the standard deviation by $\overline{\sigma}_{\text{sky}}$. It is obvious that the *sky* pixels dominate in number over the *object* pixels, and that the sky pixels with intensities below the mode are completely uncontaminated. When sorted in intensity, the pixels used for object detection are those above the detection threshold, corresponding in this example to $\beta = 4$, and illustrated here by the dashed line. These pixels are fewer in number, but otherwise easily discernible.

accurate and consistent estimates of the average sky pixel intensity.

First, we must estimate a *global mean intensity* and its dispersion, used to detect objects on an arbitrary CCD image. The object detection process (Section 2.2) then assigns all pixels with intensities above some chosen threshold as object pixels, from which a small subset of pixels correspond to object centers. This technique assumes that the image is globally flat, and we depend primarily upon our ring median filter (defined in Chapter 3) to accomplish this.

Second, we must estimate the *local sky value* in the vicinity of each object, in order to calculate accurate estimates of the total flux emitted by each object (Section 5.1). The estimate of object magnitudes is essentially an exercise in counting. We count the total number of photons received within the area of an object, and subtract from this the number of photons which would have been counted even if the object were not there (i.e., the mean sky level). This, unfortunately, is not a trivial task, and for faint objects uncertainty in the local sky level is a limiting factor in our ability to compute accurate and unbiased photometry. To compute accurate values for object total magnitudes, one must first estimate a mean sky value (in ADU) at the exact location of the object in question (starlike or non-stellar); ideally, this would be the *true* sky value at that location. However, the object and sky share the same set of pixels, hindering the the estimate of this mean sky value, and coupling the determination of the total magnitude and local sky value.

With the *global* sky estimation, we typically choose $\sim 10^4$ unique pixels, selected

at random to sample the entire image. For the *local* sky estimation, we compute a modal sky value in a sky annulus around each object. The inner radius of the annulus is set to minimize the contamination from the object flux (i.e. sufficiently large that the object's intensity level is negligible), while the outer radius is set to ensure a large number of pixels. Regardless of whether the estimate is global or local, the set of pixels must be sufficiently large, to ensure that the mean sky estimate is statistically valid and representative. In both cases the sample of pixels is contaminated by non-sky pixels, either random pixels sampling an object, or close neighbors contaminating the sky annulus of an object in question. Thus, we implement an iterative method to accurately estimate the *mode* and *standard deviation* for this vector of sky pixels, using Chauvenet's criterion to trim obviously discrepant (non-sky) pixel intensities. Our routine is based on techniques developed for DAOPHOT II (Stetson et al. 1990), and it consistently matches the results of his code when applied to similar data vectors. In Appendix A, the relevant principles and justifications of this method are discussed in the context of faint-galaxy photometry. Below, we discuss details of object detection and sky annulus selection.

2.1 Global Modal Sky and Object Detection

Provided the primary CCD image is globally flat, then object detection becomes trivial. Simply, *every local intensity maximum exceeding a global intensity threshold is associated with the center of a unique object*. Initially, we select 4×10^4 unique and

random pixel locations. The subset of these pixel values which are within the valid intensity range form the data vector, from which the global mode $\overline{z_{\text{sky}}}$ and standard deviation $\overline{\sigma_{\text{sky}}}$ are iteratively estimated.

In our implementation of object detection, we define the detection threshold (Figure 2.1) to be an intensity level, some multiple of the standard deviation $\overline{\sigma_{\text{sky}}}$ above an average sky value $\overline{z_{\text{sky}}}$. For an object to be detected it must have at least one pixel which exceeds this threshold. We define a user-specified dimensionless parameter β , typically in the range 3.5-5.0, with the lower limit set to avoid detecting bright peaks in the Poisson noise distribution (Figure 2.2). Then we group for further analysis, all pixels satisfying

$$z_i \geq (\overline{z_{\text{sky}}} + \beta \overline{\sigma_{\text{sky}}}). \quad (2.1)$$

Note that pixel values falling below the detection threshold can not (by our definition) be designated as object centers; these pixel values are immediately discarded. Figure 2.1 illustrates the distinction between the more numerous *sky* pixels, and those *object* pixels, located above the detection threshold given by (2.1).

These object pixels compose a data vector which is then sorted by intensity into descending order. These pixels are divided into two groups: (1) pixels defining the peak-flux intensity for potential object centers, and (2) those pixels which are connected neighbors of a potential object center (i.e. they belong to an existing object). By analyzing all object pixels, and separating out those in group 1, we have deter-

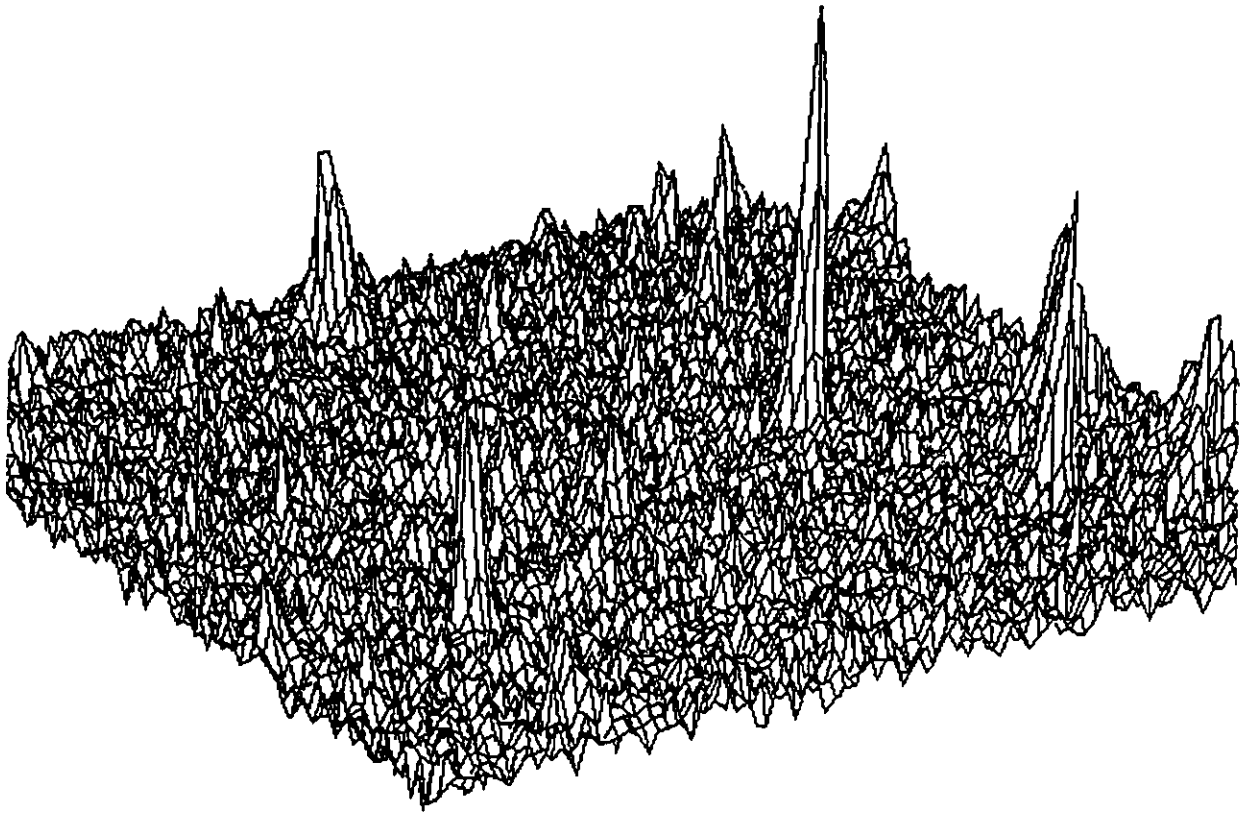


Figure 2.2: Here, the pixel intensity is plotted as a function of position for a small region on a typical CCD image. While the seven or eight of the brightest objects are obvious above the Poisson sky noise, a detection threshold is necessary to separate the faint but ‘real’ objects from those due to peaks in the sky noise.

mined all object centers. We proceed to do this separation by defining the location of the first (brightest) pixel as the peak-flux position of the first object. For the remaining objects, we take advantage of the fact that for individual objects, the pixel intensity values decrease rather smoothly as the radial distance from the center increases (at least until the Poisson noise in the object's wings begins to dominate the signal).

Thus stepping through the ensemble of all object pixels, each subsequent pixel will form an element of the first object at increasing radii, or will be the peak-flux pixel of a new object. We defined a logical function called *neighbor*, which we use to divide the pixels into their two groups; it returns *false* if the i^{th} pixel is isolated (i.e., separated from an existing peak-flux object center by lower-intensity pixel values; group 1), and returns *true* if this i^{th} pixel is separated from a peak-flux object center by less than the seeing disk radius, or if the pixel is connected to a brighter pixel of the same object, forming part of the decreasing continuum of pixels belonging to an existing object center (i.e., group 2).

By applying the *neighbor* function to the sorted vector of pixels brighter than the detection threshold, we obtain our list of center positions (integer peak-flux pixel coordinates x_{cen} and y_{cen}) for individual and unconnected objects. It is clear then that in this implementation, if the detection threshold is too low, isolated bright sky pixels will cause a multitude of spurious/false detections. In addition, only objects with (at least) one pixel above the threshold are detected; genuine low surface-brightness

objects which never peak above this threshold are not detected. In most instances this is not a problem, since we adopt a detection threshold corresponding to about one percent of the mean sky level; objects below this level will more than likely be fainter than the adopted limiting magnitude.

A brief discussion of object detection completeness is warranted here. The analysis of our artificial star and galaxy field images can not yield a universal completeness function applicable to all CCD images. This completeness function will depend strongly upon the presence and amplitude of light gradients (often arising from large, bright galaxies) and on the degree of object crowding. Furthermore, any predetection processing of the individual images, such as reducing light gradients via median filtering or isophotal ellipse fitting, will strongly affect the detection completeness function. IRAF's *noao.artdata* package for artificial star/galaxy generation provides one tool to estimate the magnitude completeness function of an arbitrary image, in a manner analogous to the artificial star experiments carried out using the ADDSTAR routine in DAOPHOT II (e.g., Harris et al. 1991; Butterworth & Harris 1992; McLaughlin et al. 1995). In Chapter 4, we adopt an alternative method, and compare detection efficiencies and photometry from overlapping images of the Coma cluster region under study.

2.2 Annulus Selection For Local Modal Sky

We consider local sky estimates computed in a sky annulus about each object

as the most appropriate and accurate method for faint galaxy photometry. We let x_{cen} and y_{cen} denote the object's peak-flux pixel position, and the parameters R_{in} and W_{ann} are specific for a given population of objects. R_{in} denotes the inner radius of this sky annulus (in pixels), a characteristic distance at which the object's signal becomes negligible. W_{ann} defines the pixel width of the sky annulus, selected to ensure that a sufficient number of pixels are used for the sky estimation. R_{in} and W_{ann} are obviously constant for stellar images (i.e., some constant times the measured FWHM), but they vary for non-stellar objects. Thus for accurate photometry of faint galaxies, this annulus must be chosen with care to reflect the projected dimensions of the galaxies.

Then for each detected object, the radial distance of the i^{th} pixel from the peak-flux pixel is given by

$$r_i = \left[(x_i - x_{\text{cen}})^2 + (y_i - y_{\text{cen}})^2 \right]^{1/2}, \quad (2.2)$$

and a data vector of intensity values is constructed from all pixels which satisfy the criteria

$$R_{\text{in}} \leq r_i \leq R_{\text{in}} + W_{\text{ann}}. \quad (2.3)$$

The resulting data vector which is passed to the statistics routine described above. The local sky mode z_{sky} and standard deviation σ_{sky} are computed, and used to derive the object's aperture magnitude and color, as described in Section 5.

In summary, we adopt the iterative trimming techniques of Stetson et al. (1990)

and Stetson (1994) to estimate the sky mode and standard deviation from a vector of pixel intensity values. Our mode estimates are consistent with those obtained by DAOPHOT II to within a scatter of ± 0.2 ADU. This technique is used for to estimate the mode sky locally (in annuli about individual objects, for accurate magnitudes), and globally (over the entire image, to set the object detection threshold).

3. TESTS WITH ARTIFICIAL CCD IMAGES

It is fundamental that we assess the validity of our general approach to automated photometry and classification, and the accuracy of our program code DYNAMO. In order to fully test and characterize these aspects, we have used IRAF's artificial image/object generation packages (*noao.artdata.gallist*, *.starlist*, *.mkobject*) to generate two realistic, artificial CCD images, which we have analyzed using DYNAMO. While any selection of galaxies and stars which span a reasonable magnitude will enable us to test our code, we carefully matched the distribution in apparent magnitude with that expected for our CCD data of the Coma cluster. In doing so, we simultaneously determine an approximate apparent magnitude at which low-S/N effects become dominant.

We generated two 1024^2 CCD images (Figure 2.3), each with a gain of 64.2 e^-/ADU , read noise of 7.51 e^- , a mean background level of 1500.0 ADU, and the corresponding Poisson noise. To each image we added one distinct population of object. The first image consists of 500 Gaussian stars, with a full-width at half of

the intensity maximum (FWHM) of three pixels (corresponding to Gaussian standard deviation of $\sigma_G = 1.27$ pixels). The second image consists of 500 exponential profile galaxies modified by seeing, with minor to major axis ratios of $0.1 \leq b/a \leq 1.0$. Our choice of an exponential profile is consistent with current observations for the majority of dwarf elliptical galaxies (Ferguson & Binggeli 1994; Chapter 5 of this thesis). The spatial distribution of all objects was determined by random sampling from a uniform distribution; in this manner, crowding effects are minimized.

The input luminosity functions of the stars and galaxies (Figure 2.4) were matched to those observed for the Coma cluster (Chapter 5), and both are defined over a range in apparent magnitude from $15.0 \leq R \leq 24.0$. With a redshift of $cz = 7000$ km/sec and a Hubble parameter of $H_0 = 86$ km/sec/Mpc, the Coma cluster distance modulus is $R - M_R = 34.55$, and this apparent magnitude range corresponds to absolute magnitudes $-19.55 \leq M_R \leq -10.55$. This range in total magnitude includes the brightest dwarf elliptical galaxies, and extends fainter than our limiting magnitude of $R = 22.5$ mag (Chapter 4). For stars, the luminosity function was defined as a power law, given by $n(m) = 10^{0.4m}$, whereas the galaxies are described by a Schechter luminosity function (see Section 3 of Chapter 5), with a characteristic R magnitude of 15.50, and a power-law exponent of $\alpha = -1.45$.

Our simulations are realistic insofar as the artificial images adhere to the observed intensity profiles, the sky pixels scatter about the mean value according to Poisson statistics, and the object luminosities (and diameters) correspond to a realis-

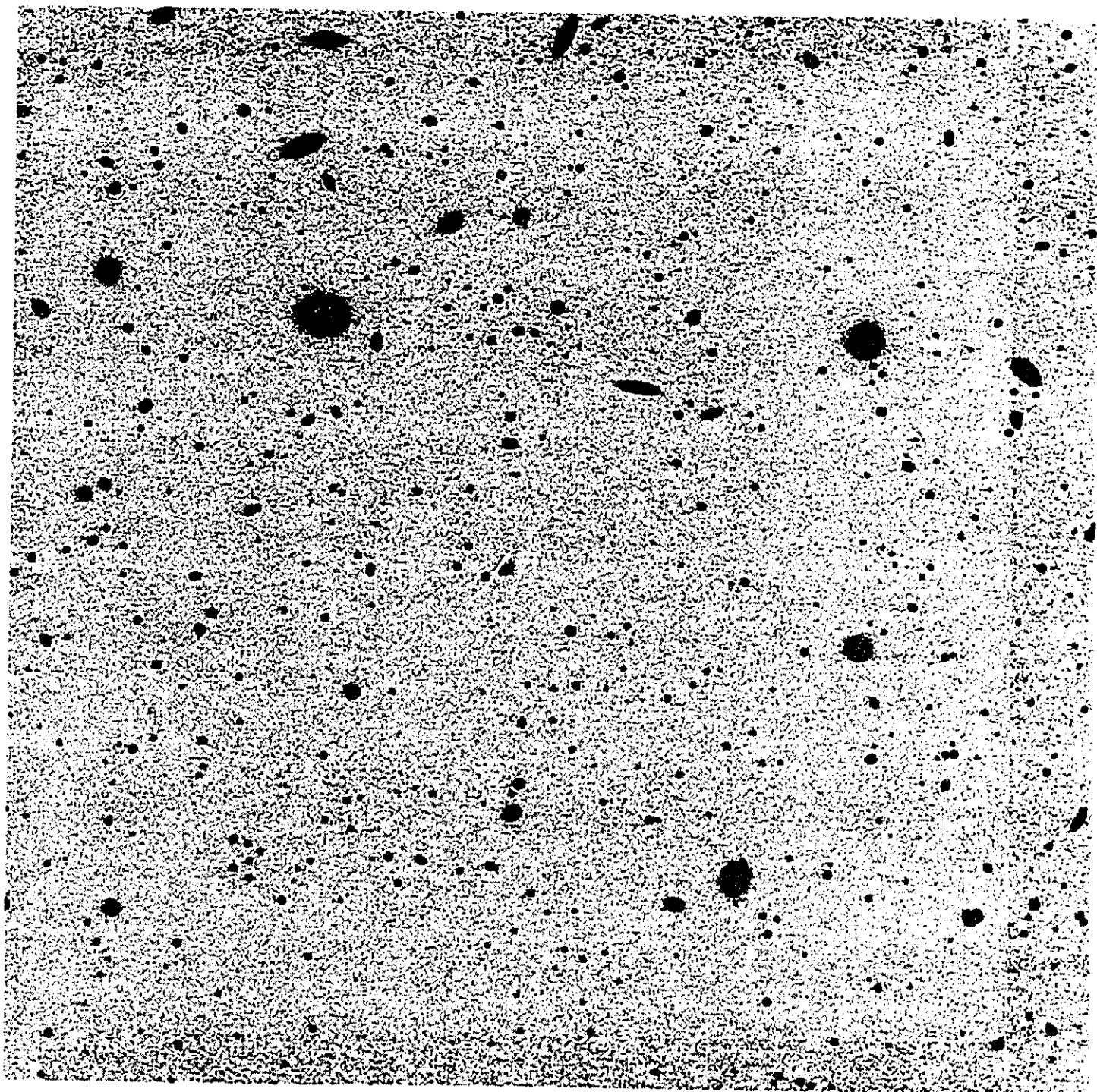


Figure 2.3: This greyscale plot illustrates the range of shape and magnitude input for exponential disk galaxies on the artificial CCD image. The 500 exponential profile galaxies are distributed uniformly (randomly) in space, and in R magnitude according to a Schechter luminosity function.

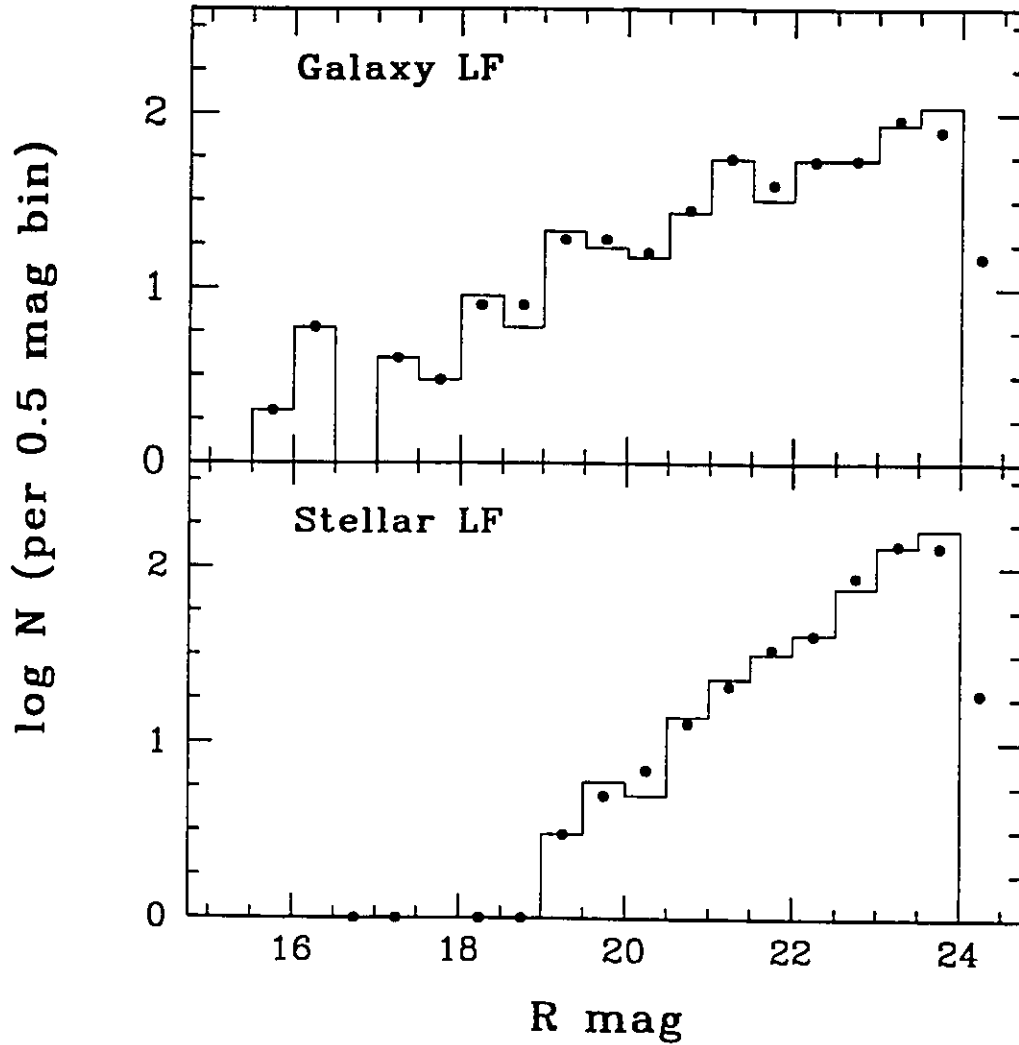


Figure 2.4: The luminosity functions for the artificial images are plotted. The solid line histogram refers to the input object luminosity functions (these are the Schechter function for the galaxies, and a power law distribution for the stars). The solid dots refer to the measured $R_{2,r1}$ magnitudes. This illustrates that even with these uncorrected total magnitudes, the measured luminosity functions agree well with the input, except for the last bin. (Objects input in the last bin of the luminosity function can scatter to fainter values).

tic range in magnitude (and surface brightness). However, our artificial CCD images are cosmetically perfect, uncrowded, and globally flat (i.e. there are no overall light gradients). These differences must be kept in mind when comparing the results of the artificial image analysis with our actual results for the Coma cluster images. The results of these simulations are described at the appropriate positions throughout this text. The results are given as a comparison between the IRAF input quantities and the values recovered by our analysis using DYNAMO, most often as a function of total magnitude. In general, we find that the total magnitude and intensity-weighted moment estimates work exceedingly well, verifying our techniques.

4. IMAGE ANALYSIS AND MOMENT DEFINITIONS

The measurement and classification of an ensemble of objects on any given digital image is based upon the intensity-weighted image moments. For our analysis of faint (low-S/N) dwarf galaxies, the calculation of these image moments depends strongly on (i) the modal sky values estimated within the vicinity of individual objects (Section 2.3), and (ii) the inclusion of pixels at large radii from the object, since these intensities are dominated by Poisson noise. In this section we define a radius R_ℓ of a circular aperture interior to which the computation of all moments is carried out; it is large enough to enclose the object, yet minimizes the number of sky pixels. Note that R_ℓ is used *only in the calculation of the image moments*, and is not used directly for any photometry calculations.

After defining this limiting radius, we go on to define and describe the calculation of intensity-weighted object centers and two radial moments. We do not attempt to estimate uncertainties for the structural parameters calculated here. The accuracy of their values depends strongly upon the S/N of the individual object, with the uncertainties related to uncertainties in mean sky level, usually dominated by Poisson noise. In general, we observe that estimates for intensity-weighted moments scatter about some true mean value, with the scatter increasing for fainter objects. This indirectly reflects the parameter uncertainties.

4.1 Limiting Radius R_ℓ for Summations

The computation of accurate intensity-weighted radial moments for low- S/N data has an inherent difficulty: one needs to know an object's extent in order to carry the radius integral outwards sufficiently far, but it is the radial moments themselves which define the objects' size. If the sums are not carried sufficiently far outwards, the resultant radial moments will be underestimated; if the sums are computed out too far, they are (often) rendered meaningless, since at large radius, the Poisson sky noise dominates the intensity contribution to the sums. We therefore define the radius R_ℓ for a given object, to be *the radius at which the object's signal drops to within one percent of the local sky value*, exterior to which the Poisson sky noise dominates (Kron 1980).

For each object, we place concentric circular apertures around its peak-flux pixel

location, and compute the mean of the pixel values within these apertures. Adopting the local sky mode z_{sky} (Section 2.3) as the *true* local sky level around the object in question, we can determine at what radius the *mean* pixel value $\langle z \rangle$ drops to the required one percent of the sky value. We denote the interior and exterior edges of each aperture by r_{in} and r_{out} ; the smallest aperture has $r_{\text{in}} = 2.5$ pixels, and for each concentric aperture, r_{in} is incremented by 0.5 pixels. We define a constant aperture width of two pixels, $r_{\text{out}} = r_{\text{in}} + 2$, such that $\langle z \rangle$ is based upon a minimum of 20 pixels, but which increases rapidly with aperture radius. For each (overlapping) concentric aperture, we compute the mean intensity for the set of pixels satisfying

$$r_{\text{in}} \leq [(x_i - x_{\text{cen}})^2 + (y_i - y_{\text{cen}})^2]^{1/2} < r_{\text{out}}; \quad i = 1, \dots, n. \quad (2.4)$$

Typical of stars and faint galaxies, this mean intensity value will decrease outwards, approaching the local sky value computed within the sky annulus. When the mean value first satisfies $z \leq 1.01z_{\text{sky}}$, we define R_ℓ to equal the geometric mean of r_{in} and r_{out} , given by

$$R_\ell = \sqrt{r_{\text{in}} r_{\text{out}}}. \quad (2.5)$$

In this manner we have computed the radius at which the object's signal terminates (at the one percent level) and merges with the local sky level. The uncertainty in our estimate of R_ℓ is due solely to the mean sky estimate $\langle z \rangle$, which for n pixels in the aperture scatters about the true mean with a standard error of $\sigma_{\text{sky}}/\sqrt{n}$. The

radial moment summations which we calculate below include pixels interior to R_ℓ ; in no way are these estimates systematically dependent upon R_ℓ , unless this limiting radius is systematically underestimated. Nearby objects could potentially cause an overestimate for R_ℓ , and we deal with these difficult cases individually and interactively. However, we are confident that in our implementation, this limiting radius can not be underestimated.

There are two details which remain to be discussed. First, when estimating annular sky values for the calculation of R_ℓ , we choose to use mean values and not the trimmed mode described in Section 2. This trimming routine was implemented to *reject* the bright pixels in a vector, in order to accurately estimate the mode. In this instance, however, we want to keep all object pixels in order to measure the effective object boundary. Thus we compute the true mean value (with contamination from the object itself) to compare to the previously calculated sky mode value. The same argument applies to using the median as an estimate of the average pixel value; it is less sensitive to bright-end contamination, and could result in a value of R_ℓ which is too small.

Second, we address the question of using a circular aperture to compute the intensity-weighted radial moments for elongated (non-circular) objects. For *circular objects*, the limiting radius is a well-defined concept; the pixel values decrease *uniformly* as the radius increases (desired). For *elongated objects*, at least some part of the object will extend into an annulus at the corresponding radius, and the cal-

culated R_t will measure the full extent of the semimajor axis. The pixels interior to this circular aperture are used to calculate the actual radial moments, and for elongated objects, parts of the circular aperture contain sky pixels. The Poisson sky noise dictates that the sky pixel intensity values will scatter about zero (i.e. $z_i - z_{\text{sky}} \neq 0$), contributing to the radial moment summations. Assuming that *at a given radius* there are equal numbers of sky pixels on either side of the elongated object, distributed in the same manner about the true sky value, then the effect of these pixels will cancel each other in the summations, and the only effect will be increased noise or uncertainty in the radial moment parameter estimates.

4.2 Intensity-Weighted Averages For Object Centers

The object detection routine discussed in Section 2.2 provides the peak-flux object centers, integer values, represented by x_{cen} and y_{cen} . Here, we compute object centers via intensity-weighted averages, positions which are accurate at the fractional pixel level. The summations are computed using all pixels interior to a small aperture, with a typical radius of two pixels; this is sufficient to constrain the center estimate to be nearby the peak-flux pixel center. Here we let x and y represent image pixels interior to this aperture, and throughout this chapter we let I represent the sky-subtracted pixel intensities, given by

$$I = z_i - z_{\text{sky}}. \tag{2.6}$$

Then, the accurate (intensity-weighted) centers are given by

$$\langle x \rangle = \frac{\sum xI}{\sum I}, \quad (2.7)$$

and

$$\langle y \rangle = \frac{\sum yI}{\sum I}. \quad (2.8)$$

Figure 2.5 illustrates that our calculated center positions compare well with the values input for the artificial images. The estimates are unbiased, and the scatter is on the order of ± 0.2 pixels for bright stars and galaxies, increasing to ± 0.4 pixels for the faintest objects.

4.3 The Intensity-Weighted Radial Moments

The intensity-weighted radial moments used here were first defined in their integral form by Kron (1980). Here, we adopt the discrete form given by, for example, Harris et al. (1991). The first moment of the radial intensity distribution is given by

$$r_1 = \frac{\sum rI}{\sum I}, \quad (2.9)$$

while the second negative moment is given by

$$r_{-2} = \left(\frac{\sum I/(r^2 + 0.5)}{\sum I} \right)^{-1/2}. \quad (2.10)$$

Above, r_i represents the distance (in pixels) of the i^{th} pixel from the object's peak-flux

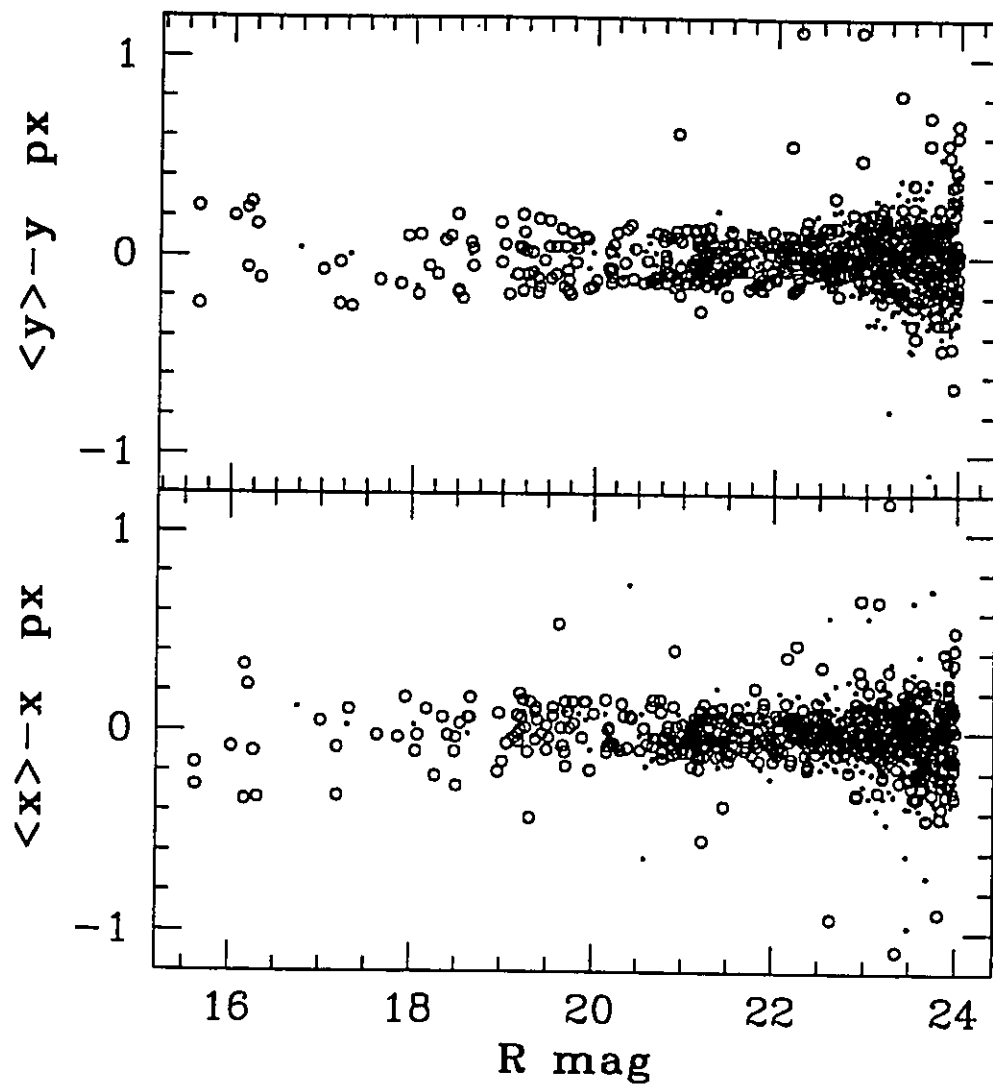


Figure 2.5: Object center positions versus the input R magnitude. The centers are derived using intensity-weighted averages. It is clear that our estimates are unbiased, with a scatter increasing from ± 0.2 pixels for bright stars and galaxies, to ± 0.4 pixels for the faintest objects.

pixel center. All summations described in this section are taken over the ensemble of pixels which satisfy the criterion

$$r_i^2 = [(x_i - x_{\text{cen}})^2 + (y_i - y_{\text{cen}})^2] \leq R_\ell^2. \quad (2.11)$$

This pixel selection differs from that used during the photometry calculations (Section 5). Provided that at least half of any pixel is interior to R_ℓ , that pixel is included in the summation. It is not logical, in this context of moment definitions, to sum fractional pixel values. In our implementation, these moments have units of pixels, and are constrained to lie in the range zero to R_ℓ .

These two radial moments provide different and complementary descriptions of the radial intensity distribution for individual objects. The moment r_1 is an indicator of the image wing spread and thus of physical dimension (see below), whereas r_{-2} quantifies the degree of central concentration of an object. For both moments, starlike objects have (similarly) low values for all magnitudes, and non-stellar (galaxy) images scatter to larger values. Since the r_{-2} moment gives highest weight to the brightest pixels, it is stable and more robust than r_1 , and in general less affected by crowding. The constant additive term equal to 0.5 (arbitrary in magnitude) is necessary to avoid singularities, and the $-1/2$ exponent is necessary to retain the dimensions of radius.

We test our implementation of R_ℓ and moment calculation by computing these two radial moments for all objects on both of our artificial CCD images. In Figure 2.6, we plot both r_1 and r_{-2} versus total magnitude, and as described above, the difference

between stellar and nonstellar objects is immediately obvious. The radial moments for the stellar objects are remarkably constant at $r_1 = 1.6$ and $r_{-2} = 1.4$ pixels over the entire magnitude range. This is as expected; for bright stars, the majority of the luminosity is measured, and the first radial moment is constant at its theoretically expected value of $r_1 = \sqrt{\pi/2}\sigma_G$. For faint stars, the r_1 and r_{-2} moments scatter about this true value, yet the average value remains remarkably constant, specifically it does not decrease. We are therefore measuring the total luminosity for these faint stars, enforced by not permitting the limiting radius R_ℓ to drop below the radius of the seeing disk.

Parameter space plots of r_{-2} versus magnitude² have been effective in culling nonstellar objects from samples of starlike objects (e.g., Butterworth & Harris 1992; Fleming et al. 1995; McLaughlin et al. 1995), and it is this technique which we adopt here for our star/galaxy discrimination. Evident in the parameter-space plots of Figure 2.6 is the scattering of non-stellar objects away from the constant stellar sequence, and it is this effect which we take advantage of for our classification. Figure 2.6 also illustrates that at some faint magnitude (i.e., in this case $R \simeq 21$ mag), the nonstellar sequence merges with the starlike sequence. Harris et al. (1991) found that this occurred about one magnitude above their limiting magnitude (a 50 per-cent detection completeness) for their CCD image. This is a direct result of image

²One could possibly obtain better discrimination between stars and galaxies as follows. Define ΔR as a measure of the total magnitude R_{2r_1} minus a fixed aperture magnitude R_{ap} . Then in a parameter space of r_{-2} versus ΔR , both parameters will show a continuous variation for nonstellar objects, away from the constant stellar sequence.

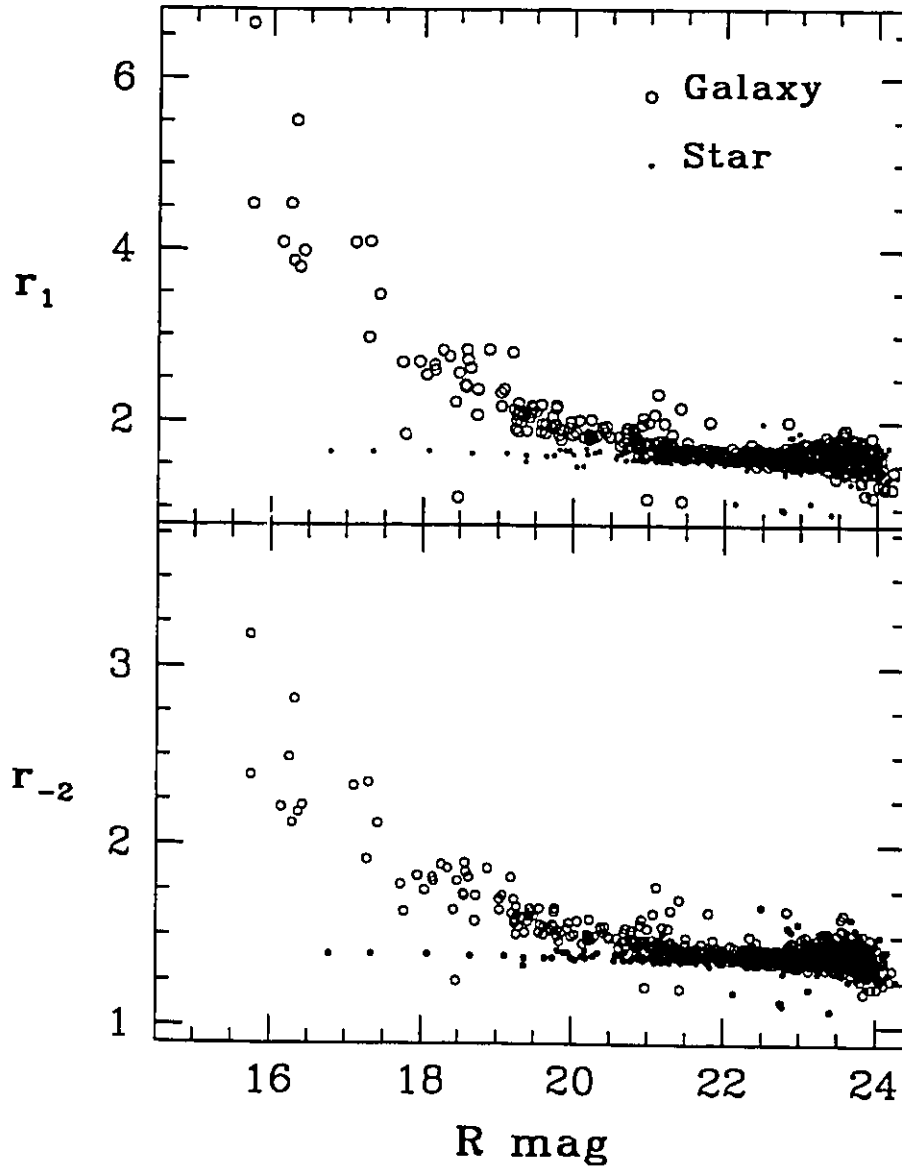


Figure 2.6: Parameter-space plots of the radial moments r_1 and r_{-2} versus the object's total input R magnitude. For both moments, the stellar sequence is constant, and the galaxies deviate from this sequence. It is in this manner that discrimination between starlike and nonstellar objects is accomplished; previous studies which used this technique preferred to make use of the r_{-2} moment, as it is (by definition) more robust to object crowding.

degradation due to finite seeing and a finite resolution due to pixel dimension, and it constrains the ability of the radial moments to discriminate between stars and galaxies at these low flux levels. However, for any CCD image, it is immediately obvious at which magnitude level this effect occurs.

As discussed above, r_1 and r_{-2} are constant for all stellar profiles, but for objects showing any deviations from stellar, these two moments are directly correlated, as illustrated in Figure 2.7, and previously discussed by Harris et al. (1991). These deviations from stellar profiles include both extended objects such as galaxies, and all faint, low-S/N objects. The justification for this correlation is purely empirical. For galaxies, the nonstellar astronomical objects we commonly observe, a decrease in central concentration is linked to an increase in the image wing spread, provided the luminosities are the same. For Figure 2.7, the resolved exponential disk galaxies are reasonably described by $r_1 \simeq 2.83r_{-2} - 2.43$, with both moments measured in pixels.

4.3.1 The Scale Radius For Exponential Profile Galaxies

In 1980, Kron suggested that the r_1 moment provides a measure of the half-light radius for galaxies, and in practice we take advantage of this to obtain accurate estimates of the scale size of faint dwarf galaxies, i.e., the scale radius for exponential profile objects. These exponential profile galaxies are defined in terms of the central

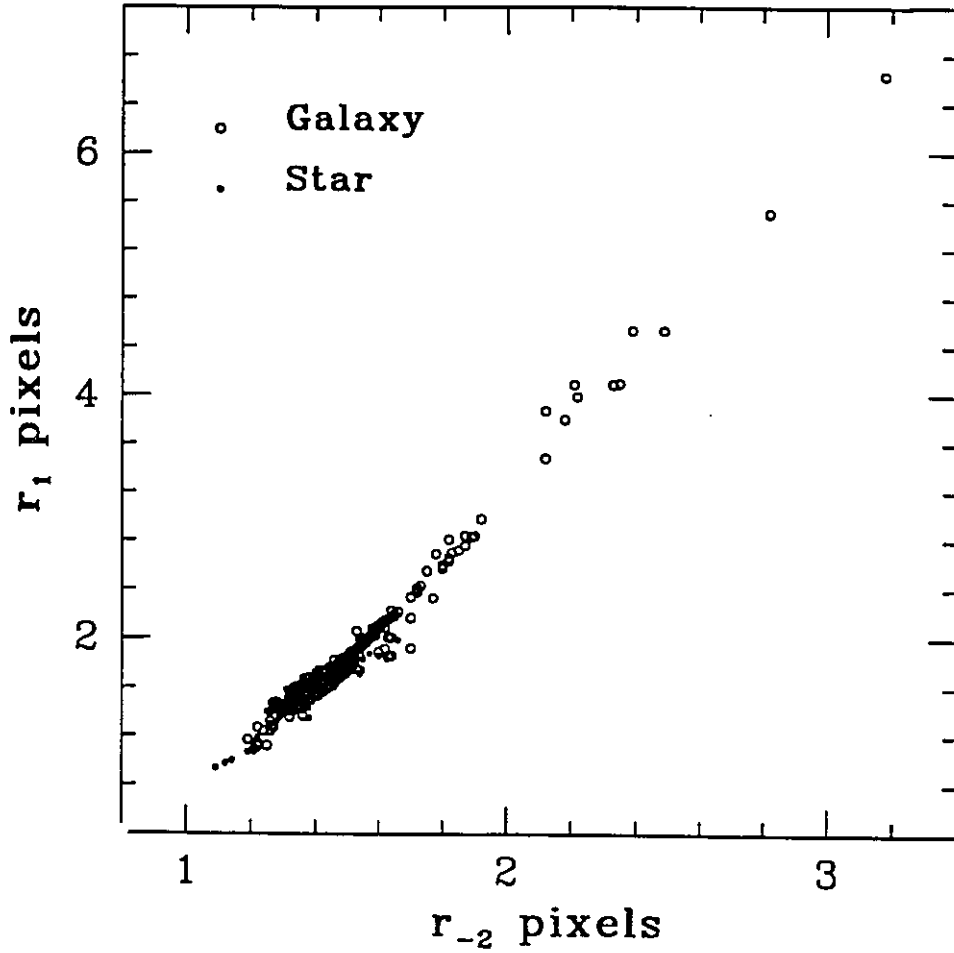


Figure 2.7: The flux-weighted radial moments r_1 and r_{-2} are directly correlated, since for deviations from stellar profiles, a decrease in central concentration is empirically correlated with an increase in image wing spread. While the radial moments for stellar objects are constant in theory, in practice they scatter along this sequence about the constant value.

surface brightness I_c , and a scale radius r_0 , given by

$$I(r) = I_c \exp(-r/r_0). \quad (2.12)$$

As discussed above, the first moment of the radial intensity distribution is defined to be

$$r_1 = \frac{\int_0^\infty r I(r) dr}{\int_0^\infty I(r) dr}; \quad (2.13)$$

for an exponential profile, this evaluates to $r_1 = r_0$. This is highly advantageous, since radial moments can be accurately estimated to (approximately) within one magnitude of the limiting magnitude, and can then yield physical meaningful diameter measurements for dwarf elliptical galaxies.

The half-flux radius provides another method to characterize the physical dimension of faint galaxies. The flux interior to a specific radius, $F(r)$, is defined by the integral of $I(r)2\pi r dr$. We compute this for the exponential profile, and divide by the total flux to obtain

$$\frac{F(r)}{F(\infty)} = 1 - (1 + r/r_0) \exp(r/r_0). \quad (2.14)$$

To solve for the half-light radius, we set this expression equal to 1/2 and solve for r_0 in terms of $r_{1/2}$. They are related by

$$r_0 = 0.596 r_{1/2}. \quad (2.15)$$

Thus the radial moment r_1 is correlated with two physical radii: the scale radius and the half-flux radius for exponential intensity profiles, such as dwarf elliptical galaxies.

We return to an analysis of the artificial galaxy image, for which the *true* half-light radius $r_{(1/2)}$ is known for each object. In Figure 2.8 we plot our calculated value of the radial moment r_1 (pixels) versus the known input quantity $r_{(1/2)}$ (pixels). Except for the smallest (faintest) galaxy images, these parameters are correlated within the scatter. The true radii for the smallest (faintest) objects are essentially unrecoverable; they are unresolved, as finite pixel size and seeing have degraded the image.

On Figure 2.8, we plot a straight line (not a regression line) of slope 0.596. With the freedom to adjust the intercept, it is clear that this theoretical line is a good fit to the the majority of the resolved objects. Thus, the scale radius for exponential disk galaxies can in principle and in practise be obtained for a multitude of faint objects, without the need to perform model fits to surface brightness profiles for the individual objects. Furthermore, we can confidently use r_1 coupled with the CCD image scale and the mean cluster distance to calculate and analyze the physical linear dimensions for the galaxy population being studied.

4.4 Other Moments of the Intensity Distribution

Above we have calculated weighted averages and radial moments, sufficient for our object classification and photometry. There are two other moments which we calculated during our simulations; while they show potential for future use, the intrinsic

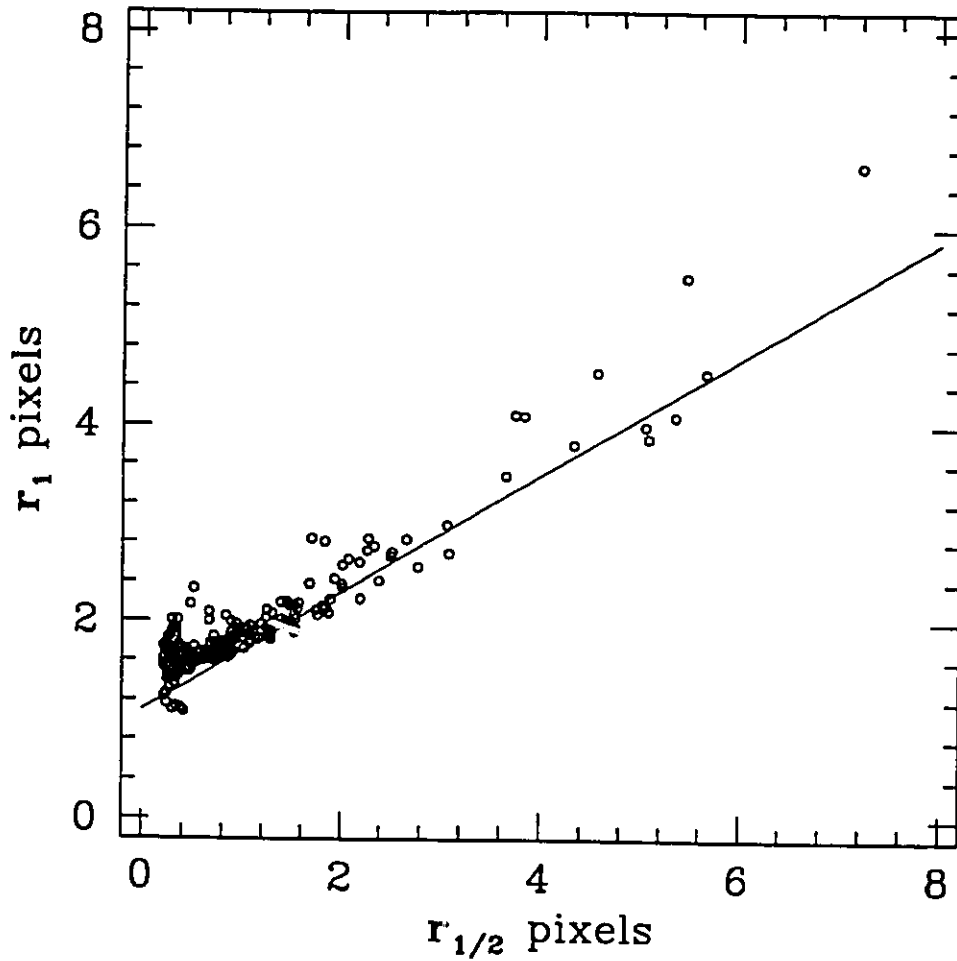


Figure 2.8: For the ensemble of exponential profile galaxies on our artificial image, the radial moment r_1 is proportional to the input value of the half-flux radius $r_{1/2}$, and therefore to the scale radius of the exponential profile. The deviation from the theoretical relationship $r_1 = 0.596 r_{1/2}$ for small radii occurs because these faint objects are unresolved. However, the two most extended galaxies with $r_1 = 5.51$ and 6.64 deviate considerably from the expected line. These two galaxies are those located at the pixel locations (802,713) and (294,731); visual inspection of the CCD image yielded no obvious reason for this discrepancy.

scatter due to the low-S/N levels limit their usefulness in this context. The first moment was the concentration index (e.g., Doi, Fukugita & Okamura 1993; Wirth, Koo & Bershadsky 1994), which has been shown effective in the discrimination between de Vaucouleurs and exponential profile galaxies. By quantifying the degree of central concentration, this moment could in principle be used to automatically distinguish between low surface brightness dwarf ellipticals and giant elliptical galaxies of the same magnitude. The results of our preliminary simulations with artificial CCD images show that, in the implementation of Doi et al. (1993), stars have a constant concentration index, equal to $c_{in} = 0.4$, and that exponential profile galaxies deviate from this sequence, as described by Doi et al. In this manner, c_{in} is well correlated with our other intensity-weighted moments, and is essentially redundant. Extensive simulations involving both exponential profile and de Vaucouleurs profile galaxies would be necessary to characterize the effectiveness and ability of c_{in} to discriminate between profiles at low S/N levels. It does appear, however, that in combination with the object's color and radial moments, the concentration index may contribute to automated analysis of galaxy morphology. We will not refer to this index further.

Second, we calculated the object's ellipticity as an estimate of its elongation. Our method involves computing the second-order intensity-weighted central moments M_{xx} , M_{yy} and M_{xy} , as described by Valdes, Tyson & Jarvis (1983), in the manner described above. In theory, these moments and hence the ellipticities computed from the object images will underestimate the true ellipticity for faint galaxy images, because

corrections for small guiding errors and finite seeing are not taken into account. An analysis of our artificial images revealed the following. For galaxies, the ellipticity is clearly underestimated for the complete range of magnitudes, but especially for the fainter galaxies. This is unfortunate, but arises simply because the moments are too unstable at these low flux levels. The opposite effect is that the ellipticity is overestimated for the faint stellar images. As for the galaxies, the moments are unstable for the low flux levels; however, it is impossible to estimate negative ellipticities, so for intrinsically round objects, the scatter must be one sided. While the ellipticity estimates for the brighter starlike and nonstellar objects are unbiased and accurate, for the faint dwarf galaxies, these estimates are too uncertain to prove useful. Again, we will not refer to them further.

4.5 Interactive Verification For Difficult Objects

In a statistical sense, the intensity-weighted moments will suffer some small degree of contamination due to errors in estimating R_ℓ , usually resulting from nearby objects. We have implemented an interactive facility to enable rapid verification of each object on an individual basis. Simple, low-resolution intensity plots are generated, centered on each object, with the calculated $2r_1$ radius clearly displayed. In this manner, it is immediately clear which objects are affected by nearby neighbors (Appendix B). Based upon this visual inspection, the limiting radius can be modified, and the radial moments recalculated with this new value. In this manner, we are confident that

our radial moment calculations are correct. At the same time, objects deemed to be cosmetic defects or multiple detections can be deleted.

5. FAINT GALAXY PHOTOMETRY

There are a wide variety of techniques which are currently used for faint galaxy photometry. These techniques include fixed or variable circular apertures, isophotal boundaries, curve-of-growth analysis and profile-fitting methods (e.g., Bershadsky et al. 1994; De Propris et al. 1995; Fischer 1995; Jarvis & Tyson 1981; Kron 1980; Lilly et al. 1993; Yee 1991). However, if the CCD images are *uncrowded* (i.e. the distance between galaxy centers is greater than twice their characteristic dimensions), conventional aperture magnitude techniques provide the *most* accurate method for *faint* galaxy photometry. Quite simply, aperture magnitudes count the photons received by the detector; nothing more, and nothing less. In addition to accuracy, aperture techniques are straight-forward; magnitudes and colors are simple to calculate and reproducible. We therefore adopt these aperture techniques, and proceed as follows.

First, we estimate the total magnitude of all objects (starlike and nonstellar) by summing the flux interior to individual aperture radii, defined individually for each object as $2r_1$, and thus equal to twice their half-light radii. Second, we compute a conventional aperture magnitude for each object, with the aperture radius constant for all objects, and selected to maximize the S/N of the population being studied. This constant aperture magnitude is measured in all bandpasses for all objects, and

is used only to compute colors. In detail, these methods are discussed below, along with techniques for calibration and uncertainty estimates.

5.1 Total Magnitude Estimation

The definition of a total magnitude for a non-stellar object is straight forward to state in principle; sum the sky-subtracted luminosity within an annulus enclosing all of the object. In practice, this is non-trivial to implement for an automated galaxy survey. The method which we adopt is to define an *individual aperture radius for each object*, a radius which is proportional to a measure of its physical dimensions. Kron (1980) showed that the radial moment r_1 (Section 4.2) provides a good estimate of the half-light radius for the ensemble of all types of (faint) galaxy images. Both Kron (1980) and Bershadsky et al. (1994) define a circular aperture of radius of $2r_1$, different for each object, which when centered on the galaxy object encloses the majority of its flux, even for rather elongated objects. They determine that the $2r_1$ radius measures about 90 percent of the flux for typical galaxy profiles, and about 95.6 percent for stellar profiles.

For interest, we performed simulations to compute the total magnitude contained within a radius of $3r_1$. Indeed, virtually the total flux is measured, and we obtain unbiased total magnitudes. However, the scatter of these magnitudes is greatly increased over the $2r_1$ magnitudes, and the larger radius poses definite problems for crowded objects. Thus a total magnitude corresponding to the net flux interior to a

circular aperture of radius of $2r_1$ provides *a compromise between high S/N , low scatter and total flux*. For a detailed discussion of this total magnitude estimation technique, its merits and application to photographic images, refer to Bershadsky et al. (1994). Briefly, it is fairly robust and easy to calculate, accurate, and based upon a physically intuitive concept. *We therefore adopt these $2r_1$ magnitudes as our measure of total magnitude*, denoted by a subscript $2r_1$, keeping in mind that a simple numerical factor will be necessary to obtain the true total magnitudes.

The computation of this total magnitude does assume that the radial moment r_1 is known accurately. As discussed previously, r_1 is a quantity which can be badly skewed by noise if the summations are allowed to be carried well past the physical extent of the object, or if the object's surface brightness is low compared with the sky noise (i.e., if it is very faint). For the intermediate and bright galaxy images, the limiting radius R_l ensures that the summations for r_1 are not carried outwards into the noise-dominated regimes. For the faintest objects, the random errors that could dominate measurement of r_1 can not affect our total magnitude, because in all cases, *we define the radius for the total magnitude aperture to be $2r_1$ or the radius of the seeing disk, whichever is the greatest*. In this manner, the magnitudes of the faintest objects include all luminosity within the seeing disk, appropriate since even point-source images are degraded to this extent.

Once r_1 has been calculated, it is straightforward to integrate the total flux contained within the aperture and compute the corresponding total magnitude. We

center our aperture on the peak-flux pixel of the object. This avoids problems from asymmetric or crowded objects, for which the intensity-weighted object centers could be offset from the true center by a distance of one or more pixels. The method used here to select pixels and sum the enclosed flux is that of Stetson et al. (1990). We compute the fraction of the i^{th} pixel which is interior to the aperture radius, and include the same fraction of the pixel's flux in the summation. In doing so, we reduce the effect of the summation of discrete pixels, which becomes very obvious for small values (in pixels) of the aperture radius. At the same time, this technique yields the total area within the $2r_1$ aperture to a fraction of a pixel. Note that this summation differs from the moment calculations, for which summations included the i^{th} pixel provided its radial distance from the objects peak-flux pixel was less than R_ℓ .

In more detail, assume that the data vector for the current object consists of $i = 1, \dots, n$ intensity values. Looping through all values of i , the radial distance to the i^{th} pixel is checked to determine whether $r_i \leq (2r_1 + 0.5)$; if not, the pixel is assumed to lie totally outside of the aperture, and is subsequently ignored. Otherwise, the fraction of the pixel interior to the aperture is computed to be

$$F_i = \max [0.0, \min(1.0, 2r_1 - r_i + 0.5)], \quad (2.16)$$

and the area interior to the aperture is incremented as

$$A_{\text{ap}} = A_{\text{ap}} + F_i. \quad (2.17)$$

As usual, the sky-subtracted intensity value is defined by (2.6), and the intensity summation is incremented as

$$\sum I = \sum I + I_i F_i. \quad (2.18)$$

After all n elements of the vector have been looped through, the total magnitude is calculated in its usual form by

$$R_t = \overline{ZP} - 2.5 \log(\sum I / t_e), \quad (2.19)$$

which is normalized to a one-second exposure by the exposure time t_e . The addition of the magnitude zero-point calibrates the total magnitude. The error estimate for the total magnitude is calculated as described in Section 5.3, with the uncertainty $\sigma(ZP)$ added in quadrature to the magnitude uncertainty.

The R_{2r_1} total magnitude was calculated for all objects on both of the artificial CCD images. Figure 2.9 illustrates that for both stars and galaxies, this R_{2r_1} magnitude consistently provides a reasonable measurement of the true total magnitude for all objects; for $R_T \lesssim 22.75$, the scatter in ΔR remains less than 0.1 mag³. It is

³The bright galaxies measured ~ 0.4 -mag too faint represent edge objects, while the 10 or so objects measured $\sim 0.1 - 0.4$ -mag too bright represent inherently faint objects superimposed on brighter objects.

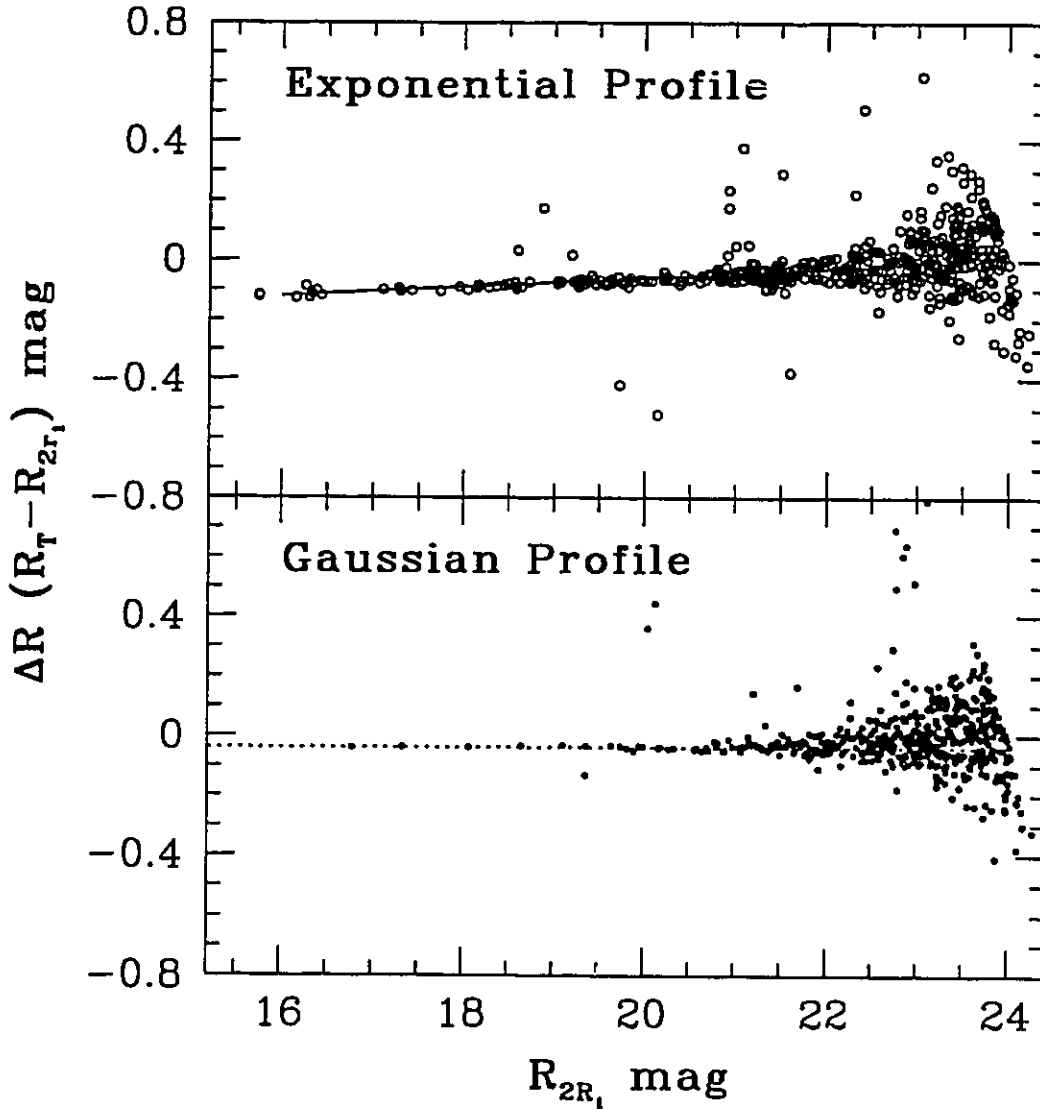


Figure 2.9: The total magnitude R_{2r_1} is defined to include all luminosity in an aperture of radius of $2r_1$; this corresponds to about 90 percent for galaxies and 96 percent for stars (Kron 1980). For both the Gaussian profile stars (filled circles) and the exponential profile galaxies (open circles), this total magnitude can accurately recover the true (input) magnitude for the uncrowded artificial objects. For the galaxies, the solid line defines the correction factor in the interval $16 \leq R_{2r_1} \leq 24$ mag. For faint and unresolved galaxies, all luminosity is measured within the seeing disk. For stars, the dotted lines illustrate the maximum value of the correction factor.

clear from this figure that, as we expect, the total magnitudes are underestimated, and we quantify this below. In the past, Kron’s magnitude was believed to measure a constant fraction of light, independent of the galaxy’s distance or apparent diameter. However, our simulations reveal that the light contained within this $2r_1$ aperture varies from about 90 percent for bright galaxies, to 100 percent for faint galaxies. This is an unexpected but intuitive result; it occurs as the successively fainter galaxies make the transition from large and resolved to small and unresolved, with all of their light then contained within the seeing profile.

As discussed above, we define the aperture radius as $2r_1$ or the radius of the seeing disk, whichever is greater. For the faintest objects, the total flux is measured, and the total magnitude estimates are unbiased. For the brightest galaxies, we adopt a correction factor constant at -0.12 mag. For galaxies in the range $16 \lesssim R_T \lesssim 24$ mag, the magnitude correction factor varies between $\simeq -0.12$ and 0.0 mag. Since the dwarf galaxies which we are most interested in lie within this interval, we adopt a simple linear relationship to correct the magnitudes, given by

$$\Delta R = 0.015 R_{2r_1} - 0.36. \quad (2.20)$$

Over the same magnitude interval, the correction factor for stellar objects varies between $\simeq 0.04$ and 0.0 . For our Coma data set, we discard objects on the stellar sequence brighter than $R_{2r_1} = 19.5$ mag, but below this we do not discriminate between starlike and non-stellar objects. Thus our final sample of objects, for which we

correct the R_{2r_1} magnitudes using (2.20), consists of stars and galaxies. Realistically however, any differences between their magnitude correction factors is completely negligible.

The primary motivation for applying these small correction factors to correct total magnitudes of the faint galaxies is to derive their luminosity function. Figure 2.4 compares the input luminosity functions (in terms of the true input R magnitude) with that defined by the uncorrected R_{2r_1} total magnitude estimates. It is interesting that *even without correcting for this slight underestimation in magnitude*, the derived luminosity function is equal to that input, within the standard Poisson statistics, and except for the faintest bin. This last bin, however, reflects the artificial nature of the simulations: while the measured objects could scatter to lower magnitudes, no fainter objects were present to scatter brightwards. Keep in mind that the R_{2r_1} luminosity function is artificially complete (Section 3). That is, our simulation with artificial CCD images were performed in order to characterize the behaviour of all parameters at faint magnitudes, and we enforced a 100 percent completeness in detection to accomplish this.

5.2 Colors Derived From Standard Apertures

Conventional fixed-aperture techniques are utilized here to generate accurate colors for the ensemble of objects detected on our CCD images. For each object, the net flux within a standard aperture of radius R_{ap} is summed, and converted to a

calibrated magnitude. The aperture radius is constant for all objects, and is usually selected from a curve-of-growth analysis to maximize the S/N of the population being studied. The validity of this approach, with respect to dwarf elliptical galaxies, is discussed in Chapter 4. We assume here that the master images in each band pass have been previously aligned and/or rotated to agree within fractional pixel accuracy with the coordinate system of the primary image. Then the calculation of the aperture color is trivial.

At the peak-flux pixel position of the i^{th} object on both the primary and the secondary images (i.e., R and B images), the local sky mode is calculated, and the sky-subtracted luminosity is summed within an aperture of radius R_{ap} (pixels). The pixel selection and luminosity summations are performed in the same manner as those described in the previous section. The color output to the photometry file is defined as the difference of aperture magnitudes (secondary minus primary; e.g. $(B - R)$), and the net uncertainty estimate on this color is computed by adding the individual aperture magnitude uncertainties in quadrature.

The intensity-weighted image moments are not computed for objects on the secondary (i.e., B) image. These are computed only once, since the S/N on the primary image is much higher. Related to this, note that many of the objects for which we measure colors would not be detected on the secondary image, with any reasonable detection threshold. This is worth further comment. In the sample of objects derived from our Coma images, we are complete in color to a magnitude limit of $R_{2r_1} = 22.5$

mag. This is much fainter than could realistically be obtained by finding objects on each of the R and B images separately, and matching coordinate lists. It is because we know in advance from the R -coordinates where the objects must be located on the B -image, that we are able to measure even very slight excesses in luminosity above the local sky value.

As mentioned in Section 1, when analyzing multiple image fields and/or different bandpasses, special care is warranted. In order to compute accurate colors for all (faint) objects, one must ensure that the image quality is the same; that is, the seeing of the best image must be degraded to that of the worst image, by performing the appropriate convolution with a Gaussian filter. The seeing of a CCD image is measured in terms of the dispersion of the Gaussian stellar profiles, related to their FWHM by

$$\sigma_G = \frac{\text{FWHM}}{2\sqrt{2\ln 2}}. \quad (2.21)$$

For two CCD images with different seeing, we denote the width of the different stellar profiles by subscripts b and w (best and worst), where $\sigma_b \leq \sigma_w$. Then the highest quality image is degraded to the seeing of the worst image, by convolution with a Gaussian filter of dispersion

$$\sigma = \sqrt{\sigma_w^2 - \sigma_b^2}. \quad (2.22)$$

In this manner the fraction of flux summed within a small aperture is independent of

seeing effects.

5.2.1 Standard Aperture Colors for Cluster dE Galaxies

The problem of estimating accurate and unbiased integrated colors for faint galaxies is difficult, and has been approached in several ways. One possibility (e.g., Tyson & Jarvis 1979) is to use isophotal magnitudes, those determined by integrating an object's luminosity outwards to a specified limiting flux, to define an isophotal color. Colors determined in this manner suffer from the difficulties inherent to isophotal magnitudes, such as the isophote measuring a different fraction of the light for objects of different profiles, and the object's flux being undersampled if the isophote is smaller than the seeing disk radius (refer to Lilly et al. 1991 for further discussion). In addition, for accurate color estimates, the same isophote must be used in all passbands, or else a correction factor must be implemented (Tyson & Jarvis 1979). Another possibility is to define the color as the difference of two $2r_1$ total magnitudes. Bershadsky et al. (1994) measure the $2r_1$ radius in one specific band and adopt this value for all other bands, reducing the dispersion in the color estimates arising from random errors in repeated measurements of the $2r_1$ radius. This approach is almost completely independent of seeing effects, profile shape and distance (the latter because r_1 is a metric radius), and is mostly insensitive/independent to color gradients within an object (since it measures virtually all of the luminosity in all bands).

We choose to measure colors within an aperture constant for all objects and on all

images, with a radius R_{ap} comparable to the FWHM of a stellar profile (as described in section 5.2 above, and for example, by Lilly et al. 1995). For our current analysis, this technique offers several distinct advantages over the methods described above. The S/N ratio within a small constant aperture is greater than that found for the full $2r_1$ aperture, and this fixed aperture technique can provide very accurate colors, if the seeing is the same in both filters. In addition, the fixed aperture colors are simple, repeatable and independent of the calculation of the r_1 radius, and for small R_{ap} it is more robust in the presence of nearby objects.

The primary concern⁴ to us is color gradients; much of the controversy over integrated colors boils down to (for this study) whether or not there are color gradients within dE and dE,N galaxies. If a uniform color gradient exists within the galaxy, i.e. if the blue light profile falls off faster than the R -band profile, then a constant radius enclosing some fraction of the total R luminosity will include a greater fraction of the B luminosity, so the measured color is too blue. However, dE galaxies in general are virtually free of the dust, gaseous emission and multiple stellar populations which can give rise to these gradients. While observations of dE galaxies in Fornax (Caldwell & Bothun 1986; Cellone, Forte & Geisler 1994) show no evidence for color gradients within the dE galaxies, observations of Virgo dwarfs (Vader et al. 1988; Durrell et al. 1995; each study examined about 10 dwarf galaxies) and field dwarfs (Chaboyer 1994)

⁴An aperture centered on the bulge of a spiral galaxy measures color which is too red to correctly indicate the true average color of the entire galaxy; this is the result of a difference in stellar populations (color) with location in the galaxy. This will have a negligible affect for our study, since spiral galaxies in the Coma core are virtually nonexistent, limited mainly to background galaxies.

show evidence for color gradients in up to 50 percent of the dwarf galaxies. In the latter cases, both red and blue gradients are observed. If supernova driven galactic winds were successful at destroying internal metallicity gradients, these observed color gradients must be the result of age effects, i.e., multiple stellar populations (Vader et al. 1988; Chaboyer 1994). This differs from giant elliptical galaxies, the majority of which are observed to become redder (i.e., more metal rich) with decreasing radius.

A final possible concern is the presence of a luminous nucleus in the brighter dE galaxies (i.e., denoted as dE,N) in our sample. These objects pose no problems, however, since the fractional luminosity contributed by the nucleus is at most 20 percent, and the colors of the nuclei in dE,N galaxies are not noticeably different from their surroundings (Caldwell & Bothun 1986; Durrell et al. 1995; Vader et al. 1988). As discussed in Chapter 4, the constant aperture radius which we adopt for color determination is 3 arcsec, which for our CCD parameters and a reasonable Coma distance modulus, corresponds to 1.18 kpc. This measures a large fraction of the total luminosity for dE galaxies, and provided that our assumption of no color gradient is correct, it measures the same fraction of light in both the R - and the B -band images. Thus we conclude that our fixed aperture colors are appropriate for the study of dE galaxies in the Coma cluster.

5.3 Calibration of Instrumental Magnitudes

In order to obtain meaningful photometry, one must calibrate the measured in-

strumental magnitudes using standard stars. Regardless of whether these are onframe standards or are located on a separate CCD image, the conceptual basis of the calibration is the same. For a set of standard stars with accurately known magnitudes and colors, one must determine the number of photons detected per second by the CCD, a number resulting from a combination of telescope optics, CCD gain and quantum efficiency and the integration time. This photon rate sets the magnitude zero point, ZP . That is, the magnitude zero point ZP represents the magnitude of a star for which the CCD would measure 1 ADU per second. Note that stars used as standards must be well-isolated and moderately bright; this avoids contamination from nearby objects and ensures that the sky noise is insignificant when compared to the total stellar flux. For these standard stars, their true magnitudes M_i and total uncertainties $\sigma(M_i)$ must be known beforehand. The following equations illustrate the procedure to compute the magnitude zeropoint from standard stars. The zeropoint obtained from these standard stars is then used in (2.19) to accurately calibrate objects of any profile, starlike and nonstellar.

We begin by defining a calibration radius R_{cal} , such that the complete stellar luminosity⁵ is enclosed by a circular aperture of non-integer area

$$A_{\text{ap}} = \pi R_{\text{cal}}^2. \quad (2.23)$$

⁵Once again, a small contribution to the star's flux continues out to large radii. Thus the calibration radius is chosen to enclose a majority of the flux, yet minimize the area dominated by Poisson sky noise.

The sky-subtracted pixel intensities (2.6) within the calibration radius are summed to yield $\sum I$ (in ADU). The image exposure time t_e is used to normalize $\sum I$ to a one-second exposure. Thus the magnitude zero-point which gives the magnitude equivalent to 1 ADU per second is defined as

$$ZP_i = M_i + 2.5 \log(\sum I / t_e). \quad (2.24)$$

The uncertainty on the zero-point estimate itself is then obtained by adding in quadrature the two relevant uncertainties, given by

$$\sigma(ZP)_i^2 = \sigma(M_i)^2 + \sigma(M_{ap})^2. \quad (2.25)$$

The value which we adopt for the actual zero-point is the weighted average of all zero-point estimates for individual onframe standard stars.

$$\overline{ZP} = \frac{\sum_i ZP_i / \sigma(ZP)_i^2}{\sum_i 1 / \sigma(ZP)_i^2}. \quad (2.26)$$

$$\overline{\sigma(ZP)} = \left[\sum_i 1 / \sigma(ZP)_i^2 \right]^{-1/2}. \quad (2.27)$$

While this zero-point for the magnitude scale is determined from stellar objects, it represents a simple conversion factor and is directly applicable to all nonstellar objects. Together with its uncertainty, these two quantities are used throughout to calibrate instrumental magnitudes, as described by (2.19). Note that ZP is simply the magnitude zeropoint. In Chapter 4 we discuss the complete calibration of our Coma photometry, which involves two additional terms: (i) a product of the the

extinction coefficient and the airmass, and (ii) a product of the color coefficient and the object's color.

5.4 Uncertainties For Aperture Magnitudes

To compute the total uncertainty on this zero-point estimate, we proceed in the manner described by Harris et al. (1991), and begin by estimating the uncertainty on $\sum I$. The total variance in $\sum I$ results from three significant contributions, each measured in electrons. We denote the area of the sky annulus (integer pixels) used to estimate z_{sky} by A_{sky} , the standard deviation of the pixel-to-pixel scatter (in ADU) in the sky annulus by σ_{sky} , and the number of pixels in the aperture containing the object by A_{ap} . First, the variance due to photon noise is given by $\sum I g$, where g is the CCD gain (e^-/ADU). Second, the random scatter in the sky pixels under the object contributes a variance equal to $A_{\text{ap}} \sigma_{\text{sky}}^2 g^2$; i.e., the number of pixels in the aperture containing the object times the variance per pixel. Third, the standard error of the mode sky intensity is given by $\sigma_{\text{sky}} (A_{\text{sky}})^{-1/2}$. Thus the variance arising from a possible systematic error in the modal sky level is given by $(A_{\text{ap}} \sigma_{\text{sky}} g A_{\text{sky}}^{-1/2})^2$.

We then sum the variances, divide by a factor of g^2 , and define the uncertainty in $\sum I$ as the standard deviation of $\sum I$, measured in ADU, and given by⁶

$$e(\sum I)_i = \left[\frac{\sum I}{g} + A_{\text{ap}} \sigma_{\text{sky}}^2 \left(1 + \frac{A_{\text{ap}}}{A_{\text{sky}}} \right) \right]^{1/2}. \quad (2.28)$$

⁶As noted by Harris et al. (1991), for faint stars with $\sum I \gtrsim 0$, and if $A_{\text{ap}} \ll A_{\text{sky}}$ as is often the case, then the Poisson sky noise dominates, and $e(\sum I)_i \simeq \sigma_{\text{sky}} \sqrt{A_{\text{ap}}}$.

To convert this to an *uncertainty in magnitude*, we estimate an upper and lower limit to $\sum I$ to be $I_{\max} = \sum I + e(\sum I)_i$ and $I_{\min} = \sum I - e(\sum I)_i$ (constrained to be greater than 1.0 ADU), such that a rough error estimate on the magnitude is given by half of the magnitude difference, given by

$$\sigma(M_{\text{ap}}) = 0.5 \left[2.5 \log \frac{I_{\max}}{I_{\min}} \right]. \quad (2.29)$$

These two equations govern the uncertainty estimates for all calculations of this type, including the magnitude zero-point, the total magnitudes, and the constant aperture magnitudes from which colors are derived.

5.5 Measures of Surface Brightness

We compute two measures of surface brightness for each object with measured photometry. The first is the central surface brightness I_c (mag arcsec²), defined in terms of the peak-flux pixel intensity. For the distance of the Coma cluster, and an image scale of 0.53 arcsec/pixel, I_c measures the central 209×209 pc². Second, we compute $SB_{2.5\sigma}$, an average surface brightness interior to an isophotal level which exceeds the local sky mode z_{sky} by $2.5\sigma_{\text{sky}}$.

We begin by letting ΔS represent the pixel area (in arcsec²), and as in previous sections, $\sum I$, t_e and \overline{ZP} represent the appropriate sky-subtracted pixel-intensity sum within the aperture, exposure time and magnitude zero-point. In addition, we let I_1 represent the sky-subtracted intensity of the peak-flux pixel. Then, the calibrated

central surface brightness, with units of mag/arcsec², is given by

$$I_c = \overline{ZP} - 2.5 \log 10(I_1) + 2.5 \log 10(\Delta S t_e), \quad (2.30)$$

where $\Delta S = 0.53^2$ arcsec² for our Coma CCD images. In Figure 2.10 we plot the central surface brightness versus total magnitude for the stars and galaxies on our artificial CCD images. As is well known, both the stellar and exponential profile decrease in central surface brightness with decreasing total magnitude. For stellar objects with their constant Gaussian profile, I_c is linearly related to R_{2r_1} , with significant scatter in the relationship beginning near $R_{2r_1} \simeq 22$ mag. At any magnitude, our exponential profile galaxies have a lower central surface brightness. In fact, star/galaxy discrimination can be performed equally well in this parameter space, with two differences from the use of radial moments. First, the calculation of I_c as described above is trivial, and does not depend upon summations sensitive to the limiting radius. Second, our technique used to estimate uncertainties for aperture magnitudes apply with only slight modification to values of I_c . In Chapter 4, however, we perform star/galaxy discrimination using the r_{-2} radial moment, as described in Section 4 of this Chapter.

The average surface brightness is defined from the total set of pixels (fractional pixels included) inside our *total* aperture of radius $2r_1$. Only those N_p pixels which have an intensity exceeding the local sky mode by 2.5 sigma (i.e., $I_i \geq z_{sky} + 2.5\sigma_{sky}$) contribute to the sum. There will be a (small) contribution from intensity peaks due to Poisson sky noise; we accept this, with the plausible assumption that the

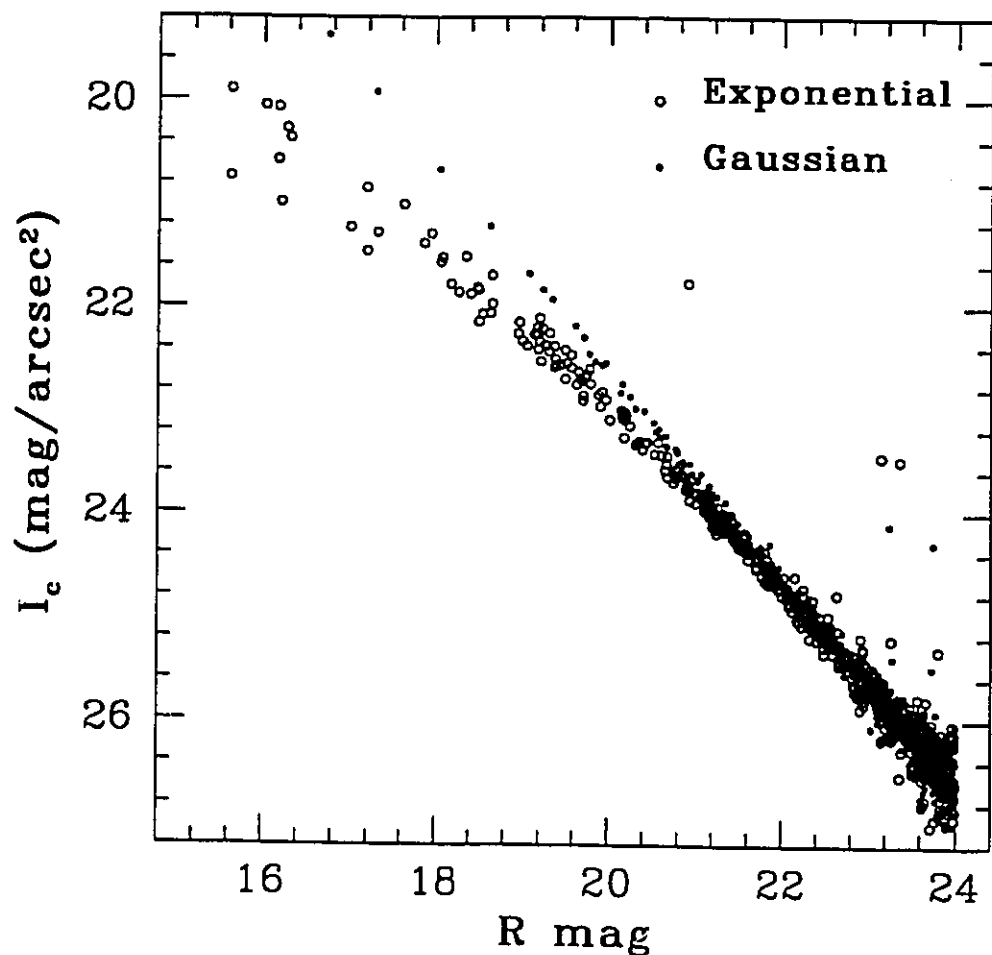


Figure 2.10: The central surface brightness I_c is calculated from the sky subtracted intensity of the central peak-flux pixel, and calibrated in the same manner as the total magnitude. When plotted in the parameter space of I_c versus the total input R magnitude, at any magnitude the faint exponential profile galaxies have a lower central surface brightness than do the stars. This plot illustrates that star/galaxy discrimination can also be performed in this parameter space.

contribution will in most instances be negligible or else cancelled by other object pixels that are lower than they should be. Then the average surface brightness is given by

$$SB_{2.5\sigma} = \overline{ZP} - 2.5 \log 10(\sum I) + 2.5 \log 10(\Delta SN_p t_e). \quad (2.31)$$

Note that this method works providing that there are no other objects within the aperture radius; otherwise, non-member pixels with a flux above $2.5\sigma_{\text{sky}}$ will also be included in the summations.

5.6 An Estimate of the Number of Overlapping Apertures and Edge Objects

As discussed in the previous sections, magnitudes and colors determined via aperture techniques are robust and accurate provided the image is not crowded. For an arbitrary CCD image, we determine whether our aperture magnitudes are contaminated by luminosity from nearby objects, as follows. We locate objects whose peak-flux pixel centers are separated by less than either R_{ap} or $2R_{\text{ap}}$; In most instances, objects of the first type will have a smaller degree of contamination from its nearest neighbor. These objects are found by a simple loop through all detected objects, which keeps track of the object-neighbor separation, and upon termination determines the fractional contribution of overlapping objects. This technique is also used to detect objects overlapping with physical image boundaries. *This aspect of the aperture photometry is fundamental; one must have a quantifiable criterion on which*

to base decisions about whether this method of photometry is valid.

Note that this technique measures a lower limit to the number of overlapping objects, since (i) only the nearest neighbor distance is checked; in the event that there are two or more objects with overlapping apertures, only the closest object pair are flagged; and (ii) contamination from extended objects can occur even if the apertures do not overlap.

Dealing with nearby objects is a common problem with aperture photometry, and unfortunately a complicated one to deal with. For crowded starlike objects, the iterative least-squares simultaneous fitting of multiple stellar profiles (e.g. DAOPHOT II; Stetson 1994) is a very efficient and accurate technique. For crowded galaxy objects, this is also possible (e.g., Fischer 1995). However, in our approach we only *determine the fraction of objects with overlapping apertures as a measure of the degree of crowding*. For the analysis of all of our Coma cluster images, the number of nearby objects is always in the range of $\simeq 2 - 4$ percent. Since this number is so low, we simply discard this set of objects, with the assumption that our final results will not be affected. In our analysis of the artificial CCD images, we do not excise these ‘multiple’ or ‘edge’ objects. Their presence is obvious in Figures 2.4 through 2.10, where these few objects deviate from the mean parameter values more significantly than is typical of the scatter.

6. SUMMARY

(1) We have developed a statistically rigorous and automated FORTRAN code to implement the detection, photometry and classification of faint objects on digital (CCD) images. We created artificial CCD images matched to our KPNO 4-m images, to characterize and verify our code over a range of eight magnitudes for star and galaxy fields consisting of Gaussian stellar profiles and exponential disk galaxy profiles.

(2) Kron's (1980) $2r_1$ magnitude is implemented, and simulations reveal it yields accurate and unbiased total magnitudes. This magnitude has been thought to measure a constant fraction of light, independent of the galaxy's apparent magnitude. However, simulations reveal that the light contained within this $2r_1$ aperture varies from about 90 percent for bright galaxies, to 100 percent for faint galaxies. This occurs as the faint galaxies transition from resolved to unresolved, with all of their light then contained within the seeing disk.

(3) We implement the iterative trimming technique of Stetson et al. (1990) to estimate the most-probable sky intensity and its standard deviation. This approach is used both to set the global detection threshold, and to compute sky-subtracted intensities for individual objects.

(4) Our intensity-weighted moments are calculated using only the pixels interior to a radius R_ℓ . This radius, which maximizes the S/N for the calculation, is computed individually for each object; automatically for the vast majority of objects, and individually for the difficult cases.

(5) Above a magnitude of $R \simeq 21$, we effectively discriminate between stellar

and non-stellar profiles in parameter space plots of r_1 , r_{-2} and I_c versus the total R magnitude. In fact, the central surface brightness I_c is easier to calculate than either of the intensity-weighted radial moments, since it does not involve summations or the estimation of a limiting radius R_ℓ .

(6) We calculate the distances between all object centers, and compare these with the constant aperture radius used to measure an object's color. By counting the number of object pairs which are separated by less than twice the aperture radius, we quantify the effects of image crowding, and determine the fractional number of objects with corrupted aperture colors and magnitude.

Chapter 3

A Ring Median Filter For Digital Images

Following is a reprint of my paper, "A Ring Median Filter For Digital Images", 1995, PASP, 107, 496-501. This material is reprinted with permission from the Publications of the Astronomical Society of the Pacific; as sole author of this material, I hereby grant an irrevocable, non-exclusive to McMaster University and the National Library of Canada to reproduce this material as part of the thesis.

The FORTRAN source code which implements the ring median filter is available electronically via anonymous FTP (the file name is `ringlet1.tar.Z`), in the same manner as described in Appendix B.

McMaster University

Department of Physics & Astronomy

Hamilton, Ontario
Canada L8S 4M1

Jeff Secker
Tel: (905) 525-9140 x 24574
Fax: (905) 546-1252
e-mail: secker@physics.mcmaster.ca

May 31, 1995

Dr. Howard E. Bond, Managing Editor
Publications of the Astronomical Society
of the Pacific
Space Telescope Science Institute
3700 San Martin Drive
Baltimore, MD 21218
USA

Dear Howard,

I am completing a Ph.D. thesis at McMaster University, entitled "The Dwarf Elliptical Galaxy Population in the Coma Cluster Core". I would like your permission to reprint the following journal article (for which I am the sole author) in my thesis:

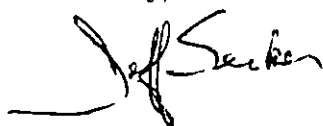
"A Ring Median Filter For Digital Images"

Secker, J. 1995, PASP, 107, 496

I am also requesting that you grant an irrevocable, non-exclusive license to McMaster University and to the National Library of Canada to reproduce this material as a part of the thesis. Proper acknowledgement of your copyright of the printed material will be given in the thesis.

If these arrangements meet with your approval, please sign where indicated below and return this full letter to me. Thank you very much (in advance).

Sincerely,



Jeff Secker

PERMISSION GRANTED FOR THE USE REQUESTED ABOVE:

Publications of the Astronomical Society of the Pacific

Authorized by: H.E. Bond

Title: Editor

Date: 6/12/95

Signature: H.E. Bond

A Ring Median Filter for Digital Images

JEFF SECKER

Department of Physics and Astronomy, McMaster University, Hamilton, Ontario, Canada L8S 4M1
Electronic mail: secker@physics.mcmaster.ca

Received 1994 December 28; accepted 1995 February 28

ABSTRACT. The ring filter is defined as a median filter which assigns weight only to selected pixels in an annulus. Its advantage is that it has a sharply defined scale length: that is, all objects with a scale size less than the radius of the ring are filtered and replaced by the local background level. It provides a fast, simple, and intuitive method to remove the small-scale objects (independent of morphology) from a digital image, leaving behind the large-scale objects and overall light gradients. The ring filter is much faster than the more commonly used filled-box median filter, and completes in one or two passes what previously required a long iterative procedure. Several examples of its use are presented.

1. MOTIVATION

The light distribution on images of galaxies and galaxy clusters is formidably complex. Bright stars and large galaxies combined with the diffuse intracluster light produce convoluted large-scale light gradients across the image, which hamper measurement of faint objects in the field (faint galaxy populations within the cluster, globular clusters around individual galaxies, and so forth). Only by removing the isophotal contours of the giant galaxies and other light gradients is it possible to obtain a globally flat background level, on which photometry of the faint objects can be carried out reliably. The homogeneous conditions provided by the flat background enhance the visibility of the faint, discrete images, and the objects detection and measurement process is greatly simplified (for early examples of this filtering, see for example, Strom et al. 1981; Harris et al. 1983). The most common technique to obtain a globally flat image (leaving the small-scale higher-frequency objects unaffected) uses a filter which is insensitive to the small, faint, discrete objects, and which creates an artificially smoothed copy of the image (for a thorough discussion of the properties of median filters and their applications to image processing in astronomy, refer to Sulentic et al. 1985). This smooth image is then subtracted from the original, leaving behind the small discrete object sources on a flat background.

There are many methods to accomplish this task. However, most are iterative, requiring a great deal of CPU time, and are specific to an individual object morphology. A now-standard approach is based upon a subtraction of the starlike images followed by the application of a filled-box median filter. This method is thoroughly described by Fischer et al. (1990) and has been frequently used (e.g., Fleming et al. 1995; Secker et al. 1995; Hopp et al. 1994; Zepf et al. 1994; Butterworth & Harris 1992). A profile-fitting software code such as DAOPHOT (Stetson 1987) is used iteratively in conjunction with a box median filter: after a first pass of FIND/PHOT/ALLSTAR, the star-subtracted image is median-filtered with a box that is large compared to the stellar FWHM, and subtracted from the original image. Additional iterations of FIND/PHOT/ALLSTAR and the median-filtering can then be performed, with progressively smaller filter sizes. Each time, FIND is performed on the median-filtered subtracted image (allowing for the detection of faint stars missed on the first pass), and this new set of stars is subtracted from the original

image. The progressively smaller filters allow for increased resolution and better subtraction of the integrated galaxy light profile and other large-scale light gradients. However, this is a time-consuming process, and is so far limited to stellar objects, for which accurate profile-fitting software exists.

The adopted size of the filled-box median filter is of some concern: it is clear that a small box size is *desired* to conserve the detail in the light gradient and shape of large objects, but a large box size is *required* to median filter away the effects of small objects and retain a measure of the true-sky values. However, a filled-box median filter does not have a strictly defined, preferred dimension. Objects on the picture vary in size and shape, and portions of them (particularly the nonstellar objects) will get passed through the box-filtering process in ways that are not always desirable or easily predictable. Thus in practice, the diameter of the box median filter which is required is larger than in theory should be necessary, and will result in a loss of detail on the filtered image.

In this paper I define a “ring median filter.” It is fast and effective, and it circumvents several of the problems of an unweighted box median filter. In Sec. 2 this ring median filter is defined, and in Sec. 3 its use is illustrated and compared with conventional techniques.

2. FILTER DEFINITION AND PROPERTIES

A general class of median filters for digital images has been discussed by Brownrigg (1984); adopting his notation, we define our ring filter as a *weighted median filter*, with

```

0 0 0 0 1 0 0 0 0
0 1 0 0 0 0 0 1 0
0 0 0 0 0 0 0 0 0
0 0 0 0 0 0 0 0 0
1 0 0 0 0 0 0 0 1
0 0 0 0 0 0 0 0 0
0 0 0 0 0 0 0 0 0
0 1 0 0 0 0 0 1 0
0 0 0 0 1 0 0 0 0

```

FIG. 1—An example of an eight-pixel ring median filter. With a characteristic radius of $r_c = 4$ pixels, this filter is suitable for starlike objects with a FWHM of ≈ 2 pixels.

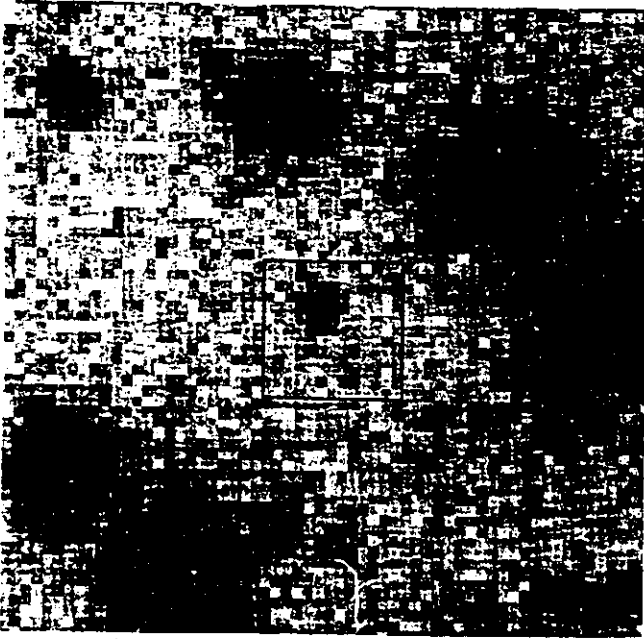


FIG. 2—A 61×61 pixel image section taken from the A2199 R-band CCD image in Fig. 3. The boxes show example locations for a ring median filter with $r_c = 6$ pixels, illustrating its behavior on and around objects of various sizes. The crosses indicate the individual pixels which are used for the median operation. Three boxes are marked: The central box location illustrates that for objects smaller than the characteristic radius of the filter, the ring filter will accurately estimate the local sky value, independent of how the filter is placed with respect to the object. The other two box locations illustrate the behavior of the filter when applied to pixels near an object of scale size equal to or greater than the ring filter. For the lower-left location, the filter will underestimate the true pixel flux at that position (in this case since five of the eight pixels are at a larger radius). In the upper right location, the median will exceed the local background level, yet will underestimate the true central flux.

weight given only to pixels in a narrow annulus. At each pixel in the image, the intensity value is replaced by a median of the weighted pixels in this annulus. The weighted pixels essentially measure the local-sky value about a given pixel, at a radial distance r_c large enough to ensure that there is no significant contribution from the object within the annulus. An example of the ring median filter, using just eight pixels at 45-degree intervals around the annulus, is illustrated in Fig. 1.

In this case, the characteristic radius r_c of the ring median filter is set equal to four pixels, suitable (say) for starlike objects with a FWHM of ≈ 2 pixels. This eight-pixel median filter works extremely effectively in removing all structure with scale size $r \leq r_c$ (see the examples below), for a population of objects that only sparsely covers the image. There are many obvious extensions of this simple ring median filter, two of which are mentioned here: (a) include all pixels in the annulus, which may help in crowded fields, and (b) rotate the filter so that no weighted pixels will be directly on the same row or column as the central pixel, which will make the filter insensitive to bad rows or columns (cf. Fig. 5). Additionally, a filter modeled after a filled-box median filter, but with the weighted pixels sparsely distributed, would combine computational speed with the true pixel sampling of a filled-box median filter.

It is clear that if *any* object with $r < r_c$ is contained and centered within this filter, the ring filter gives weight only to those pixels outside of the object, such that the median value corresponds to the genuine background sky level (Fig. 2). These objects will be completely eliminated during the median-filter operation, such that the subtracted image is suitable for photometry. For objects whose sizes far exceed that of the ring filter, the placement of the weighted pixels has no special significance, and the true local-background-sky level is again recovered. However, intermediate objects with $r \approx r_c$ will not be completely eliminated; these objects will appear on the filtered image, but with their total flux reduced. Note also that the ring filter is well behaved at edges and corners. For the example filter definition given, edge pixels on the filtered image correspond to the median of five pixels, and corner pixels correspond to the median of three pixels.

Evidently, the selection of the characteristic radius r_c is important. If the population of interest is starlike, r_c should be selected to be some standard multiple of the measured FWHM of the profile (i.e., $2.12 \times \text{FWHM} \approx 5\sigma_G$, a radius at which the stellar profile usually drops to a level unimportant compared with the background level). However, for a population of faint resolved galaxies (which have no single FWHM), the characteristic radius r_c must be selected to exceed the apparent radius (semimajor axis) of the largest galaxies of interest.

By definition, this ring median filter has a *sharply defined preferred scale length*, unlike the filled-box median filter. It is insensitive to all objects with diameters less than r_c , filtering (smoothing) them away completely in a single pass; there is no need to iteratively subtract objects and median filter. The ring filter is therefore exceedingly fast by comparison.

It is worthwhile to mention that application of this ring median filter to an image is equivalent to the following median operation: for example, for the eight-pixel filter defined above, eight disregistered copies of the original image are created by shifting it by r_c pixels in eight different radial directions separated by 45 degrees. Then the final filtered image is defined to be the median of these eight disregistered images. The resultant filtered image is identical to the one created by passing the ring filter across the original image. A simple task can be defined to utilize the existing IRAF¹ routines to perform this ring median filter operation (see the Appendix).

3. SAMPLE RESULTS

Two example images have been selected with which to demonstrate the effectiveness of the ring median filter. In the first example we illustrate the effect of a large filter (a radius matched to dwarf galaxies in the distant galaxy cluster Abell 2199) and its success with nonstellar objects. This image was filtered (in a single pass) using the eight-point ring filter as implemented in the Appendix; note that the image shifts

¹IRAF is distributed by the National Optical Astronomy Observatories, which are operated by the Association of Universities for Research in Astronomy, Inc., under contract of the National Science Foundation.



along 45 degree angles were rounded to integer pixel values, avoiding the need for subpixel interpolation. For the second example, a small characteristic radius for the ring median filter is used to filter only the high-frequency starlike objects (discussed further below).

In Fig. 3(a), we show a KPNO 4-m *R*-band image of a

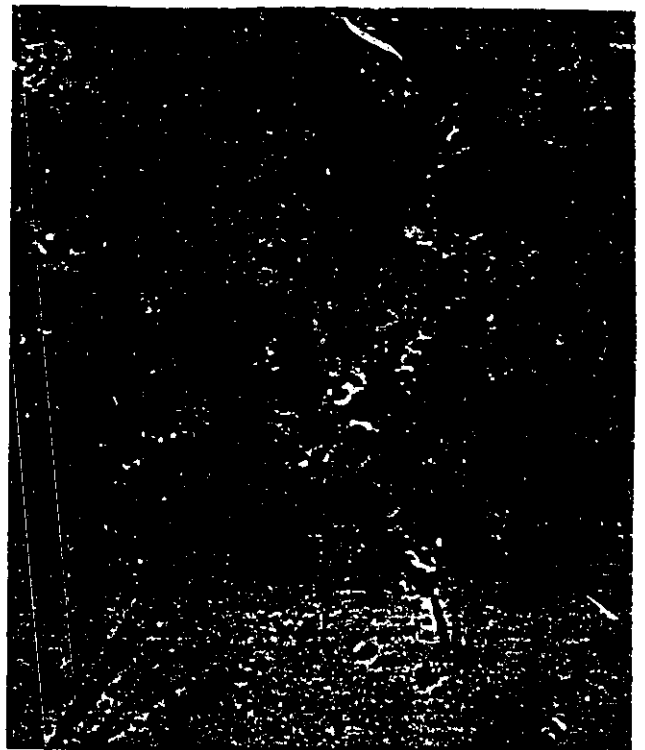


FIG. 3—(a) A large-format *R*-band CCD image of the rich cluster Abell 2199. The target objects are the faint, nonstellar dwarf galaxies within this cluster. (b) The filtered image. An eight-pixel ring median filter with a radius of $r_c=20$ pixels was used, sufficiently large to include the largest dwarf galaxies. The multitude of locations of residual light on this smoothed image is a direct result of the numerous cluster galaxies whose diameters exceed that for our ring filter. (c) The subtracted image. The filtered image was subtracted from the original to yield this globally flat image.

field around NGC 6166, the cD galaxy at the center of Abell 2199 ($v=9000 \text{ km s}^{-1}$). This field is quite complex, containing large numbers of galaxies at all scale sizes (including many near-starlike dwarfs), as well as the overall light gradient from the cD galaxy, and scattered light from bright stars off the corners of the frame. The dimension of the im-

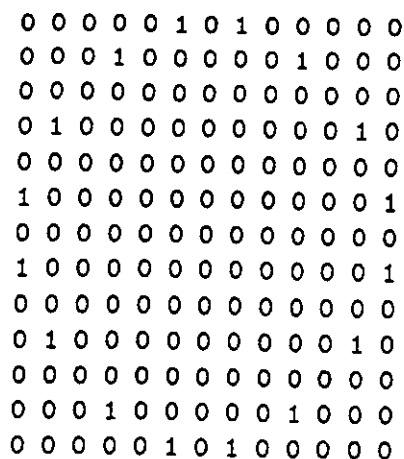


FIG. 5—A 16-pixel ring median filter with a characteristic radius of $r_c = 6$ pixels. This filter was used effectively on the innermost regions of the NGC 3311 image (Fig. 4), where the starlike images are crowded and steep light gradients dominate. Note that a filter of this design is less sensitive to bad rows or columns, since no weighted pixels are located on the same row or column as the central pixel.

for use when the target population is nonstellar.

Secker et al. (1995) and McLaughlin et al. (1995) recently studied the globular-cluster system of NGC 3311, the supergiant cD galaxy at the core of Abell 1060. Their master image is a median of a 10×1000 s exposure series in the Washington filter T_1 taken with the CTIO 4 m. The stellar profiles have a FWHM of about 2.8 pixels, and the image scale is $0''.47$ mag per pixel. Here, in Fig. 4(a), we show the central 512×512 pixel section of the full image, which includes NGC 3311 and below it, NGC 3309 (the other giant-E galaxy in the core of Hydra I). Note the profuse quantity of faint globular star clusters, superimposed upon the steep background intensity gradient resulting from the combined light of NGC 3311 and NGC 3309. This is perhaps the most challenging region to filter, and it provides an extreme test for the ring median filter. Figure 5 illustrates the filter used in this example. It has a characteristic radius $r_c = 6$ pixels (equivalent to $5\sigma_G$ for the stellar profile), and due to the steep gradients and crowded nature of the innermost regions, assigns weight to 16 pixels.

On the resulting filtered version of the original image, the high-frequency fluctuations (the starlike objects) are indeed erased, while the large-scale features remain intact. However, also present in the innermost 100 pixels about the galaxy cores (i.e., the steepest part of the gradient) was a faint, residual mottling, an artifact of the filtering. In order to eliminate this residual pattern, we performed a second filtering pass on this image with a filled-box median filter (diameter of 7 pixels). Note that a ring filter was not necessary for this second pass, as all the small objects were already removed during the first pass. The result of the two-pass median filter combination is shown in Fig. 4(b); it was very effective at smoothing the original image, leaving behind the galaxy isophotes. Other locations where residual light is noticeable result from faint, nonstellar objects whose characteristic radii exceed that of the ring filter.

In Fig. 4(c), the two-pass filtered image has been subtracted from the original image. The results are impressive:

stellar objects are clearly visible a great distance into the galaxy cores, and the background remains remarkably flat. Three other effects are immediately noticed. First, the stellar (and small nonstellar) objects immediately stand out on the globally flat background, and the visibility of objects which were previously obscured by the steep light gradients of either NGC 3311 or NGC 3309 is enhanced. Second, the increased noise towards the center of the large galaxies is a manifestation of the Poisson noise, which appears independent of filtering technique, eventually degrading the image quality in these central regions to such an extent that dependable object detection is not possible. Third, the effects of the three intermediate-luminosity galaxies and the two saturated stars are still evident. These objects are larger than the ring filter, and the steeply rising intensity profiles result in an underestimation of the true flux at these pixel locations.

A comparison of the ring median filtering technique with the more traditional iterative filled-box median filtering process as applied to this NGC 3311 field is shown in Fig. 4(d). To obtain Fig. 4(d), four iterations of FIND/PHOT/ALLSTAR with two passes of FIND per iteration were performed, with diameters for the filled-box median filters of 21, 15, 9, and 9 pixels. In both Figs. 4(c) and 4(d), the regions containing the central cores of each galaxy must be discarded (this is always the case unless the galaxy profile is modeled and subtracted prior to the filtering). However, the core region in Fig. 4(d) appears smaller and better contained than the corresponding region in Fig. 4(c). This is an inherent limitation present in the ring filter; in practice, the characteristic radius should be larger than the effective radius of the stellar profile (in this case an exact diameter of 12 pixels). This is compared to the iterative filled-box median filter, which for this example had a maximum extent of 9 pixels. Thus in this aspect, the ring filter cannot resolve the light gradients to as fine detail. A second obvious difference between Figs. 4(c) and 4(d) is the presence of unphysical fuzzy, diffuse patches connecting objects in many places on Fig. 4(d). These artifacts often show up in the iterative box-filter technique. However, the ring-filtered image [4(c)] does not show these patches (nor does the original image). We suggest that they could be a manifestation of the iterative process, in which objects are incorrectly subtracted (i.e., nonstellar objects which are only partially subtracted, or stellar objects which are over subtracted), causing the residual light to "grow" during the filled-box filtering.

In summary, the ring filter is exceedingly fast and filters all objects below a well-defined scale size, independent of their morphologies. A simple filter with a mere eight weighted pixels is sufficient for filtering many uncrowded images, and a two-pass filtering technique impressively filters even the most extreme regions in the cores of large bright galaxies.

This work was supported by a grant to W. E. Harris from the Natural Sciences and Engineering Research Council of Canada, and an Ontario Graduate Scholarship to the author. My thanks go to Bill Harris for his extremely helpful comments, discussions, and manuscript editing. In addition, I

would like to thank an anonymous referee for useful comments.

APPENDIX

Included here is an example of the implementation of a ring median filter utilizing existing IRAF tasks. Using *imshift*, a set of disregistered images is created, corresponding to a set of relative displacement vectors. Next, *imcombine* is used to perform a median of these shifted images, yielding the filtered image. This filtered image is then subtracted from the original image, and the mean sky level is added back. In this example, the characteristic radius used is $r_c = 20$ pixels; all shifts are rounded to integer values, avoiding unnecessary interpolations. To correct for edge effects, the boundary value extension is set to a large negative constant, which is subsequently rejected during the median operation. (The nonzero value for the low threshold allows for pixel values which are genuinely negative). In this example, a high threshold is included at the *imcombine* step, to reject saturated pixels during the median operation. Note that for large-format CCD images and digitized photographic plates, these operations require significant (temporary) disk space. An alternative method to perform the ring-filter operation is with a specific FORTRAN code, available from the author.

```
imshift image.imh s1.imh xshift=20. yshift=0. boundary=constant
constant=-30000.
```

```
imshift image.imh s2.imh xshift=14. yshift=14. boundary=constant
constant=-30000.
```

```
imshift image.imh s3.imh xshift=0. yshift=20. boundary=constant
constant=-30000.
```

```
imshift image.imh s4.imh xshift=-14. yshift=14. boundary=constant
constant=-30000.
```

```
imshift image.imh s5.imh xshift=-20. yshift=0. boundary=constant
constant=-30000.
```

```
imshift image.imh s6.imh xshift=-14. yshift=-14. boundary
=constant constant=-30000.
```

```
imshift image.imh s7.imh xshift=0. yshift=-20. boundary=constant
constant=-30000.
```

```
imshift image.imh s8.imh xshift=14. yshift=-14. boundary=constant
constant=-30000.
```

```
imcombine s?.imh imfilter.imh combine=median lthreshold=-1000.
hthreshold=30000.
```

```
imarith image.imh-imfilter.imh imflat.imh
```

```
imarith imflat.imh+1120.0 imflat.imh
```

REFERENCES

- Brownrigg, D. R. K. 1984, *Commun. Assoc. Comput. Machinery*, 27, 807
- Butterworth, S. T., and Harris, W. E. 1992, *AJ*, 103, 1828
- Fischer, P., Hesser, J. E., Harris, H. C., and Bothun, G. D. 1990, *PASP*, 102, 5
- Fleming, D. E. B., Harris, W. E., Pritchett, C. J., and Hanes, D. A. 1995, *AJ*, 109, 1044
- Harris, W. E., Smith, M. G., and Myra, E. S. 1983, *ApJ*, 272, 456
- Hopp, U., Wagner, S. J., and Richtler, T. 1995, *A&A* (in press)
- McLaughlin, D. E., Secker, J., Harris, W. E., and Geisler, D. 1995, *AJ*, 109, 1033
- Sandage, A., and Binggeli, B. 1984, *AJ*, 89, 919
- Secker, J., Geisler, D., McLaughlin, D. E., and Harris, W. E. 1995, *AJ*, 109, 1019
- Stetson, P. B. 1987, *PASP*, 99, 191
- Strom, S. E., Forte, J. C., Harris, W. E., Strom, K. E., Wells, D. C., and Smith, M. G. 1981, *ApJ*, 245, 416
- Sulentic, J. W., Arp, H., and Lorre, J. 1985, *AJ*, 90, 522
- Zepf, S. E., Geisler, D., and Ashman, K. M. 1994, *ApJ*, 435, L117

Chapter 4

The Dwarf Elliptical Galaxy Population In The Coma Cluster Core. I. Photometry And Sample Definition.

1. INTRODUCTION

In this Chapter we apply the image analysis methods described in Chapters 2 and 3 to our images of the Coma galaxy cluster and a control (non-cluster) field. The result is a sample of dwarf galaxy candidates, complete in color and in magnitude to $R = 22.5$ mag, for a central 700 arcmin^2 of the cluster core. It is this sample of objects which is further analyzed in Chapter 5. In Section 2, we describe the data acquisition, preprocessing and our DYNAMO analysis. In Section 3 we describe the magnitude completeness function and the calibration, and we compare photometry for multiply detected objects (i.e., those located in the program field overlap regions). Section 4 describes the process of star/galaxy discrimination using intensity-weighted radial moments, specifically the removal of the bright stellar objects. In Section 5 we determine a mean number density of objects on the control field, construct

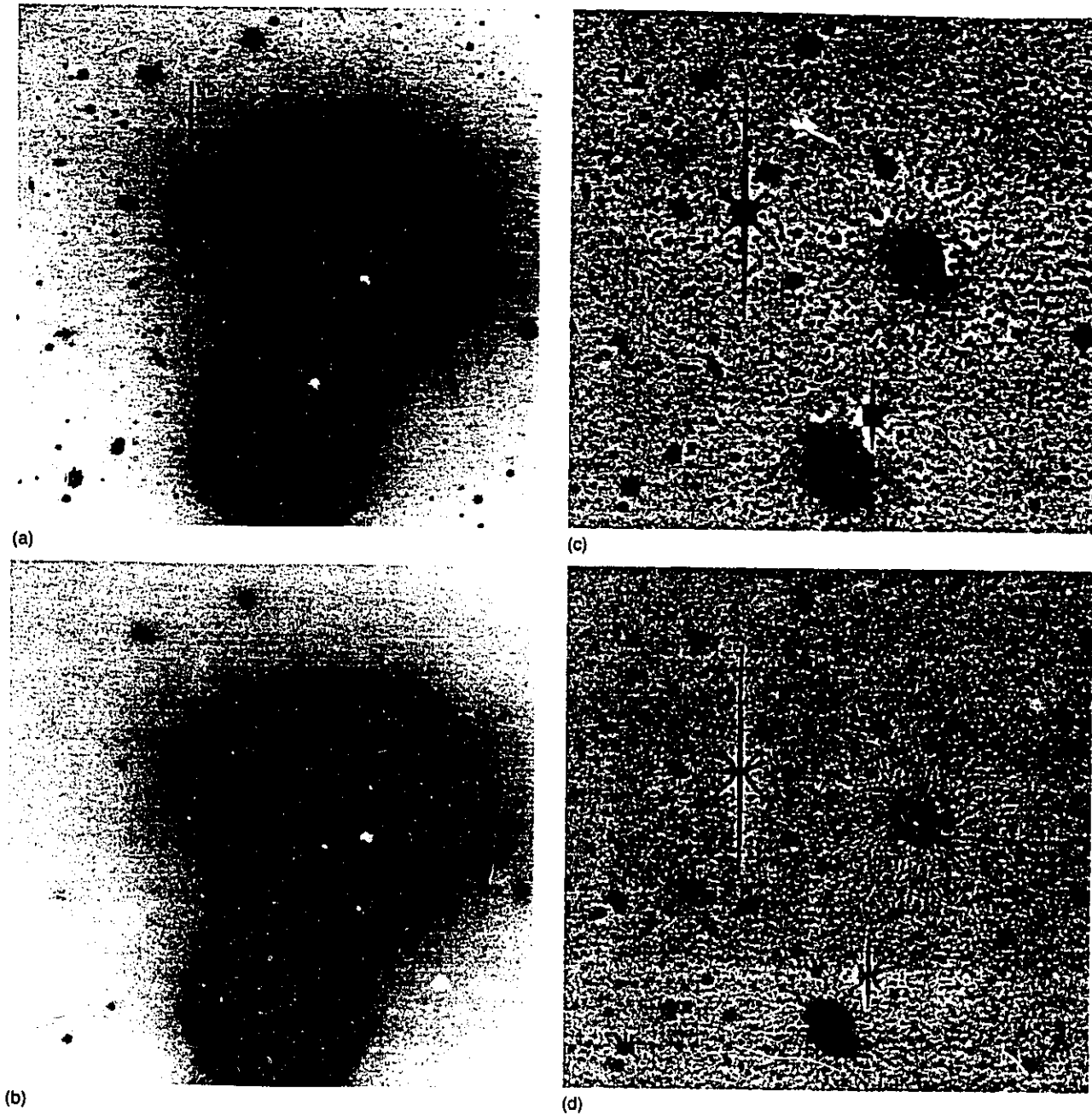


FIG. 4—(a) The original image. A 512×512 image of the field including NGC 3311 and NGC 3309 (lower supergiant galaxy) taken in the Washington T_1 filter. Note the multitude of globular clusters (the faint starlike objects) in the vicinity of these galaxies. (b) The filtered image. The characteristic radius for the ring filter was chosen to be $r_c = 6$ pixels, matched to the FWHM of the stellar profile. A second pass with a box filter of width seven pixels was then made to yield the smoothed image shown. (c) The subtracted image. The filtered image was subtracted from the original to yield this globally flat image. The visibility of the stellar objects is greatly enhanced, and other objects previously obscured by the steep light gradients are now visible. (d) For comparison, the analogous image created by iterative filled-box median filtering, as described in Sec. 3.

age shown is 2044×1700 pixels, at a scale of 0.53 mag per pixel.

In order to optimize the ring median filter for the dwarf galaxy population in A2199, we adopt a characteristic radius of $r_c = 20$ pixels, corresponding roughly to a physical diameter $d \approx 12$ kpc, sufficient to include even the huge, low-surface brightness types of dwarf galaxies (Sandage and Binggeli 1984). Figure 3(b) illustrates the filtered image, in which the smoothed galaxy profiles merge with an uneven

light distribution over the CCD image. The multitude of features on this filtered image result directly from the regular cluster members, whose scale sizes exceed that of the ring filter. In Fig. 3(c) we illustrate the filtered-subtracted image of A2199: NGC 6166 has been effectively removed and the image background is globally flat. The large galaxies which appear on the filtered image will have their fluxes underestimated when measured on Fig. 3(c), but the population of dwarf galaxies is unaffected. Thus, the ring filter is effective

and analyze color-magnitude diagrams for all four sets of master images, and define our final data set of dwarf galaxy candidates. It is here, on these color-magnitude diagrams and plots of r_1 versus R_{2r_1} mag, that the dwarf elliptical galaxy population is most evident, as a significant excess of objects which are not present on the control field.

2. OBSERVATIONS AND DATA REDUCTION

2.1 Field Placement and Cluster Coverage

The galaxy population of the Coma galaxy cluster is discussed in detail in the next Chapter, while in this Section we limit our description of the cluster to those details relevant to the field placement. On the nights of April 9 and 10, 1991, the KPNO 4-m telescope plus Prime Focus camera plus the TE 2K CCD was used to mosaic-image the cluster core. Exposure series (3×900 sec; but see Section 3.1) of three overlapping fields were obtained, in both the R - and B -bands, as well as a control field placed outside of the cluster. Provided in Table 4.1 are the field centers as specified in the image headers; these are as accurate as the level of the telescope pointing. In Table 4.2 we provide a summary of parameters relevant to these images, which we return to throughout this Section. In addition to the program and control fields, throughout both nights numerous images of standard star fields were obtained (Table 4.3), which were used for calibration.

Chapter 4

The Dwarf Elliptical Galaxy Population In The Coma Cluster Core. I. Photometry And Sample Definition.

1. INTRODUCTION

In this Chapter we apply the image analysis methods described in Chapters 2 and 3 to our images of the Coma galaxy cluster and a control (non-cluster) field. The result is a sample of dwarf galaxy candidates, complete in color and in magnitude to $R = 22.5$ mag, for a central 700 arcmin^2 of the cluster core. It is this sample of objects which is further analyzed in Chapter 5. In Section 2, we describe the data acquisition, preprocessing and our DYNAMO analysis. In Section 3 we describe the magnitude completeness function and the calibration, and we compare photometry for multiply detected objects (i.e., those located in the program field overlap regions). Section 4 describes the process of star/galaxy discrimination using intensity-weighted radial moments, specifically the removal of the bright stellar objects. In Section 5 we determine a mean number density of objects on the control field, construct

TABLE 4.1: Telescope coordinates of the *R*-band CCD fields.

FIELD	α h:m:s	δ deg	Epoch
NGC 4874	12:59:10.00	28:00:21.00	1991.3
NGC 4889	13:00:05.00	28:00:38.00	1991.3
NGC 4874 SOUTH	12:59:14.00	27:46:10.00	1991.3
CONTROL	13:08:39.00	28:02:46.00	1991.3

The placement of the three program fields is shown on Figure 4.1, where North is to the top and East is towards the right. The NGC 4874 field is roughly centered the cD galaxy NGC 4874, and overlaps (by about 400 pixels) with both of the other fields. The NGC 4889 field includes the supergiant galaxy NGC 4889, and extends outwards to the east. The NGC 4874 SOUTH field is located below NGC 4874, with the southern-most edge extending $\simeq 23.33$ arcmin, or $\simeq 552$ kpc, from NGC 4874. (For $v = 7000$ km/sec and $H_0 = 86$ km/sec/Mpc, we obtain a Coma cluster distance of 81.4 Mpc, such that 1 arcmin equals 23.68 kpc and $(R - M_R) = 34.55$.) The CONTROL field is located a full 2.09 degrees¹, or 2.98 Mpc, almost directly east of the cluster center NGC 4874.

The TE 2K CCD has 27 micron pixels, an image scale of 0.53 arcsec/pixel, a gain

¹This is derived from the coordinates in Table 4.1, and the angular separation in spherical coordinates, defined by $\cos \theta = \cos(\alpha_1 - \alpha_2) \cos \delta_1 \cos \delta_2 + \sin \delta_1 \sin \delta_2$.

TABLE 4.2: Properties of the master CCD images.

FIELD	Filter	Night	$\bar{\lambda}$	Exp Time (sec)	Master	Gain (e^-/ADU)	Readnoise (e^-)	# PSF	FWHM PSF	σ_G	\bar{z}_{sky} (ADU)	$\bar{\sigma}_{\text{sky}}$ (ADU)
NGC 4874	R	1	1.22	3 × 900	WAvg	64.2	7.51	6	2.77	0.52	1728.95	7.33
	B	1	1.09	3 × 900	Med	42.8	9.19	6	3.00			
NGC 4889	R	2	1.22	3 × 900	WAvg	64.2	7.51	7	2.34	0.74	1268.96	6.16
	B	1	1.25	2 × 900	Avg	42.8	9.19	7	2.93			
SOUTH OF NGC 4874	R	2	1.04	3 × 900	WAvg	64.2	7.51	7	2.77	0.42	1457.20	6.40
	B	2	1.01	2 × 900	Avg	42.8	9.19	7	2.88			
CONTROL	R	1	1.02	3 × 900	WAvg	64.2	7.51	4	2.92	0.39	1249.34	9.98
	B	1	1.07	3 × 900	Med	42.8	9.19	4	3.06			



Figure 4.1: A composite image illustrating the size and location of the three Coma cluster CCD fields. In this figure, North is towards the top and East is to the right. Each field is $15' \times 18'$ arcmin², and has a significant overlap with the neighboring field. From left to right, the two supergiant galaxies are NGC 4874 and NGC 4889, and the object above NGC 4874 is a very bright star.

TABLE 4.3: Summary of April 1991 KPNO 4m standard star fields.

NIGHT	Region	Standard Stars	Filter	Exp Time (sec)	X
1	M67	11	B	10	1.07
	M67	11	R	5	1.07
	NGC 2419	19	R	20	1.09
	NGC 2419	10	B	50	1.10
	M92	18	B	30	1.03
	M92	20	R	10	1.03
	M92	21	R	10	1.02
	M92	20	B	30	1.03
	M92	20	B	30	1.03
2	M67	11	R	5	1.07
	M67	11	B	10	1.07
	NGC 4147	12	B	50	1.45
	NGC 4147	16	R	20	1.42
	NGC 4147	19	R	20	1.09
	NGC 4147	11	B	50	1.12

(1) Nights 1 and 2 correspond to the nights of April 9th and 10th, 1991.
Observations made with the TE 2K CCD at PF of the KPNO 4m.

of $21.4 \text{ e}^-/\text{ADU}$ and a readnoise of 13 e^- . During these two (photometric) nights, the seeing ranged between $1.1 - 1.3 \text{ arcsec}$; thus, nonstellar objects are fairly well resolved. This TE 2K CCD suffered from rather poor cosmetics, dominated by the completely unusable columns 1701 through 2044. When trimmed, the field of view is about $18' \times 15'$. With this and the overlapping regions taken into account, *the total observed area is approximately 700 arcmin^2 ; this represents a significant fraction of the Coma cluster core.* The trimmed CONTROL field has an area of 270 arcmin^2 ; where appropriate, results such as number counts are scaled to the observed area of the cluster core. Originally the intention was to image an additional two fields south of NGC 4874 (to provide continuous radial coverage almost a degree outwards from

the cluster center) and an additional control field (to improve the statistical number correction). However, midway through the observing run the CCD detector suffered electronic failure, thus terminating the data acquisition.

The preprocessing of all images was accomplished in a typical manner. The raw images were first overscan corrected, trimmed and bias subtracted. Flatfields were constructed from dome flats, twilight sky flats and dark sky flats (i.e., the sparsely populated CONTROL field). These composite flatfield images were used fairly successfully to obtain a globally uniform response from the CCD. Section 3.3 compares the photometry and colors measured for common objects in the two overlap regions. Our conclusion is that the flatfielding, while not perfect (a slight $\simeq 0.05$ -mag differences in magnitude across the frame), there is no measurable effect on the color estimates.

2.2 Pre-DYNAMO Processing

Originally, we had obtained 3×900 -second exposure series for both R - and B -band images of the program and control fields. Unfortunately, two of the 900 sec B -band images were corrupted, and thus discarded; one for each of the NGC 4874 SOUTH and NGC 4889 fields. The remaining individual exposures were averaged together to yield *eight master images*; R - and B -band images for each of the three program fields and the control field. As specified in Table 4.2, the B -band master images represent either (i) a straight average of the two available images, or (ii) a median of the three

exposures. This latter option was chosen to reduce to some degree the numerous cosmic ray events.

The *R*-band master images are all weighted averages of three individual 900 sec exposures. The weighting scheme we implemented maximizes the S/N of the master image, by taking into account the mean sky level of the image, as well as the profile of a bright (but unsaturated) isolated star. For n individual exposures, the weighting factors are given by

$$w_i = \frac{1}{\sum_{i=1}^n w_i} \left(\frac{I_i}{z_{s,i}^2 \sigma_i^2} \right). \quad (4.1)$$

Here, $z_{s,i}^2$, σ_i^2 and I_i represent the mean sky level in the vicinity of the star, the star's FWHM and a measure of its sky-subtracted central intensity. Thus higher weights are assigned to those exposures with higher image quality: that is, lower sky values (less Poisson sky noise) and sharper seeing profiles (more signal in a smaller area). Thus, the *R*-band master images represent the maximal S/N images derived from 3×900 -sec exposures², and in this manner form a homogeneous set. This is desirable, as it is these images on which objects are detected, and we wish to have a consistent detection limit between fields. Note that the S/N ratio of the *B*-band images is lower

²These exposures yield an effective S/N equal to that which would be obtained by a single 2700 second exposure, as follows. For photometry of faint objects on long exposures, the S/N increases with length of exposure as $S/N \propto t^{1/2}$. In many instances, the CCD readnoise is low in comparison to the Poisson sky noise. If this is the case, the average of three 900 sec exposures yields the same overall S/N as the 2700 sec exposure. However dividing the total exposure time into multiple exposures has two distinct advantages. First, it reduces the number of bright stars and galaxy cores which saturate the detector, and second, combining the individual images provides a useful tool for eliminating cosmic ray events.

than for the corresponding *R*-band images. These images are used here only to obtain color estimates, and so this difference is essentially unimportant.

The *B*-band master images of each field were aligned with the *R*-band master images, using the flux-conserving IRAF routines *images.geomap* and *images.geotran*. In each case, between 14 and 20 stars were used to derive the geometric transformation, and the transformed images agree to within $\simeq \pm 0.2$ -pixel accuracy. At the same time, the transformations between program fields were derived (again using *geomap* and *geotran* and a large number of stars in the overlap regions), to map both the NGC 4889 field and the NGC 4874 SOUTH field to the coordinates of the NGC 4874 field. All coordinates from here on in will be given in terms of the NGC 4874 coordinate system. In this system, the centers of NGC 4874 and NGC 4889 are located at approximately (1061,1010) and (1875,1124), and the bright (saturated) star above NGC 4874 is located at (1000,1735).

In order for our measured aperture colors to be accurate, we must ensure that the sky-subtracted intensities summed within the individual apertures are independent of differences in seeing between the *B*- and *R*-band master images. Accurate estimates of the seeing on each image were obtained as follows. Photometry and radial moments from an initial (preliminary) pass of DYNAMO was used to construct parameter space plots of r_{-2} versus R_{2r_1} magnitude. From these plots, a number of bright, isolated and unsaturated stars were selected and measured with IRAF's *images.imexamine*. An average of the stellar FWHM was used to accurately estimate the seeing of each master

image (Table 4.2). For all four fields, the image quality of the R -band master image was significantly better than the corresponding B -band master images. We therefore degraded all R master images to the seeing of the B -band masters by convolving (smoothing) with a Gaussian filter of width σ_G given in Table 4.2. The end result is that for all four fields, the seeing of the R -band master images agrees with the B -band images to an accuracy of about $\Delta\text{FWHM} \simeq 0.01$ pixels. At this level of accuracy, we can be sure that our color estimates are consistent and independent of seeing effects. Note that we found, as did Bershadsky et al. (1994), that the $2r_1$ magnitude is robust to changes in seeing. Thus the small variations in seeing between the R -band master images does not affect our estimates of total magnitude.

We have median filtered all eight of the master images, using the ring filter method described in Chapter 3, and the FORTRAN code included as Appendix D, providing the homogeneous conditions which facilitate faint object detection and photometry. The characteristic radius r_c of the ring filter was chosen as small as possible for the population of interest, in order to obtain the best resolution and subtraction of light gradients. We chose to use a ring filter with a characteristic radius $r_c = 16$ pixels, and with 16 weighted pixels (Figure 4.2).

For a Coma distance of 81.4 Mpc, the 0.53 arcsec/pixel image scale translates into a physical scale of 0.2092 kpc/pixel. Then our characteristic radius corresponds to Coma cluster dwarf galaxies with radius less about 8.5 arcsec or 3.35 kpc. Visual inspection shows that this radius is appropriate for all but the 100 of so brightest

the CONTROL field images. These ring filtered images were then subtracted from the original master images, and the appropriate sky levels were added back.

2.3 DYNAMO Image Analysis

With the images aligned to a common coordinate system, pairs of R and B master images matched in seeing, and global light gradients removed, we are ready to detect, measure and classify objects. For all R -band images, the global sky value $\overline{z_{\text{sky}}}$ and the standard deviation $\overline{\sigma_{\text{sky}}}$ are given in Table 4.1, and we set our detection threshold level to $\beta = 4.0$. For the sky values typical to the R -band images, this $4\overline{\sigma_{\text{sky}}}$ detection threshold corresponds to about 1.5 – 2 percent of the mean sky level, or about 4.5 – 4.25 magnitudes fainter. Although objects with a central surface brightness lower than this level are measurable (i.e., the corresponding objects on the B -band image), attempts to detect these faintest objects also yields spurious detections (Poisson noise peaks). We do not impose any secondary constraints at this stage, since (for example) an object diameter constraint could bias against compact (starlike) E, S0 and dwarf elliptical galaxies. Discrimination between nonstellar objects and contaminating objects (e.g., starlike, cosmic ray events, cosmetic defects, etc.) is accomplished using parameter space plots and visual inspection. On each master R -band image we detected on the order of 4 000 objects to this central surface brightness threshold; of these objects, at least 50 percent end up being fainter than our adopted limiting magnitude.

For each detected object we computed the local sky level, limiting radius, the intensity-weighted centers and radial moments, followed by the $2r_1$ total magnitude, the constant-aperture color and the central surface brightness. The computation of these quantities is described in detail in Chapter 2, and constrained by our choice of parameter input: (a) The radius of the constant aperture used to measure the $(B-R)$ color was set to $R_{ap} = 3$ pixels, and (b) the seeing disk radius was set to 3.5 pixels³. For total magnitude estimation, the $2r_1$ radius was not permitted to shrink below this seeing disk radius; (c) The intensity-weighted average centers were computed using only those pixels within a 2 pixel radius from the object's peak flux pixel position. The parameter input described in (a), (b) and (c) are the same for all master images and all detected objects.

The only parameter differences come in the sky annulus definition, as well as the gain and readnoise. The detected objects are separated into three sets, dependent upon their apparent diameters. These groups are (i) the brightest and most extended giant galaxies, (ii) other giants and the brightest dwarfs, and (iii) the most numerous dwarf galaxies. Objects in the latter group are measured on the filtered-subtracted images, with a sky annulus of inner radius 24 pixels and a width of 4 pixels. Objects in first two groups are measured on the original master images with the sky annuli chosen appropriately: an inner radius of 95 pixels for group (i) and 45 pixels for group

³The Gaussian seeing is related to the FWHM by $\sigma = \text{FWHM}/2\sqrt{2\ln 2}$. Thus 3.5 pixels roughly corresponds to a 3σ radius, which encloses 99.73 percent of the flux for starlike objects.

(ii), and a width of 4 pixels in both cases. The gain and readnoise per CCD exposure are modified to account for the type of averaging, and these are specified for each master image in Table 4.1.

We then proceeded to visually inspect every object, looking mostly for obviously false detections and for the effect of nearby neighbors on the computed value of the limiting radius R_l (refer to Appendix B for relevant examples). Where possible, we modified estimates of the limiting radius R_l to exclude neighboring objects. In addition, we deleted a multitude of obviously “false” objects, such as CCD defects, charge overflow columns and diffraction spikes around bright stars. The only “contaminating objects” which remain in significant numbers after the visual inspection are those 2–4 percent of objects whose light profiles overlap with others to such a degree that the computed total magnitudes are incorrect. These objects were discarded from our data set, as were objects whose light profiles overlap the physical edge of the image. We assume that the deletion of these objects in no way biases our final sample of dwarf galaxy candidates. For interest, we include two 512×512 sections of the NGC 4889 *R*-band master CCD image as Figures 4.3 and 4.4. The population of dwarf galaxies (faint and nonstellar) is difficult to discern in Figure 4.1, because of the pixel binning necessary to create the image. Here, this numerous dwarf galaxy population is very evident as those low surface brightness objects showing central concentration, down to the faintest smudges available to the eye.

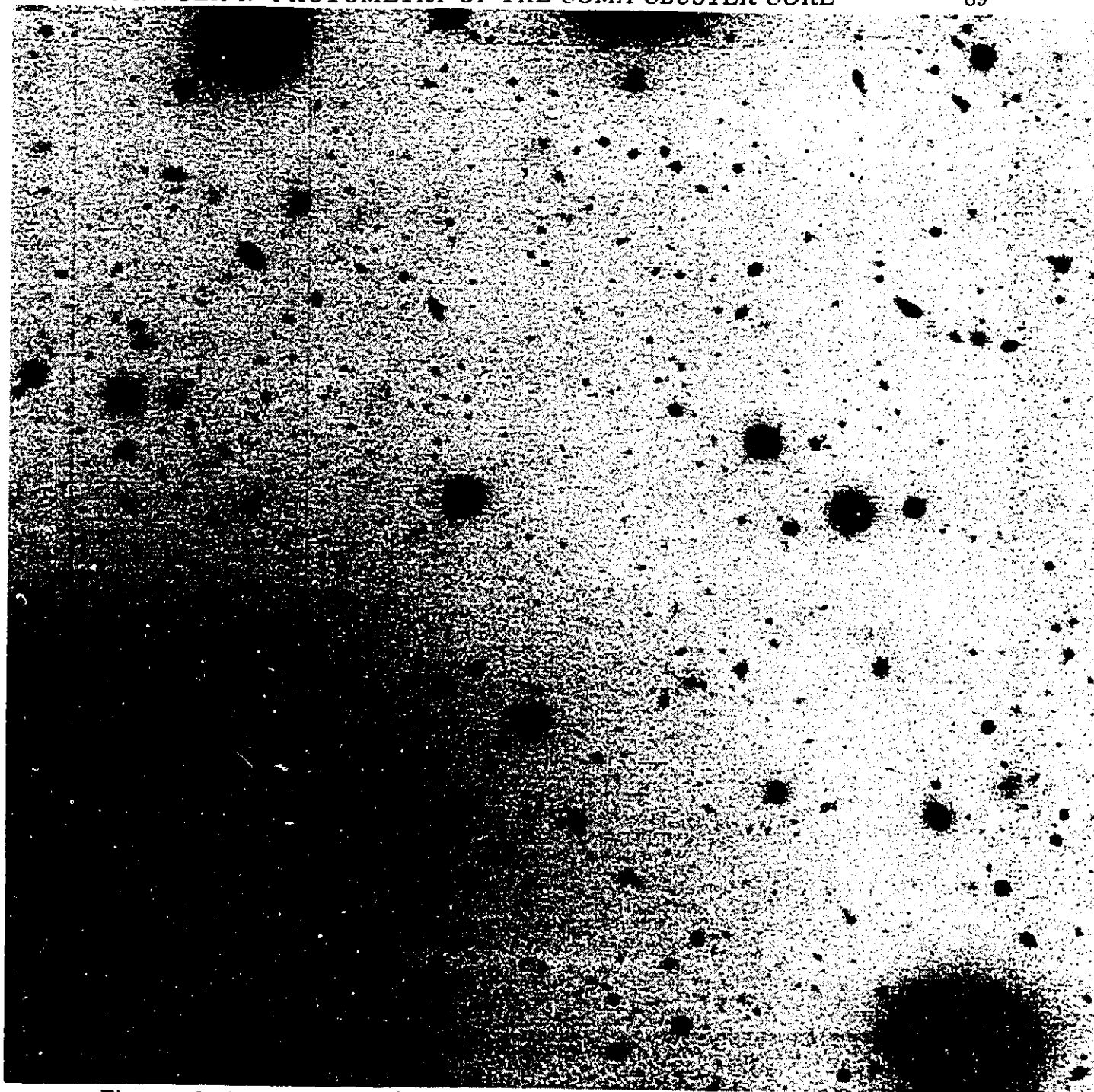


Figure 4.3: A 512×512 pixel² section of the Coma cluster core. In this *R*-band image, NGC 4889 is visible in the bottom left corner, and the image extends to the North (upper) and East (right). The largest cluster giants are easy to discern; the remaining objects are divided between low surface brightness dwarf elliptical galaxies, compact ellipticals, foreground stars and noncluster galaxies. Note the contrasting surface brightnesses between the objects in a pair near the top center.

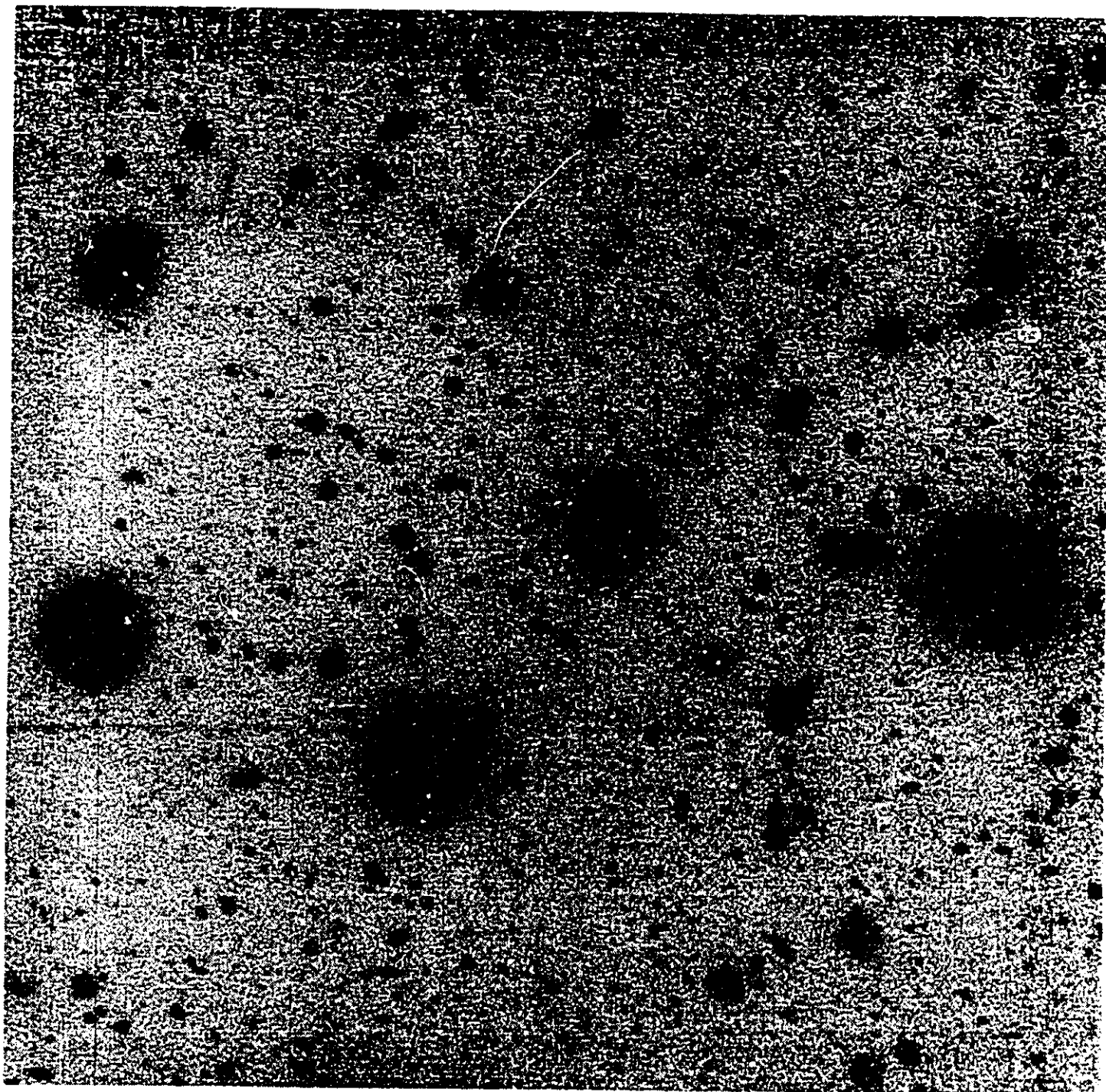


Figure 4.4: A 512×512 pixel² section of an *R*-band image, located North of both NGC 4874 and NGC 4889. The general description given in the previous figure is relevant here as well. Note the prominent nucleated dwarf elliptical in the lower right corner.

3. CALIBRATION, COMPLETENESS AND PHOTOMETRIC ERRORS

3.1 Calibration Procedure

The calibration of our (B, R) magnitude scales (i.e., magnitude zeropoints and other calibration coefficients) was accomplished using repeated observations of four standard star fields: M67 (Schild 1983), M92, NGC 2419 and NGC 4147 (Davis 1990), summarized in Table 4.3. To our B - and R - standard star measurements we fit the familiar photometric transfer equations given by

$$r = R + ZP_R + a_1 X_R + a_2 (B - R), \quad (4.2)$$

and

$$b = B + ZP_B + a_3 X_B + a_4 (B - R). \quad (4.3)$$

Here, b and r represent instrumental aperture magnitudes of the standard stars, and ZP_B and ZP_R denote the magnitude zeropoint terms. The b and r magnitudes were derived with DAOPHOT (Stetson 1987), by summing the pixel intensity within a 10-pixel aperture radius $\sum I$, subtracting the mode of the sky distribution I_{sky} (i.e., sky annulus with inner radius of 20 pixels and width of five pixels) and normalizing to a 1 second exposure; for example,

$$r = -2.5 \log \left((\sum I - I_{\text{sky}}) / t_e \right). \quad (4.4)$$

Also, a_1 and a_3 represent the extinction coefficients, while a_2 and a_4 represent the

color coefficients. We assume that the color coefficients are constant from night to night (for a given filter), whereas the zeropoint term and the airmass coefficient can vary between nights.

For both nights, the coefficients of these linear transformation equations were determined using the simultaneous multilinear least squares reduction method developed by Harris et al. (1981). To best constrain our solutions, we adopted typical values for the extinction coefficients of $a_1 = 0.130$ and $a_3 = 0.283$ (Landolt 1982). Reducing both nights of data simultaneously (but R and B separately) yielded the zeropoints and coefficients given in Table 4.4.

When it comes to actually calibrating our instrumental magnitudes and colors, we rewrite these photometric transfer equations in a more physical manner. Rearranging (4.2) and (4.3) and solving for the calibrated magnitude and color, we obtain

$$R = r - ZP_R - a_1 X_R - a_2 (B - R), \quad (4.5)$$

and

$$(B - R) = \frac{[(b - ZP_B) - (r - ZP_R)] - a_3 X_B + a_1 X_R}{1 - (a_3 - a_1)}. \quad (4.6)$$

With the mean airmass values given in Table 4.2, all quantities on the right-hand side of (4.5) and (4.6) are known, and our magnitudes and colors are completely calibrated.

3.2 A Magnitude (and Color) Completeness Level

TABLE 4.4: Calibration summary for April 1991 KPNO 4m run.

NIGHT	Total Standards	Filter	ZP_R	a_1	a_2	ZP_B	a_3	a_4
1	71	R	22.418 ± 0.016	0.130	-0.002 ± 0.013			
1	59	B				21.081 ± 0.016	0.283	-0.042 ± 0.014
2	46	R	22.408 ± 0.018	0.130	-0.002 ± 0.013			
2	34	B				21.109 ± 0.018	0.283	-0.042 ± 0.014

(1) No errors are provided for parameter a_1 ; these values were obtained from Landolt (1983), and represent average CTIO extinction coefficients.

We consider regions of 1500×450 pixels and 280×2000 pixels, corresponding to the overlap regions of the NGC 4874 SOUTH and NGC 4889 fields with the NGC 4874 field. These overlapping regions of our Coma program fields provide a convenient sample of objects with which to compare the final calibrated photometry and derive the magnitude completeness function (defined as the probability $f(m)$ than an object at a given magnitude m will be detected). For all objects detected on the NGC 4874 image, we search for objects near (within a 5 pixel radius) the same location on the other images, and if more than one object is detected, the nearest object is selected as the match. This task assumed that the coordinate systems were transformed to the common system of the NGC 4874, and makes use of the method and FORTRAN code described in McLaughlin et al. (1995). From a comparison of the object detections in the overlapping regions, we derive a completeness function which is used to statistically correct the cluster luminosity function in the next chapter. The derived magnitude completeness function is thus averaged over different regions of the cluster core, from the strong light gradients between NGC 4874 and NGC 4889 to the relatively flat sky levels south of NGC 4874. This is appropriate for the complex nature of the light distribution (i.e., galaxies plus global light gradients) in the cluster core.

We adopt this method to define a magnitude completeness function as opposed to the artificial star/galaxy simulations which are often used (e.g., McLaughlin et al 1995; Fleming et al. 1995). The objects we compare are “real”, all of which have been through the complete range of image preprocessing, pre-DYNAMO processing,

ring median filtering, detection and measurement. In this manner we believe that this method is superior to the artificial simulations. It should also be kept in mind that we are comparing detection efficiencies and photometry for vastly differing images: the mean sky levels differ by up to 500 ADU, the total sky noise differs by a small amount, and these regions correspond to opposite sides of the large format CCD detector. In this way it is an extreme test. Based upon an inspection of the completeness plots given in this section, and the photometric error plots given in the next two sections, *we adopt a limiting magnitude of $R_{2r_1} = 22.5$ mag*, and discard all objects with total magnitudes below this limit. As well, we discard a circular region of radius 150 pixels centered on both of the two supergiant galaxies, and a circular region of radius 100 pixels centered on the bright saturated star located above NGC 4874. On the original master images, the light gradients in these regions were too extreme to permit adequate filtering and useful photometry.

Consider the two overlap regions separately, and for each define the “total” set of objects as all objects detected and measured on the overlap regions of the separate images $N_T(m)$, above $R_{2r_1} = 23.5$ mag. The subset of matched objects $N_m(m)$ is taken as those detected/measured on the NGC 4874 image, and detected/measured at any magnitude on the corresponding overlap region. The remaining number of unmatched objects is represented by $N_u(m)$. Then the fractional completeness in

each 0.5-magnitude interval is defined to be

$$f(m) = \frac{N_m(m)}{N_T(m)}, \quad (4.7)$$

where the object's "true" magnitude is adopted to be that measured on the NGC 4874 master image. We define the uncertainty in $f(m)$ in proportion to the total number of objects in the magnitude bin; that is, the fractional Poisson error on N_T , multiplied by the completeness fraction, given by

$$\sigma(f) = \left(\frac{\sqrt{N_T}}{N_T} \right) \frac{N_m}{N_T}. \quad (4.8)$$

In Figure 4.5 we plot the derived completeness function for the two overlap regions, combined together to yield an averaged completeness function (the small-number statistics of the combined function are somewhat reduced). There are two different completeness functions plotted here. The *open circles* denote the completeness function derived using *all* measured objects. However, our analysis in the next Chapter is based exclusively on a restricted subsample of objects, those dE candidates in the color range $0.7 \leq (B - R)_{ap} \leq 1.9$ mag; the completeness function for this color restricted sample is plotted in Figure 4.5 as *solid circles*, and we refer to this as the dE completeness function. While these two functions are consistent within their uncertainty ranges, the actual data points imply that the dE function is more complete down to our limit at $R_{2r1} = 22.5$ mag. This probably results from the exclusion of the extreme color objects, which are more probably false detections. Note that the object

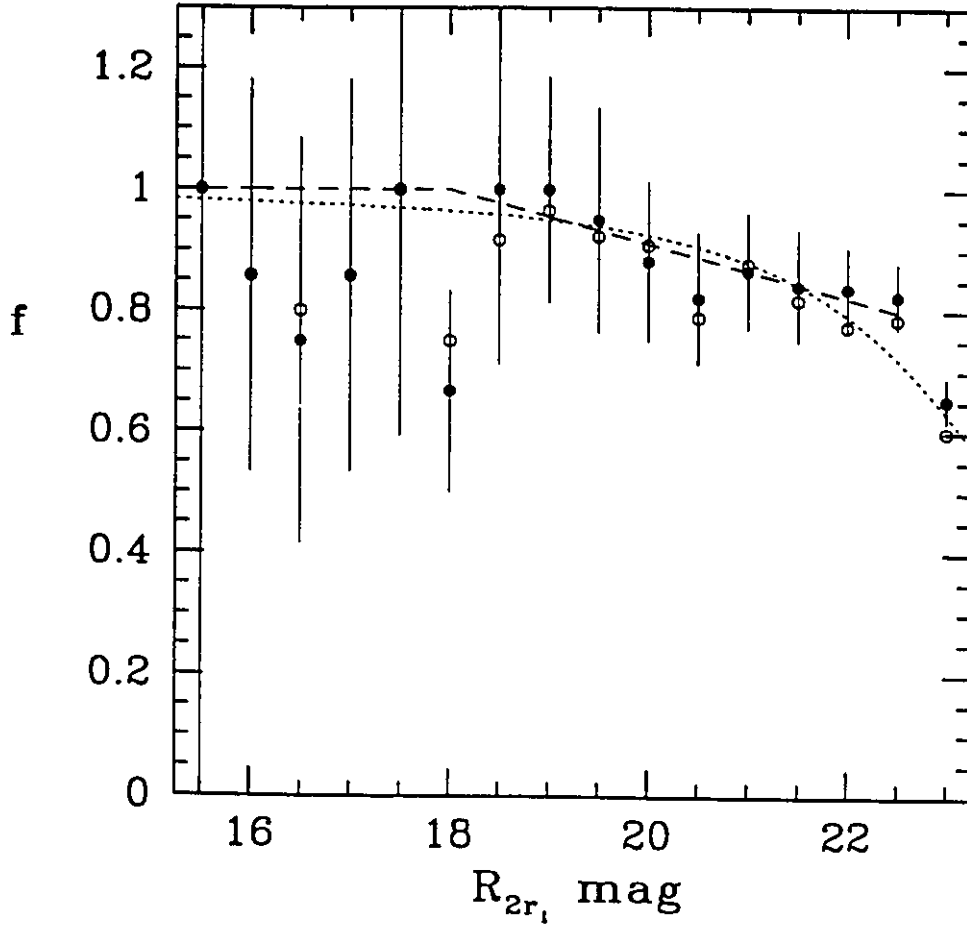


Figure 4.5: The completeness function was derived by comparing photometry for overlapping regions of the program field. The solid circles represent the completeness function for objects restricted to the color range $0.7 \leq (B - R) \leq 1.9$ mag, the color range of our dE galaxy sample. The open circles represent the completeness function for all objects, shown here for comparison. The straight dashed line is our adopted completeness function, illustrating that our final object lists are 80 percent complete at the limiting magnitude $R_{2r_1} = 22.5$ mag. The dotted line is shown just for comparison: it is an appropriate fit of an analytic function to the open circles.

sample used to define these functions is truncated at $R_{2r_1} = 23.5$. While the faintest objects have scattered to fainter magnitudes, the scatter in the total magnitude is about 0.1-mag at $R_{2r_1} = 22.5$ mag, so our derived completeness function is valid to this magnitude level.

In Figure 4.5, and for $R_{2r_1} \lesssim 18.5$ mag, there are very few objects per magnitude bin, and the results of small-number statistics are evident in the large error bars and in values of $f(m) < 1$. One cause of the $f(m) < 1$ values lies with edge objects; that is, objects found along a physical edge of one overlap region are discarded. However, the corresponding location on the other image is well away from the physical edge, and the objects are thus included in the sample. A second reason is that we are biased against finding objects near to brighter cluster members, numerous in the cluster core. Third, there are several bad rows at the bottom of the CCD detector. This affects the NGC 4874 field, but only to a lesser degree the other overlap regions. This discussion, however, is only relevant to the bright end of the completeness function, and in this analysis we assume that this incompleteness for $R_{2r_1} \lesssim 18.5$ mag is simply due to the small-number statistics, and do not correct for it.

The derived (binned) luminosity function is useful to correct the magnitude distribution, specifically the luminosity function of Chapter 5. An analytic formula provides a method to interpolate between the 0.5-mag bins of the derived luminosity function, and to smooth out physically meaningless irregularities resulting from small number statistics. We use two different functions, as follows. The first form (due to C.

Pritchett; see, e.g., Fleming et al 1995) is expressed in terms of the parameters α and m_ℓ , which describe the shape of the completeness curve and an effective 50 percent complete limiting magnitude. It is given by

$$f(m) = \frac{1}{2} \left[1 - \frac{\alpha(R_{2r_1} - m_\ell)}{\sqrt{1 + \alpha^2(R_{2r_1} - m_\ell)^2}} \right], \quad (4.9)$$

and with the parameters $\alpha = 0.45$ and $m_\ell = 23.6$ mag, it provides a good fit (dotted line) for the total sample of objects (open circles). However, the subsample defined in terms of color does not fall off so rapidly, and in the range $18 \leq R_{2r_1} \leq 22.5$ mag is better represented by a straight line, as plotted in Figure 4.5 (dotted line), and given here as

$$f(m) = \begin{cases} -R_{2r_1}/22.5 + 1.8; & 18 \leq R_{2r_1} \leq 22.5 \text{ mag} \\ 1.0; & R_{2r_1} < 18.0 \text{ mag} \end{cases} \quad (4.10)$$

It is this analytic formula for the completeness function which we adopt for interpolation purposes in the next chapter.

In addition to the above determined magnitude incompleteness, incompleteness can also occur in the *color* and the *spatial* distributions. Above the $R_{2r_1} = 22.5$ magnitude limit we were able to measure on the *B*-band master images virtually all objects detected on the *R*-band images. (We discarded a handful of unmeasured objects, but well less than one percent.) *Thus, we are essentially 100 percent complete for the color measurements.*

Within the area of the Coma cluster core covered by our CCD images, there are

certain areas for which photometry is not possible. Above, we specified two such areas: the circular regions centered on the cores of the two supergiant galaxies. However, to a lesser extent all of the giant (bright and extended) cluster galaxies contribute to a small (but non-negligible) degree of spatial incompleteness. The effect of these giant galaxies is twofold. First, we simply cannot measure a small faint object detected upon a larger brighter object using aperture photometry. These objects, if detected, are discarded, and *this results in a fractional spatial incompleteness in our survey*, not to be confused with incompleteness due to object detection. Second, these giant galaxies have the effect of increasing the photometric uncertainty for nearby objects (i.e., their projected neighbors). Note that these two effects would be greatly reduced if the giant galaxies were initially modeled and subtracted before analysis of the faint galaxy population.

We state above that our sample of objects suffers from a small degree of spatial incompleteness due to the projected area covered by the giant galaxies, dominated by the two supergiant galaxies. While the level of this incompleteness is less than about two percent, it is necessary to question whether or not this incompleteness will bias our sample in any manner. The area localized to the vicinity of giant cluster galaxies is special insofar as some small fraction ($\lesssim 7$ percent; Ferguson 1992) of the total cluster population is contributed by genuinely bound companion galaxies. While this is a small fraction of the total population, we stipulate that our data set should not be used to study aspects of the cluster population relevant to companion

galaxies. In the next chapter we make a small correction to the area when performing the surface density analysis. Otherwise, it should be kept in mind that this spatial incompleteness, a paucity of faint objects near and superimposed upon large brighter objects, is inherent in our sample.

3.3 Photometric Uncertainties

In Figure 4.6 we plot the uncertainties in total magnitude (dots) and color (crosses) versus total magnitude (above our limiting $R_{2r_1} = 22.5$ mag), for all detected and measured objects on the four fields. The uncertainty in magnitude was derived using equation (2.28) of Chapter 2. The color uncertainties are always larger as expected; these were obtained by adding in quadrature the individual uncertainties for the R - and B -band uncertainties. A comparison of the last column (i.e., $\overline{\sigma_{\text{sky}}}$) of Table 4.2 with Figures 4.6 (a) through (d) shows that at any magnitude, an average of the uncertainties computed for the individual objects reflect the nature of the images sky noise; this is most evident when comparing the CONTROL field with the NGC 4889 field. In summary, typical uncertainties for $R_{2r_1} < 22.5$ mag are $\lesssim \pm 0.6$ mag in total magnitude, and $\lesssim \pm 0.12$ mag in color.

3.4 Photometry Comparison For Objects Matched in Overlap Regions

Figure 4.6 of the previous section illustrates that our computed quantities are very accurate, but it remains to be shown that this photometry is consistent and mean-

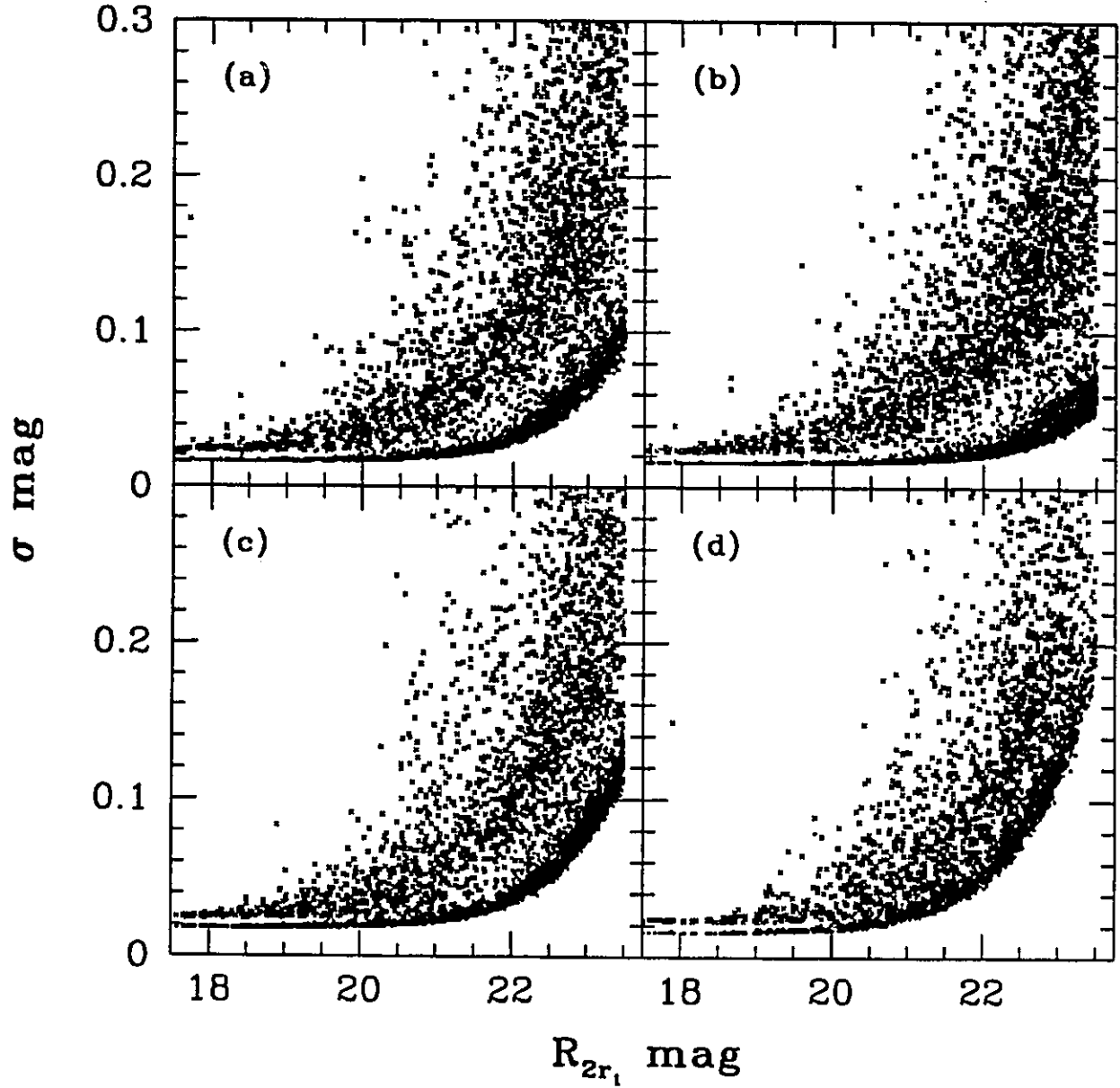


Figure 4.6: Errors in photometry for colors (crosses) and total magnitudes (solid circles), for all objects above 22.5 mag on all four fields: (a) NGC 4874, (b) NGC 4889, (c) NGC 4874 SOUTH, and (d) CONTROL. Typical uncertainties are $\lesssim \pm 0.06 \text{ mag}$ in total magnitude, and $\lesssim \pm 0.12 \text{ mag}$ in color.

ingful. From the set of all objects used above to define the magnitude completeness function (i.e. those detected on the overlap regions of the NGC 4874 *R*-band master image), we consider only objects which were also detected on another of the program fields. For this subset of the detected objects (i.e., the majority), we compare total magnitudes and colors as a function of apparent total R_{2r_1} magnitude. It is worthwhile to briefly mention that these comparisons are rather harsh. This photometry includes errors accumulated at all steps, from the initial preprocessing through the median filtering and finally in the measurement.

In Figure 4.7 we plot the magnitude difference ΔR_{2r_1} mag versus the total magnitude, ranging from our completeness limit up to $R_{2r_1} = 14.5$ mag. On this figure, ΔR_{2r_1} is defined as the NGC 4874 magnitude minus the other measured magnitude; the cross symbols denote the 416 objects matched with the NGC 4889 field, and the solid circles denote the 448 objects matched with the NGC 4874 SOUTH field. It is immediately obvious that our magnitude scale is consistent between fields: the vast majority of the objects have $\Delta R \lesssim 0.10$, while those near the completeness limit have $\Delta R \lesssim 0.20$ mag. However, a small bias exists, in the sense that the magnitudes measured on the NGC 4889 field are about 0.05-mag brighter at all magnitudes. If this effect is evident at all for the other overlap region, it is at a much lower level, and only occurs for the brighter objects. This discrepancy is most likely due to flat-fielding errors, and while not completely negligible, these differences are sufficiently small that we do not attempt to correct it.

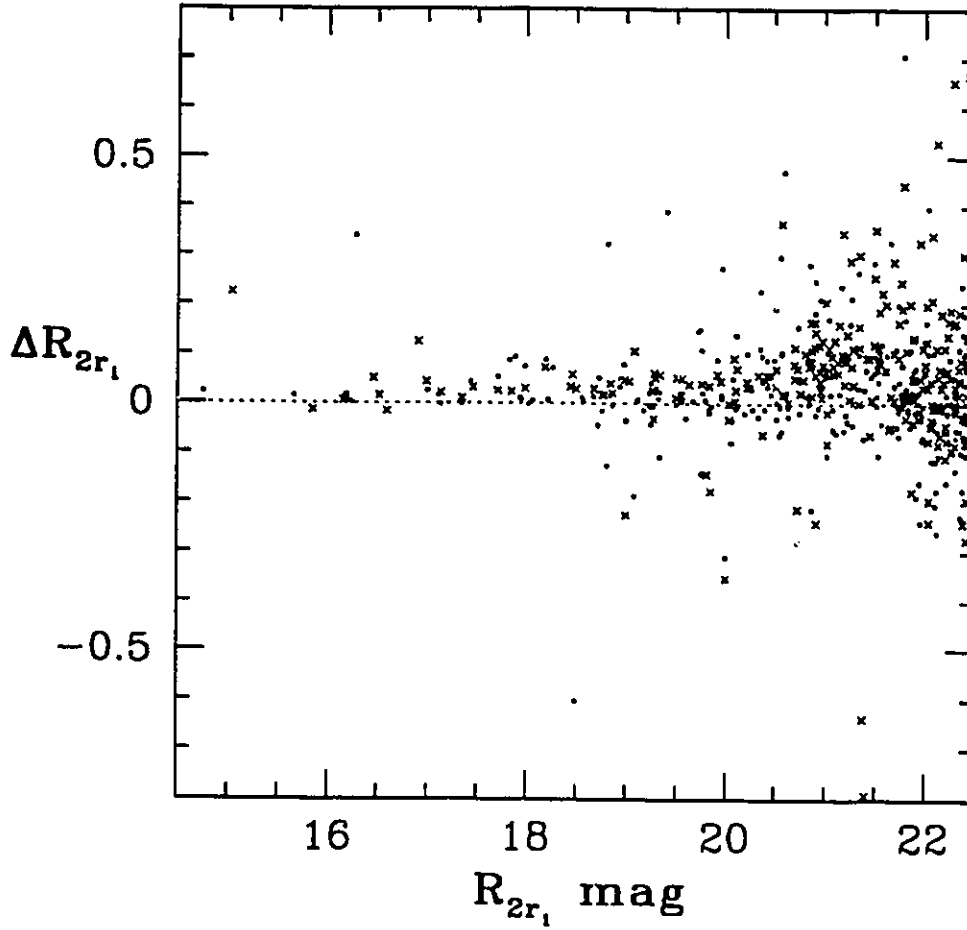


Figure 4.7: The objects matched on the program field overlap regions: crosses denote the 416 objects on the NGC 4889 field, while the solid circles denote the 448 objects on the NGC 4874 SOUTH field. The scatter in the magnitude estimates is consistent with the photometric errors presented in Figure 4, yet there is a slight $\simeq 0.05$ -mag bias between total magnitudes measured on the NGC 4889 field and those measured on the NGC 4874 field.

In Figure 4.8 we plot the color difference $\Delta(B - R)$ mag versus the total R_{2r_1} magnitude, for the same objects and the same magnitude range of the previous figure. It is evident that at all magnitudes, the agreement between the color scales is excellent, with no evidence for bias between fields. This supports the hypothesis that flatfielding errors are the source of the discrepancy in the magnitude scale, since these errors would most likely affect both the B and the R master images in the same manner, leaving the derived colors unaffected. Note also the increased scatter in $\Delta(B - R)$ below $R_{2r_1} \simeq 20$ mag when compared to ΔR_{2r_1} ; this is expected, and it is discussed further in the next section.

4. IMAGE MOMENTS FOR STAR/GALAXY DISCRIMINATION

In this Section we discriminate between starlike and nonstellar objects in the r_{-2} versus R_{2r_1} parameter space, as described in Chapter 2, for each of the four master images individually. In all three of the program fields, the cluster dwarf elliptical galaxies are immediately obvious as an excess over and above the population of objects in the control field. Note that at this point the problem objects (i.e., saturated stars, objects overlapping the edge of the image, and multiple objects for which aperture photometry yields invalid results) have been discarded from the object lists.

4.1 The Radial Moment r_{-2} and Object Discrimination

In Figure 4.9 we plot the intensity-weighted radial moment r_{-2} (measured in

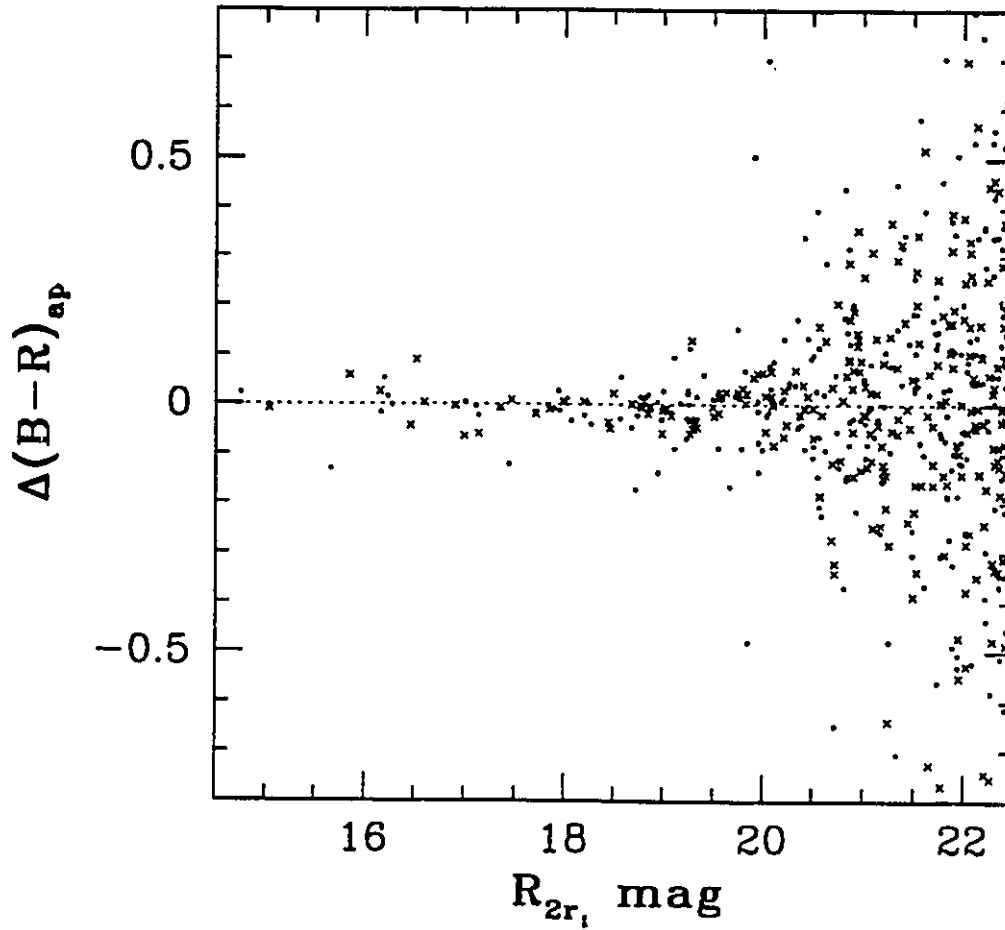


Figure 4.8: The objects matched on the program field overlap regions, as described in the previous figure. The scatter in the magnitude estimates is consistent with photometric errors, and there is no bias in color estimates between fields.

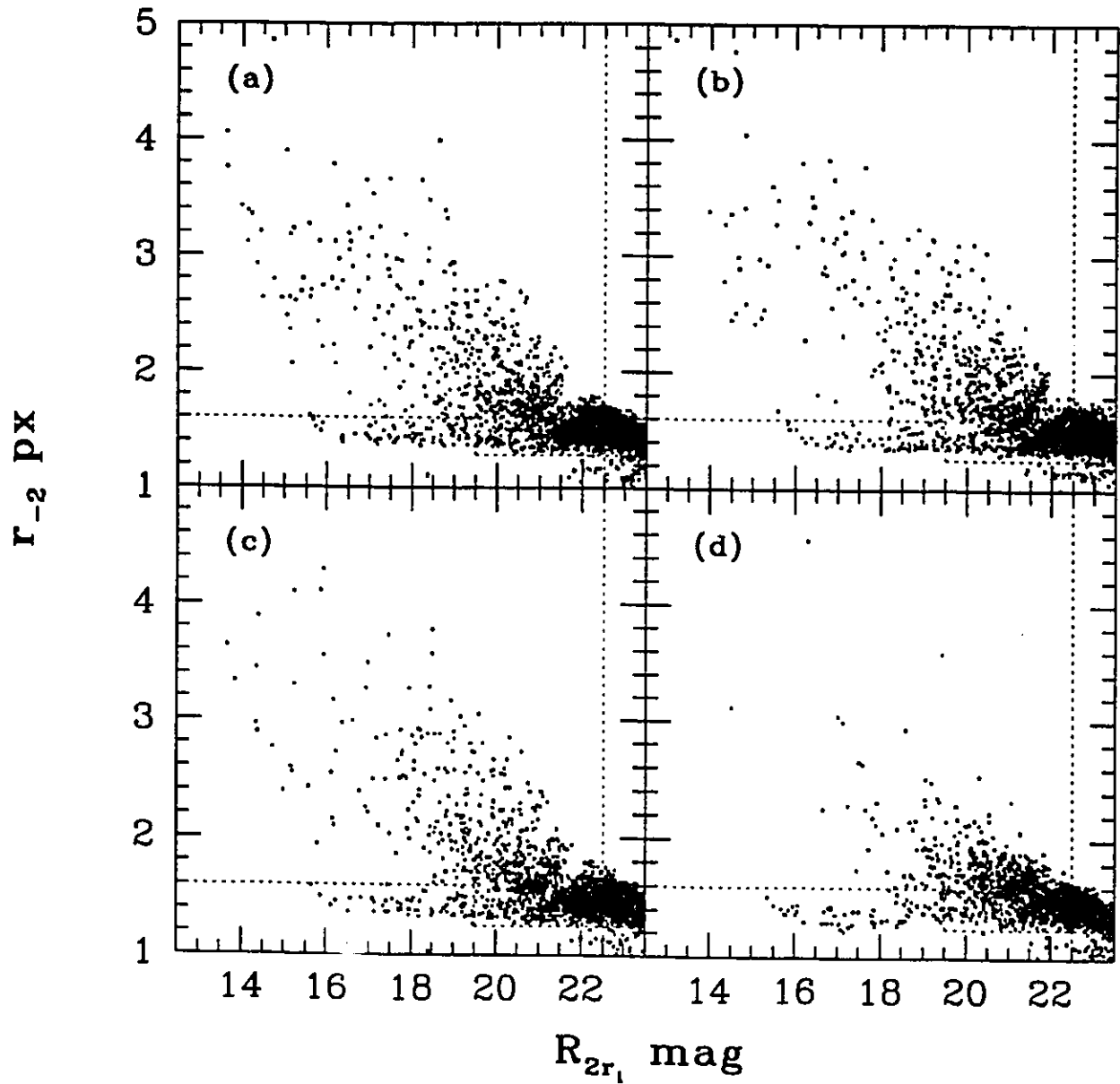


Figure 4.9: The radial moment r_{-2} (pixels) versus the total R_{2r_1} mag, for all objects detected and measured on the four master R -band images: (a) NGC 4874, (b) NGC 4889, (c) NGC 4874 SOUTH, and (d) CONTROL. The large number of dE galaxies in the cluster core is evident as the excess nonstellar objects on the program field plots, as compared to the control field. The horizontal dotted line excludes the bright starlike sequence and the point-like objects, while the vertical dotted line corresponds to our limiting magnitude.

pixels) versus the total apparent R_{2r_1} magnitude for objects on the four R -band master images. The points represent the individual objects detected and measured by DYNAMO, down to $R_{2r_1} = 23.5$ mag. Common to all fields are several general trends. The numerous nonstellar objects are present at all magnitudes, and are those deviating towards larger r_{-2} , away from starlike objects. The stellar sequence (i.e., $r_{-2} \lesssim 1.6$ pixels) extends from the brightest magnitudes down to the faintest limits, and at $R_{2r_1} \simeq 19.5$ mag, the nonstellar objects begin to merge with the stellar sequence. Below $R_{2r_1} \simeq 21.5$ mag, as the nonstellar objects become faint and starlike, the r_{-2} moment loses its ability to discriminate between these different types of objects, resulting in a clump of objects. On the plots for the three program fields, the brightest end of the stellar sequence rises slightly. This is the result of either bright compact galaxies, or a change in image structure due to the CCD detector behavior near saturation. There is a population of detected objects which are faint and pointlike. That is, they have an r_{-2} moment which is computed to be less than that of a stellar profile. These must arise from cosmic rays, hot pixels or CCD defects, since observed stars and galaxies cannot have a profile which is sharper than the well-defined seeing limit.

The dotted lines in Figure 4.9 are used to restrict our sample of objects. The vertical line at $R_{2r_1} = 22.5$ mag corresponds to our magnitude limit, and all objects fainter than this are discarded. The upper horizontal line is used to reliably exclude objects in and below the bright stellar sequence, with $r_{-2} \leq 1.6$ and $R_{2r_1} \leq 19.5$

mag. The number of starlike objects in this region are 63, 59, 67 and 64 for the fields as listed in Table 4.2. Within Poisson statistics, these numbers are consistent with each other, as expected. The point-like objects located below the lower horizontal line near $r_{-2} \simeq 1.25$ are discarded.

We do not want to bias our sample of cluster galaxy candidates against compact galaxies, and it is for this reason that we do not discard the entire sequence of starlike objects. We are confident that the fractional contribution of galaxies in the range $R_{2r_1} \leq 19.5$ mag and $r_{-2} \leq 1.6$ is negligible. However, for $R_{2r_1} > 19.5$ mag the starlike sequence is also populated with faint compact galaxies. These are more numerous on the program fields, and to discard the sequence would impose an extreme bias against these compact objects. In this region we depend upon statistical correction using the CONTROL field to account for the contamination by starlike objects.

4.2 Quantization of the radial moments

In our Figure 4.9, there is an apparent quantization of the r_1 moment. This effect is also evident in Figure 4.16, and in other studies involving radial moments, whose implementation and computation differs from ours (e.g., Harris et al. 1991; McLaughlin et al. 1995). This quantization results from the discrete sampling and the small number of pixels making up the faint objects. This quantization is strongest in the parameter space of r_1 versus the central surface brightness I_c (Figure 4.10), for $24 \lesssim I_c \lesssim 26$ and $r_1 \lesssim 3$ pixels. While generally unimportant, this quantization effect

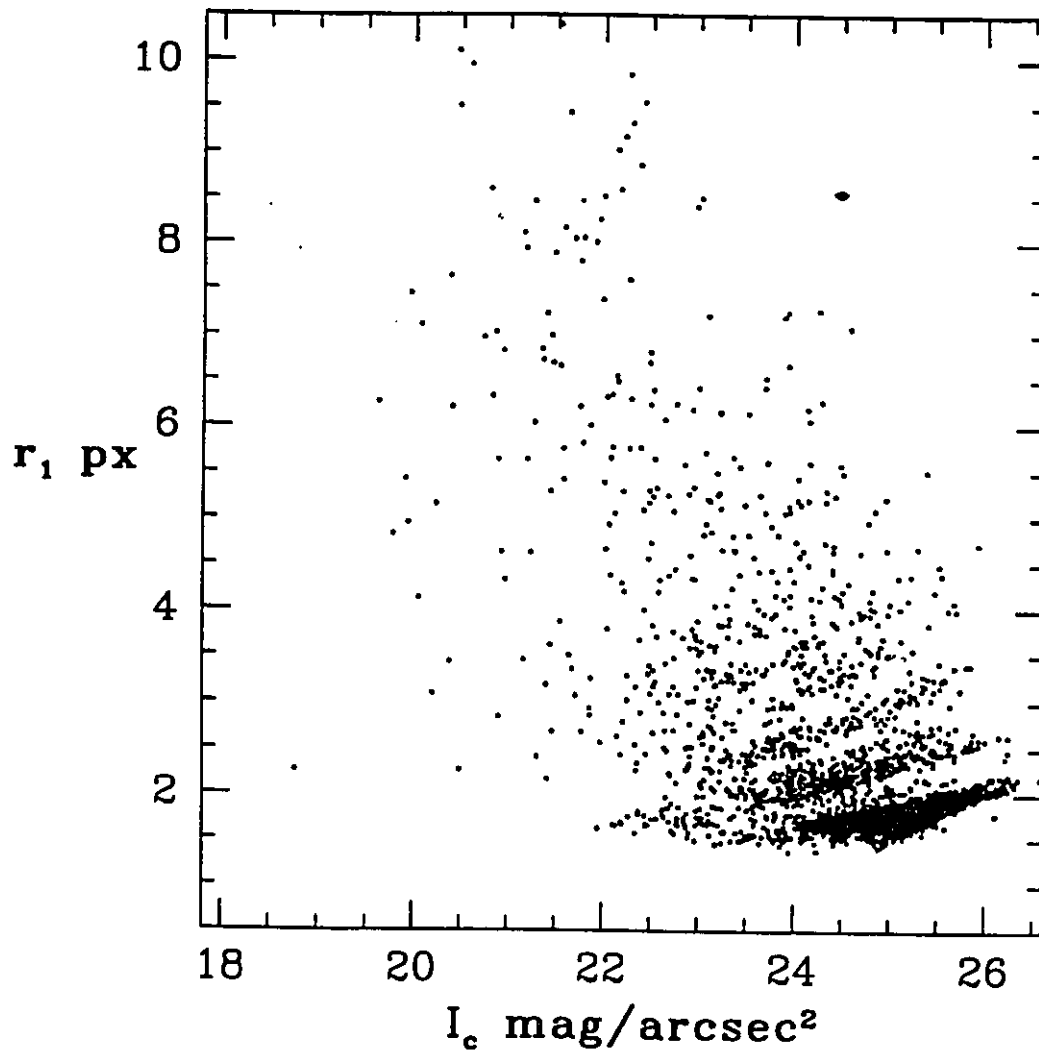


Figure 4.10: At low luminosities, the radial moments r_1 and r_{-2} are quantized for small scale size objects. This is most clearly demonstrated in the parameter space of r_1 versus I_c .

becomes important if other quantities of interest, such as the R_{2r_1} total magnitude, are directly based upon the radial moment estimates. However, in our analysis, we force the aperture radius for the total magnitude to be the larger of $2r_1$ or the seeing disk radius, in this case defined to be 3.5 pixels. Then as is clear from Figure 4.10, our $2r_1$ magnitudes will not be affected by the discrete nature of the r_1 moment for small and faint objects.

5. COLOR CONSTRAINTS AND THE DWARF ELLIPTICAL GALAXY SEQUENCE

In this Section we take the “bright-star removed” object lists defined above for the four master R -band images and plot these on color-magnitude diagrams (CMDs). In this parameter space the cluster dwarf elliptical galaxies manifest themselves as a tight, well-defined correlation. It is this dwarf galaxy sequence that discriminates the program field CMDs from the control field CMD, and galaxy cluster members from more remote nonmember galaxies. We then combine the object lists for the three program fields, and define our final sample of dE candidates as a color restricted subset of these objects. Following this sample definition, we illustrate the behavior of these candidate dwarf elliptical galaxies in parameter spaces involving r_1 , r_{-2} , R_{2r_1} and I_c .

5.1 Details Of The Control Field Analysis

Due to unfortunate circumstances involving the CCD detector characteristics, the stellar profile of objects on the R -band master image of the CONTROL field differ in a significant aspect from the program fields. Charge overflow columns appear for most objects which have a peak-flux pixel intensity exceeding about 10^4 ADU, and there is a noticeable variation in the image structure (i.e., the stellar FWHM) outwards from the center of the image. This arouses concern for two reasons: (a) it is next to impossible to obtain accurate photometry for the *bright* starlike (high I_c) objects, and (b) the color estimation may be affected. This is an indication that we should proceed with caution, yet I will show that these features do not inhibit us from extracting reliable number counts and photometry from this control field.

Of the 64 bright starlike objects culled from the CONTROL field objects list in Section 4.1, on the order of 30 had apparent charge overflow columns. These objects were dealt with individually during the visual inspection, at which time we constrained R_t to equal 2 pixels. With the intensity summations recalculated within this radius, the radial moments r_1 and r_{-2} are confined to be less than 2 pixels. As some of the flux is lost in the charge overflow columns, the magnitudes for these bright stellar objects will be underestimated. However, our primary motivation was to distinguish these from bright nonstellar objects, and we have accomplished this task. The starlike objects near $R_{2r_1} \gtrsim 19.5$ mag do not appear to be affected in this manner: visual inspection does not reveal charge overflow columns, and a normal stellar sequence is visible in Figure 4.9(d).

The other difficulty with the control field is the effect of the variable stellar profile on the object photometry. The $2r_1$ aperture radius is computed individually for each object and is directly proportional to the stellar FWHM (Chapter 2), and therefore the total R -band magnitude is virtually independent of seeing (i.e., changes in the FWHM). However, the object's $(B - R)$ color is sensitive to seeing. We therefore compare the measured color distributions between all objects and a subset, those detected in the central region of the CCD image.

After performing the r_{-2} discrimination (as described in Section 4) for the CONTROL field as a whole, there are 1146 objects in total, 694 of which are within the color range $0.7 \leq (B - R) \leq 1.9$. Within a central region⁴ of area 1000^2 pixels, there is a total of 337 objects, 225 of these which are within the color range $0.7 \leq (B - R) \leq 1.9$. It is the distribution of colors for these two samples which we compare, to determine if colors derived for objects in the center region of the CONTROL field CCD image differ significantly from the overall image.

In Figure 4.11 we compare histograms of these two regions. The solid circles denote the histogram for the entire 1700×2044 pixel² image, where the error bars represent the Poisson uncertainties. The solid line shows the distribution of colors for objects in the central region only, where the number of objects per bin have been scaled by 3.4748, the ratio of areas. These distributions look very similar, especially within the restricted color range. To quantify this similarity or difference, we calculate the

⁴In x and y pixel coordinates, this region is enclosed by the boundary [350:1350,500:1500].

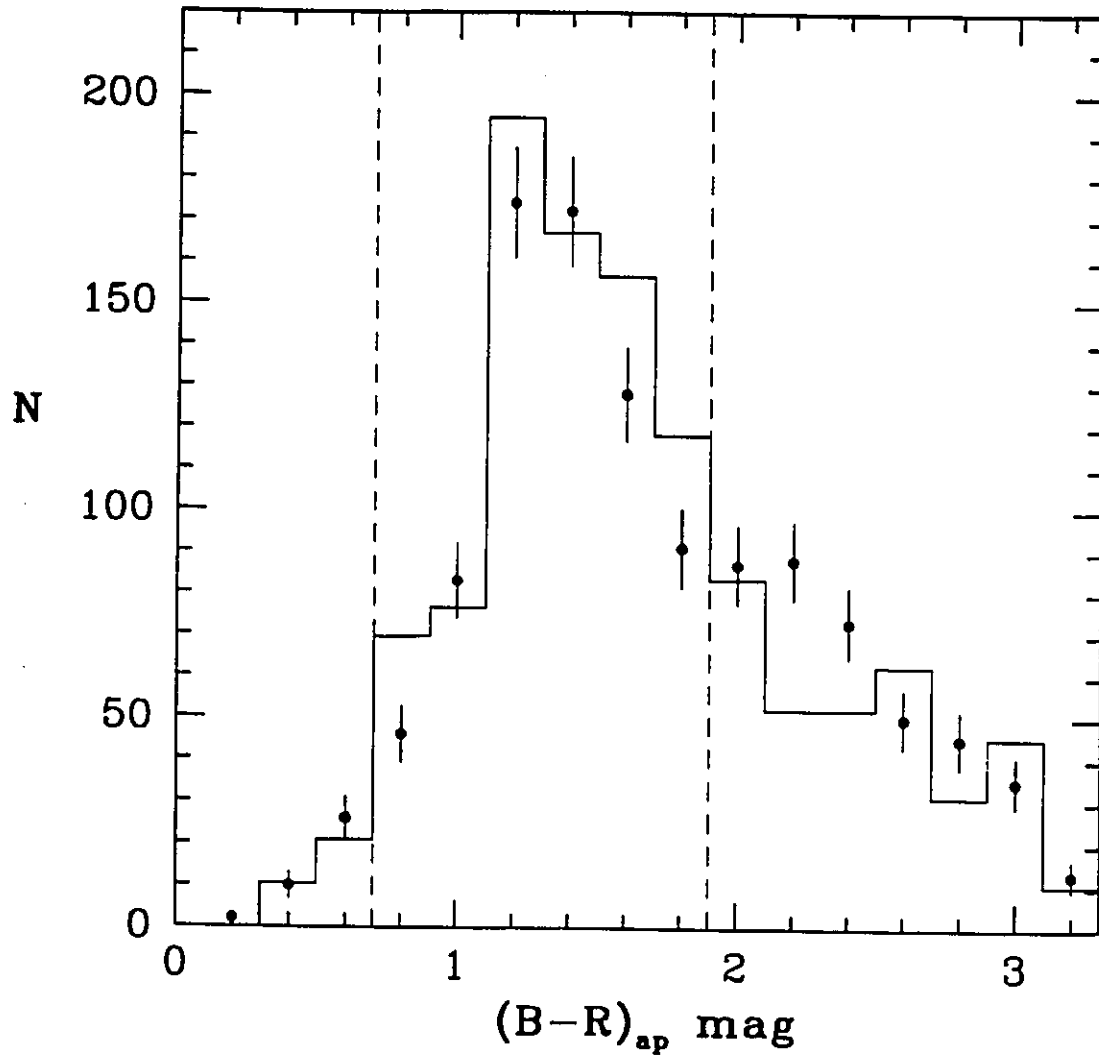


Figure 4.11: A comparison of the distribution of object colors on the CONTROL field. The solid circles denote the histogram for the entire 1700×2044 pixel² image (with Poisson uncertainties), and solid line illustrates the distribution of colors for objects in the central region only. In the latter case, the number of objects per bin have been scaled by 3.4748, the ratio of areas. These distributions look very similar, especially within the restricted color range.

Kolmogorov-Smirnov (KS) statistic, which provides a robust statistical measurement of the overall differences between the cumulative distribution functions. In Figure 4.12, we plot the cumulative distribution functions for object colors within the central region (dotted line) and the entire image (solid line). The maximum vertical difference between these two functions, together with the number of objects per data set, yield a probability $P = 0.294$; this is the probability that the two distributions are the same. In fact though, this intermediate probability is not statistically significant, and we conclude that the two distributions are not significantly different. We therefore adopt the color-magnitude diagram defined by the entire control field, which we use in Chapter 5 to statistically correct the sample of dE galaxy candidates on the program field.

There are two final quantities to derive, which are necessary for the statistical correction of number counts on the program fields. These are (i) the ratio of the total area of the program field to the area of the control field, and (ii) the mean number density of nonstellar objects on the control field, integrated over all magnitudes, within the restricted color range. The total area of the Coma cluster core covered by our program field is $3 \times 1700 \times 2044$ pixels², minus the area of the overlap regions and the discarded regions around the cores of the two supergiant galaxies. The resulting area is $A_p = 8.951124 \times 10^6$ pixels², while the total area of the CONTROL field is $A_c = 3.474800 \times 10^6$ pixels². Thus the area conversion factor between the total

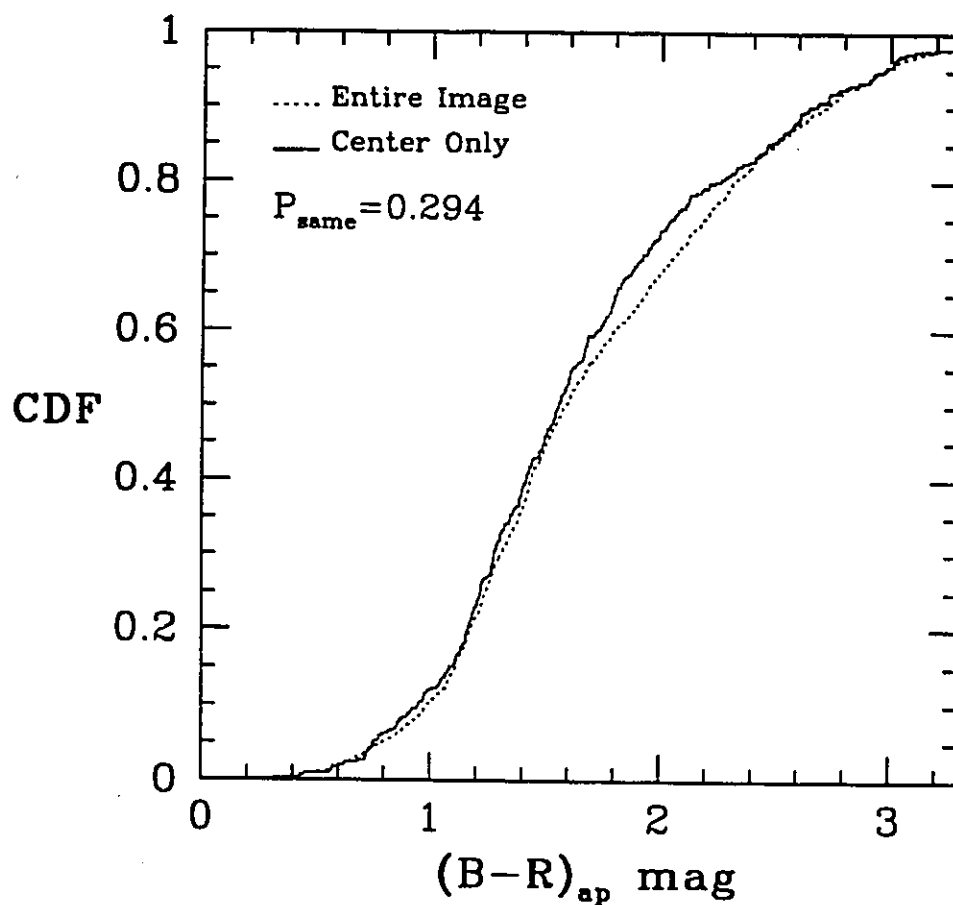


Figure 4.12: To quantify the difference between the color distributions, we plot the cumulative distribution functions and calculate the Kolmogorov-Smirnov (KS) statistic. Here, the dotted line represents object colors within the central region, while the solid line represents the entire image. Calculation of the KS statistic yields a probability $1 - P = 0.706$ that the two distributions are different: i.e., they are not significantly different.

program field and the control field is given by

$$\frac{A_p}{A_c} = 2.5760. \quad (4.11)$$

As stated above, there are a total of 694 objects in the color restricted range $0.7 \leq (B - R) \leq 1.9$. Using the relevant pixel scale (Section 2) the control field area corresponds to $A_c = 271.1309 \text{ arcmin}^2$. Then the number density of objects on the CONTROL field (integrated over all magnitudes) is given by

$$\overline{N}_c = 2.560 \pm 0.097 \text{ arcmin}^{-2}. \quad (4.12)$$

In Chapter 5, a luminosity function defined by the 694 objects (the color-restricted sample) on this control field is used to correct the raw luminosity function observed on the program field. In addition, we use the integrated spatial number density (computed above) to statistically correct the surface density profiles for our cluster dE galaxies. We do this with the knowledge that it is *only* a first-order correction, and that it effectively eliminates the effect of uniformly distributed foreground stars and noncluster galaxies. This correction is worth further comment.

A single control field allows us to accurately calibrate the number counts arising from the noncluster galaxies and foreground stars visible in our R - and B -band images. For genuine Galactic stars, this nearby control field provides an accurate estimate (to within Poisson uncertainties) of the number of stars, together with their luminosity and color distributions. As is the case though, a larger field-to-field variance arises in

the number counts of faint galaxies. This variance is predominately due to large-scale structure: the nature of background galaxies is to reside in clusters and superclusters, with apparent angular diameters of these remote galaxy clusters on the order of several arcminutes. With excess number counts arising in this manner, the field-to-field variance in the observed number counts will definitely be larger than the Poisson \sqrt{N} uncertainties. One possibility is to image a number of randomly-offset control fields, to reduce independently and average, arriving at a more accurate mean number density and control field luminosity function (e.g., Bernstein et al. 1995).

In our analysis we utilize accurate estimates of an object's integrated color to discriminate between cluster and non-cluster galaxies. As illustrated by Biviano et al. (1995), determination of cluster membership in this manner is comparable in effectiveness to redshift selection. In this manner we reduce the field-to-field variance arising from nonmember galaxies, part of the large-scale structure behind the Coma cluster. The objects which remain in our control field sample, after the color discrimination, turn out to be dominated by objects uniformly distributed across the image, similar to the contamination remaining in our cluster fields. We therefore conclude that the analysis of our single randomly-offset control field is sufficient for the purposes of statistical correction, as discussed above.

5.2 Color-Magnitude Diagram Analysis

In Figure 4.13 we plot the CMDs for objects measured on the three program fields

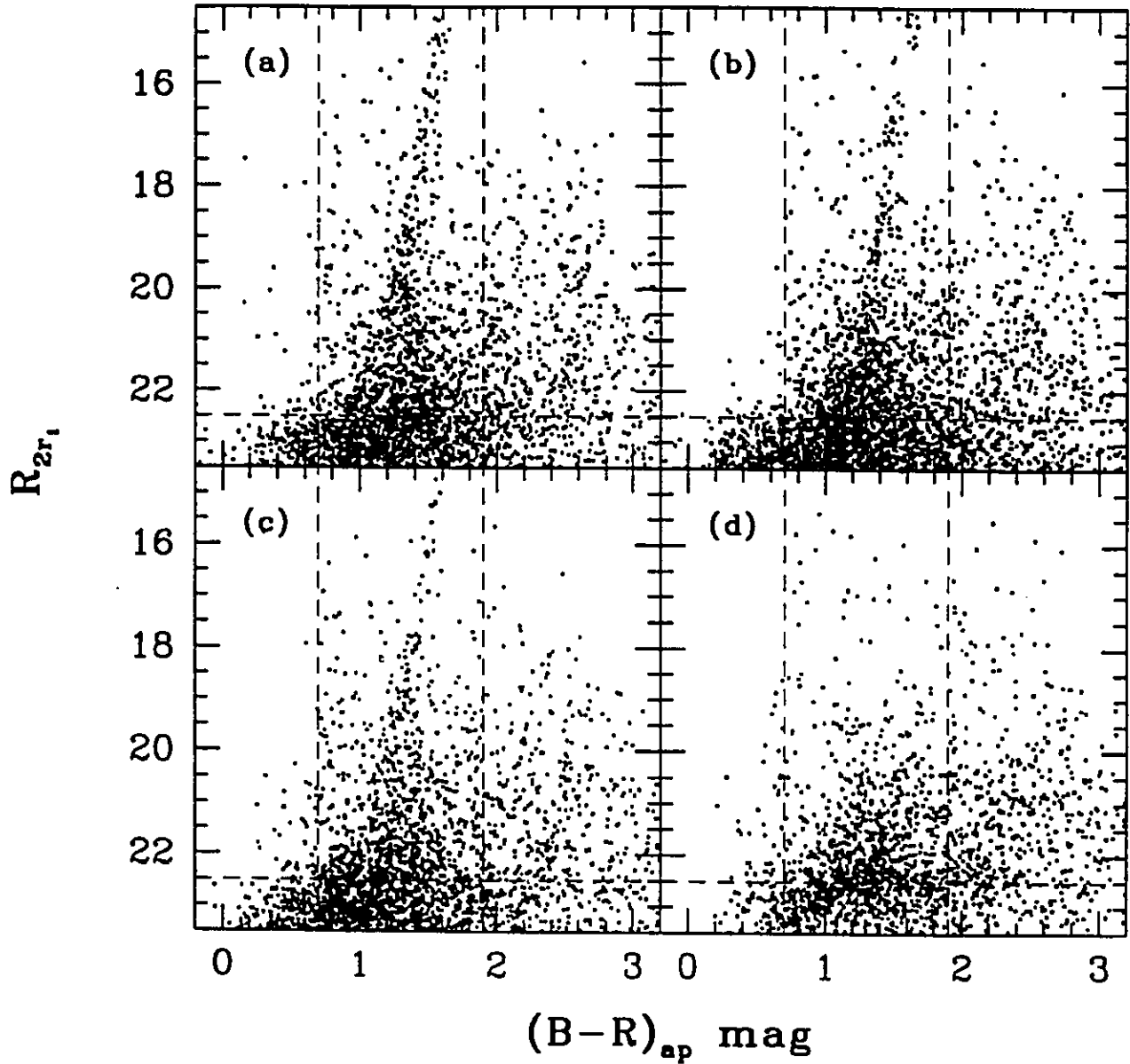


Figure 4.13: Color-magnitude diagrams (CMDs) for all objects detected and measured on the four master R -band images: (a) NGC 4874, (b) NGC 4889, (c) NGC 4874 SOUTH, and (d) CONTROL. The cluster dE galaxies are immediately obvious as the tight sequence of objects not present on the control field CMD. The vertical dashed lines represent generous color limits to this dE sequence. The horizontal dashed line illustrates our adopted completeness limit.

and on the control field. The dwarf elliptical (dE) galaxies are immediately obvious as a well-defined sequence of objects which begins at $R_{2r,1} = 15.5$ near $(B - R) = 1.6$ mag; it is a continuation of the sequence defined by the brighter cluster giants. The dE sequence extends down to the limiting magnitude at $R_{2r,1} = 22.5$ mag, spreading in width due to the photometric errors (in both magnitude and color) as illustrated in Figure 4.6. Comparing the three program field CMDs with that of the control field, it is clear that the galaxy sequence is continuous, and that its faint end merges with the faint noncluster galaxies and foreground stars (Galactic G and K dwarfs and post-main sequence giants). Near $R = 21$ mag, the number of background objects begins to increase rapidly, but there is still an excess of dE galaxies on program field (i.e., see Chapter 5, and analysis of the cluster luminosity function). The location of the dE sequence in the CMD is consistent with colors found by Thompson & Gregory (1993; and see Chapter 5) for Coma cluster dwarf ellipticals, and with the integrated colors of globular star clusters (e.g., Secker et al. 1995; Hopp et al. 1995). The behavior of the dwarf elliptical galaxy color with total magnitude is discussed further in Chapter 5 (Section 2).

The color-magnitude diagram provides a convenient parameter space to further cull the sample of objects and remove the obvious noncluster galaxies; in this manner we greatly decrease the contamination in our sample of candidate dE galaxies. The lower horizontal dotted line at $R_{2r,1} = 22.5$ mag corresponds to our adopted magnitude and color completeness limit; as discussed in Section 4, at this magnitude limit we

are 80 percent complete in detection and almost 100 percent complete in color. All objects fainter than this limit are discarded, but shown here to illustrate the effect of the increased photometric error below this limit. The two vertical dotted lines represent generous limits to the dwarf galaxy sequence, i.e., $0.7 \leq (B - R) \leq 1.9$ mag; within this range, and above $R_{2r_1} = 22.5$ mag, the dE galaxies are clearly the dominant population. The region defined by $(B - R) \lesssim 0.7$ and $R_{2r_1} \lesssim 22.5$ mag is very sparsely populated on all four CMDs. For $(B - R) \gtrsim 1.9$, the density of objects on the program field CMDs appears the same as for the control field, consistent with our interpretation of these objects as noncluster galaxies, much more distant than Coma. In the next chapter, we adopt a value of $R_{2r_1} = 15.5$ mag to distinguish between the faint cluster giants and the brightest expected dwarf elliptical galaxies. As noted above however, this is a continuous galaxy sequence in the CMD.

It is clear that there are objects on the CONTROL field CMD which are faint, nonstellar and within this restricted color range. These objects are both stellar objects fainter than $R_{2r_1} = 19.5$ mag (i.e., the magnitude at which the galaxy sequence begins to merge with the stellar sequence in our parameter space plots of r_{-2} versus R_{2r_1}) and distant faint galaxies. This is exactly the purpose of a control field. We can use the distribution of objects in this CMD to adjust the sample of objects detected on the program fields, in a statistical sense, to further reduce the effects of these contaminating objects.

As a final note, below the horizontal dotted line at $R_{2r_1} = 22.5$ mag, there appears

to be an increase in the number of blue objects on each of the three program field CMDs, over and above the number on the CONTROL field. This excess is consistent with a spread in the measured dE colors, and not an additional population of faint galaxies in the cluster core. This spread is due to photometric errors in the color estimate, which tend to increase dramatically at $R_{2r_1} \simeq 23$ mag. This spread in objects is not uniform about the mean value of the dwarf galaxy sequence (it does not extend redder than $(B - R) \simeq 2.0$ mag), and we attribute this to the incompleteness in color; a longer exposure in the B -band images would be required to measure these objects.

5.3 Final Sample of Probably Cluster Galaxies

The final object lists from the three program fields were combined to obtain one master list of dwarf galaxy candidates for the Coma cluster. To summarize, we discard objects located within the bright stellar sequence defined by $r_{-2} < 1.6$ pixels and $R_{2r_1} < 19.5$ mag, all objects with total magnitude $R_{2r_1} > 22.5$ mag, and objects with a measured color outside of the range $0.7 \leq (B - R) \leq 1.9$ mag. The three program fields share a considerable overlapping area, and we do not want to include the same objects twice in our final sample. For the vertical overlap region, the final object list and photometry is taken from the East edge of the NGC 4874 field, while for the horizontal overlap region, the object list and photometry is taken from the North edge of the NGC 4874 SOUTH field. Note that we did not merge the object lists

in the overlap regions, as this would artificially inflate the detection completeness in these regions. This selection method is valid, as we have shown that the photometry is consistent between program fields,

For reference, over the entire color range $0.2 \leq (B - R) \leq 3.2$ mag yet still above the magnitude limit, there are 3734 objects in the final sample of program field objects, versus 1146 objects on the control field. However, our final sample of dE galaxy candidates for the Coma cluster core consists of 2535 objects, 70 of which are brighter than $R = 15.5$ mag (a large fraction of which are cluster giants; Chapter 5). Within the same limits, there is a total of 694 objects on the control field⁵. In Chapter 5 we perform certain analyses on a more restricted subset of the candidate dE galaxies, in order to obtain a sample with less contamination from objects other than dE galaxies. In the range $1.0 \leq (B - R) \leq 1.8$ mag and $15.5 \leq R \leq 20.0$ mag, there are 383 dE galaxy candidates and 54 objects on the control field. (The number density of these bright objects on the CONTROL field is then 0.199 ± 0.027 per arcmin², using the area of the CONTROL field as defined in Section 5.1.)

Up to this point in the analysis, we have used the measured R_{2r_1} total magnitude, uncorrected for the slight $\simeq 0.1$ -mag correction factor discussed in Chapter 2. This correction factor, as described in (2.20), Section 5.1 of Chapter 2, has been applied to these final object photometry lists, and all analysis from this point on uses the cor-

⁵Using the ratio of areas from Section 5.1, this scales up to $\simeq 1788$ objects for the area of the program fields. Thus in a statistical sense, on the order of 750 candidate objects measured within the Coma cluster core can in fact be dE galaxies. This is quantified further in the analysis of the dwarf-to-giant ratio in Chapter 5.

rected apparent total magnitude, which we simply denote as R . In the analysis in this and the next Chapter, we use the observed colors, since the reddening and extinction is negligible towards the Coma cluster (i.e., the North Galactic pole). We have not tabulated photometry for the 70 brightest cluster members. The total magnitudes and colors we compute are as accurate as possible given our analysis method, and we use these values for our analysis in Chapter 5. However, more accurate photometry is possible, by considering these objects *individually*, excluding nearby neighbors, performing profile deconvolution and possibly isophote fitting techniques. The photometry tables for this bright, color restricted sample of 383 dE galaxies is included as Table 4.5 in Appendix E. The photometry tables for the full sample of 2535 cluster galaxies are available in electronic form from the author.

There are three parameter spaces in which the cluster dE galaxies are very obvious and their distributions informative. In Figures 4.14, 4.15 and 4.16 below, we illustrate these distributions, and in each instance we compare the sample of dwarf galaxy candidates with the objects detected on the control field. In Figure 4.14, we plot color-magnitude diagrams for the sample of 3734 objects in the cluster core, and the 1146 objects in the control field. The control field sample is merely Figure 4.9(d), replotted within these limits for a direct comparison with the cluster sample. As expected, the dE galaxy sequence is more densely populated, and it completely dominates the region of the CMD restricted to $0.7 \leq (B - R) \leq 1.9$ mag. As well, this sequence stands out even more clearly above the contaminating objects. One subtle feature of

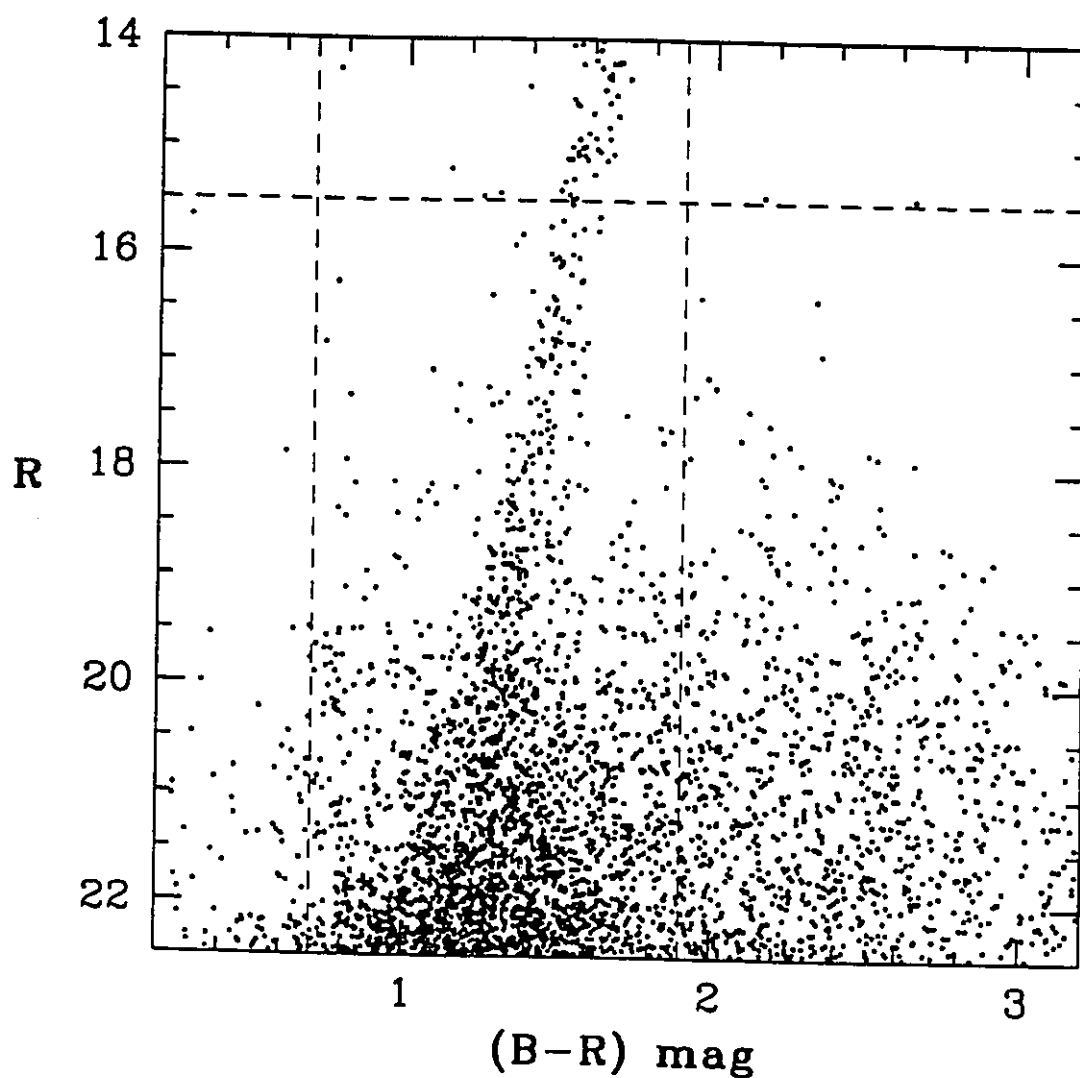
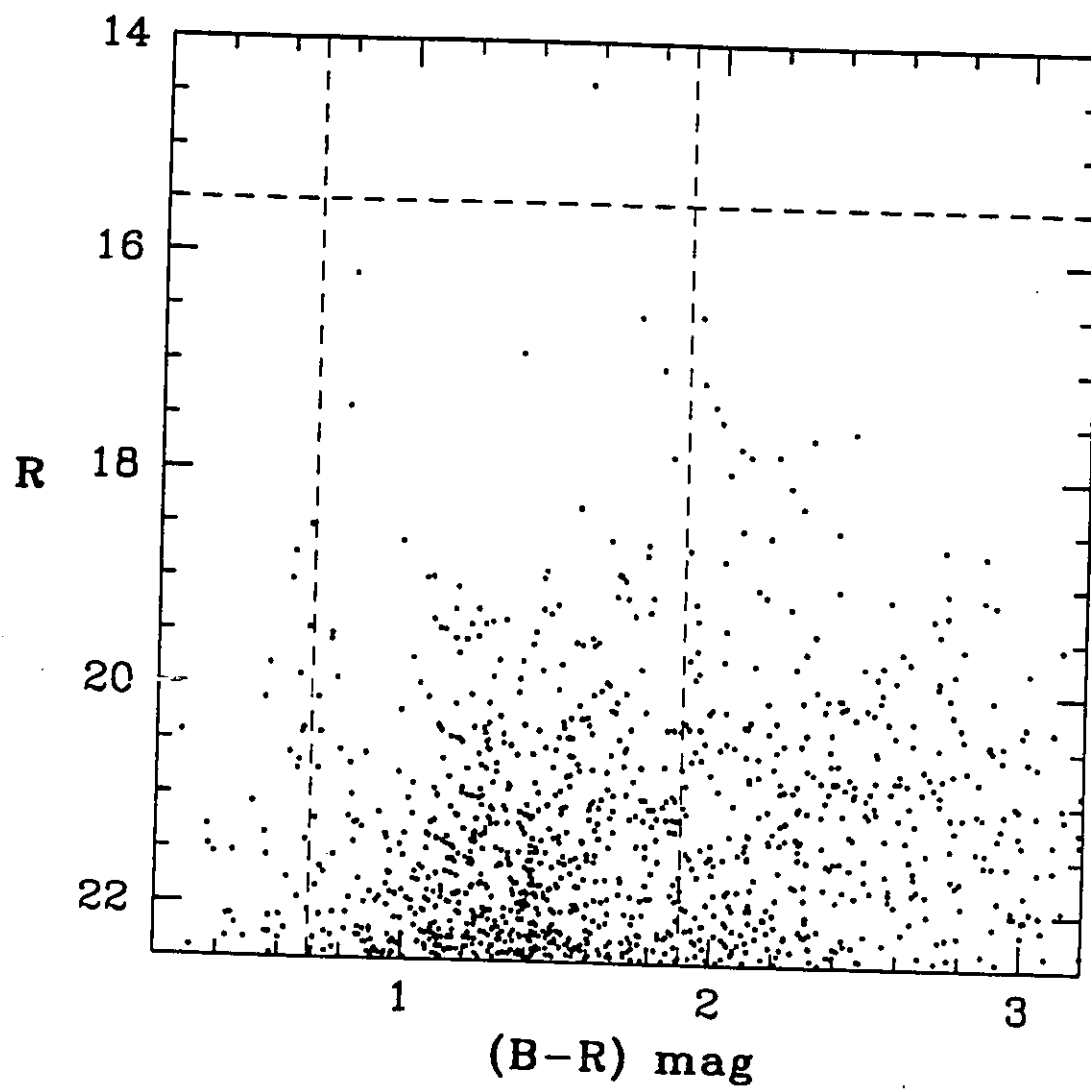


Figure 4.14: (a) This page: The object lists for the three program fields have been added together, and the final composite CMD for 3734 objects (2535 within the restricted color range) is illustrated here. (b) Next page: The control field CMD is replotted within the same limits, for comparison. It consists of a total of 1164 objects, 694 of which are within the restricted color range.



the cluster CMD which is worth pointing out, is the increase of objects, within the restricted color range and below $R = 19.5$ mag. Since we limited our star/galaxy discrimination in the r_{-2} versus R_{2r_1} parameter space to $R \leq 19.5$ mag, this scatter about the dE sequence corresponds in part to the stellar population.

In Figure 4.15 we plot the central surface brightness, I_c , versus the total R magnitude for the sample of 2535 E and dE cluster galaxies and 694 control field objects. The presence of the large population of dE galaxies is evident as the sequence of objects for which I_c is less than the stellar sequence. This well-defined dE sequence is continuous from the bright dEs to the faint dS0s, with no obvious breaks. As well, the width of the dE galaxy sequence is greater than observed in the stellar sequence, at all magnitudes. It is clear that the bright starlike objects have been removed, as the stellar sequence can be seen to begin at $R = 19.5$ mag; below $R \simeq 20$ mag the dE sequence merges with this stellar sequence. The magnitude cutoff at $R_{2r_1} = 22.5$ mag is evident here; while we are complete in *magnitude* above this limit, it is clear that the central surface brightness is only complete above $\simeq 25$ mag/arcsec². However, we must stress that *we detect all objects above $\simeq 26.5$ mag/arcsec²*, such that our sample is genuinely complete to $R_{2r_1} = 22.5$ and *is not biased against low surface brightness dE galaxies*.

Finally, in Figure 4.16 we plot the radial moment r_1 against the total R magnitude, again for the sample of 2535 E and dE galaxy candidates and 694 control field objects. The large excess of cluster galaxies, over and above the control field population, is

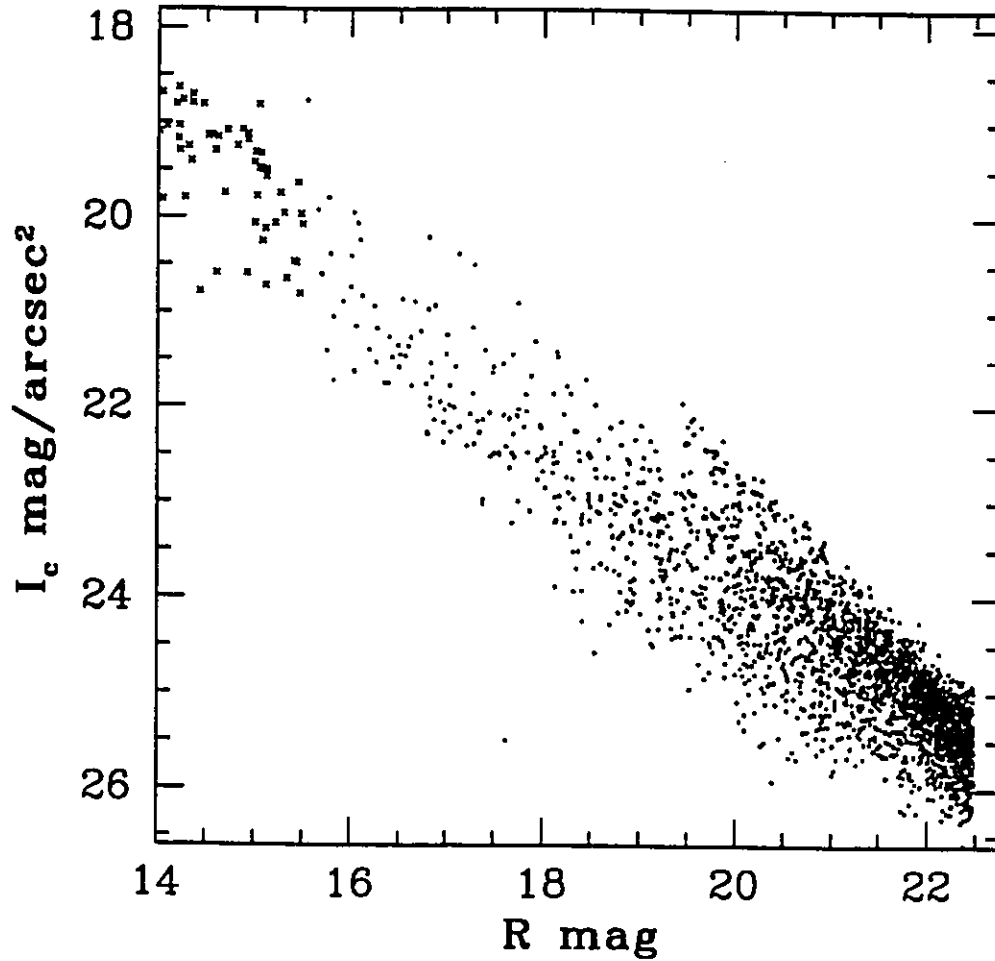
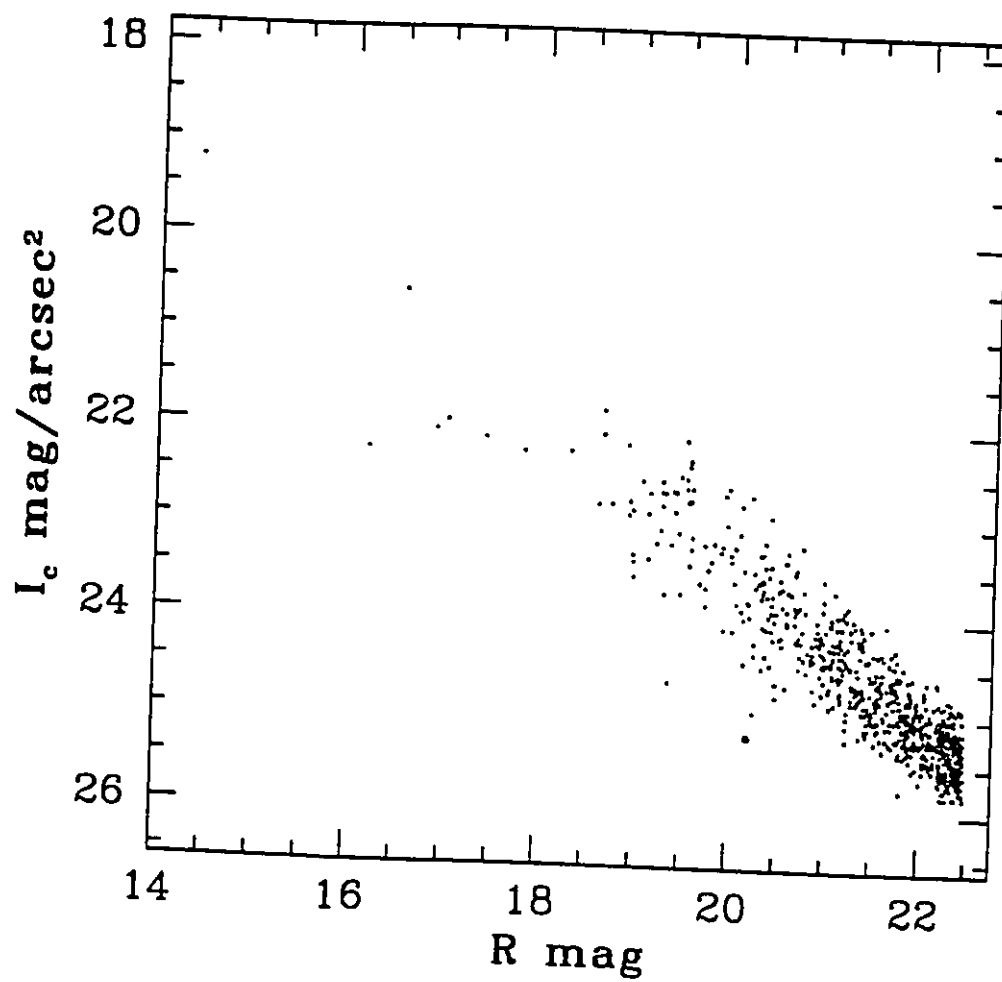


Figure 4.15: The central surface brightness I_c versus the total magnitude R , for (a) the final samples of dE candidates (this page) and (b) the control field objects (next page). The dE galaxy candidates define a loose sequence of objects, below the higher surface brightness starlike objects. These starlike objects have been eliminated down to $R_{2r_1} = 19.5$ mag, but below this the dE galaxies merge into the starlike sequence. The crosses denote all galaxies above $R = 15.5$ mag.



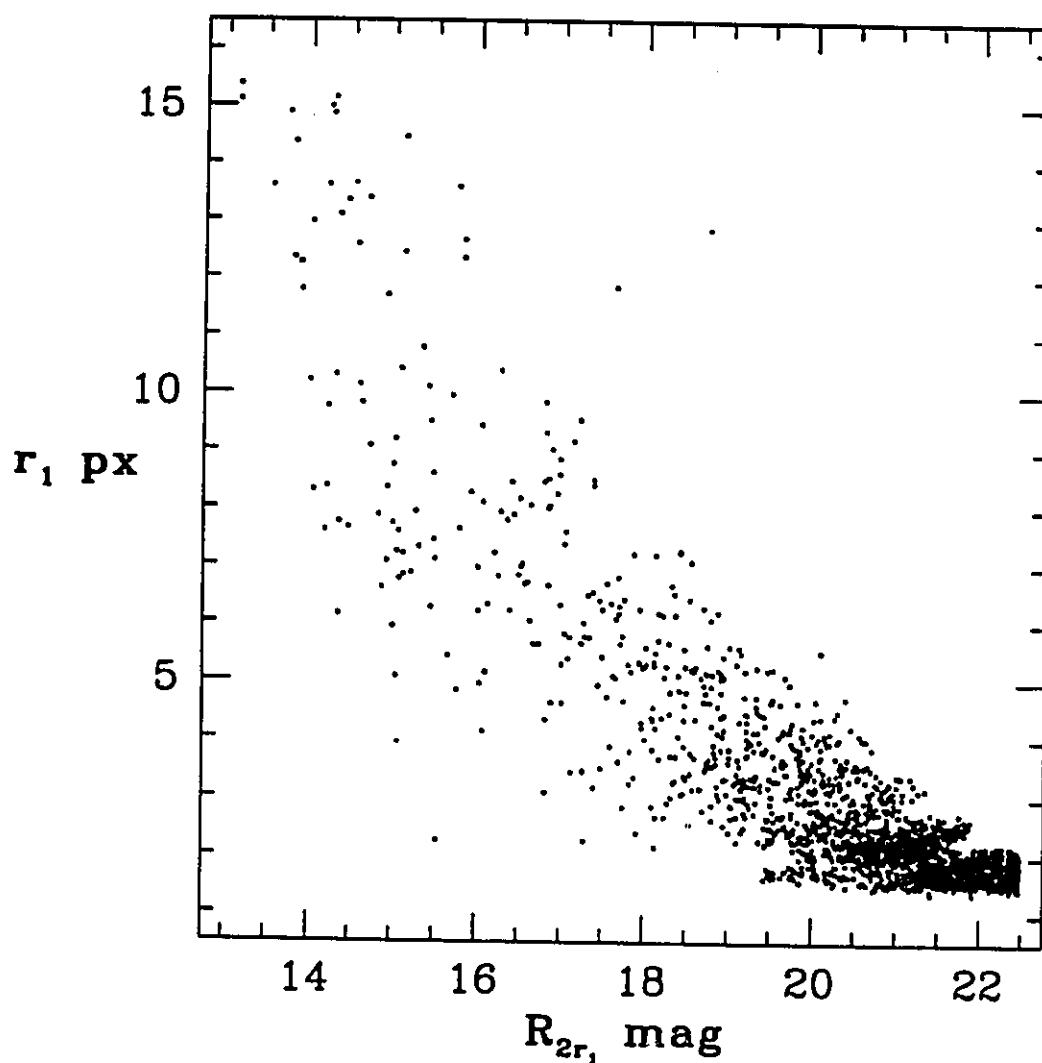
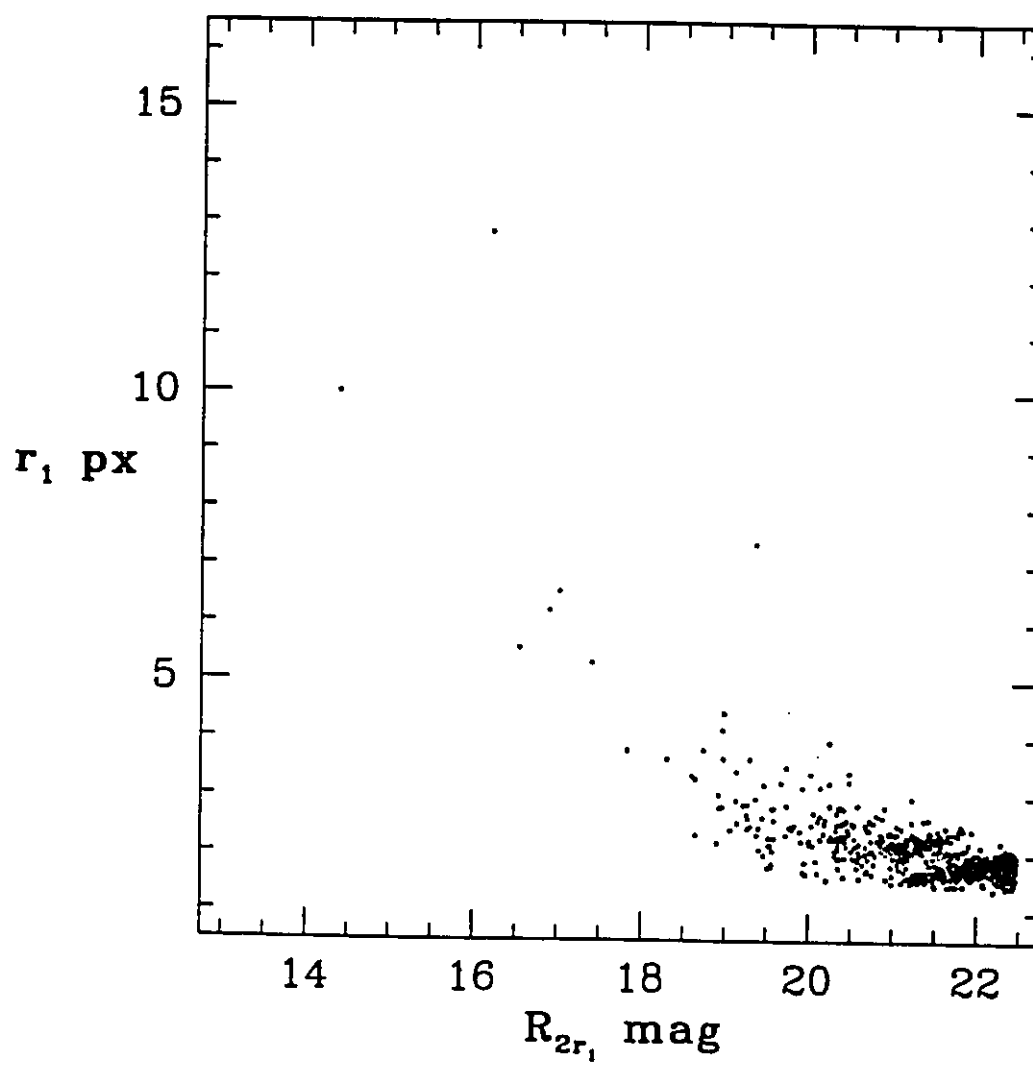


Figure 4.16: The scale radius of the cluster galaxies is traced by the radial moment r_1 , and plotted here as a function of the apparent total R magnitude. We have plotted (a) the final samples of dE candidates (this page) and (b) the control field objects (next page); the dE galaxies are apparent as an excess of nonstellar objects at all magnitudes.



evident. As well, we are able to resolve galaxies down to $R \simeq 21$ mag. The *most extended dE galaxies* have a measured $5 \lesssim r_1 \lesssim 11$ pixels; for a pixel scale of 0.2092 kpc/pixel, this corresponds to an exponential disk scale radius of $1.05 \lesssim r_0 \lesssim 2.30$ kpc, and a half-flux radius of $1.76 \lesssim r_0 \lesssim 3.86$ kpc (see Section 4.3.1 of Chapter 2). The faintest dE galaxies which we can clearly resolve are at $R = 21$ mag; here, $2 \lesssim r_1 \lesssim 3.25$ pixels, which corresponds to $0.42 \lesssim r_0 \lesssim 0.68$ kpc and $0.705 \lesssim r_0 \lesssim 1.14$ kpc. These values are consistent with the study of Bernstein et al. (1995), who measure scale radii in the range $250 \lesssim r_0 \lesssim 450$ pc for their very faint dE galaxies $22.5 \leq R \leq 23.0$ mag.

6. SUMMARY

(1) We have detected and measured total R magnitudes and $(B - R)$ colors for a sample of 3741 objects in Coma cluster core and 1164 objects on a remote control field, complete to a limiting magnitude of $R_{2r_1} = 22.5$ mag. The typical uncertainties are ± 0.06 and ± 0.12 mag in total magnitude and color respectively. The dwarf elliptical galaxies are confined to a color range given by $0.7 \leq (B - R) \leq 1.9$ mag; within this region there are 2535 dE candidates on our fields in the cluster core, and 694 objects on the control field.

(2) By scaling the number of objects on the control field to the area of the program fields, we are left with about 750 candidate dwarf elliptical galaxies. This population of cluster dE galaxies is evident in parameter space plots as an excess of objects

over and above the number on the control field. On the CMD of Figure 4.14, the dE galaxies are located along a well-defined sequence dominating the CMD in that region. In Figure 4.16 we plot the radial moment r_1 versus total magnitude, and here the dE galaxies are evident as an excess of nonstellar objects at all magnitudes.

(3) An important constraint in the computation of total magnitudes is that the total $2r_1$ aperture must be defined as $2r_1$ or radius of seeing disk, whichever is larger. This requirement ensures that all of the object's luminosity is included in summations, and it avoids the effects of quantized r_1 values.

Chapter 5

The Dwarf Elliptical Galaxy Population In The Coma Cluster Core. II. Analysis.

1. INTRODUCTION

The most convincing display of our detection of numerous dE galaxies is Figure 4.14, in the previous chapter. In this color-magnitude diagram, the dE galaxy sequence clearly stands out above the background, and covers a full seven magnitudes in R . In this Chapter, we use this large sample of early-type dwarf galaxies to address (in a statistical manner) four significant properties of the dwarf galaxy population in the core of the Coma cluster.

In Section 2, we analyze the $(B - R)$ color distribution (both in magnitude and radially outwards from NGC 4874) for the dwarf galaxy sequence. We limit this analysis to the brightest 5 magnitudes of the dE sequence, to avoid introducing the scatter apparent at the fainter magnitudes. Our detection of a radial color gradient leads to an interpretation based upon the formation scenario of Babul & Rees (1992). In Section 3, we calculate the slope of the faint-end of the galaxy luminosity function,

and investigate the variation in mean dE galaxy magnitude radially outwards from NGC 4874. Section 4 is devoted to a comparison of the radial surface density profiles between the brighter cluster members and the faint dE galaxies, at which point we clearly show that our CCD fields are all contained within the cluster core. In Section 5, we compute the early-type dwarf-to-giant ratio for our sample of galaxies in the cluster core. The fundamental parameter of interest is the width of the log-normal distribution used to model the giant galaxies. Varying this parameter within the range of acceptable values ($0.8 - 1.2$ mag) allows us to constrain the dwarf-to-giant ratio with realistic uncertainties. Finally, in Section 6, we discuss several issues of relevance, including a possible local enhancement of dwarf galaxies between NGC 4874 and NGC 4889, and a constraint on the origin of the diffuse intergalactic light of the Coma cluster.

2. $(B - R)$ COLOR DISTRIBUTION FUNCTIONS

An analysis of the photometric colors of dwarf and other low surface brightness (LSB) galaxies can provide valuable insights into both (i) the properties of individual galaxies, and (ii) the statistical correlations for populations of galaxies (Caldwell & Bothun 1987; Evans, Davies & Phillipps, 1990; Garilli et al. 1992; Cellone, Forte & Geisler 1994). The broadband photometric color $(B - R)$ was measured for all objects in our sample, and used primarily as a discriminator to eliminate contamination due to non-cluster galaxies and foreground stars (refer to the previous chapter). However,

the $(B - R)$ color index, like $(B - I)$ and the Washington $(C - T_1)$ color, is also a sensitive and accurate estimator of the total heavy element abundance (metallicity) for old stellar populations (Couture, Harris & Allwright 1991, 1992; Geisler & Forte 1990). While both age and metallicity affect absorption features in the spectra (and therefore the integrated color) for systems of old stellar populations, the effect of metal abundance dominates over age effects in the observed $(B - R)$ color of old populations (Worthey 1994). Thus in our sample of galaxies, *we assume that the redder galaxies are, on a relative scale, more metal rich than the bluer galaxies.*

2.1 The Color-Magnitude Relation

In the previous chapter we presented the final datasets for the Coma galaxy fields and the control field, and the resulting color-magnitude diagrams (CMD) for these fields. These diagrams spanned a range in color defined by $0.2 \leq (B - R) \leq 3.2$ mag, and in magnitude defined by $14.5 \leq R \leq 22.5$ mag. In order to restrict our galaxy sample to those most probable members of the Coma cluster, we restricted the color range to $0.7 \leq (B - R)_{ap} \leq 1.9$ mag. These color restrictions represent generous limits on the early-type dwarf galaxy (dE plus dE,N plus dS0) sequence, and nicely exclude the large contribution from red background galaxies. While our sample of galaxies will contain a small number of late-type dwarf irregular (dIr) galaxies, this contamination is negligible (see the discussion below) and will not affect the correlations found in this Section. Note that all analysis in this chapter is performed on the observed colors,

which are uncorrected for reddening (almost negligible at the location of Coma), and on the total R magnitudes (i.e., K -corrections are applied only when comparing our magnitudes with the results of FS91 for the Virgo cluster; Section 5).

The dE galaxy sequence, which begins near $(B - R) \simeq 1.6$ mag at $R \simeq 15$, shows a strong trend for fainter dE galaxies to have (on average) a bluer color (also observed for Coma's brighter dEs by TG93 and Biviano et al. 1995), and at any R magnitude, the width of the dE sequence is greater than can be accounted for by photometric error. These results are discussed further here. In the right panel of Figure 5.1, we reproduce a subset of the total galaxy field CMD, restricted to the 383 dE candidates given in Table 4-5; i.e., $15.5 \leq R \leq 20$ mag and $1.0 \leq (B - R)_{\text{ap}} \leq 1.8$ mag. It is in this region of the CMD that the dE galaxies are the least contaminated by other objects. The solid line superimposed upon the data points is an approximate fiducial line, providing an expected mean color for early-type dwarf galaxies as a function of their R magnitude. The slope of this fiducial line is such that a one magnitude brightening in R magnitude corresponds to a redder color by 0.062 mag. It is difficult to determine the behaviour of the fiducial CMD line for $R \gtrsim 20$ mag, due to the significant contamination from the background galaxies and faint foreground stars. However, looking at the spread of the sequence in this magnitude range (refer to Figure 4.14 of the previous chapter) it appears that an extrapolation of this linear fiducial downward would overestimate the blueward color change for the faintest dwarf galaxies. This bluing trend can be compared to Fornax dE and LSB galaxies. For

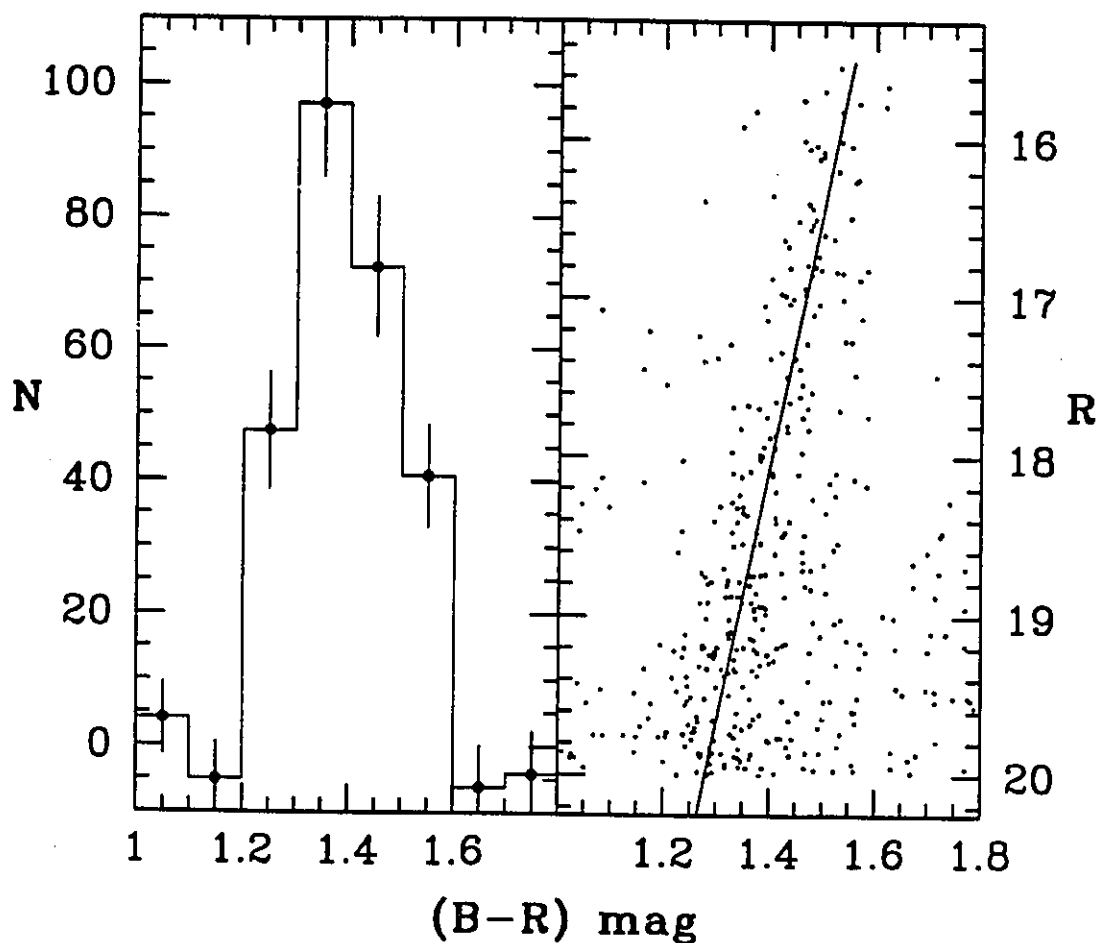


Figure 5.1: A sample of 383 dE candidates in the range $15.5 \leq R \leq 20.0$ mag and $1.0 \leq (B-R) \leq 1.8$ mag. (a) The left panel shows the number of galaxies in the galaxy field CMD, in 0.1 mag bins, corrected for the number of objects in the background field CMD. (b) The right panel illustrates the trend for brighter dE galaxies to have a redder color. The fiducial dE sequence indicates that a one magnitude brightening in R corresponds to a redder color by $(B-R) = 0.062$ mag.

the dE galaxies, Caldwell & Bothun (1987) find an decrease of 0.08 mag in $(U - V)$ for each magnitude decrease in total B magnitude. Cellone, Forte & Geisler (1994) measure a similar trend for the Fornax dE galaxies, using the metallicity sensitive Washinton color $(C - T_1)$. Based upon their CMD, we estimate a decrease of 0.08 mag in $(C - T_1)$ for each magnitude decrease in total T_1 magnitude.

In Figure 5.1, the spread in the dE sequence, about the fiducial line and at any magnitude, exceeds that predicted by our photometric errors. In the restricted (bright-end) range $15.5 \leq R \leq 18$ mag, the total width σ_{obs} appears nearly constant and close to 0.15 mag. In the previous chapter (Figure 4.6), we plotted the photometric error in magnitude and color for our sample of objects, and in this magnitude range the typical color uncertainty is less than 0.025 mag. The intrinsic width σ_{int} of the dE sequence adds in quadrature to the scatter introduced by the photometric error (i.e. $\sigma_{\text{int}}^2 = \sigma_{\text{obs}}^2 - \sigma_{\text{err}}^2$). Since the photometric error is three times less at these magnitudes, we conclude that the intrinsic width in the color of dE galaxies (at any magnitude) is about 0.15 mag. We hypothesize that this intrinsic scatter in the dwarf galaxy metallicity could reflect fragment-to-fragment differences in an early epoch of pre-enrichment, or local variations in the density of the intergalactic gas pressure (refer to Section 2.2; Babul & Rees 1992).

In the left panel of Figure 5.1 we present a binned version of the CMD shown in the right panel. The total number of objects in each 0.1-mag bin were obtained by taking the number on the galaxy field minus the number on the control field CMD

($N = 54$) for the same magnitude range (i.e. $15.5 \leq R \leq 20$ mag). The object number on the control field CMD was scaled (by the factor 2.5760) to account for differences in field area, and the error bars plotted on the histogram represent the \sqrt{N} errors from both histograms added in quadrature. Redder than $(B - R) \simeq 1.6$ mag and in this magnitude range, the number of dE galaxies is consistent with zero. As well, the number of dE galaxies is consistent with zero for $(B - R) \lesssim 1.2$. Fainter than $R = 20$ mag, the dE sequence spreads to such a degree that this distinction would not be as clear.

Thus the majority of faint galaxies in our sample are dE galaxies which lie along a tight sequence in the CMD. If we were to measure the small contribution of dIr galaxies in the Coma cluster core, we would expect them to be bluer (in the mean) than the dE sequence, probably within the color range $1.0 \lesssim (B - R) \lesssim 1.1$ mag (again, for this magnitude range). In this bin, there exists a small positive (but not significant) excess of galaxy candidates.

As our CCD images cover only the cluster core, this is consistent with results from TG93. They find a significant decrease in the number density of dIr galaxies in the core, with typical values of 14-40 dIr per square degree (to a limiting magnitude of $m_b = 20$ mag). Scaling these densities to our 0.194 arcmin^2 field, we can expect to see about $3 - 8$ dIrs for $R \lesssim 18.6$ mag, consistent with our blue-most bin. We conclude therefore that while there is evidence for a small population of dIr galaxies, their contribution to the total sample of early-type dwarf galaxies is essentially negligible.

2.2 A Radial Color Gradient

Several recent theories pinpoint the intracluster gas as a dominant factor in the formation and evolution of dwarf galaxies in a cluster environment. Measurement of the color distribution for the dwarf galaxies radially outwards from the cluster center will help discriminate between competing theories. In Figure 4.2, colors of 383 individual dE candidates (Table 4-5) are plotted versus the logarithmic projected clustercentric radius (adopting NGC 4874 as the center of the cluster)¹. Superimposed upon the scatterplot of Figure 4.2 are larger solid circles, which represent the *median* ($B - R$) color in a given annulus. It is because of the significant scatter in color at any given radius that we adopt the median value as our estimate of a mean color. By its definition, the median is less sensitive to outlying data values, and thus provides a robust estimate of the true average color. The median values are computed in two arcmin radial bins, and are plotted at the geometric mean radius $r = \sqrt{r_i r_j}$ of the bin. The trend for decreasing median color with increasing radius is evident, though obscured to some degree by the scatter in the binned values. The solid line is the result of a least-squares fit to the median values, weighted by the semi-interquartile range (SIQR) uncertainties (the plotted error bars). The median values with their associated SIQR values are provided in Table 5.1. It is evident that for the sample of

¹ An inspection of this scatterplot leads to the impression that there is a deficit of galaxies with extreme colors interior to a radius of four (or five) arcminutes from NGC 4874. This is a manifestation of the small area of the Coma field covered by the annuli out to this radius (compared to the annuli at larger radius), and therefore the smaller fraction of background galaxies that would be expected at these color extremes.

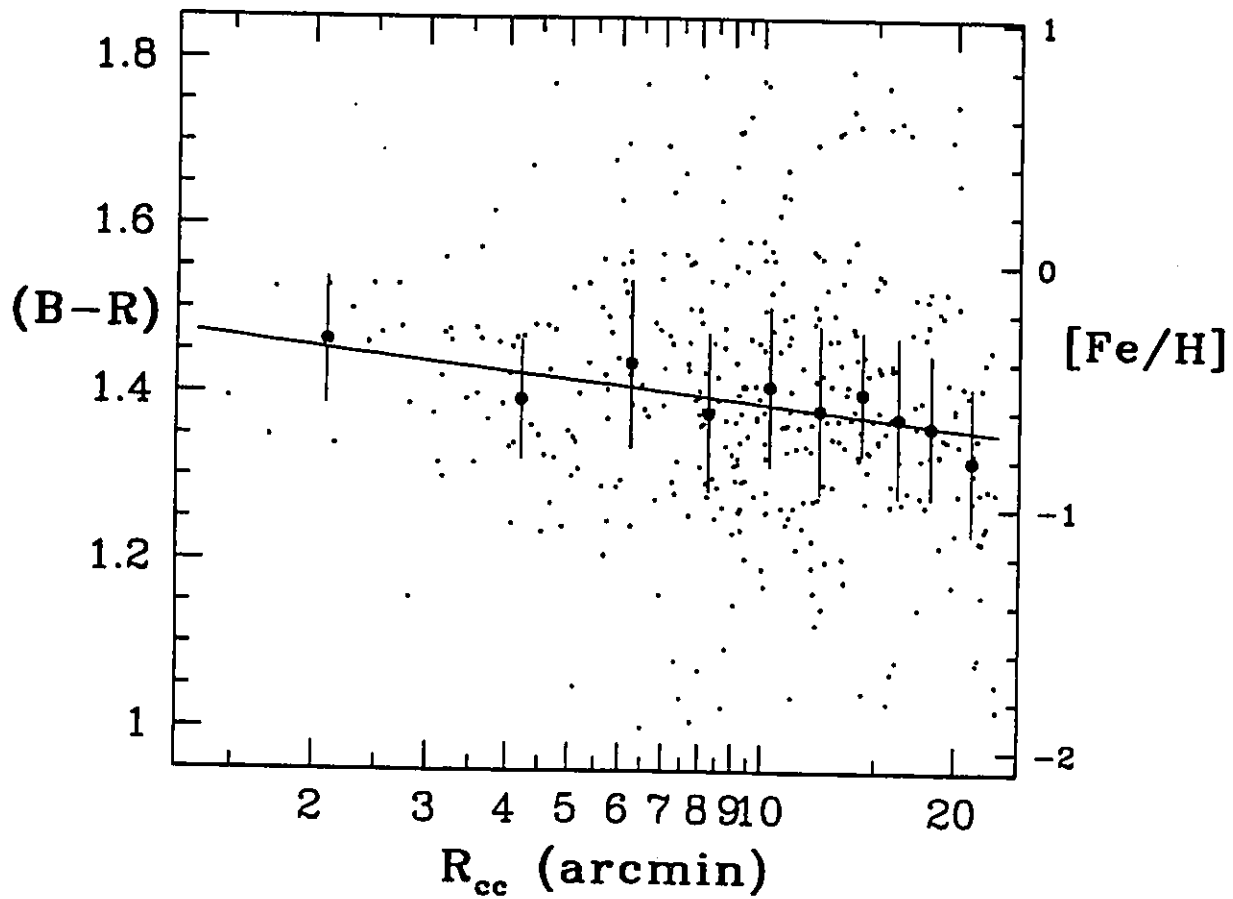


Figure 5.2: For the sample of 383 dwarf galaxies, we plot the median $(B-R)_{ap}$ color (and the SIQR uncertainties) as a function of the logarithmic (projected) cluster-centric radius. The weighted least-squares regression line (fit to the median values) is plotted as the solid line.

TABLE 5.1: Radial distributions for bright dE candidates.

R'_{in}	R'_{out}	\bar{R}'	N	$\langle (B - R) \rangle$ mag	$\langle [\text{Fe}/\text{H}] \rangle$ dex	$\langle R \rangle$ mag
1.33	3.33	2.10	21	1.46 ± 0.08	-0.32	18.24 ± 1.05
3.33	5.33	4.21	38	1.39 ± 0.07	-0.56	18.92 ± 0.97
5.33	7.33	6.25	49	1.44 ± 0.10	-0.41	18.92 ± 1.02
7.33	9.33	8.26	67	1.38 ± 0.10	-0.61	18.81 ± 0.97
9.33	11.33	10.28	57	1.41 ± 0.09	-0.50	18.99 ± 0.62
11.33	13.33	12.28	40	1.38 ± 0.10	-0.60	19.15 ± 0.51
13.33	15.33	14.29	34	1.40 ± 0.07	-0.53	18.53 ± 0.85
15.33	17.33	16.29	22	1.37 ± 0.10	-0.63	19.01 ± 0.75
17.33	19.33	18.30	19	1.36 ± 0.09	-0.66	19.10 ± 0.59
19.33	23.33	21.23	35	1.32 ± 0.09	-0.80	19.28 ± 0.42

(1) Here, $\bar{R} = \sqrt{R_{\text{in}} R_{\text{out}}}$, the geometric mean radius.

dE galaxies analyzed here, the median color of the early-type dwarf galaxies decreases outwards from the cluster center.

The slope and intercept of this regression line are given by $\Delta(B - R)/\Delta(\log R) = -0.103 \pm 0.084$ and $(B - R) = 1.49 \pm 0.08$ mag at $R = 1$ arcmin. Although there is a considerable scatter at any radius (reflected by the large formal uncertainties), we conclude that there is a significant radial color gradient in the population of bright dE galaxies in the Coma cluster core. Note that this gradient persists even if we include our entire sample of dE candidates, complete down to $R_{2r_1} = 22.5$ mag. However, the increased scatter in the $(B - R)$ color versus logarithmic radius, resulting from these fainter measured objects, results in a larger uncertainty on the regression slope.

As found by us and (for example) Cellone, Forte & Geisler (1994), a well defined

luminosity-color relationship exists for dwarf galaxies, in the sense that the redder galaxies have a brighter total magnitude (and therefore higher surface brightness). Thus our determination of a radial color gradient for the dwarf galaxies in the Coma cluster core is equivalent to a *radial luminosity gradient*, with the median dwarf galaxy luminosity decreasing outwards from NGC 4874. We will return to this point in Section 3.2.

As noted in the Introduction of this Chapter, we assume that dE galaxies with redder colors are, on a relative scale, more metal rich than the bluer dE galaxies. In this section we adopt a color-metallicity relationship derived from Galactic globular clusters, which is valid to first order for our sample of dE galaxies. (As discussed in the Introduction, the stellar population of cluster dE galaxies is likely to be both metal poor and old, similar to globular star clusters.) In Figure 5.3 we plot $[\text{Fe}/\text{H}]$ versus the integrated $(B - R)$ color for 82 Galactic globular clusters, derived from the list compiled by W.E. Harris. These metallicities are on the Zinn and West (1985) scale, with typical uncertainties ~ 0.12 dex. A least-squares regression fit to these points yields the solid line, given by

$$[\text{Fe}/\text{H}] = (3.439 \pm 0.088)(B - R) - (5.349 \pm 0.103). \quad (5.1)$$

Three points are worth mentioning. First, this color-metallicity relationship is calibrated over the range $0.85 \lesssim (B - R) \lesssim 1.45$ mag, which we linearly extrapolate to $(B - R) = 1.8$ mag. Second, the $(B - R)$ color is indeed an excellent metal-

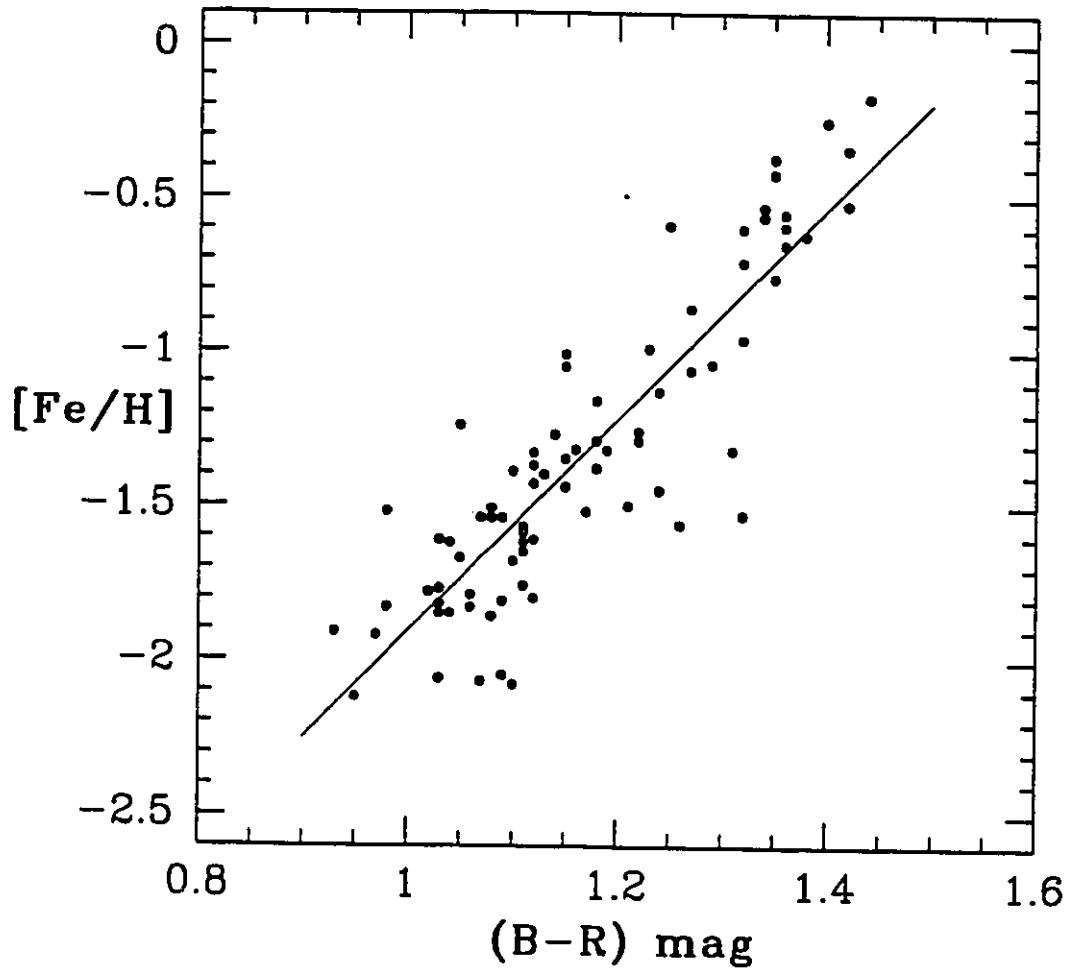


Figure 5.3: Globular cluster metallicity (on the Zinn 1985 scale) versus the integrated $(B - R)$ color. The solid circles denote the 82 Galactic globular clusters, with the least least-squares regression line to these points. A typical uncertainty in metallicity is $\simeq 0.12$ dex.

licity discriminator, spanning a range of 0.5-mag for the corresponding 2 dex in metallicity. Third, combined uncertainties in the photometric calibration, reddening and the metallicity calibration give rise to typical external uncertainties on the order of 0.2 dex. The right-side axis of Figure 5.2 labels this metallicity scale, valid for the 383 individual dE galaxies and the median values (Table 5.1). In terms of metallicity, the slope and intercept of the regression line are given by $\Delta[\text{Fe}/\text{H}]/\Delta(\log R) = -0.324 \pm 0.084$ and $[\text{Fe}/\text{H}] = -0.248 \pm 0.08$ dex at $R = 1$ arcmin. As above, we conclude there is a significant radial metallicity gradient $Z \propto R^{-0.32}$ in the population of bright dE galaxies in the Coma cluster core.

This color/metallicity distribution of the early-type dwarf galaxies, as a function of radial distance from the cluster center, is worth further discussion in the context of dwarf galaxy formation and evolution in a cluster environment. Babul & Rees (1992) introduced a model in which dE galaxies were formed recently (i.e., $z < 1$), and which ties together the field and cluster populations. In their model, they postulate that the intracluster medium plays a dominant role in the evolution of dwarf galaxies, as an external pressure which confines the supernova-driven gas, preventing gas loss in a way that the dark halos themselves cannot. This X-ray luminous intracluster gas is frequently found in rich clusters, and the total mass in cluster gas is on the order of the mass of all luminous matter in the cluster (Fabian et al. 1984). It is diffuse, with a number density in the range $10^{-2} - 10^{-4} \text{ cm}^{-3}$, which peaks in the cluster core. It is hot, with temperatures in the range of $10^7 - 10^8 \text{ K}$, emitting X-rays via thermal

bremsstrahlung (free-free transitions).

Babul & Rees postulate that if this intracluster gas were to exert a confining pressure (greatest near the cluster core), and if this pressure dominated over ram-pressure stripping, it could halt the outflow of metal-rich gas from the young dEs. They attribute the paucity of dwarf elliptical galaxies in the field to the lack of confinement pressure; the field dwarf galaxies more easily expelled their gas (inhibiting further star formation and enrichment) and have subsequently faded away. Following their logic, the dEs nearest to the cluster center should be both *more massive*, and on average, *more metal rich*, than dEs farther from the cluster core. This would result in an observable radial metallicity gradient. Thus our observation of *a radial color gradient for the dwarf galaxy population is consistent with the theory of Babul & Rees (1992)*.

The model of Babul & Rees (1992) assumes a constant star formation rate with position in the cluster (on the order of $4M_{\odot} \text{ yr}^{-1}$ over the first few million years until the first generation of supernovae explode). However, it is possible that the star formation rate (not the efficiency), is dependent upon the intracluster pressure, in the sense that an increase in pressure results in an overall increase in star formation rate. If this were indeed the case, it could work in a similar direction to Babul & Rees: dwarf galaxies nearest the cluster center would convert a greater fraction of their gas into stars during the initial starburst period.

Also relevant to this analysis of dE galaxy metallicities is the “late- accretion”

model of Silk, Wyse & Shields (1987) for galaxies in a cluster environment. Briefly, their model postulates that the intracluster gas was enriched by the metal-rich gas outflows from dEs at an early epoch, say $10 > z > 5$. Then during the epoch of cluster formation, this diffuse gas is compressed and cools, subsequently infalling (mini-cooling flows) and accreting into the halos of the most massive dwarf galaxies (only these massive dwarfs can successfully accrete intracluster gas when competing against the other cluster galaxies); vigorous starbursts can then follow. Their model applies to dwarf galaxies in a cluster environment, and describes a transition from dE galaxies to dIr galaxies during the (present) epoch of galaxy cluster formation. However, their accretion mechanism could also supply the gas necessary for star formation in the nucleus of the more massive dE galaxies (as is observed), for which an observable metallicity gradient within the dE,N population must ensue.

Silk et al. assume that the fundamental parameter governing the star formation within a dwarf galaxy is the gas accretion rate, which is in turn, regulated by the proximity of the dwarf galaxy to a more massive companion. That is, the tidal field of the large galaxy more effectively strips gas from the nearest dwarf galaxies, such that the gas accretion rate and subsequently the star formation rate decreases towards the cluster center. In this manner they explain the spatial distribution of dwarf galaxies: i.e., the paucity of dIr galaxies at the cluster centers. As noted above, the dwarf galaxies compete for gas: only galaxies with the largest gravitational potential wells accrete this gas, leading to the observed turnover in the dIr luminosity function.

As mentioned above, Silk et al. suggest that this late accretion model can explain the presence of a nucleus in the brighter dE galaxies. The sample of 383 galaxies that we analyzed above includes all detected dE galaxies in the absolute magnitude range $-19 \lesssim M_R \lesssim -14.5$ mag. Within this magnitude range, and within our sample, we expect the fraction $N(\text{dE},N)/N(\text{dE})$ to vary from nearly 100 percent for the brightest down to 20 or 30 percent for the fainter dwarfs (van den Bergh 1986); that is, our sample of bright dE galaxies will be dominated by nucleated dE galaxies. If these dE,N galaxies are the result of this late accretion, the expected end result, as predicted by Silk et al., would be an observable reverse radial metallicity gradient. Thus the radial metallicity gradient which we detect in the bright dE galaxies is not consistent with this scenario.

From a study of dwarf irregulars and dwarf ellipticals in the Local Group and Fornax, Richer & McCall (1995) determine that the oxygen-to-iron ratios $[\text{O}/\text{Fe}]$ are significantly greater for the dE galaxies (near solar values) at all luminosities, than for the dIr galaxies. This $[\text{O}/\text{Fe}]$ ratio provides a measure of the rate at which star formation proceeded in the parent galaxy, since oxygen and iron originate predominately in Type II and Type I supernova, respectively. Thus the dE galaxies consumed their gas at a faster rate than did the dIr galaxies, a differing star formation history, which is then also inconsistent with the Silk, Wyse & Shields model.

3. THE GALAXY LUMINOSITY FUNCTION

A probability distribution function or a histogram for galaxy luminosity is known as a luminosity function. For galaxies in a cluster environment, the luminosity function is a fundamental observable quantity, as it places physical constraints on galaxy formation and subsequent dynamical evolution (both in the mean cluster potential and via galaxy-galaxy interactions). From a CDM, self-similar, stochastic model for galaxy formation (Press & Schechter 1974), Schechter (1976) derived a robust analytical form to parameterize the luminosity function. The Schechter luminosity function $\Phi(L)$ defines the number of galaxies in the luminosity interval L to $L + dL$ in terms of three parameters. On a plot of $\log \Phi$ versus $\log L$, L_* is a characteristic luminosity at which the slope of the Schechter function changes (fairly abruptly), α is the slope of the power law for $L \ll L_*$, and ϕ_* provides the normalization (number per unit volume). Then the Schechter luminosity function is give by

$$\Phi(L)dL = \phi_* \left(\frac{L}{L_*} \right)^\alpha \exp \left(-\frac{L}{L_*} \right) \frac{dL}{L_*}. \quad (5.2)$$

For a given ensemble of galaxies, the Schechter luminosity function provides a convenient model for the comparison of galaxy populations between differing environments. As well, it provides a reasonable model with which to extrapolate the luminosity function below the limiting magnitude of the survey, thereby estimating the number of unseen faint galaxies and their contribution to the total mass of the galaxy cluster.

Recent observations strongly dictate that there is no universal luminosity function: not only does it appear to change between field and cluster environments, there is sig-

nificant observed variation between different cluster environments. While it appears that individual galaxy morphological classes have unique LFs, their relative contribution is a product of environment (Binggeli, Sandage & Tammann, 1988). It is in this manner that the composite luminosity function differs, and thus cannot be universal. Although the Schechter function does not adequately describe the composite galaxy (giants plus dwarfs) luminosity function for the Coma cluster, it does provide a good fit to the dwarf elliptical galaxy luminosity function (Sandage, Binggeli & Tammann 1985; TG93; Biviano et al. 1995; and see Section 5).

As is commonly done, in our analysis we plot the the galaxy luminosity function as the number of galaxies per unit *magnitude*. Therefore it is useful to perform a change of variables with the Schechter luminosity function. Using the definition of magnitude

$$m = m_{\star} - 2.5 \log \left(\frac{L}{L_{\star}} \right), \quad (5.3)$$

one immediately obtains its derivative

$$dm = \frac{-2.5}{\ln 10} \left(\frac{L}{L_{\star}} \right)^{-1} \frac{dL}{L_{\star}}, \quad (5.4)$$

and a useful expression for the luminosity

$$\left(\frac{L}{L_{\star}} \right) = 10^{0.4(m_{\star} - m)}. \quad (5.5)$$

Rearranging (5.4), we obtain the Jacobian for the luminosity-to-magnitude transfor-

mation

$$\left| \frac{dL}{dm} \right| = \frac{\ln 10}{2.5} \left(\frac{L}{L_*} \right) L_*, \quad (5.6)$$

where

$$\Phi(m) = \Phi(L) \left| \frac{dL}{dm} \right|. \quad (5.7)$$

Combining (5.4), (5.5), (5.6) and (5.7), and setting

$$\kappa = \frac{\phi_* \ln 10}{2.5} \quad (5.8)$$

we obtain the required form of the Schechter function:

$$\Phi(m) = \kappa \left\{ 10^{0.4(m_* - m)} \right\}^{(\alpha+1)} \left[\exp \left(-10^{0.4(m_* - m)} \right) \right]. \quad (5.9)$$

For our analysis, it is important to define the conversion between the faint-end slope (i.e. $m \gg m_*$) of the luminosity function we measure on a $\log \Phi(m)$ versus $\log m$ plot, and the parameter α of the original Schechter luminosity function. From

$$\log(\Phi(m)) = \log(\kappa) - 0.4(m - m_*)(\alpha + 1), \quad (5.10)$$

we obtain

$$\alpha = -2.5 \left(\frac{\Delta \log(\Phi(m))}{\Delta m} \right) - 1. \quad (5.11)$$

3.1 The Faint-End Slope

In their 1993 study, Thompson & Gregory (1993) find that $\alpha \simeq -1.43$ for the faint-end of the dwarf luminosity function in Coma. This value is consistent with findings for both the Virgo and Fornax clusters (Binggeli, Sandage & Tammann 1985; Sandage, Binggeli & Tammann 1985; Ferguson & Sandage 1988). Recently however, de Propris et al. (1995) determined luminosity functions for the cores of four rich galaxy clusters, and found these to be much steeper (with $\alpha \simeq -2$) at their limiting magnitudes. They (de Propris et al.) suggest that the luminosity function for the Coma cluster may possibly rise more steeply at the faintest magnitudes (below the limiting magnitude of TG93). If so, the faint-end slope for the Coma cluster could rise above the value of $\alpha \simeq -1.43$ and become consistent with their values for other rich clusters.

The deepest and most recent study of the luminosity function for the Coma cluster core is that by Bernstein et al. (1995), as described in the Introduction. Over the range in magnitude of $15.5 \leq R \leq 23.5$ mag, they determine that the slope of the faint-end power law is $\alpha = -1.42$, consistent with TG93, and with a constant faint-end slope over this entire magnitude range. Thus the purpose of our analysis is to determine the slope for the faint-end of the luminosity function *as defined by our sample of dE galaxies in the cluster core*, and to compare this to the findings above.

Our sample of cluster E and dE galaxies was defined in Section 5.3 of the previous chapter: 2535 galaxy candidates in the cluster core and 694 objects on the CONTROL field, with objects in both samples satisfying $R \leq 22.5$ mag and $0.7 \leq (B - R) \leq$

1.9 mag. In Figure 5.4 we plot (in 0.5-mag bins) the raw luminosity functions for both the scaled background field objects (open circles) and the raw counts for the Coma program field (filled circles). Both are corrected for magnitude incompleteness (Section 3, Chapter 4) and plotted with their Poisson uncertainties. Weighted least-squares regression lines are plotted for both components, valid over a range $19.0 \leq R \leq 22.5$ mag. For the cluster fields, this yields a slope of $\Delta \log(N)/\Delta m = 0.31 \pm 0.01$, as compared to a slope of the background field, given by $\Delta \log(N)/\Delta m = 0.40 \pm 0.01$. Although the luminosity function for the background objects is rising more steeply, over the magnitude range considered here the number of objects in the Coma cluster fields does exceed the number of objects in the background field, as expected (see Section 5.3 of Chapter 4, and below).

Now, the only meaningful luminosity function is one statistically corrected for the object counts on the control field. We plot the net (subtracted) luminosity function in Figure 5.5 (see also Table 5.2). The contribution of the giant galaxies ($R \lesssim 16$ mag) to the composite luminosity function is immediately obvious (within the scatter of small-number statistics) as a distribution peaked near $R = 14.5$ mag. However, this composite luminosity function is dominated (in number) by the dwarf galaxies. These are first noticed near $R \simeq 16.5$ mag, and their numbers continue to rise towards fainter R magnitudes. In the faintest three bins, the number of cluster galaxies appears to decrease. This is not due to incompleteness, but these three points result from subtracting similarly large numbers (see Figure 5.4 and Table 5.2); they are therefore

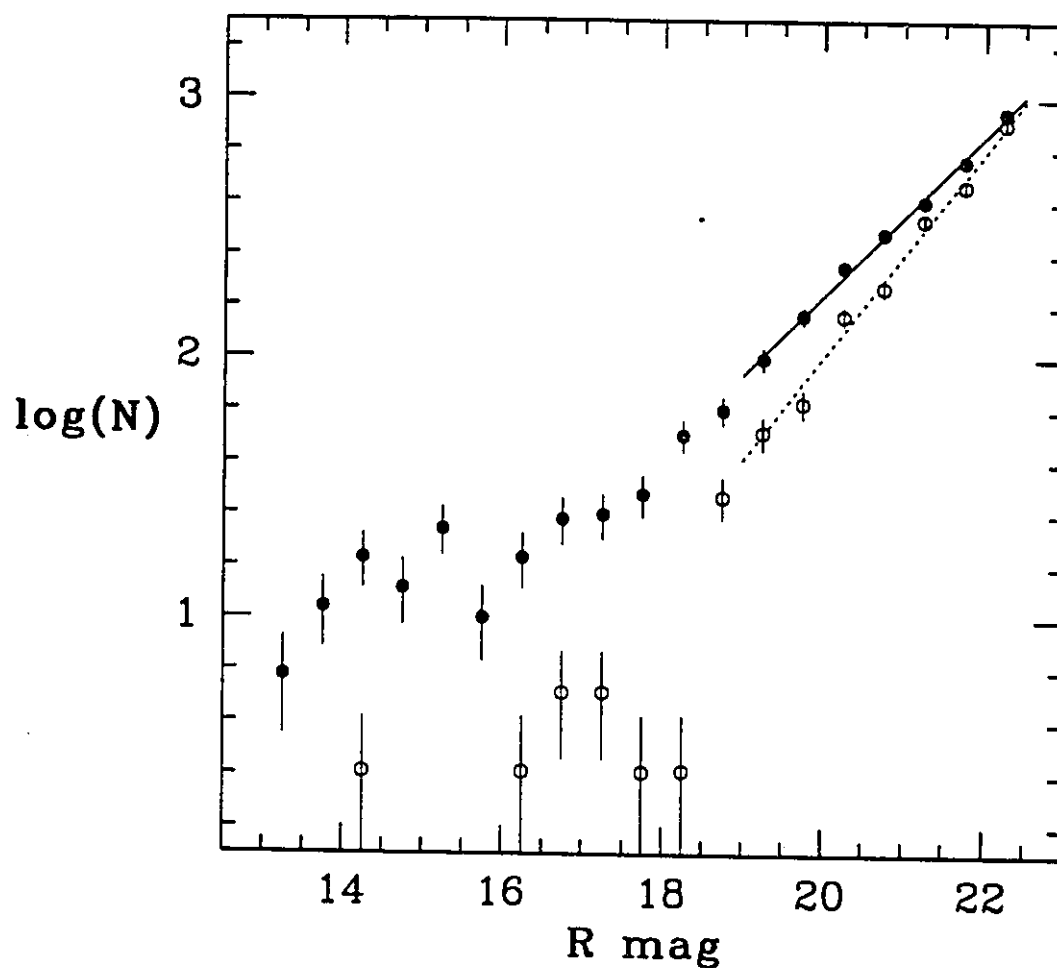


Figure 5.4: The completeness corrected luminosity functions for the galaxy field and background field. The open circles denote the background field, the solid circles the galaxy field, and the error bars Poisson \sqrt{N} uncertainties. The solid and dotted lines are power law fits to the faint-end slopes of the raw luminosity functions.

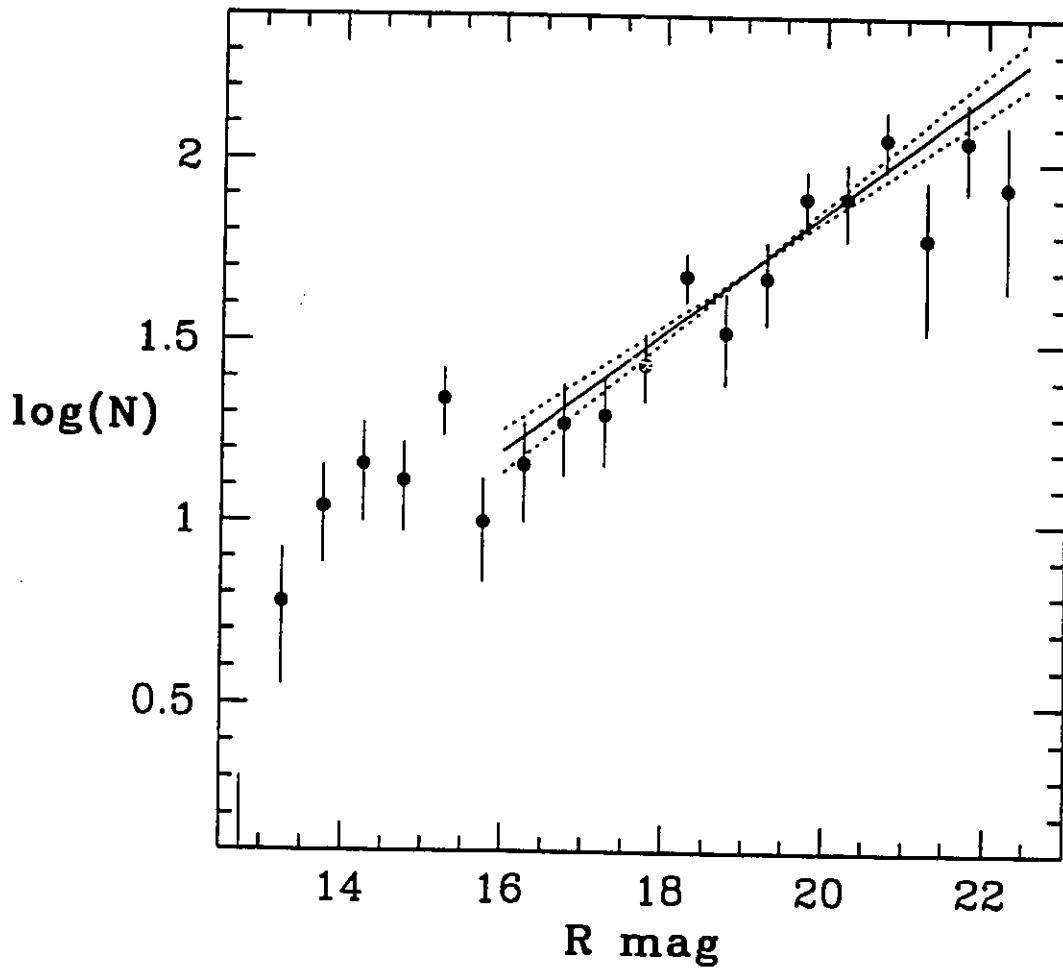


Figure 5.5: The net luminosity function for our sample of Coma cluster galaxies, as defined in Table 5.2. The solid line is a weighted least-squares fit over the range shown, and the slope to $\alpha = -1.41 \pm 0.05$ for the Schechter luminosity function.

TABLE 5.2: Luminosity function for the Coma cluster galaxies.

R mag	N_{Galaxy}	$N_{\text{Background}}$	$f(R)$	N_{Total}
12.75	1	–	1.000	1 \pm 1
13.25	6	–	1.000	6 \pm 2
13.75	11	–	1.000	11 \pm 3
14.25	17	2.6	1.000	14 \pm 4
14.75	13	–	1.000	13 \pm 4
15.25	22	–	1.000	22 \pm 5
15.75	10	–	1.000	10 \pm 3
16.25	17	2.6	1.000	14 \pm 4
16.75	24	5.2	1.000	19 \pm 5
17.25	25	5.2	1.000	20 \pm 5
17.75	30	2.6	1.000	27 \pm 6
18.25	50	2.6	0.989	48 \pm 7
18.75	61	28.3	0.967	34 \pm 10
19.25	94	48.9	0.944	48 \pm 12
19.75	135	61.8	0.922	79 \pm 15
20.25	203	131.4	0.900	80 \pm 19
20.75	267	164.9	0.878	116 \pm 22
21.25	346	293.7	0.856	61 \pm 27
21.75	482	386.4	0.833	114 \pm 32
22.25	721	651.7	0.811	85 \pm 41

- (1) Non-integer values for $N_{\text{Background}}$ result from the ratio of areas, equal to 2.576, applied to correct number counts in each magnitude bin.
(2) N_{Total} is obtained from $f \times (N_{\text{Galaxy}} - N_{\text{Background}})$, rounded to the nearest integer.

uncertain and sensitive to errors in the mean background level. We do not take these faintest three points to indicate significant evidence for a decreasing luminosity function, and we do include them in the following powerlaw fits.

The faint-end slope of our dwarf galaxy luminosity function was obtained via weighted least-squares regression over the magnitude range $15.5 \leq R \leq 22.5$ mag. The upper magnitude limit marks approximately the onset of dwarf elliptical galaxies. The

slope of the least-squares regression line is given by $\Delta \log(N)/\Delta m = 0.166 \pm 0.019$; this best-fit line and its uncertainties are plotted over the corresponding magnitude range on Figure 5.5. This line clearly reflects the rising trend set by the strongest points, and is affected very little by the faintest three bins. We use (5.11) to express this slope in terms of the corresponding Schechter luminosity function, and obtain $\alpha = -1.41 \pm 0.05$.

Our value for the faint-end slope of the Coma cluster luminosity function is therefore completely consistent with that obtained by TG93 and Bernstein et al. (1995). At this point it appears quite evident that the much steeper slope, as suggested by de Propris et al., cannot be reconciled with current observations for Coma. In its own right, this is an interesting and fundamental result. Coma and the four clusters studied by de Propris et al. (i.e., Abell 2052, Abell 2107, Abell 2199 and Abell 2666) are all Bautz-Morgan class I or II clusters, richness-class 1 or 2, with dominant cD galaxies. Therefore, further deep imaging studies of rich galaxy clusters are essential to map all of the cluster parameter space and pinpoint the origin of the steep cluster luminosity functions. Note that the possibility that all clusters have $\alpha \simeq -1.4$, and that the de Propris et al. result is due to erroneous background estimates, is discussed by Bernstein et al. (1995).

3.2 Radial Dependence

In Figure 5.6, R magnitudes of the 383 dE candidates in Table 4.5 (i.e., those used

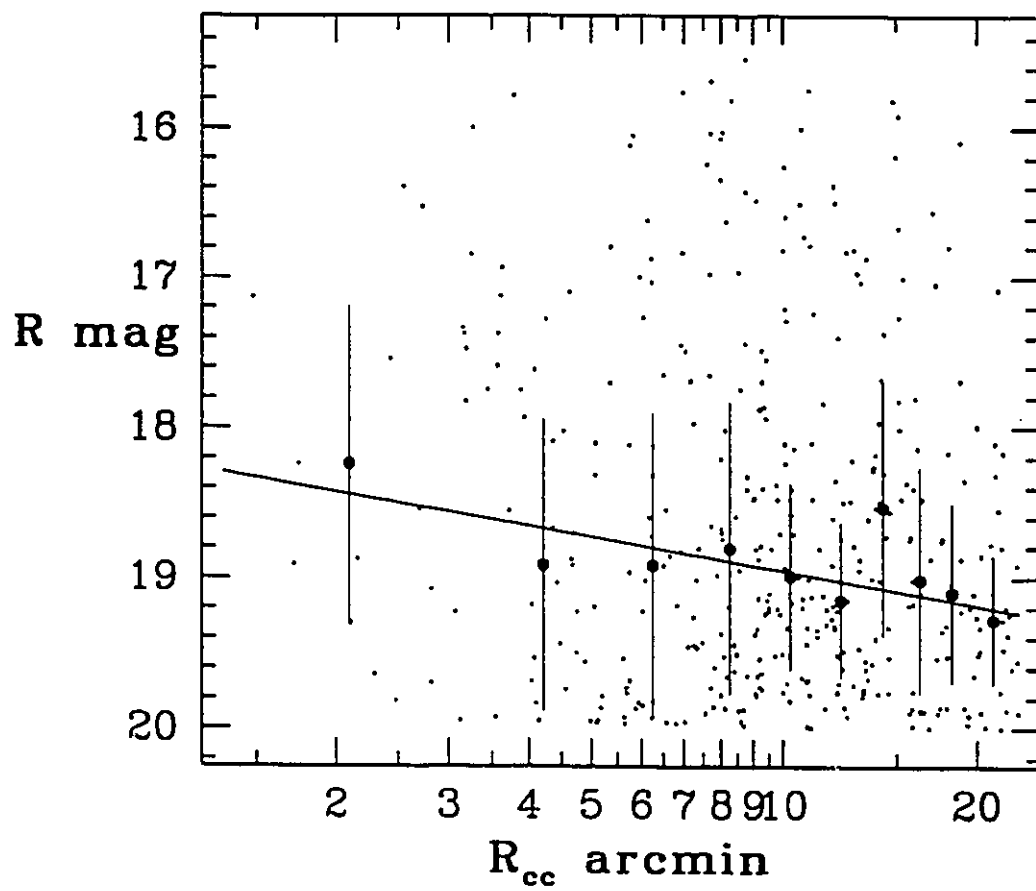


Figure 5.6: For the sample of 383 bright dwarf galaxies, the median R magnitude decreases with increasing clustercentric radius. The weighted least-squares regression line is plotted, as are the SIQR uncertainties for the median values.

for Figure 5.3 in Section 2.1) are plotted versus the logarithmic projected cluster-centric radius, and superimposed upon this scatterplot are the *median* R magnitudes in a given annulus. The solid line is the result of a regression fit to the median values, weighted by the semi-interquartile range (SIQR) uncertainties (the plotted error bars). The median values with their associated SIQR values are provided in Table 5.1. It is evident that the sample of dE galaxies analyzed here, *the median magnitude of the early-type dwarf galaxies decreases outwards from the cluster center*. The slope and intercept of the regression line are given by $\Delta R_{2r_1} / \Delta(\log R) = 0.75 \pm 0.87$ and $R_{2r_1} = 17.95 \pm 0.96$ mag at $R = 1$ arcmin. Since Figure 5.6 is in effect a plot of $\log L$ versus $\log R_{cc}$, we can express this radial luminosity gradient as $\bar{L} \sim R_{cc}^{-0.30}$. It is the considerable scatter in R of the individual data points at any given R_{cc} which gives rise to the large formal uncertainties on the median bin values, and therefore to the large uncertainty on the slope estimate. Regardless of this scatter of the individual data points about the regression line, we conclude that there is a radial luminosity gradient in the population of the brighter dE galaxies in the Coma cluster core.

This analysis shows that *the luminosity function for the dE galaxies in the cluster core depends upon the radial distance from the cluster center*; in this form the variation is easier to visualize than a comparison of binned luminosity functions. In Section 2.2 we attributed the radial color gradient to dwarf galaxy formation dominated by a confining intracluster gas pressure à la Babul & Rees (1992). This scenario is completely relevant here. The confinement pressure indeed forces the primordial

dwarf galaxies nearest the cluster core to retain a larger fraction of their residual metal-rich gas, but at the expense of a larger average mass and luminosity. If this view is correct, the radial color and luminosity gradients are due to their mode of formation, and not to the subsequent dynamical evolution in the cluster gravitational potential.

4. GALAXY SPATIAL DISTRIBUTIONS

In 1980, Dressler defined the *morphology-density relationship* for giant galaxies: the morphological fraction of galaxies at any location in a galaxy cluster is independent of the cluster's global parameters (e.g., richness), and is governed solely by the local projected galaxy density at that location. During their reexamination of the morphological fraction of galaxies in clusters, Whitmore, Gilmore & Jones (1992) determined that a *morphology-clustercenter radius* relationship is in fact more fundamental than Dressler's morphology-density relationship (as evidenced by their improved correlations). In this section we analyze the spatial distribution of the dwarf galaxy population in the Coma cluster core, motivated by the observed correlations between morphological fraction and clustercenter radius. As discussed in Section 3.3 of Chapter 4, our sample of dE galaxies is to some degree biased against companions of the large extended galaxies. Therefore, we do not look for clustering of dEs around individual giant galaxies, and we concentrate on analyzing their overall distribution in the cluster core. Specifically, do the dwarf galaxies trace the substructure about

NGC 4874 (i.e., does their projected number density continue to rise inwards to the center, as do the brighter galaxies), or are they distributed uniformly throughout the cluster core as a whole?

The morphology-density relationship holds true for dwarf galaxies, for both the Virgo cluster (Binggeli, Tammann & Sandage 1987; Binggeli, Tarenghi & Sandage 1990; Ferguson & Binggeli 1994) and the Coma cluster (Thompson & Gregory 1993; Bernstein et al. 1995). For the Coma dwarf galaxies, TG93 adopt NGC 4874 as the cluster center and determine that brighter dwarf elliptical galaxies follow the distribution of the early-type giant galaxies throughout the cluster, rising steeply towards the center. While the faint dEs are distributed as the bright dEs in the outer regions, inwards of 0.35 arcmin there is a deficit of faint dEs galaxies. The results of Bernstein et al. (1995) are in general agreement with TG93, and they also show that besides NGC 4874, no other giant galaxies show evidence for a local concentration of faint dwarf galaxies.

In Figure 5.7 we plot our sample of 455 cluster galaxies (giants plus bright dwarf ellipticals) selected by color to have $1.0 \leq (B - R)_{ap} \leq 1.8$ mag, and brighter than $R \leq 20.0$ mag. Immediately noticeable is the *strong clustering of bright galaxies in the core, especially around NGC 4874, and a rapid decrease in the number density of galaxies outwards from this cluster center*. There are two notes relevant to this figure. First, we have assigned R -magnitudes of 10.93 and 11.03 mag to NGC 4889 and NGC 4874, based upon B_T magnitudes (from RC3) and an assumed color of

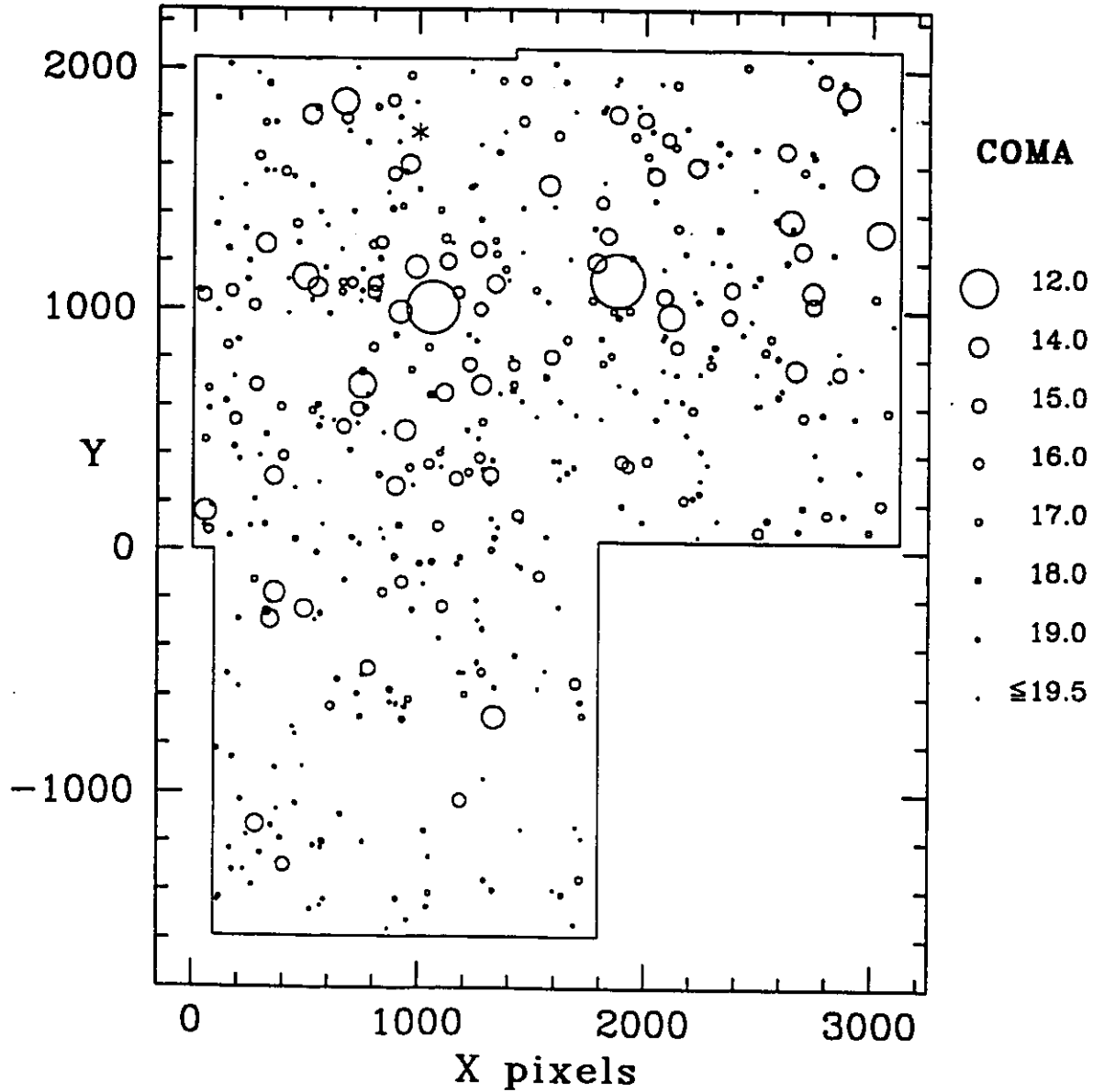


Figure 5.7: The spatial distribution of our sample of 455 Coma cluster E and dE galaxies brighter than $R = 20$ mag. Notice the obvious clustering of bright galaxies around NGC 4874 and NGC 4889, located in this plot at (1061,1010) and (1875,1124) respectively.

$(B - R) = 1.6$ mag. Second, our sample is partially incomplete within a radius of 150 pixels around both NGC 4874 and NGC 4889 (refer to the previous chapter).

In Figure 5.8 we plot our full sample of 2465 cluster dwarf galaxies selected by color to $0.7 \leq (B - R) \leq 1.9$ mag, and limited in magnitude to $15.5 \leq R \leq 22.5$ mag. This sample is dominated in numbers by the faint dwarf galaxies and includes a contribution from a spatially-uniform background population. In contrast to Figure 5.7, there is no apparent strong concentration of dwarf galaxies.

4.1 The Radial Profile For Cluster Galaxies

The spatial (radial) number density profiles for these two samples of galaxies (i.e., the bright galaxies and the faint dE galaxies) are derived simply by summing the number counts within radial annuli, and normalized to the useable area of the annuli. In Figure 5.8 the dotted circles designate the boundaries of the radial annuli, which are used for both galaxy samples. The inner annulus begins 1.325 arcmin from NGC 4874, the outer annulus ends at 23.325 arcmin, and the region in between is divided evenly into 2 arcmin bins (except for the outer annulus; see Table 5.3). (These are the same radial bins used for the analysis of the radial color and luminosity distributions.) The actual area of the annuli used in calculations is that which intersects useable regions of the CCD images, as designated by the solid line boundary in Figure 5.8. Also plotted in Figure 5.8 are smaller solid circles. The largest of these represent incomplete regions due to NGC 4787, NGC 4889, and a very bright star north of NGC 4874,

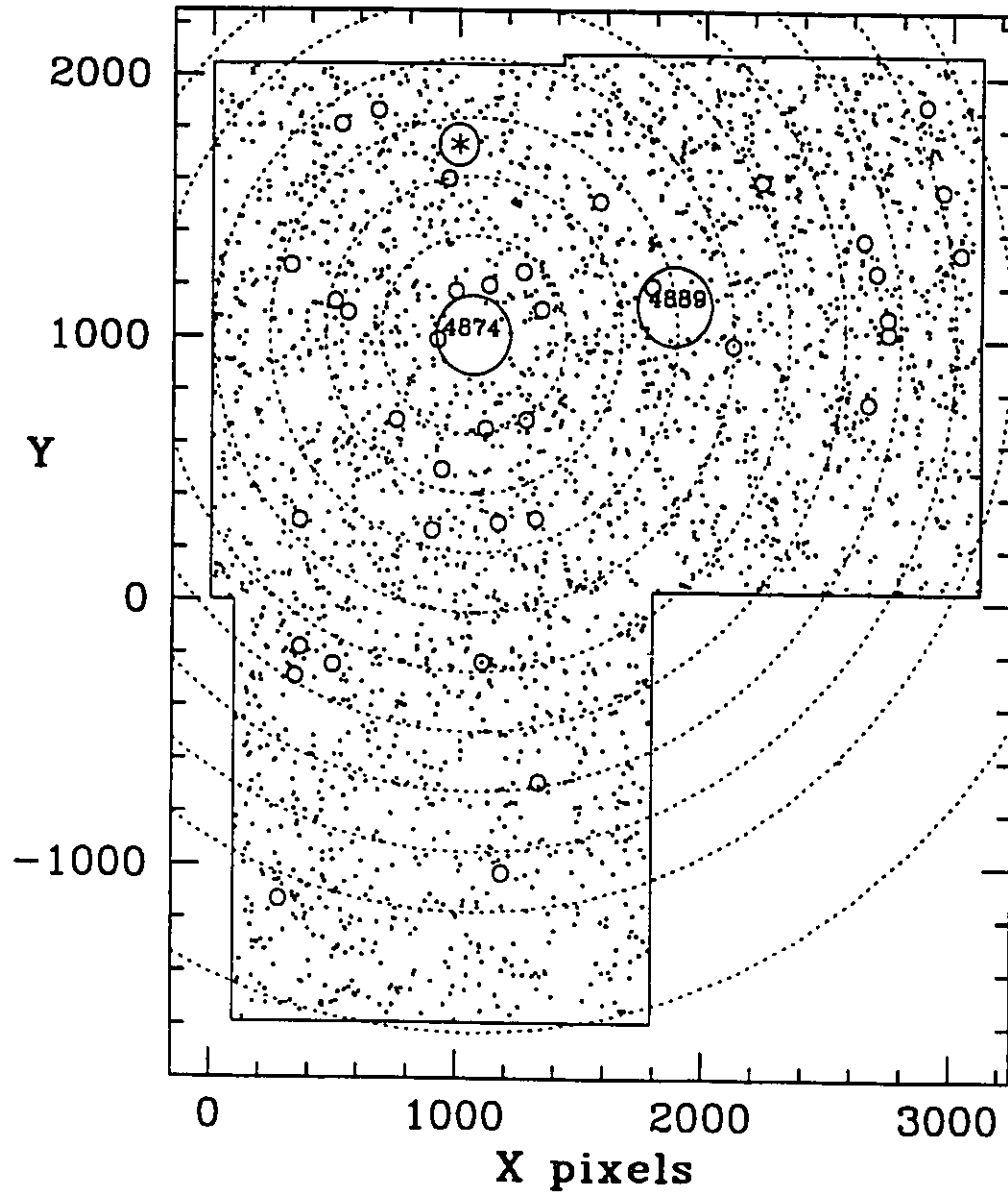


Figure 5.8: The spatial distribution of our full sample (bright and faint) of 2465 dwarf elliptical galaxies. The dotted circles are centered on NGC 4874, and denote the annular boundaries used for computing the radial surface density profiles. The small solid circles denote incomplete areas, corresponding to NGC 4874, NGC 4889, a bright star, and other extended galaxies.

TABLE 5.3: Radial number densities for cluster galaxies.

R'_{in}	R'_{out}	\bar{R}'	N_{bright}	Area arcmin ²	σ_{bright} N/arcmin^2	N_{faint} arcmin ²	Area N/arcmin^2	σ_{faint}
1.33	3.33	2.10	30±5.5	29.28	0.86±0.19	114±11	28.04	1.47±0.39
3.33	5.33	4.21	42±6.5	53.91	0.65±0.13	213±15	52.77	1.48±0.29
5.33	7.33	6.25	54±7.4	76.96	0.55±0.10	259±16	73.01	0.99±0.24
7.33	9.33	8.27	77±8.8	102.60	0.57±0.09	391±20	99.20	1.35±0.22
9.33	11.33	10.28	62±7.9	93.03	0.49±0.09	334±18	92.50	1.03±0.22
11.33	13.33	12.29	49±7.0	77.25	0.44±0.09	309±18	76.34	1.49±0.25
13.33	15.33	14.29	40±6.3	70.08	0.37±0.09	229±15	68.82	0.77±0.24
15.33	17.33	16.30	22±4.7	68.83	0.15±0.08	238±15	68.77	0.90±0.24
17.33	19.33	18.30	23±4.8	58.35	0.20±0.09	189±14	57.73	0.71±0.26
19.33	23.33	21.23	35±5.9	61.66	0.42±0.10	187±14	61.53	0.48±0.24

(1) The bright sample includes 455 cluster members with $R \leq 20.0$ mag, while the faint sample includes 2465 dE galaxies with $15.5 \leq R \leq 22.5$ mag. Both samples are incomplete within 150 pixels (1'.325) of NGC 4874 and NGC 4889.

(2) The slight differences in annular area between the bright and faint samples results from the excluded regions illustrated in Figure 5.8.

(3) The number densities given in columns 6 and 9 are corrected for the mean control field levels: 0.199 ± 0.027 per arcmin² and 2.560 ± 0.097 per arcmin² respectively.

(4) $\bar{R} = \sqrt{R_{in} R_{out}}$, the geometric mean radius.

while the smaller circles are located at the positions of extended giant galaxies. All of these incomplete regions are taken into account when computing the area of the annuli, and thus represent a first-order correction to the spatial incompleteness (see Section 3.2 of Chapter 4 for a discussion of this spatial incompleteness).

We compute the spatial number density of cluster galaxies for both of the samples discussed above: that is, the *bright cluster galaxies*, which includes cluster giants and bright dE galaxies, and the *complete dE galaxy population* (both included in Table 5.3). These spatial distributions are illustrated in the N per arcmin² versus R_{cc} space (Figure 5.9), and in the $\log(N/\text{arcmin}^2)$ versus $\log(R_{cc}/\text{arcmin})$ space (Figure

5.10); the number densities are plotted at the geometric mean radius (i.e., $r = \sqrt{r_i r_j}$) of the annulus, and are corrected for the mean number density of objects (for the appropriate galaxy sample) on the CONTROL field.

It is clear in the upper panels of Figures 5.9 and 5.10 (as described for Figure 5.7), that the number density of both early-type giants and bright dwarfs continue to rise into our innermost bin at $R_{cc} = 2.1$ arcmin. Also evident for these bright galaxies is the noise inherent in the last three radial bins. The radial surface density profile for the dE galaxies (lower panel) is very flat, and we observe just to the edge of this constant number-density core. It is the relative differences of the core radii for these two samples of galaxies which we are primarily interested in, and below we quantify the shapes of these radial profiles using models fit to the data. Note first, however, that the outermost three points in both radial profiles correspond to only a small fraction of the total cluster area at that radius, and are thus very spatially incomplete around the annulus. Since the number density of bright galaxies is so low at these radii, the last three points in the upper panel suffer from extreme small number statistics. However, the number density of dE galaxies in these last three annuli is sufficiently large that the entire dE galaxy profile (lower panel) is certain. (If the spatial distribution of dE galaxies about NGC 4874 were ellipsoidal, this incomplete spatial sampling could bias our radial profile). Nevertheless, we include these three points in all model fits performed below.

To both of these (projected) radial surface density profiles we fit an isotropic,

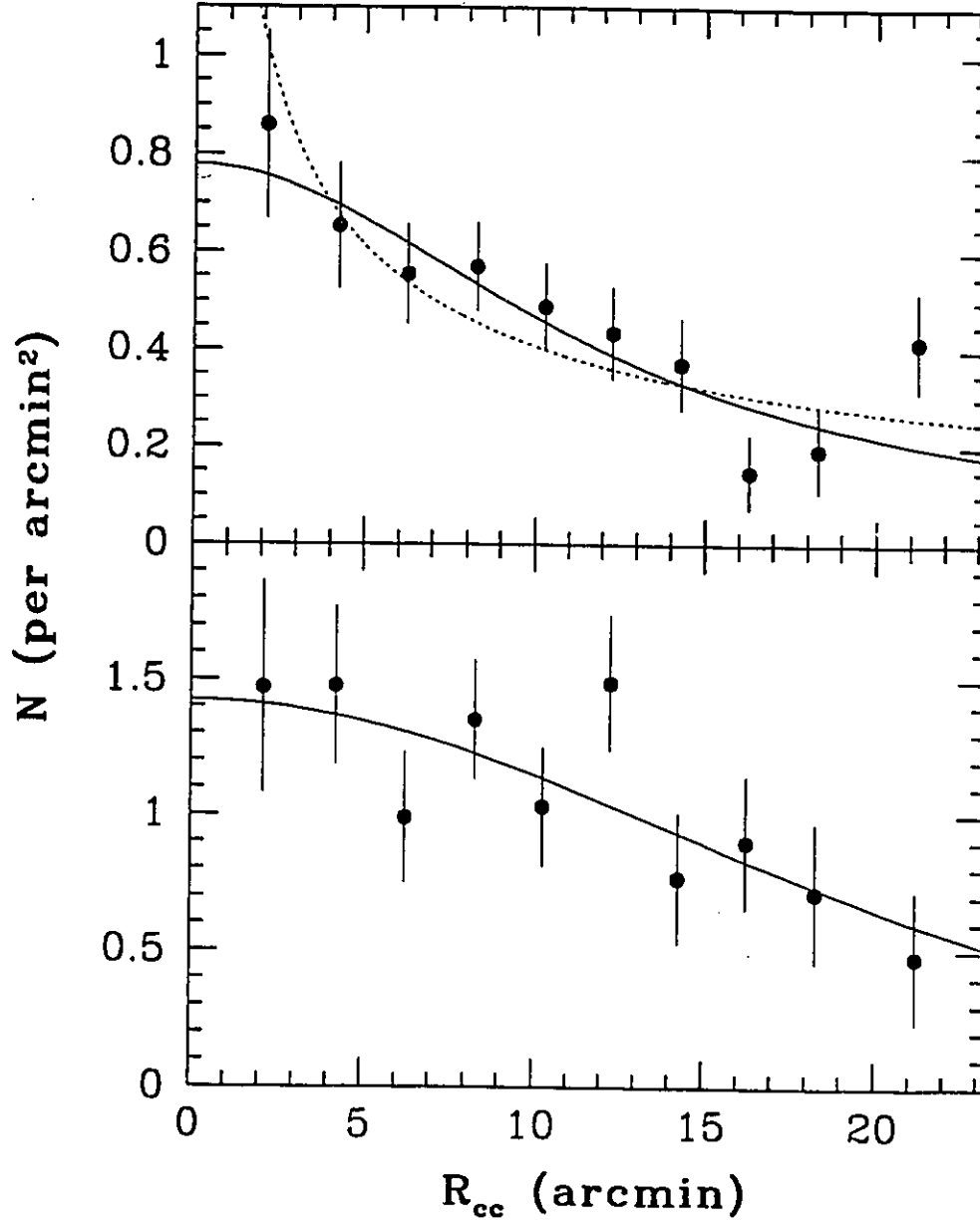


Figure 5.9: Radial surface density profiles for Coma cluster galaxies, plotted over the clustercentric range $0 \leq R_{cc} < 23$ arcmin. Top panel: the sample of 455 cluster giants and bright dE galaxies, as illustrated in Figure 5.7. Two models describe well the plotted radial distribution: the dotted line represents the best-fit powerlaw, while the solid line gives the best-fit King model. Bottom panel: the sample of 2535 dE galaxies, as illustrated in Figure 5.8. A King model (solid line) fits well to this radial distribution, and indicates that the core radius for this dE population is 18.7 arcmin, as compared to 12.3 arcmin for the bright galaxies.

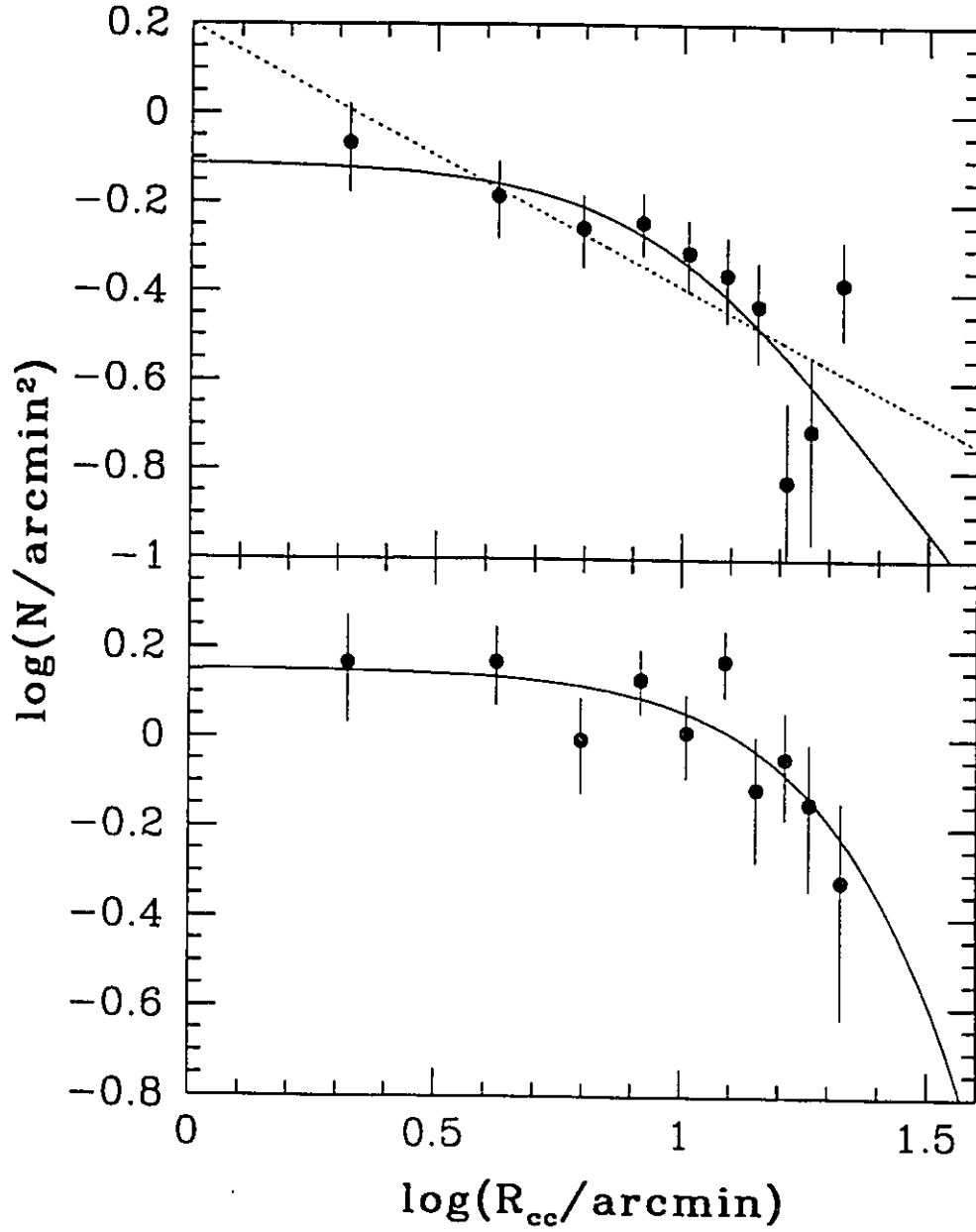


Figure 5.10: These are the same radial surface density profiles for the Coma cluster galaxies as described in the previous figure, but plotted in log-log parameter space. The comments from the previous figure apply here.

single mass King model (King 1966), which describes a truncated isothermal sphere (i.e., a self-gravitating system supported against collapse by the radial velocities of the member objects, with a velocity dispersion that remains constant with radius). This King profile is essentially a three parameter model: the concentration index c governs the overall shape of the profile, while the core radius R_c denotes the distance at which the surface density falls to one half of its central value, represented by Σ_0 . In practice, we numerically compute² King models for various values of the concentration index, which we then shift vertically and horizontally until they best fit the observed data (McLaughlin et al. 1995). The model which, when shifted, provides the minimum χ^2 statistic, is taken to be the best fit to the data. While these King models were originally proposed to model globular star clusters, they have also been used successfully to model galaxy clusters (Bahcall 1977; Binggelli et al. 1987). *Our main interest in King models is that they fit well to our radial density profiles, and thus provide a convenient method to compare the core radius and central surface densities between our two galaxy samples.*

To the bright galaxy radial profile only, we also fit a powerlaw of the form

$$N = \beta R_{cc}^\alpha + \sigma_b, \quad (5.12)$$

where N approaches σ_b as $R_{cc} \rightarrow \infty$. In Figures 5.9 and 5.10, and in the model fits,

²Analytic approximations to the center regions of these King models (for specific values of the concentration index) are described in (for example) Bahcall 1977.

we have $\sigma_b = 0$, since we have subtracted the mean control field number density³. In our Figure 5.10 of $\log(N)$ versus $\log(R_{cc})$, α is the slope of the powerlaw falloff while β is the intercept (at $R_{cc} = 1$ arcmin). By minimizing the χ^2 statistic, we determine α and β for the best-fit model, along with a reasonable uncertainty range.

Our results for the radial distribution of bright galaxies (Figure 5.7 and the top panels of Figures 5.9 and 5.10) are as follows. The best-fit King model (a reduced χ^2 value of 1.33) has a central surface density $\Sigma_0 = 0.777 \pm 0.001$ arcmin⁻², a core radius $R_c = 12.32 \pm 0.02$ arcmin (corresponding to $R_c = 291.8 \pm 0.5$ kpc), and a concentration index of $c = 3.1 \pm 0.5$. This is illustrated as the solid line in the top panel of both figures. Our measured core radius is comparable to a value of 9 arcmin obtained by Kent & Gunn (1982), with the difference most probably arising from our limited radial coverage. The best-fit powerlaw (reduced χ^2 value of 1.53) is plotted as a dotted line; it has a slope of $\alpha = -0.6 \pm 0.1$ and an intercept $\beta = 1.6 \pm 0.3$ (at $R_{cc} = 1$ arcmin). It is clear from the comparison of these two fits to the observed data points, and from the reduced χ^2 values, that the King model provides a better fit to the radial profile for these bright galaxies.

For the ensemble of dE galaxies (Figure 5.7 and the lower panels of Figures 5.9 and 5.10), the best-fit King model (a reduced χ^2 value of 0.93) yields a central surface density $\Sigma_0 = 1.424 \pm 0.001$ arcmin⁻², a core radius $R_c = 18.73 \pm 0.01$ arcmin (correspond-

³Harris (1986) has shown that when fitting a function of this form to a radially decreasing distribution, σ_b will always be underestimated if the number counts are still decreasing outwards past the boundary of the field. Thus we subtract the (already-known) mean control field number density, $\sigma_b = 0.199 \pm 0.027$ per arcmin², and solve for the slope and intercept.

ing to $R_c = 443.5 \pm 0.1$ kpc), and a concentration index of $c = \log(r_t/r_c) = 0.39 \pm 0.06$. Accordingly, the tidal radius r_t of the Coma cluster is $\simeq 87$ arcmin; although this is a rather large extrapolation, it is consistent with TG93, as the radial profile which they measure for the dE galaxies reaches the mean density of background galaxies at a radius of 83 arcmin.

Thompson & Gregory (1993) tentatively proposed that the core of the Coma cluster is deficient in the number of faint dE galaxies, and they argued that dynamical effects (tidal disruption) in the rich environment of the cluster core could be responsible for partially destroying this population of faint dE galaxies. However, they cautioned that this relatively flat distribution for the faint dE galaxies may be a manifestation of a uniformly distributed population of faint noncluster galaxies. We are in a slightly better position, as we have established cluster membership primarily via color-magnitude discrimination, and as discussed in Chapter 4 and by Biviano et al. (1995), this method is essentially free of contamination by noncluster galaxies. In addition, we have further eliminated the effects of uniformly distributed noncluster galaxies by statistically correcting our radial profiles based upon the analysis of the noncluster control field image. Therefore we can restate their primary conclusion, but with increased confidence: Scaling the radial profile of the bright sample of galaxies to that of the dE population only, we see that the number density of the bright galaxies continues to rise farther into the core of the cluster (i.e., it has a smaller core radius),

and in this manner the cluster core is deficient in the numbers of faint dE galaxies⁴.

5. THE DWARF-TO-GIANT RATIO

In their seminal study of dwarf galaxy populations in nearby groups, Ferguson and Sandage (1991; hereafter referred to as FS91) defined the early-type dwarf-to-giant ratio (EDGR) as the total number of early-type dwarf galaxies N_d normalized to the number of early-type giant galaxies, N_g . For the seven groups which they studied, they determined that the EDGR is strongly correlated with the richness of the group, in the sense that it increases monotonically with cluster richness, and appears to be independent of distance from the cluster center. That is, in simple terms, dE galaxies are most frequently found in rich cluster environments. It is thought that the correlation of EDGR with environment richness will provide insights into the effect of cluster environment on processes governing both (i) the initial formation of dE galaxies, and (ii) the environmental influences on their subsequent evolution. The best test of this correlation is to then extend the analysis to the richest cluster environments, and eventually to survey a sufficient number of rich clusters that correlations with other cluster properties (such as X-ray luminosity, Bautz-Morgan class, substructure, etc.)

⁴A galaxy cluster will relax via two-body encounters on a timescale which is dependent on number density, velocity dispersion and mass. While this two-body relaxation can give rise to observable spatial segregation in mass and luminosity, the timescale is such that it is only relevant for the brightest two magnitudes of galaxies in the cores of the richest clusters (Bachall 1980). For typical dE galaxies, orbital decay via dynamical friction acts on a timescale of 10^{15} years, which is negligible in this context (Merritt 1985). Thus the spatial distributions in magnitude and clustercentric radius which we observe must be primordial in nature, and not a manifestation of subsequent dynamical evolution.

can be determined.

In their calculations, FS91 determine the EDGR for four limiting magnitudes, from $M_{B_T} = -15.5$ down to $M_{B_T} = -12.5$ mag. In each case, N_d and N_g include all early-type galaxies above that limiting magnitude, such that the EDGR value increases for fainter limiting magnitudes. A thorough description of their classification procedure is given in FS91. The main point to note here is that the galaxies in their samples have been assigned into morphological classes using visual inspection, which differs from our procedure, described below. As a result, their computation of the EDGR becomes a straight-forward calculation: for early-type dwarfs and giants, they assign $N_d = N(\text{dE}+\text{dE,N}+\text{dS0})$ and $N_g = N(\text{E}+\text{S0})$.

In the analysis of FS91, the most convincing demonstration of this EDGR correlation was obtained by using the number of giant galaxies as a measure of the cluster richness. This is a raw number, uncorrected for spatial or magnitude incompleteness. Then their analysis, which plots $\log N_d$ versus $\log N_g$, shows clearly that the number of dwarfs rises faster than the number of giants. In comparison to a straight line of slope one (i.e. a constant EDGR with intercept scaled to match the data), their data clearly deviate: the number of dwarfs for Virgo, Antlia and Fornax (Abell richness classes 1, the richest clusters in their study) rise above this line, whereas N_d for Leo and Dorado (the poorest groups) fall well below this line. This trend can be observed in our Figure 5.12 below.

In a separate study of dwarf galaxies near early-type galaxies, Vader and Sandage

core to the Coma cluster as a whole, such that we can put our derived value on the richness scale used by FS91 and VS91 (i.e. $\log N_g$). We adopt $N(E+S0)=291$ (TG93) as a measure of the total number of giants in the entire Coma cluster. Adopting this value places the the Coma cluster as the richest galaxy cluster in this sample, in agreement with the Abell richness class rankings. Thus the purpose of this section is to determine if the Coma cluster EDGR value exceed that measured for Virgo, and thus if the EDGR correlation continues to the extremely rich environment of the Coma cluster core. The data set which we consider here is that which defined the net (control field corrected) luminosity function in Section 3.1 (Table 5-2), based upon the color and magnitude restricted sample defined in Section 5.3 of Chapter 4 (Table 4.5).

Brighter than $R \simeq 15.5$ mag, our sample includes *all* galaxies, except the supergiants NGC 4874 and NGC 4889, with the remaining giant galaxies following a log-normal distribution in magnitude (TG93, Biviano et al. 1995). Since the number of late-type giants in the cluster core is negligible, their inclusion can only lead to an underestimate of the true EDGR value. As discussed in the previous chapter, our sample of galaxies is incomplete within an arcmin of the supergiant galaxies, and is biased against measuring dwarfs very near to brighter cluster giants. For $R \gtrsim 15.5$ mag, our composite luminosity function is dominated by the early-type dwarf galaxies (i.e. dE and dE,N together with dS0 and dSph). We do not attempt to divide these dwarf galaxies into their morphological subgroups, simply because

(1991) confirm the observed correlation for the EDGR value to increase with environment richness. They found that giant galaxies in the richest groups are typically overabundant in companion dE galaxies (by a factor of 2) when compared to the mean value of their sample. In contrast, isolated field galaxies are typically underabundant in number of dE companions (by a factor of ten). The mean value adopted by Vader and Sandage is an EDGR equal to 2.5, to a limit of $M_B = -13$ mag. This is consistent with the extrapolated mean values found by FS91.

It is worthwhile to note that the definition of richness used by FS91 and VS91 differs from the well-known Abell richness class. Abell (1958) defined his “richness class” as a number ranging from 0 to 5, which corresponds to the number of counted galaxies which are not more than two magnitudes fainter than the third brightest member. However, there is considerable variation within individual richness classes, and for consistency requires imaging of the entire cluster field. Therefore, the FS91 definition of richness (i.e., $\log N_g$) provides a suitable scheme for ordering the groups according to their richness class, provided that a considerable and consistent fraction of the cluster is analyzed.

5.1 The EDGR For The Coma Cluster Core

We now turn to the Coma galaxy cluster (richness-class 2), and use our large sample of dwarf galaxies to establish, with appropriate uncertainties, an EDGR value for the cluster core. We scale the number of measured dwarf galaxies for the cluster

we have insufficient resolution. As discussed in Section 2.1, and evident from our color-magnitude diagram, the contribution of dIr galaxies to our sample is essentially negligible above $R = 20$ mag. Below this, our photometry is sufficiently uncertain that the dE sequence spreads, such that this distinction is no longer possible. However, the luminosity function for dIr galaxies is bounded at faint magnitudes, unlike the luminosity function for dE galaxies, which continues to rise at faint magnitudes. Then overall the contribution of dIr galaxies is negligible within our sample of cluster dwarf galaxies. We ignore this contribution, as the uncertainties on our computed EDGR values will encompass this effect.

To compute the EDGR value, we must separate from the composite luminosity function the contribution of giant galaxies from the dwarf galaxies. In their analysis of the Virgo dwarf population, FS91 visually classified all galaxies into their respective morphological groups. In this manner the early-type dwarf-to-giant ratio was straight-forward to compute. In their analysis of the Coma galaxies, TG93 also used a data set which had been classified visually (with surface brightness as the primary discriminator between giants and dwarfs). However, the exposure on their Coma plates differed from the comparison plates, and in the region of similar magnitudes (i.e., the brightest dE galaxies compared with faint E galaxies), the lower surface brightness dE galaxies could not be systematically differentiated from the normal E galaxies. This led TG93 to develop an alternative method for computing the EDGR based upon decomposing the total galaxy luminosity function.

TG93, and more recently Biviano et al. (1995) determined that the composite luminosity function for the Coma cluster is well fit by a log-normal distribution for the bright cluster members and a Schechter function for the dwarf galaxies. The sum of these two functions, with the appropriate parameters and normalization, has been found to provide a better representation of the total luminosity function than a single Schechter function. Conveniently, the resulting scaled functions provide the relative contribution to the composite luminosity function by each of the dwarf and giant galaxy populations. It is this technique which we adopt in principle to determine the EDGR value for our sample of cluster galaxies. Thus, we perform weighted least-squares fits of a Gaussian plus a Schechter function to our luminosity function, solve for the relative contribution from each of the giant and dwarf galaxy populations, and use these values to compute an EDGR for our data set.

This functional fit involves a total of six parameters: κ_2 , m^* and α for the Schechter function (see equation 5.9), and the peak m^0 , dispersion σ and relative scaling κ_1 of the Gaussian function, given by

$$\gamma(m) = \kappa_1 \exp \left[-\frac{(m - m^0)^2}{2\sigma^2} \right]. \quad (5.13)$$

The solution obtained by allowing all six parameters to vary technically yields the minimum reduced χ^2 value, yet the dispersion of the Gaussian luminosity is inconsistent with values obtained using a larger sample of giant galaxies, and the faint-end slope is inconsistent with the value we determined independently above. We there –

fore constrain the faint end slope of the luminosity function to its value found in Section 3.1 (i.e., $\alpha = -1.41$), and allow the dispersion of the log-normal distribution to vary between the range $0.8 < \sigma < 1.2$ mag, as described below. In order to best fit the Gaussian plus Schechter function to our composite luminosity function, we assign the faintest three magnitude bins a weight of zero, as they adversely affect the normalization of the Schechter function.

When calculating the EDGR value in this manner, the width adopted for the log-normal distribution describing the giant galaxies is fundamentally important. In fact, the EDGR value is strongly correlated with σ , in the sense that a larger value of σ must result in a lower value for the EDGR. (This occurs because the bright tail of the giant galaxy luminosity function has a well-defined limit.) We therefore constrain the Gaussian dispersion σ to lie within a more realistic range $0.8 \lesssim \sigma \lesssim 1.2$ mag (see TG93 and Biviano 1995). In this manner, the extreme values for σ will define our upper and lower limits to the EDGR, while the adopted EDGR value will correspond to the average of these values, nearest to $\sigma = 1.0$ mag. We therefore perform 5 fits of the Gaussian plus Schechter model to the net galaxy luminosity function, corresponding to $\sigma = 0.8, 0.9, 1.0, 1.1$ and 1.2 mag. The results are summarized in Table 5.4, and based upon the reduced χ^2 values we can accept the fit of all five models to the cluster luminosity function.

In order to remain consistent with the limiting magnitudes used by FS91, it is necessary to convert our apparent R total magnitudes to their absolute total magnitudes

TABLE 5.4: Fits of Gaussian plus Schechter functions to the Coma luminosity function.

Fit	κ_1	m^0	σ	κ_2	m^*	α	χ^2/ν
1	15.32 \pm 10	14.49 \pm 0.01	0.80	13.66 \pm 20	15.40 \pm 0.48	-1.41	0.83
2	15.40 \pm 8	14.64 \pm 0.01	0.90	16.26 \pm 24	15.80 \pm 0.37	-1.41	0.83
3	15.17 \pm 7	14.77 \pm 0.01	1.00	18.62 \pm 29	16.10 \pm 0.32	-1.41	0.88
4	14.86 \pm 6	14.91 \pm 0.01	1.10	20.73 \pm 35	16.34 \pm 0.30	-1.41	0.96
5	14.58 \pm 6	15.04 \pm 0.01	1.20	22.62 \pm 41	16.53 \pm 0.29	-1.41	1.04

M_{B_T} . To do so, we adopt the same parameters used by TG93: a Virgo-Coma relative distance modulus of 3.68 and a B -band K -correction of 0.12 mag for Coma. To this we add the Virgo distance modulus of 31.7 used by FS91⁵, and subtract the Virgo B -band K -correction of 0.02 mag. Finally, we adopt a mean dE color of $(B - R) = 1.4$ mag, calculated from our CMD (Figure 5.1) for $R \simeq 18.0$. This leads to a conversion factor, from our R mag to a M_{B_T} mag on the FS91 scale, of $M_{B_T} = R - 34.1$. Then the four limiting magnitudes which we adopt are $R = 18.6, 19.6, 20.6$ and 21.6 mag, corresponding to $M_{B_T} = -15.5, -14.5, -13.5$ and -12.5 mag respectively.

We integrate the Gaussian function over the interval $12.5 \leq R \leq 18.5$ mag, and obtain values of $N(\text{E+S0}) = 30.52, 34.44, 37.58, 40.37$ and 43.02 for model fits 1 through 5. In Table 5.5 we provide the corresponding $N(\text{dE+dE,N+dS0})$ and

⁵This is not the currently accepted Virgo distance modulus, and its only purpose here is for comparison.

TABLE 5.5: Early type dwarf-to-giant ratio (EDGR) for different function fits and limiting magnitudes.

<i>R</i> -Mag Limit	Fit #1	N(dE+dE,N+dS0)				Coma EDGR	Virgo EDGR
		2	3	4	5		
18.6	70.7	65.3	60.1	56.8	53.4	1.78±0.54	2.12
19.6	124.5	119.5	115.4	111.4	108.1	3.30±0.78	3.61
20.6	204.5	200.9	198.1	195.0	192.5	5.59±1.11	5.77
21.6	322.1	321.0	320.6	319.3	318.4	8.98±1.58	9.31

(1) N(E+S0) is computed in the range $12.5 \leq R \leq 18.5$ mag, and equals 30.52, 34.44, 37.58, 40.37 and 43.02 for Fits 1 through 5.

(2) The Virgo EDGR values are taken from Ferguson & Sandage (1991).

Coma EDGR values, obtained by numerically integrating the Schechter function over the appropriate magnitude ranges, using the parameter values relevant to the five different fits. In Figure 5.11, we illustrate one of the model fits (i.e., for $\sigma = 1.0$ mag) to the composite luminosity function. The dotted lines designate the individual contributions at any magnitude, while the solid line shows the fit of this Gaussian plus Schechter model to the luminosity function.

Of interest here is whether our computed EDGR value for the Coma cluster exceeds that measured for the Virgo cluster, thereby continuing the trend for larger EDGR values in richer environments. In Figure 5.12, we compare Coma cluster EDGR values with those computed by FS91, in two different manners. In the top panel, the solid circles denote the Coma EDGR values and their uncertainties, from

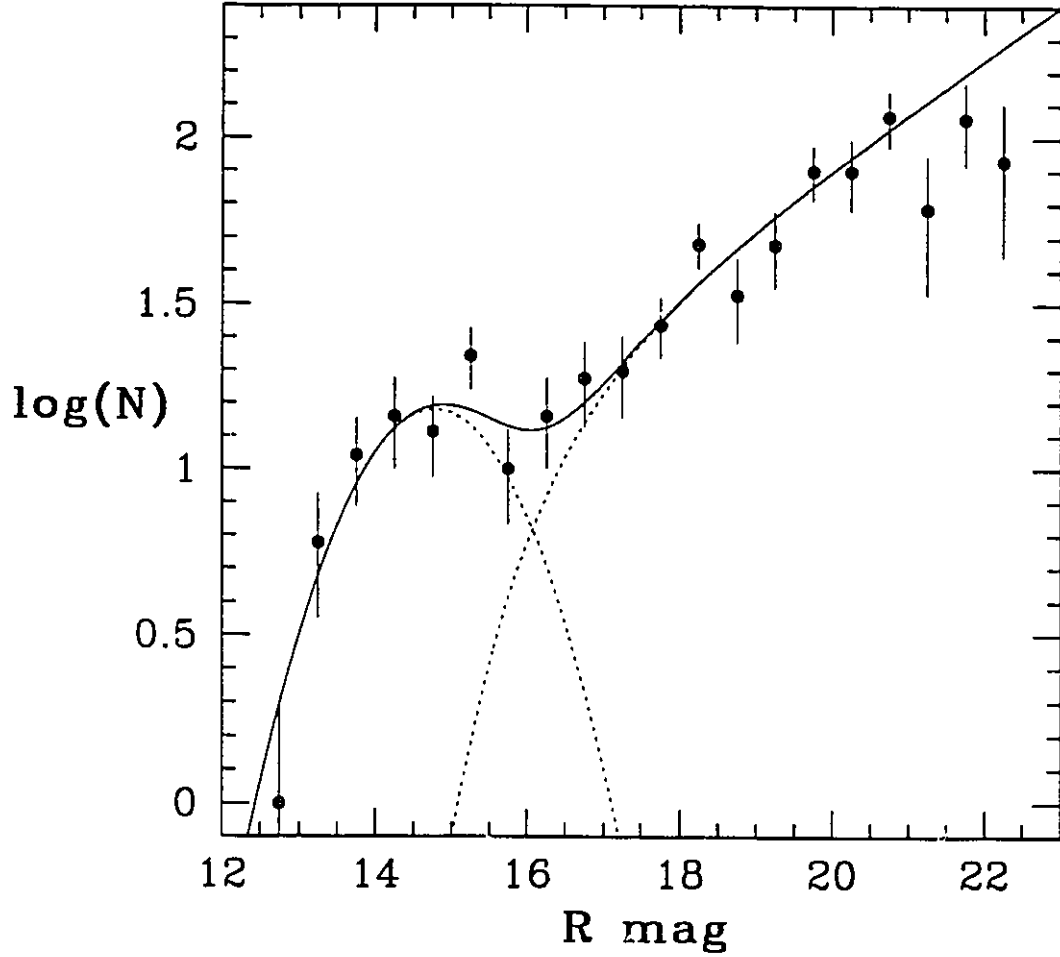


Figure 5.11: Decomposition of the composite luminosity function (Figure 5.5) for the Coma cluster core, into the contribution from the giants (i.e., the log-normal distribution) and from the dwarf ellipticals (i.e., the Schechter function). In this plot, the Gaussian has a dispersion of 1.0 mag; the other relevant parameters are given in Tables 5.4 and 5.5. Note that the three faintest points were not included in the fit.

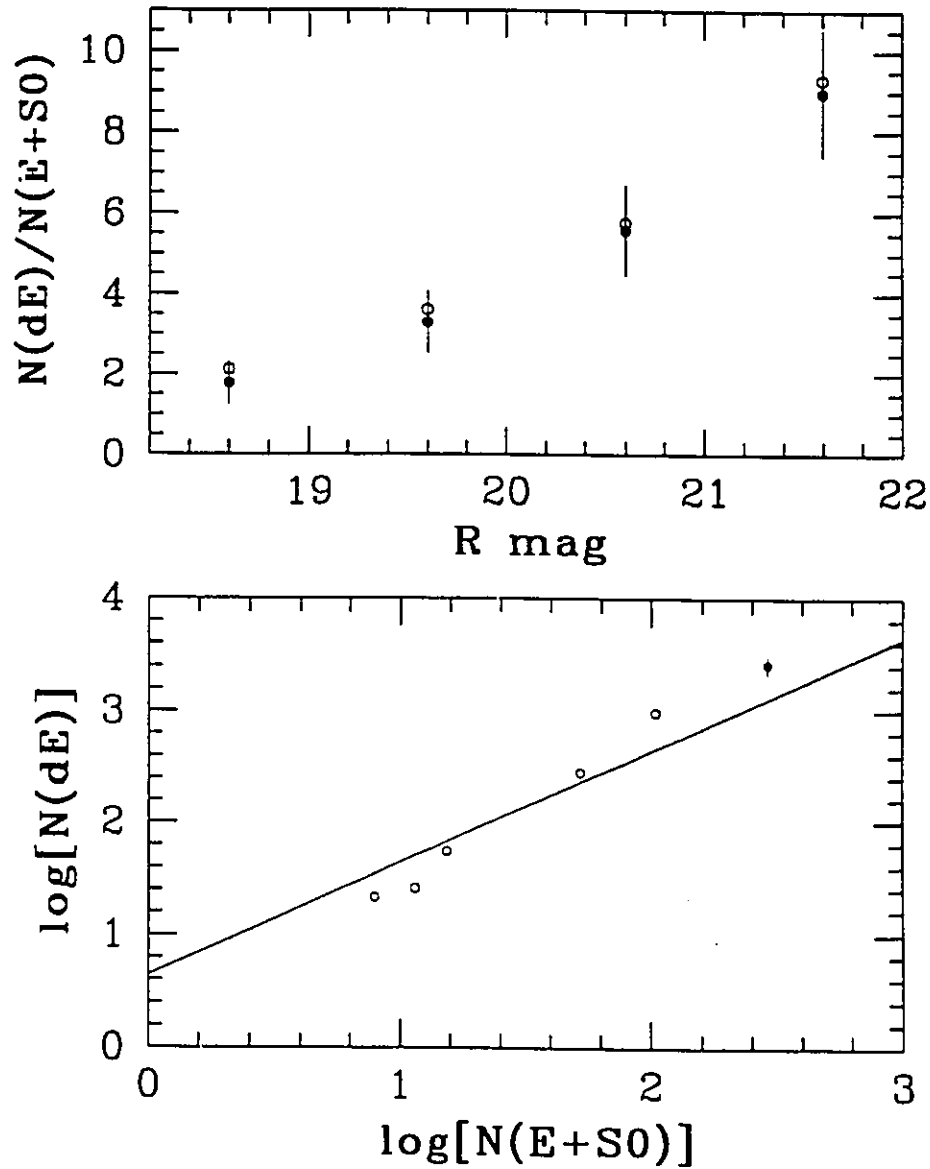


Figure 5.12: The early-type dwarf-to-giant ratio for the Coma cluster. In both panels, the solid circles with the error bars correspond to the Coma cluster. In the top panel we compare the EDGR values for Coma and Virgo, which are consistent within the uncertainties. Here, the R magnitude denotes the lower limit for the numerical integration of the Schechter function. The lower panel corresponds to a limit of $R = 21.6$ mag, and the open circles represent Leo, Dorado, NGC 1400, Fornax and Virgo, from left to right. The solid line has a slope of one.

Table 5.5, while the open circles (the error bars are not plotted) correspond to the Virgo Cluster FS91. These two sets of values are consistent within the uncertainty ranges, at all four limiting R magnitudes. Note that to a limit of $R = 18.6$ mag, Thompson & Gregory (1993) measured an EDGR value of 1.52, consistent with but slightly lower than our value. While a primary difference between our values results from a difference in the modeling of the log-normal distribution, it must also be due to our inclusion of very low central surface brightness dwarf galaxies in our final sample (see Figure 4.15 of Chapter 4).

In the bottom panel of Figure 5.12, in a parameter space of $\log(N_d)$ versus $\log(N_g)$, we plot the EDGR values (i.e., to limit of $R = 21.6$ mag) for several galaxy groups (FS91). The open circles represent the Leo, Dorado, NGC 1400, Fornax and Virgo groups, from left to right, while the solid circle represents our value for the Coma cluster. To place Coma on this figure, we took $N(E+S0) = 291$ (TG93) and a Coma EDGR equal to 8.98 ± 1.58 (Table 5.5). Since the solid line has a slope of one, it represents a constant EDGR with increasing richness. This is possibly the best parameter space in which to visualize the correlation of the EDGR with galaxy cluster richness: it is clear that the Fornax, Virgo and Coma clusters rise above this line, while the Leo, Dorado, and NGC 1400 groups fall below.

In these figures there are two details worth mentioning. In the top panel, the EDGR values for Coma and Virgo are essentially the same at all limiting magnitudes, and this reflects the fact the the luminosity function faint-end slopes are consistent

between clusters. In this manner, the EDGR values increase at the same rate. In the bottom panel, the intercept of constant EDGR line (i.e., at $\log(N_g) = 0$) is $\log(N_d) = 0.623$, or about 4 dwarfs per giant galaxy. This intercept value corresponds to the number of dwarfs expected per giant galaxy in an isolated environment, to a limit of $R = 21.6$ mag.

It is clear then, that *the EDGR value for the Coma cluster is consistent with that found for the Virgo cluster, within our calculated uncertainties*. While our mean values are slightly less than the corresponding Virgo values, we can confidently rule out a falling EDGR value. In Section 6.1 we discuss a possible reason for why the Coma EDGR is not significantly larger than measured for Virgo.

6. DISCUSSION

6.1 The Effects Of Cluster Substructure On The EDGR

Rich galaxy clusters do not form a coherent or consistent class within themselves, as they exhibit considerable variation within individual richness classes. This variation includes properties such as: (i) whether a cD galaxy occupies the cluster center, as compared to a regular supergiant galaxy, or perhaps no large central galaxy at all; (ii) the Bautz-Morgan class, which measures the magnitude difference between the first- and second- ranked cluster galaxies; (iii) whether or not the cluster is luminous in X-ray emission; (iv) whether or not the cluster shows considerable substructure

(West 1994, Binggeli 1994).

We suggest galaxy cluster substructure as a dominant factor in determining the clusters early-type dwarf-to-giant ratio, and thus the variable with the most noticeable consequences. Consider the following scenario. Two or more richness-class 1 galaxy clusters have (or are in the presence of) merging to form a richer galaxy cluster environment. Now, a straight forward application of the EDGR (i.e., the early-type dwarf-to-giant ratio) versus cluster richness correlation would predict an EDGR value much greater than would be measured for a richness-class 1 cluster. However, one must assume that to first order, the total number of dwarf and giant galaxies is conserved during the cluster merger. In this manner, the measured EDGR would remain constant and equal to the value for a richness-class 1 cluster, even when one plots $\log N_d$ against $\log N_g$.

This interpretation is consistent with the Coma cluster being the result of a significant number of merger events, as discussed in the Introduction. We postulate that to measure an EDGR value which increases over and above the Coma and Virgo values, it is necessary to survey a cluster environment which is *genuinely* rich. That is, a galaxy cluster which is rich by birth, rather than by subsequent dynamical evolution and mergers. In this manner, if the correlation of increasing EDGR with cluster richness is expected to be relevant to the formation and evolution of dE galaxies and the galaxy cluster itself, one must disentangle the effects of richness and substructure. In order to accomplish this, we must obtain better number statistics, by surveying the

dwarf galaxy population in a large number of galaxy clusters, both those with and without substructure.

6.2 A Reduced EDGR In The Coma Core

As stated above in Section 5, FS91 find no evidence to support a significant difference for their computed values of the EDGR. They determined this by computing EDGR values in annuli of width one degree as a function of radius outwards from the Virgo cluster center. As such, they conclude that only a single value for the EDGR is necessary to characterize the Virgo cluster, and postulate that this is true for all individual galaxy clusters. To first order, this is true in the Coma cluster as well. But given the difference in spatial distributions between the cluster giants and bright dE galaxies compared to the faint dEs (Section 4), this is worth further consideration.

From the King model fits to our radial galaxy distributions (Figures 5.9 and 5.10 of Section 4) we determine that the faint dwarf galaxies have a 18.73 arcmin core radius, as compared to 12.32 arcmin for the cluster giants and brighter dE galaxies. Thus interior to about 18 arcmin, the faint dE population has essentially a constant number density, in contrast to the number density of the brighter galaxies, which is still increasing. For large radial distance from the cluster center, TG93 find that at about 20 arcmin from the center (NGC 4874), the powerlaw falloff of the faint dE galaxies is consistent with that of the bright dEs and the E+S0 galaxies.

The question is then, what effect will this difference in core radii have on the

calculation of the EDGR value; that is, how will the EDGR value vary with cluster-centric distance. Outside of an 18 arcmin radius from the cluster center, the number of faint dE galaxies decreases in proportion to the number of bright galaxies. Then an EDGR value *computed at any limiting magnitude* should be constant for any larger radius. Following this logic, interior to the 18 arcmin core radius, the number density of bright dE and E+S0 galaxies increases more rapidly than does the number density of faint dE galaxies. Thus a value for the EDGR limited to and calculated within this small central core, as our value is, may underestimate the EDGR for the galaxy cluster as a whole. This underestimation will only occur *if the limiting magnitude to which the Schechter function is numerically integrated includes the faintest dwarf galaxies.*

The first two values we compute for the EDGR in the Coma cluster core, i.e., to limits of $R = 18.6$ and 19.6 mag, will therefore be representative of the Coma cluster as a whole. However, our fainter limiting magnitudes of $R = 20.6$ and 21.6 mag are sufficiently faint that they include the more smoothly distributed faint dE galaxies, and these estimates of the EDGR value may not be applicable to the cluster as a whole.

6.3 Diffuse Intracluster Light

The diffuse intergalactic component of the Coma cluster light is estimated to be on the order of 25 – 30 percent of the total light (Thuan & Kormendy 1977; Melnick,

White & White 1977; see also Uson et al. 1991 for a more recent discussion of the difficulties inherent in measuring this intracluster light). One possible origin of this low surface brightness, diffuse light is from matter (stars) which were tidally stripped from the outer regions of their parent galaxies. Thuan & Kormendy report that, for Coma, the diffuse light appears to be bluer than the light of the giant galaxies, at least within 14 arcminutes of the core. This is supported by Mattila (1977), whose photoelectric photometer measurements yield $(B - V) = 0.54 \pm 0.18$ mag, in an area free of galaxies. This is a very blue color: compared to typical globular clusters, which are in the range $0.55 \lesssim (B - V) \lesssim 0.85$ mag, it is consistent with the most metal-poor old stellar populations.

As we determined in Section 2.1, the faint dE galaxies are the most metal poor (bluest) galaxies in this environment, and they are the most easily disrupted. Not only that, but a significant population of these dE galaxies have been dynamically destroyed in the cluster core (Section 4.1). Therefore, it is interesting to compare the color of this intracluster light with the median color for faint dE galaxies. Using the program field CMD (Figure 4.14), an approximate median color for the dE galaxies (at $R = 21.5$ mag) is $(B - R) \simeq 1.3$ mag. To convert this to a $(B - V)$ color, we use a result of Durrell, Harris & Pritchett (1994). They construct a $(B - V) - (B - R)$ color-color relation (their figure 11) valid for individual halo giants. If we assume this is approximately correct for the integrated colors of dE galaxies, our $(B - R)$ dE color corresponds to $(B - V) = 0.85$ mag, which is *redder* than that found by Mattila

(1977).

This result prompts us to question either (i) the origin of the intergalactic matter, (ii) the epoch of formation of dE galaxies, or (iii) the accuracy of the diffuse-light color measurement. If the diffuse light does indeed originate as tidally stripped stars, and if a major component of this intergalactic light is from (stars stripped from) the numerous faint dwarf galaxies, then at all radii, the mean color of this light must be redder than (or at least consistent with) that of the dE galaxies. If we accept these assumptions and the diffuse intergalactic light is bluer than the dE galaxies, one would be led to infer that the dE galaxies formed after the intracluster matter (stars), and were thus more metal rich.

In the past it was proposed that the diffuse component of the cluster light actually originates from the integrated light of all (unresolved) faint dE and dS0 galaxies. If this were true in the case of the Coma cluster, the corresponding diffuse light would indeed be more metal-poor than our sample of dE galaxies, and possibly more consistent with the value determined by Mattila (1977). However, in their study of Abell 029, Uson et al. (1991) determine that at most 4 percent of the diffuse intracluster light could originate from a population of unresolved dwarf galaxies. It would be interesting to obtain accurate CCD photometry with *B* and *R* filters, to better compare the metallicity of the Coma cluster diffuse light with that of the faint dwarf galaxy population.

6.4 An Increased Density of dE Galaxies Between the Supergiant Galaxies

In their analysis of ROSAT X-ray images, White, Briel & Henry (1993) observe an intensity peak in the diffuse X-ray emission, approximately two-thirds of the way between NGC 4889 and NGC 4874. This peak is also predominant in EINSTEIN satellite X-ray observations of the cluster core (Davis & Mushotzsky 1992). This location does not correspond to any large cluster member or obvious background galaxy, and Davis & Mushotzsky and White et al. postulate that this peak might result from a remnant of gas, tidally stripped from NGC 4889 by interaction with NGC 4874, during its passage through the cluster core. It is a possible relationship between this gaseous remnant (tidal debris) and dwarf galaxies which we discuss here.

The ensemble of all dwarf galaxies in this cluster environment would include dE which have evolved from the formation-epoch protogalactic fragments (as discussed above), but recent evidence from numerical modeling (Barnes & Hernquist 1993) and observations (Mirabel, Dottori & Lutz 1992) support the formation of bound stellar systems of dwarf-galaxy size in the tails of tidally-stripped debris from interacting disk galaxies. As well, recent high-resolution (CFHT+HRCam and HST) observations of high-redshift galaxy clusters (Pierce, McClure & Lavery 1995; Dressler et al. 1994) reveal that a large fraction of the galaxies are binary or interacting, suggesting that this tidal-debris formation mechanism for dwarf galaxies could be significant in other rich galaxy clusters. Thus gravitationally-significant interactions in the high-density

environment of the Coma cluster core could have in the past lead to the formation of a large number of dwarf galaxies, even though there are no gas-rich spirals at the present epoch.

We placed a small circular aperture of radius 150 pixels (1.325 arcmin) at the location of this peak in the diffuse X-ray emission. On our $x - y$ coordinate system, this corresponds to a pixel position of (1566,1010). Considering the sample of cluster dE galaxies (i.e., that used in Section 4.2), we computed a total of 27 dE galaxies in this circular region of area $A = 5.52 \text{ arcmin}^2$. The resulting number density is 2.33 ± 0.95 per arcmin^2 (corrected for the mean control field number density), as compared to the value of 1.424 ± 0.001 per arcmin^2 computed in Section 4.1 (Chapter 5) for the central (spatial) number density. Then the number density of dwarf galaxies is increased above the core value, within an area restricted to a 2.65 arcmin diameter circle, centered upon a peak in the diffuse X-ray emission.

Davis & Mushotzsky calculate that once stripped from NGC 4889, this gas would relax and merge with the cluster gas in about 10^8 years, which also gives a lower limit to the galaxies crossing time. Thus any dE galaxies formed in this gas are still associated with this special position. It would be of great interest to conclude that some fraction of the dwarf galaxies in the Coma cluster have formed through this tidal-debris mechanism, and to be able to pinpoint a specific location of the cluster where this has occurred.

However, we can not make this conclusion, for the following reasons. First, while

marginally significant, this observation may simply be due to small number statistics. (A visual inspection showed no obvious background galaxy cluster at this location). Second, from a quick inspection of the position of these objects on a color-magnitude diagram, the colors do not appear to be (on average) any bluer, as would be expected if these dE galaxies were young. (The color can be used to distinguish young dE galaxies from old-population dE galaxies until they reach an age of about 3 Gyrs, an order of magnitude longer than the timescales predicted above). At the least, a careful reanalysis of the colors and other properties of dwarf galaxies within this region is warranted, to determine if there are any correlations specific to this area which were washed out on the large scale.

7. SUMMARY

(1) Our sample of dwarf galaxy candidates is dominated by dwarf elliptical galaxies, with a negligible contribution from dwarf irregular galaxies. The dwarf elliptical sequence is well-defined in the color-magnitude plane, and for each one magnitude increase in R , the dEs become redder (in the mean) by 0.062 mag in $(B - R)$. At any magnitude, the spread in color is about 0.15 mag about the median dE color.

(2) We calibrate a color-metallicity relationship based upon Galactic globular clusters, and we find that a significant metallicity gradient (i.e., $Z \propto R^{-0.32}$) exists in the radial distribution of the dwarf elliptical galaxies, outwards from NGC 4874. This color gradient corresponds to a radial luminosity gradient, which gives rise to a

radial variation in the cluster luminosity function.

(3) The faint-end slope of the luminosity function is given by $\alpha = -1.41 \pm 0.05$. This slope is consistent with the results of Bernstein et al. (1995) and Thompson & Gregory (1995), and consistent with accepted faint-end slopes for the Virgo and Fornax clusters. It is inconsistent with the very steep slopes found for other rich clusters by de Propris et al. (1995).

(4) In the cluster core, the radial number density profile of both the bright dE galaxies and the cluster giants is well-fit by a King model of core radius 12.32 arcmin, a distance at which the surface density falls to one half of its central value. The radial surface density profile for the faint dE galaxies is also well fit by a King model, but with a core radii of 18.73 arcmin.

(6) The composite luminosity function for Coma galaxies is modeled as the sum of a log-normal distribution for the giant galaxies and a Schechter function for the dwarf elliptical galaxies. For a Gaussian dispersion ranging from 0.8 to 1.2 mag, and with $\alpha = -1.41$, the characteristic magnitude of the Schechter function varies from $R = 15.4$ to $R = 16.53$ mag.

(7) The early-type dwarf-to-giant ratio (EDGR) for the Coma cluster core is consistent with the Virgo cluster, and with the Coma cluster being built up from the merger of many richness-class 1 galaxy clusters.

Chapter 6

The Emphasis Of Future Research

In this thesis, we have analyzed dwarf elliptical galaxies in Coma, the richest local galaxy cluster. However, determining the characteristics of dwarf galaxies in all types of clusters represents a huge effort, to cover parameters such as cluster richness, morphology, and redshift range. Thus as expressed throughout this thesis, observations of this type must be extended to many other clusters. For example, Lopez & Yee (1995) are analyzing CCD images of many X-ray selected galaxy clusters, of varying richness, and computing their early-type dwarf-to-giant ratios. As well, we are beginning a study of two other clusters.

During the KPNO 4m observing run in which the Coma cluster images were obtained, a single *R*-band 900 sec exposure of the rich galaxy cluster Abell 2199 was obtained (see Section 3 of Chapter 3). A determination of the dE galaxy spatial structure and early-type dwarf-to-giant ratio for this richness-class 2 cluster would provide an interesting comparison to our results of the Coma cluster. This project is well underway: the supergiant cD galaxy NGC 6166 has been modeled and subtracted, from

which we have an accurate and calibrated *R*-band CCD surface brightness profile. A preliminary analysis with DYNAMO reveal a significant number of faint nonstellar objects. As in Coma, a large fraction of these will be cluster dwarf elliptical galaxies. Since we do not have a corresponding *B*-band image, we can not estimate object colors, and defining cluster membership is therefore difficult. Nor do we have an associated control field. However, we will be able to use published number counts to correct radial surface density profiles of the two galaxy populations, from which we can compare their core radii (with each other, and with those determined for the Coma cluster).

In April 1993, W.E. Harris and I observed the Hydra I galaxy cluster using the CTIO Curtis Schmidt telescope with a 1024^2 CCD in both *R*- and *B*-bands. Hydra I (Abell 1060, $v = 3500$ km/sec, richness-class 1) is a spatially isolated galaxy cluster, the core of which contains the cD galaxy NGC 3311 and the supergiant E galaxies NGC 3309 and NGC 3308. We observed a total of four overlapping cluster fields, and an additional two remote control fields, located about 2 deg from the cluster center. The CCD fields are each 30×30 arcmin², which overlap each other by ~ 5 arcmin: they extend radially outwards from the cluster center, offset from the cluster core (to avoid NGC 3311). With an image scale of 1.84 arcsec/pixel, a large fraction of the dE galaxies which we observe will be resolved. The reduction of these images, in a manner similar to that used in Chapters 2 and 3, will result in a sample of highly-probable cluster dwarf galaxies. From this sample, we will be able to determine,

among other things, the EDGR and spatial structure of the Hydra I galaxy cluster.

There are two analyses, related to this thesis, which would yield further insights into dwarf galaxy populations. First, a reanalysis of the Coma program field R - and B -band images would be worthwhile, to determine the small-scale clustering properties of the dwarf elliptical galaxies near the brighter cluster giants. Using the isophote-fitting methods of STSDAS, the majority of the bright cluster giants could be modeled and subtracted. A new round of object detection, photometry and classification in and around the vicinity of the subtracted giant galaxies would yield a sample of dE galaxies essentially unbiased by the location near to the giant galaxies. The result would provide insights to small-scale clustering properties of dwarf galaxies, and an average radial profile for these “companion” dwarf galaxies. Simultaneously, this analysis would yield accurate and calibrated CCD surface brightness profiles, in both R - and B -bands, for the Coma cluster giants. Second, an individual analysis (i.e., new higher-resolution images) of the brightest dE galaxies in our sample would provide R -band CCD surface brightness profiles, and an atlas of enlarged visual images for these galaxies. While our resolution is not sufficient to separate these bright dE galaxies into morphological subgroups (i.e. dE versus dE,N), these surface brightness profiles would be sufficient to discriminate between faint E and bright dE galaxies in the majority of cases.

Chapter 7

References

- Abell, G.O. 1958, ApJS, 3, 211
- Babul, A. & Rees, M.J. 1992, MNRAS, 255, 346
- Bahcall, N.A. 1977, ARA&A, 15, 505
- Barnes, J.E. & Hernquist, L. 1993, Nature, 360, 715
- Bassino, L.P., Muzzio, J.C. & Rabolli, M. 1994, ApJ, 431, 634
- Bender, R., Paquet, A. & Nieto, J.-L. 1991, A&A, 246, 349
- Bernstein, G.M., Nichol, R.C., Tyson, J.A., Ulmer, M.P. & Wittman, D. 1995, AJ, submitted
- Bershady, M.A., Hereld, M., Kron, R.G., Koo, D.C., Munn, J.A. & Majewski, S.R. 1994, AJ, 108, 870
- Binggeli, B. 1993, Habilitationsschrift, Universität Basel
- Binggeli, B., Sandage, A. & Tammann, 1988, ARA&A, 26, 509
- Binggeli, B., Tammann, G.A. & Sandage, A. 1987, AJ, 94, 251
- Binggeli, B., Tarenghi, M. & Sandage, A. 1990, A&A, 228, 42

- Biviano, A., Durret, F., Gerbal, D., Le Fèvre, O., Lobo, C., Mazure, A. & Slezak, E. 1995, *A&A*, 297, 610
- Blakeslee, J.P. & Tonry, J.L. 1995, *ApJ*, 442, 579
- Butterworth, S.T. & Harris, W.E. 1992, 103, 1828
- Caldwell, N. & Bothun, G.D. 1987, *AJ*, 94, 1126
- Chaboyer, B. 1994, in *ESO/OHP Workshop on Dwarf Galaxies*, eds. G. Meylan & P. Prugniel, (ESC, Garching) in press
- Couture, J., Harris, W.E. & Allwright, J.W.B. 1990, *ApJS*, 73, 671
- Couture, J., Harris, W.E. & Allwright, J.W.B. 1991, *ApJ*, 372, 97
- Davis, L. 1990, private communication (GC standard star photometry, unpublished)
- Davis, D.S. & Mushotzky, R.F. 1993, *AJ*, 105, 409
- De Propris, R., Pritchet, C.J., Harris, W.E. & McClure, R.D. 1995, preprint
- de Vaucouleurs, G., de Vaucouleurs, A., Corwin, H.G., Jr., Buta, R.J., Paturel, G. & Fouqué, P. 1991, *Third Reference Catalogue of Bright Galaxies* (Springer, New York)
- Dekel, A. & Silk, J. 1986, *ApJ*, 303, 39
- Doi, M., Fukugita, M. & Okamura, S. 1993, *MNRAS*, 264, 832
- Dressler, A. 1980, *ApJ*, 236, 351
- Dressler, A. 1984, *ARA&A*, 22, 185
- Dressler, A., Oemler, A., Jr., Sparks, W.B. & Lucas, R.A. 1994, *ApJ*, 435, L23

- Durrell, P.R., Harris, W.E. & Pritchett, C.J. 1994, *AJ*, 108, 2114
- Durrell, P.R. 1995, in preparation
- Escalera, E., Slezak, E. & Mazure, A. 1992, *A&A*, 264, 379
- Fabian, A.C., Nulsen, P.E.J. & Canizares, C.R. 1984, *Nature*, 310, 733
- Ferguson, H.C. 1992, *MNRAS*, 255, 389
- Ferguson, H.C. & Binggeli, B. 1994, *A&A Rev*, 6, 67
- Ferguson, H.C. & Sandage, A. 1988, *AJ*, 96, 1520
- Ferguson, H.C. & Sandage, A. 1990, *AJ*, 100, 1
- Ferguson, H.C. & Sandage, A. 1991, *AJ*, 101, 765
- Fischer, P. 1995, in preparation
- Fitchett, M. & Webster, R. 1987, *ApJ*, 317, 653
- Fleming, D.E.B., Harris, W.E., Pritchett, C.J. & Hanes, D.A. 1995, *AJ*, 109, 1044
- Garilli, B., Bottini, D., Maccagni, D., Vettolani, G. & Maccacaro, T. 1992, *AJ*, 104, 1290
- Geisler, D. & Forte, J.C. 1990, *ApJ*, 350, L5
- Griffiths, R.E., Casertano, S., Ratnatunga, K.U., et al. 1994, *ApJ*, 435, L19
- Harris, W.E. 1986, *AJ*, 91, 822
- Harris, W.E. 1987, *ApJ*, 315, L29
- Harris, W.E. 1991, *PASP*, 103, 32
- Harris, W.E. & van den Bergh, S. 1981, *AJ*, 86, 1627
- Harris, W.E., Allwright, J.W.B., Pritchett, C.J. & van den Bergh, S. 1991, *ApJS*,

76, 115

Harris, W.E., Fitzgerald, M.P., and Reed, B.C. 1981, PASP, 93, 507

Hopp, U., Wagner, S.J. & Richtler, T. 1995, A&A, 296, 633

Ichikawa, S., Wakamatsu, K. & Okamura, S. 1986, ApJS, 60, 475

Impey, C., Bothun, G. & Malin, D. 1988, ApJ, 330, 634

Jarvis, J.F. & Tyson, J.A. 1981, AJ, 86, 476

Karachentsev, I.D., Karachentseva, V.E., Richter, G.M. & Vennik, J.A. 1995, A&A, 296, 643

Kendall, M.G. & Stuart, A. 1977, *Distribution Theory, Volume One, Third Edition*, Charles Griffin & Company Ltd. (London)

King, I.R. 1966, AJ, 71, 64

Kormendy, J. 1977, ApJ, 218, 333

Kron, R.G. 1980, ApJS, 43, 305

Landolt, A. 1983, AJ, 88, 439

Lilly, S.J., Cowie, L.L. & Gardner, J.P. 1991, ApJ, 369, 79

Lopez, O. & Yee, H.K.C. 1995, in preparation

Matthews, L.D., Gallagher, J.S. & Littleton, J.E. 1993, in *Massive Stars: Their Lives in the Interstellar Medium*, ASP Conf. Ser., vol. 35, edited by J.P. Cassinelli and E.B. Churchwell (Astron. Soc. of the Pacific, San Francisco)

Mattila, K. 1977, A&A, 60, 425

McLaughlin, D.E. 1995, AJ, 109, 2034

- McLaughlin, D.E., Secker, J., Harris, W.E. & Geisler, D. 1995, AJ, 109, 1033
- Melnick, J., White, S.D.M & Hoessel, J. 1977, MNRAS, 180, 207
- Merrifield, M.R. & Kent, S.K. 1991, AJ, 101, 783
- Merritt, D. 1985, ApJ, 289, 18
- Mirabel, I.F., Dottori, H. & Lutz, D. 1992, A&A, 256, L19
- Mohr, J.J., Fabricant, D.G. & Geller, M.J. 1993, ApJ, 413, 492
- Parratt, L.G. 1961, *Probability and experimental errors in science*, John Wiley & Sons, Inc. (New York)
- Peterson, R.C. & Caldwell, N. 1993, AJ, 105, 1411
- Pierce, M.J., McClure, R.D. & Lavery, R.J. 1995, preprint
- Pierce, M.J., Welch, D.L., McClure, R.D., van den Bergh, S., Racine, R. & Stetson, P.B. 1994, Nature, 371, 385
- Press, W.H. & Schechter, P. 1974, ApJ, 187, 425
- Pritchett, C.J. & Harris, W.E. 1990, ApJ, 355, 410
- Richer, M.G. & McCall, M.L. 1995, ApJ, 445, 642
- Rood, H.J. & Sastry, G.N. 1971, PASP, 83, 313
- Sandage, A. & Binggeli, B. 1984, AJ, 89, 919
- Sandage, A., Binggeli, B. & Tammann, G.A. 1985, AJ, 90, 1759
- Sarajedini, A. & Layden, A.C. 1995, AJ, 109, 1086
- Schechter, P. 1976, ApJ, 203, 297
- Schild, R.E. 1983, PASP, 95, 1021

- Schombert, J.M., Phildis, R.A., Eder, J.A. & Oemler, A.Jr. 1994, BAAS, 26, 1396
- Secker, J. 1995, PASP, 107, 496
- Secker, J. & Harris, W.E. 1994, BAAS, 26, 1497
- Secker, J., Geisler, D., McLaughlin, D.E. & Harris, W.E. 1995, AJ, 109, 1019
- Silk, J., Wyse, R.F.G. & Shields, G.A. 1987, ApJ, 322, L59
- Stetson, P.B. 1994, PASP, 106, 250
- Stetson, P.B., Davis, L.E. & Crabtree, D.R. 1990, in CCDs in Astronomy, edited by G.H. Jacoby, PASP Conf. Ser., 8, p. 289
- Thompson, L.A. & Gregory, S.A. 1980, ApJ, 242, 1
- Thompson, L.A. & Gregory, S.A. 1993, AJ, 106, 2197
- Thompson, L.A. & Valdes, F. 1987, ApJ, 315, L35
- Thuan, T.X. & Kormendy, J. 1977, PASP, 89, 466
- Tody, D. 1986, *A User's Guide to Fortran Programming In IRAF; The IMFORT Interface*, NOAO
- Tyson, J.A. & Jarvis, J. F. 1979, ApJL, 230, L153
- Uson, J.M., Boughn, S.P. & Kuhn, J.R. 1991, ApJ, 369, 46
- Vader, J.P., Vigroux, L., Lachèze-Rey, M. & Souviron, J. 1988, A&A, 203, 217
- Vader, J.P. & Chaboyer, B. 1992, PASP, 104, 57
- Vader, J.P. & Sandage, A. 1991, ApJ, 379, L1
- Valdes, F., Tyson, J.A. & Jarvis, J. F. 1983, ApJ, 271, 431

- van den Bergh, S. 1986, AJ, 91, 271
- West, M.J. & Richstone, D.O. 1988, ApJ, 335, 532
- White, S.D.M., Briel, U.G. & Henry, J.P. 1993, MNRAS, 261, L8
- Whitmore, B.C., Gilmore, D.M. & Jones, C. 1993, ApJ, 407, 489
- Wirth, G.D., Koo, D.C. & Bershad, M.A. 1994, presented at *Quantifying Galaxy Morphology at High Redshift*, a workshop held at STSCI, Baltimore MD, April 27-29
- Worthey, G. 1994, ApJS, 95, 107
- Wyse, R.F.G. & Silk, J. 1985, ApJ, 296, L1
- Yee, H.K.C. 1991, PASP, 103, 396
- Zinn, R. 1985, ApJ, 293, 424

Appendix A

Estimates Of The Mode And Variance

ESTIMATING THE MODE AND VARIANCE FOR A SET OF PIXEL VALUES

The technique we adopt for the estimation of the mode and standard deviation is based upon the *iterative* techniques of Stetson et al. (1990), with the further implementation of Stetson's (1994) weighted-mean technique for quantized data vectors. Small changes in the data vector, for example from a slight change in annulus definition, results in a small scatter ($\sim \pm 0.2$ ADU) in the final mode estimate. The result is robust and stable, and for the same data vector, our results are consistent with those obtained by Stetson's DAOPHOT II. Below, the most important aspects of our statistics routine are described, while other details of our implementation are documented in our program code. The modal sky value and the standard deviation (both in ADU) are represented by $\overline{z}_{\text{sky}}$ and $\overline{\sigma}_{\text{sky}}$. In this section these quantities can refer to intermediate values obtained during the iteration process; however, in all subsequent sections they refer to the final estimated values.

In the technique which we adopt here to estimate the mean sky value for an arbitrary vector of sky pixels, it is neither desirable or advantageous to first profile-fit and subtract objects from the region in question. Our aperture magnitudes are computed from pixel intensities which are affected by the same (or similar) nearby bright stars, unresolved faint objects, and global light gradients, as are found in the regions used to estimate sky values. Thus the presence of these contaminating objects is actually desired, and *the mode of the intensity distribution is the average sky value we desire*, as it is the maximum-likelihood estimate of the most probable intensity value in the data vector being analyzed. As a result, we iteratively trim the data vector by removing the obvious non-sky pixel values, converging towards a robust solution for the vector's *mode* and *standard deviation*.

We base our estimates for the *mode* of the data vector on estimates of the mean and median. If the mean is less than the median, the intensity distribution is negatively skewed. In this case, contamination by non-sky pixels must be slight, and the mode is set equal to the mean value. However, if the mean exceeds the median, the mode is calculated to be

$$\overline{z}_{\text{sky}} = 3\overline{z}_{\text{median}} - 2\overline{z}_{\text{mean}}. \quad (\text{A.1})$$

This is strictly valid only for unimodal curves of moderate asymmetry (Kendall & Stuart 1977). In our statistics routine, we estimate the spread (noise) in pixel values about the mode, by computing the *standard deviation* of a normal distribution numerically from the data vector itself, to accurately reflect the true nature of the local sky noise. In theory, however, a lower limit to the standard deviation of the sky pixel intensity values is given by Poisson statistics to be the square root of the estimated modal number of photons (i.e., \sqrt{N}). Is this contradictory? In any (pure)

sky region, the probability of a given pixel receiving a certain number of photons N (equal to a constant sky photon rate Z_s times a known integration time t) is governed by an underlying Poisson (random) process, such that $\sqrt{N} = \sqrt{Z_s t}$. Although the Poisson distribution is asymmetric for very low N , it quickly converges to the normal distribution at large N . Thus for any reasonable integration time this approximation is completely valid, and we compute the standard deviation using the well-known formula for this normal distribution. This is the origin of the typical \sqrt{N} uncertainties quoted so often in astronomy. They arise from the low-count nature of the Poisson distribution; the lower the peak value, the less likely multiple events will occur.

The initial estimates (but only these first estimates) for the *mode* and *standard deviation* for an arbitrary data vector are obtained as follows. Our estimate of the mode is simply given by the median of the raw data vector, the simplest approach when the degree of contamination is not yet known. Then, with the lowest and highest intensity values given by z_{\min} and z_{\max} , we trim the data set on either side of the median value, an amount given by

$$\text{trim} = \min(\bar{z}_{\text{median}} - z_{\min}, z_{\max} - \bar{z}_{\text{median}}). \quad (\text{A.2})$$

It is clear then, that we necessarily assume that the data vector of intensity values suffers from asymmetric (bright side) contamination only, and that all values outside of the valid data range (e.g., especially cold pixels) are previously discarded. Then the initial estimate for the standard deviation is computed using this trimmed data set, with the usual formula for the variance (i.e., see equation A.5 and corresponding notes below).

Once the initial estimates of \bar{z}_{sky} and $\bar{\sigma}_{\text{sky}}$ have been obtained, intensity values exceeding some number of standard deviations above the mode (i.e. contaminating pixels from a non-Poisson sky origin) must be trimmed. In this manner the pixel distribution more closely resembles the moderately symmetric unimodal distribution required by Kendall & Stuart, and a better estimate of the *true* mode can be estimated. Since the majority of the n pixels in the annulus represent sky pixels, their pixel intensity values will follow a normal distribution. Then the probability of obtaining a deviant pixel in the data vector is independent of n , but the total number of these deviant pixels is directly proportional to the sample size n . Chauvenet's criterion (Parratt 1961) depends only upon the total number of data points, n , from which the mean, median and standard deviation are estimated, and it provides an objective method to determine at what number of standard deviations above the mean value outlying data points should be rejected.

For the normal distribution, the calculation of Chauvenet's rejection criterion depends upon the error function, and an appropriate interpolation formula (Stetson

et al. 1990) is given by

$$z_{\text{ch}} = -0.1042(\log_{10} n)^2 + 1.1695 \log_{10} n + 0.8895. \quad (\text{A.3})$$

Note that z_{ch} increases with increasing n ; that is, the larger the sample size, the more confidently one can extend the trimming threshold to larger multiples of $\overline{\sigma_{\text{sky}}}$. Then for each iteration after the first, the *original* data vector is checked, and we trim pixel intensity values satisfying

$$|z_i - \overline{z_{\text{sky}}}| > z_{\text{ch}} \overline{\sigma_{\text{sky}}}; \quad (\text{A.4})$$

that is, they are excluded from the next iteration of parameter estimates, but are not discarded from the original vector. A minimum value of $z_{\text{ch}} > 2$ is imposed to limit this interpolation formula to its valid range ($n \gtrsim 20$); we do not attempt to estimate the mode or standard deviation if the number of initial (or subsequently trimmed) data points is less than 20.

In this Section, we have described how our initial estimates of the mode and standard deviation are obtained, and how we utilize Chauvenet's criterion to trim outlying intensity values from our data set. With this trimmed data vector, we reestimate the mode and standard deviation, and a new value for Chauvenet's z_{ch} criterion. We iterate in this manner, each time obtaining a more accurate estimate of the mode and standard deviation, until convergence is reached. This convergence (for which the parameter estimates no longer change) is typically achieved in fewer than 10 iterations. We adopt the resulting values for $\overline{z_{\text{sky}}}$ and $\overline{\sigma_{\text{sky}}}$ as our solution. In the next subsection, we briefly describe two further considerations.

Further Details of the Implementation

Two further comments are in order. First, it is necessary to account for the (potentially) undesirable effect of roundoff error in a specific calculation. In the usual estimate of variance, for large i and typical z_i , the term $(\sum z_i)^2$ can become extremely large. We therefore scale downwards, subtracting the median intensity value from the individual data values, prior to performing the above summation, thereby reducing any potential round-off errors. The median value is added back to the appropriate quantities after the summations are complete. The variance is then given by

$$\overline{\sigma_{\text{sky}}}^2 = \frac{\sum_i (z_i - \overline{z_{\text{median}}})^2}{n} - \left(\frac{\sum_i (z_i - \overline{z_{\text{median}}})}{n} \right)^2. \quad (\text{A.5})$$

Second, in the event that the intensity data is quantized, special care must be taken when using Kendall and Stuart's analytic expression to calculate the mode. In general, a small change in the sky annulus or object center can result in the addition

or deletion of one or more pixels at either end of the data vector being analyzed. Although this seems rather harmless, Stetson (1994) points out that if the data is quantized it could change the *median* estimate by one (ADU), which translates directly to a change in the mode of up to three (ADU). To avoid this problem, Stetson defines the median as the weighted mean of a group of pixels centered on the median (here we use the central ten percent), with weighting inversely proportional to the distance from the estimated mode. With z_i and \bar{z}_{median} denoting the intensity of the i^{th} pixel and the median of the data vector, the weighting factor is then given by

$$w_i = \left[1.0 + \left(\frac{(z_i - \bar{z}_{\text{median}})^2}{2(Q^2 + \bar{z}_{\text{median}})} \right) \right]^{-1}, \quad (\text{A.6})$$

where $(Q^2 + \bar{z}_{\text{median}})$ is a measure of the total variance, with Q representing the CCD read noise. The nature of this weighting factor dictates that the pixel nearest the adopted median is given the largest weight, and pixels on either side of the median are assigned a weight which decreases continuously with $(z_i - \bar{z}_{\text{median}})^2$.

Finally, those readers who are interested in the actual computer code are referred to Appendix C, specifically the subroutine CSTATS, where we implement the above described techniques.

Appendix B

A Brief Introduction And User's Manual For DYNAMO

A BRIEF INTRODUCTION AND USER'S MANUAL FOR DYNAMO

1. INTRODUCTION

DYNAMO implements in a semiautomated manner, the detection, photometry and classification of objects on digital images. It is coded in standard FORTRAN 77 and implemented to run in a UNIX environment accessing images via IRAF's library routines. We adopt Stetson's (1990) iterative trimming techniques to estimate the mode and standard deviation for a vector of pixel intensity values. Our object detection process is implemented on the primary (i.e., deepest) image by locating objects with peak-flux pixel exceeding a user-defined intensity threshold.

For all objects, we compute the following useful intensity-weighted quantities: the radial moments r_1 and r_{-2} , average object centers $\langle x \rangle$ and $\langle y \rangle$, the ellipticity ϵ and the concentration index c_{in} . We define a limiting radius R_ℓ , the radial distance from the peak-flux pixel at which the object's flux drops to one percent of the local sky value. To minimize effects of Poisson noise, the radial moments are calculated within a circular aperture of radius R_ℓ .

We use Kron's (1980) definition of total magnitude and sum the sky-subtracted luminosity contained in a circular aperture of radius $2r_1$. Constant radius apertures are used to measure accurate integrated colors, independent of object morphology. For both the magnitude and color, we compute statistically rigorous uncertainties. For all objects we compute the central surface brightness I_c , and $SB_{2.5\sigma}$, an average surface brightness interior to the $2r_1$ radius.

DYNAMO provides an option for fast and accurate visual inspection of detected objects and their computed quantities. DYNAMO has been tested on artificial CCD images for both starlike and nonstellar object profiles, and applied to our CCD images of the Coma galaxy cluster; it is accurate, robust and versatile. In addition to this general approach, DYNAMO can be used in combination with other image analysis software to compute specific quantities of interest. For example, for a set of predefined object centers (e.g., from FOCAS or DAOPHOT II), it can compute accurate radial moments ellipticities, surface brightnesses and the concentration index.

This brief document describes important details, relevant to those who wish to analyze their own images with DYNAMO. We emphasize the required parameter input, the format of four optional input files, and describe the format of the output photometry file. Finally, we describe the interactive visual inspection stage for a typical CCD image analysis, and describe several issues of relevance (i.e., hints).

2. GETTING STARTED WITH DYNAMO

2.1 Preliminary Image Analysis

For the successful application of DYNAMO to an arbitrary CCD image, there are several required steps which must first be completed:

- All images must have had the usual and required preprocessing (e.g., bias and flatfield corrected) to remove the instrumental signature.

- All images of the same field (and the same bandpass) must be averaged together in some manner to yield a single, higher-S/N image for each field.
- All secondary images must be registered with fractional pixel accuracy to the reference frame of the primary image of the field.
- To measure an accurate color via fixed aperture techniques, the image quality of the two images must be the same. If different, the highest quality image must be degraded (via convolution with a Gaussian function) to match the lower quality image.

In most cases, these four steps can be completed within the IRAF environment using the tasks *noao.imred.ccdred.ccdproc*, *images.imcombine*, *images.geomap/geotran*, and *images.gauss*. Finally, the detection routine as implemented requires that the mean sky level of the image (on which objects are to be found) is near to globally flat. This is usually accomplished by using a median filter (such as that described in Chapter 3 and Appendix C) to remove global light gradients, and/or by subtraction of the brightest galaxies and stars using isophote or profile fitting techniques (e.g., DAOPHOT, VISTA, STSDAS).

2.2 FORTRAN Source Code

The software which implements DYNAMO consists of 13 FORTRAN source code files (Appendix B), four archived IRAF libraries, a UNIX Makefile script and an input file named *dynamo.par* from which parameter values are read. These files are all included in a single compressed TAR file, available via anonymous FTP from *physun.physics.mcmaster.ca*. Once obtained, the TAR file should be placed in a directory dedicated to the DYNAMO files. In this directory, the TAR file is uncompressed, and the individual files are extracted. These steps are described in Figure A.1.

The UNIX executable script *Makefile* controls the compilation of the individual files, and links these together with the IRAF libraries. This script is invoked by typing *make* at the command prompt; note that *Makefile* must be present in the current working directory. When compiled, the executable file is called *dynamo*. For any image dimension up to 2048², it occupies 352 KB of disk space, and requires 24 MB of internal memory to execute. For information on larger images, refer to Section 6. A result of copying the IRAF archived libraries is that during the linking stage, a warning message may be issued, similar in meaning to:

```
ld: ./libimfort.a: warning: table of contents for archive
is out of date; rerun ranlib(1)
```

If this warning does occur, it is easily remedied by executing the UNIX command *ranlib*, which updates these libraries.

3. PARAMETER INPUT AND PROGRAM OPTIONS

Parameter input to DYNAMO is accomplished by modifying the input file *dynamo.par*, and by the use of optional files with predefined names, described below. In all instances,

```

secker@crocus [1] % ftp physun.physics.mcmaster.ca
Connected to physun.physics.mcmaster.ca.
220 physun FTP server (Version 6.10 Wed Oct 6 17:30:33 EDT 1993) ready.
Name:      anonymous
331 Guest login ok, send e-mail address as password.
Password:  secker@physics.mcmaster.ca
230-This is the McMaster University Department of Physics and Astronomy
230-anonymous FTP service.  Guest login ok, access restrictions apply.
ftp> cd pub
ftp> binary
ftp> get dynamo1.tar.Z
ftp> quit
secker@crocus [2] % uncompress dynamo1.tar.Z
secker@crocus [3] % tar xvf dynamo1.tar

```

Figure A.1: The latest version of the DYNAMO source code can be obtained via anonymous FTP. Once in hand, the single file is uncompressed, and the individual files are extracted from the TAR file.

DYNAMO automatically searches the current working directory for these files. If `dynamo.par` is not found, the DYNAMO program will terminate.

3.1 Fundamental Parameter Input

The parameter file `dynamo.par` consists of 23 lines, with each line containing an explanatory comment and the parameter value(s); refer to Figure A.2. The structure of the file cannot change; DYNAMO performs an unformatted read of a `character*50` string followed by the parameter values. The photometry and intensity-weighted moments output by DYNAMO are only as accurate as the input parameter values; thus, these must be determined with care for the CCD image being analyzed. The first 16 lines are relevant to the primary image; that is, the image on which objects are detected and object moments are computed (e.g., R). The last seven lines specify the parameters relevant to the secondary image (e.g., B), used to obtain object colors (e.g., $(B - R)$). If the flag in line 17 is set to *false*, the last six lines of this parameter file are ignored. Note that the CCD parameters may change between the primary and secondary images.

To avoid spurious detections, it is essential that the detection threshold parameter (i.e., β from Chapter 2) not be set too low; a typical value is in the range 3.5–5. For accurate photometry and radial moments, it is necessary to specify realistic inner and outer radii for the sky annulus and an optimal value for the aperture radius. These depend on whether the population of interest is starlike or nonstellar. For roughly calibrated magnitudes, a known magnitude zeropoint (i.e., normalized to a one-second exposure) and an exposure time (i.e. per exposure) can be specified. The CCD gain and readnoise are important for accurate uncertainty estimates, and they must be adjusted to reflect the nature of the composite/master image. For example, a master CCD image which represents the *average* of N images (each with readnoise

```

' Name of PRIMARY IMAGE:           ', galfld.imh
' Global DETECTION threshold (in sigma): ', 4.0
' Inner radius of SKY ANNULUS (pixels): ', 24.0
' Width of SKY annulus (in pixels): ', 4.0
' APERTURE radius (pixels) for m_ap: ', 3.0
' Minimum SEEING disk radius for photometry (px): ', 3.5
' CCD Image SCALE (arcsec/pixel): ', 0.530
' Default ZERO-POINT offset and uncertainty: ', 22.418,0.016
' Exposure TIME - primary image (seconds): ', 900.0
' LOW/HIGH bad pixel value cutoffs (in ADU): ', 1650.0,29000.0
' Radius, intensity-weighted centers (pixels): ', 3.0
' CALIBRATION radius, PSF stars (pixels): ', 6.0
' GAIN - primary image - (in electrons per ADU): ', 64.2
' READ NOISE - primary image - (in electrons): ', 7.51
' Concentration index parameter (0 < alpha < 1): ', 0.3
' Output FIND/MOMENT/PHOTOMETRY file name: ', galfld.phot
' Perform COLOR measurements:           [t/f] ', .f.
' Name of SECONDARY IMAGE:           ', image.imh
' Default ZERO-POINT offset and uncertainty: ', 21.081,0.016
' Exposure time - secondary image (seconds): ', 900.0
' LOW/HIGH bad pixel value cutoffs (in ADU): ', 50.0,29000.0
' GAIN - secondary image - (in electrons per ADU): ', 42.8
' READ noise - secondary image - (in electrons): ', 9.19

```

Figure A.2: The parameter file `dynamo.par` read upon initialization of the DYNAMO program code.

Q and gain g) has a readnoise of Q/\sqrt{N} and a gain of Ng .

3.2 Optional Parameter Input Files

There are several options available to this implementation of DYNAMO. If any (or all) of the following text files exist in the current working directory, then the corresponding actions are taken when appropriate.

- `dynamo.fnd`: This input file specifies x and y object coordinates in column one and two, in a decimal format. If this file exists, the image global sky value is not determined and the object detection process is bypassed. DYNAMO continues on from this point, with these specified object centers. This option is useful for obtaining intensity-weighted moments and photometry for positions obtained via other software, and for the subset of bright (or otherwise special) objects located by visual inspection.
- `dynamo.cul`: This input file specifies regions on the CCD image which are to be ignored (for any reason); e.g., saturated stars, galaxy cores, guidestar probes or other instrumental defects. The pixels interior to these regions are excluded from the global sky calculation and the object detection process. Each exclusion region must be specified on a separate line, and the syntax differentiates between circular and quadrangular regions. Below we provide two examples. A circular region of radius 25 pixels, centered upon

the pixel location (156,82), and a quadrangular region denoting a square rotated by 45 degrees. These coordinates can be specified using decimal pixel values.

```
156 82 25 0 0 0 0 0
100 150 150 200 200 150 150 100
```

Note that the coordinates of the quadrangle must be provided in a very specific manner. The left-most point is specified first, followed by the upper point, then the right-most point, and finally the lower point. The lower point is assumed to connect to the left-most point. In addition, the slopes for these four line segments cannot be zero or infinity, and must alternatively be positive, negative, positive and then negative. With this syntax, arbitrary quadrangular regions can be specified.

Finally, note that no consideration is taken for objects whose aperture extends into an excluded region. This must be taken into account when defining the boundaries of these excluded regions.

- **primary.psf**: Columns 1-2 specify the (x,y) centers of up to 30 onframe standard stars, while columns 3-4 specify their magnitude and uncertainty. The standard stars in this file (if measurable) are used to calculate the magnitude zeropoint for the *primary* image. If this file does not exist, then the default magnitude zero-point specified in the parameter file is adopted. Note that the calibration radius specified in the parameter file must be set large enough that all flux from the standard star is measured.

In addition to the zeropoint, the intensity-weighted moments M_{xx} , M_{yy} and M_{xy} are computed for the PSF stars at these locations. These moments are useful for characterizing the stellar shape, and the mean values are written to the header of the output file. Objects in this file for which the input magnitude is given as 99.999 are not included in the zeropoint calculation, but are used in the moment calculation.

- **secondary.psf**: Columns 1-2 specify the (x,y) centers of up to 30 onframe standard stars, while columns 3-4 specify their magnitude and uncertainty, to determine the magnitude zeropoint for the *secondary* image. If this file does not exist, then the default zeropoint specified in the parameter file is adopted.

4. FORMAT OF OUTPUT PHOTOMETRY FILE

The name of the data file output by DYNAMO is specified in line 16 of the parameter file `dynamo.par`. It is a pure text file, beginning with a 22 line header which describes the image(s) and specifies the parameters used in the data reduction; an example data file is included as Figure A.3. The format statements for this header are defined in the FORTRAN file `dynamo.f`. Appended to this header are descriptor lines, one for each measured object. Each line has a total of twenty columns, and the format statement for these lines is specified in the include file `format.inc`. The first 19 columns are numeric, while the last column is a `character*6` string. Here we describe each column.

```

# DYNAMO VERSION 1.0 (1995):
# OBJECT DETECTION, PHOTOMETRY AND CLASSIFICATION FOR CCD IMAGES
#
# PRIMARY IMAGE:
# LOW and HIGH bad values (ADU):          1400.0 31000.0
# Exposure TIME (seconds):                900.0
# GAIN (e-/ADU) and READNOISE (e-):      64.2    7.5
# ZERO-POINT offset and READNOISE (e-):   22.418  0.016
# PSF moments Mxx, Myy, Mxy:              0.00  0.00  0.00
# Average SKY over frame:                 1499.64 +/- 5.16
#
# Dimensions:    1024 1024    Analysis area:    1 1024    1 1024
#
# FIND threshold (Std Dev above background):  4.00
# SKY radius, SKY annulus:                   24.00 4.00
# APERTURE radius, SEEING disk (pixels):      3.00 3.50
# CENTER radius (pixels)                     6.00
# CALIBRATION radius (pixels)                0.53
# Image SCALE (arcsec^2/pixel):              0.53
#
# * ID  Xp  Yp  <X>  <Y>  SKY  SDEV  M_ap  err  COLOR  err  N_tot  err  r_1  r_2  ell  cin  SB  Ic  CLASS
#
# 1 273 892 272.96 891.88 1499.44 4.81 16.721 0.016 9.999 0.000 15.748 0.016 4.54 2.39 0.42 0.30 20.406 19.904 -----
# 2 518 1000 517.95 999.85 1499.74 5.30 16.954 0.016 9.999 0.000 16.147 0.016 4.11 2.21 0.52 0.34 20.456 20.054 -----
# 3 590 666 590.11 665.88 1500.29 5.04 17.016 0.016 9.999 0.000 16.299 0.016 3.84 2.11 0.55 0.33 20.339 20.060 -----
# 4 954 686 953.98 686.08 1499.01 4.95 17.148 0.016 9.999 0.000 16.372 0.016 3.80 2.18 0.31 0.32 20.643 20.278 -----
# 5 293 994 292.89 993.86 1500.40 4.94 17.238 0.016 9.999 0.000 16.429 0.016 3.99 2.22 0.43 0.30 20.759 20.368 -----
# 6 686 201 686.15 201.09 1499.99 5.05 17.329 0.016 9.999 0.000 16.256 0.016 4.54 2.49 0.13 0.28 20.915 20.582 -----
# 7 294 731 293.96 731.08 1501.81 6.15 17.385 0.016 9.999 0.000 15.745 0.016 6.64 3.18 0.13 0.28 21.227 20.746 -----
# 8 140 1015 140.00 1014.77 1500.04 4.82 17.807 0.016 9.999 0.000 17.282 0.016 2.98 1.92 0.25 0.29 21.023 20.853 -----
# 9 802 713 802.08 713.08 1500.77 5.32 17.674 0.016 9.999 0.000 16.320 0.016 5.51 2.82 0.05 0.26 21.396 20.991 -----
# 10 1009 262 1009.08 261.87 1500.12 5.09 18.119 0.016 9.999 0.000 17.733 0.016 2.69 1.78 0.42 0.36 21.160 21.018 -----
# 11 799 421 799.02 420.97 1499.13 5.23 18.030 0.016 9.999 0.000 17.104 0.016 4.09 2.33 0.04 0.31 21.533 21.233 -----
# 12 412 820 412.11 819.80 1499.92 4.92 18.141 0.016 9.999 0.000 17.421 0.016 3.48 2.12 0.20 0.28 21.502 21.282 -----
# 13 659 642 659.10 642.11 1500.12 5.00 18.394 0.016 9.999 0.000 18.043 0.016 2.55 1.75 0.35 0.39 21.347 21.297 -----
# 14 630 177 629.97 176.83 1499.80 5.08 18.388 0.016 9.999 0.000 17.951 0.016 2.70 1.83 0.16 0.34 21.480 21.350 -----
# 15 92 770 91.85 769.99 1499.73 4.96 18.243 0.016 9.999 0.000 17.296 0.016 4.10 2.35 0.00 0.31 21.731 21.463 -----
# 16 297 857 297.26 857.18 1499.59 4.84 18.682 0.016 9.999 0.000 18.438 0.016 2.23 1.64 0.31 0.31 21.484 21.517 -----
# 17 479 826 478.96 826.11 1499.35 5.18 18.551 0.016 9.999 0.000 18.157 0.016 2.60 1.80 0.09 0.36 21.600 21.527 -----
# 18 29 734 28.83 733.78 1499.81 5.04 18.568 0.016 9.999 0.000 18.145 0.016 2.66 1.82 0.18 0.35 21.637 21.569 -----
# 19 878 907 878.23 907.04 1500.19 4.88 18.915 0.016 9.999 0.000 18.722 0.016 2.08 1.58 0.29 0.24 21.624 21.699 -----
# 20 476 261 476.10 260.94 1499.81 5.34 18.758 0.016 9.999 0.000 18.265 0.016 2.83 1.89 0.13 0.31 21.899 21.781 -----
# 21 344 706 343.83 706.17 1500.48 4.93 18.903 0.016 9.999 0.000 18.577 0.016 2.41 1.72 0.24 0.26 21.839 21.818 -----
# 22 749 980 748.94 979.76 1499.76 5.03 18.899 0.016 9.999 0.000 18.569 0.016 2.43 1.73 0.10 0.26 21.871 21.838 -----
# 23 468 494 467.82 493.94 1499.49 5.31 18.828 0.016 9.999 0.000 18.355 0.016 2.76 1.87 0.05 0.32 21.938 21.859 -----
# 24 325 374 324.96 374.11 1500.12 4.92 18.889 0.016 9.999 0.000 18.488 0.016 2.57 1.80 0.01 0.36 21.908 21.876 -----
# 25 641 734 641.27 733.91 1499.09 5.38 19.046 0.016 9.999 0.000 18.728 0.016 2.38 1.72 0.14 0.26 21.979 21.975 -----

```

Figure A.3: An example photometry file output by DYNAMO. Note that the * symbol in line 22 is used by DYNAMO to denote the end of the file header and beginning of the data.

Col. 1: Sequential and unique integer identification number. Skipped numbers correspond to detected objects, deleted because the photometry was not measurable.

Col. 2-3: The x and y pixel coordinates (integer). If the objects were detected by DYNAMO, these coordinates represent the peak-flux pixel of the object. Otherwise, these coordinates correspond to those input from `dynamo.fnd`.

Col. 4-5: Accurate x and y object centers computed as the intensity-weighted average of pixels within a three-pixel radius of the peak-flux center. This radius is set in line 11 of the parameter file.

Col. 6-7: The local sky mode and standard deviation, in ADU, as computed within the sky annulus.

Col. 8-9: A fixed-aperture magnitude and its uncertainty, measured on the primary image. The aperture radius is defined in line 5 of the parameter file. If this aperture magnitude is not measurable (set to 99.999 by the photometry subroutine), the object is deleted from the photometry file.

Col. 10-11: A color and uncertainty derived from fixed-aperture magnitudes, as the difference between that measured on the secondary and on the primary image (e.g., $(B - R)$ mag, where objects are detected on the primary R image). If no secondary image exists, or if the object is not measurable on the secondary image, this value is set to 9.999.

Col. 12-13: A total magnitude and uncertainty, defined within a radius of $2r_1$ pixels, centered on the peak-flux coordinates. Note that this magnitude is subject to a small (≈ 0.1 -mag) correction factor.

Col.14: The first intensity-weighted radial moment r_1 (in pixels), measured on the primary image.

Col.15: The second negative radial moment r_{-2} (in pixels), measured on the primary image.

Col.16: The ellipticity; objects with a calculated ellipticity outside of the range 0.0 – 0.99 are set to -9.99.

Col.17: The concentration index c_{in} as defined by Doi et al. (1993), but measured within a radius of $2r_1$. The default value for their parameter α is 0.3, specified in the parameter file `dynamo.par`.

Col.18: Average surface brightness (mag/arcsec²) of all pixels interior to the $2r_1$ radius with sky-subtracted pixel intensities which exceed $2.5\sigma_{sky}$.

Col.19: Central surface brightness I_c calculated for the peak-flux pixel, with units of magnitudes per arcsec².

Col.20: A `character*6` string used to flag objects. When no flags are set, the string consists of six dashes `-----`. If any flags are set, the dash in any of positions 1 through 6 are replaced as described in Figure A.4. As an example, a character string given by `b-u---` represents an object such as a cosmic ray, whose intensity exceeds the valid upper limit on the primary image, but is not measured on the secondary image.

5. THE DYNAMO REDUCTION PROCEDURE

Assuming that the preliminary image processing described in Section 2.1 has been completed, image analysis with DYNAMO is straight forward and accurate. In Section 5.1 we illustrate the manner in which the analysis of a typical CCD image proceeds, and in Section

POSITION	FLAG	INDICATION
1	b	Intensity of the object's peak-flux pixel exceeds the upper intensity threshold defined in parameter file.
2	e	The fixed-radius aperture overlaps the image's edge.
2	E	The $2r_1$ -radius aperture overlaps the image's edge. Note that E takes preference if both apertures overlap.
3	u	Object's color is undefined.
4	c	The intensity-weighted center position differs from the peak-flux center by more than the radius specified in line 11 of <code>dynamo.par</code> . This may occur, but only for ultrafaint or spurious detections.
5	m	The peak-flux center of another object is located within a distance of 1 aperture radii from the current object.
5	M	The peak-flux center of another object is located within a distance of 2 aperture radii from the current object.
6	r	The limiting radius R_l has been modified interactively; r_1 and r_{-2} have been recalculated.

Figure A.4: Description of the DYNAMO flags which can be set for individual objects.

5.2 we describe the use of DYNAMO's interactive plotting routine, with four examples of typical situations. In Section 6 we discuss some specific issues of relevance.

5.1 Object Detection and Photometry

In Figure A.5 we illustrate the screen output generated by DYNAMO while analyzing the artificial CCD image used in testing. This screen output is in addition to the photometry file, described above in Section 4. While Figure A.5 is itself fairly self-explanatory, it is worthwhile to mention several points. First, the three main facilities that make up DYNAMO are FIND, PHOTOMETRY and PLOT, and these would typically be run consecutively. However, DYNAMO is equally happy if for any reason you wish to quit after the FIND stage, go for a hike, and then restart the program and proceed directly with PHOTOMETRY.

Once computed, the global sky level can be accepted or modified, the latter option available to force a specific global sky level. If the file `dynamo.fnd` exists, the global sky level is not computed and DYNAMO continues with `Creating output file` For the objects detected on the primary image, the local sky levels and intensity-weighted quantities are computed and written to the output file. The warning message issued in Figure A.5 indicates that the sky annuli for these three objects contains too few pixels for accurate sky estimation, in this case because the sky annulus extends over the physical boundary of the image.

The photometry proceeds in a straight-forward manner, with measured magnitudes for all

```

secker@impatiens [48] % ../dynamo

>>>  OBJECT DETECTION, PHOTOMETRY AND CLASSIFICATION FOR CCD IMAGES  <<<
      DYNAMO VERSION 1.0

PRIMARY image: galfld.imh           Dimensions:    1 1024    1 1024

Proceed with FIND? (t/f) t

Computing global SKY level ...
Global sky = 1499.64+/- 5.16      Accept? [t/f/q] t

FINDING objects 4.00 SIGMA above sky ...
GLOBAL sky value is: 1499.64+/- 5.16
Total of 500 objects found on primary frame

Creating output file ...
Computing accurate local sky levels
and intensity-weighted moments ...

WARNING (skypix): only 24 pixels at ( 1, 169)
WARNING (skypix): only 24 pixels at (1024, 540)
WARNING (skypix): only 24 pixels at ( 1, 718)

Proceed with PHOTOMETRY? (t/f) t

Measuring objects ...
Discarding objects with undefined magnitudes ...
Photometry obtained for 500 objects ( 0 were not measurable)

Flagging multiple nuclei objects ...
Multiple objects compose 1.20 percent of the measured sample

Proceed to PLOT and VERIFY images? (t/f) f

Exiting DYNAMO ...
Hasta la vista

200.440u 10.480s 4:23.41 80.0% 0+8868k 1+34io 0pf+0w
secker@impatiens [49] %

```

Figure A.5: DYNAMO's screen output for the analysis of an artificial galaxy field CCD image.

detected objects (the number in parentheses indicates the number of detections for which the photometry was not measurable). For this example, no secondary image was specified, and no colors are measured. The multiple object message warns us that an estimated 6 of the 500 objects (i.e., three pairs of objects) have a neighbor closer than six pixels; that is, twice the three pixel radius defined in `dynamo.par`. This must be considered only an approximate estimate, since extended objects can contaminate their nearest neighbors, even if their separation exceeds twice the defined aperture radius.

Finally, in this example we exit DYNAMO, choosing to visually inspect the measured objects at a later time.

5.2 Interactive Verification

For the vast majority of detections on an uncrowded CCD image, the initial values for moments and photometry are accurate and correct. Whether the detections themselves correspond to real objects, Poisson noise or cosmic rays is not the question here; the latter two detections are successfully eliminated using parameter space plots of r_1 , r_{-2} and/or I_c versus a measure of magnitude. Refer to Chapter 4 for an example.

However, a small fraction of detections are unphysical, corresponding to CCD cosmetic defects or, for example, occurrences such as charge overflow columns. In addition, a small fraction of the calculated moments for real objects are affected by nearby objects. It is these latter two situations which we refer to as *the difficult individual cases*, and it is these for which visual inspection via DYNAMO's interactive plotting routine is most beneficial. To provide a feel for this visual inspection, we illustrate several common situations in the following figures.

The intensity plots included here were generated by DYNAMO for the artificial galaxy field CCD image `galfld.imh`. Along with each intensity plot, a two line header provides a summary of information from the photometry file. On these plots, DYNAMO uses different symbols to denote various intensity ranges above the global (or local) sky values. A period (i.e., `.`) denotes the range $2.5\sigma \leq z < 4.0\sigma$, while the symbols `=`, `+`, `#` respectively denote ranges of $4.0\sigma \leq z < 5.5\sigma$, $5.5\sigma \leq z < 7.0\sigma$ and $z \geq 7.0\sigma$. In addition, the `+` symbols denote the radius of the calculated $2r_1$ aperture. Keep in mind that the intensity array being plotted is square. It is the difference in the width of rows and columns on a computer screen that give rise to the apparent rectangular nature of the box. Thus, *inherently round objects will appear elongated in these plots*.

Figure A.6 shows one of the large-diameter galaxies on the image, and illustrates that even a quick visual inspection serves many purposes. Since the border of the intensity plot corresponds to the radius of the inner sky annulus, it is immediately evident that the sky annulus specified in the parameter file `dynamo.par` is sufficient large. As well, it is clear this is a real detection, with a $2r_1$ radius appropriate for a galaxy image. (Note that for bright stellar objects, while the intensity plot may show an extended object, the $2r_1$ radius is constant, independent of magnitude.)

Provided that the object's flux drops to zero before a neighbor's flux profile begins, the limiting radius R_l is correctly calculated. This is clearly illustrated in Figure A.7, where the computed $2r_1$ radius is appropriate for the object centered in the plot box. Note that for small scale-size objects, the $2r_1$ radius cannot shrink below the seeing disk radius specified within

ID: 15 Flags: ----- Sky: 1499.73+/- 4.960
 Xcen: 92 Ycen: 770 ell: 0.00 Mtot: 17.296+/- 0.016

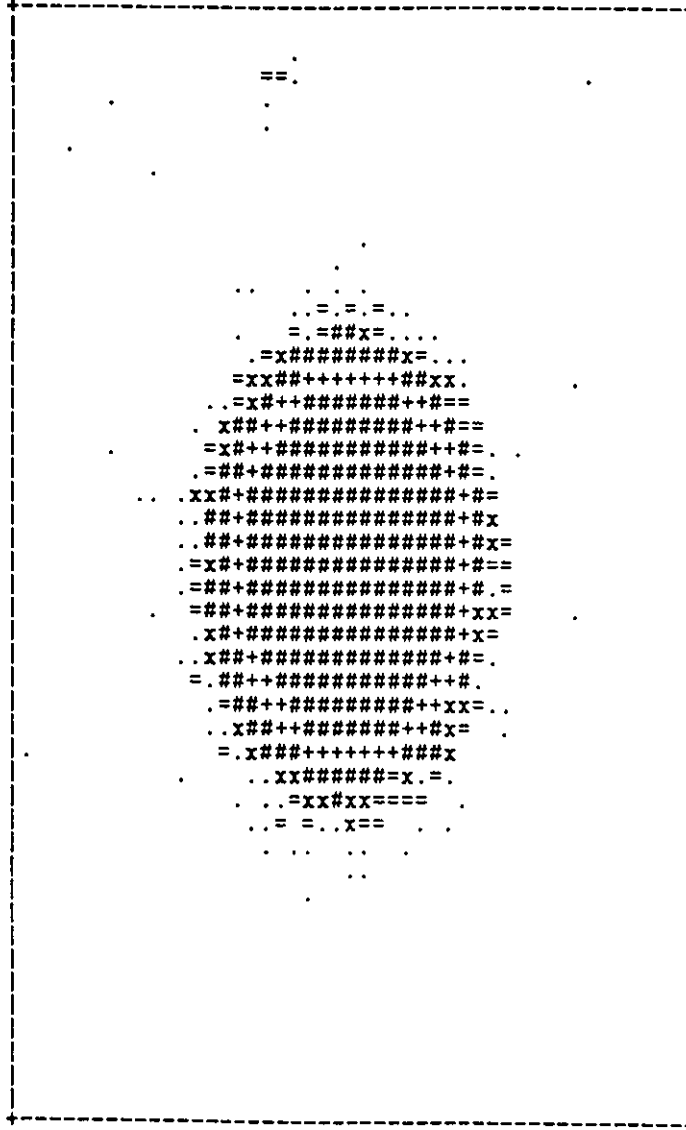


Figure A.6: One of the large diameter galaxies on the artificial CCD image, with a correct estimate of the $2r_1$ radius.

dynamo.par.

In Figures A.8 and A.9, the automated estimate for the $2r_1$ radius is much too large. This occurred in both instances because R_ℓ measured the combined light profile of the object plus its nearby neighbor. The DYNAMO plot routine provides a facility to correct this interactively, and the radial moments are simultaneously recalculated within the specified limiting radius. However, to recalculate the object's total magnitude for this new $2r_1$ aperture radius, it is necessary to run DYNAMO's PHOTOMETRY routine, but this time bypassing the initial FIND process. Consider these examples individually.

In Figure A.8, the galaxy at the center of the plot box a close neighbor which affects its light profile. In cases like these, the calculation to determine the limiting radius R_ℓ measures the full distance out to where the combined light profile terminates; thus, the r_1 moment and the $2r_1$ aperture radius are too large. DYNAMO allows this limiting radius to be modified; in this case, we specify $R_\ell = 4$ pixels. The resulting (recalculated) moments and total magnitude will be only slightly affected by the neighbor in this case.

The situation presented in Figure A.9 here differs from the Figure A.8 in two ways. First, as indicated by the DYNAMO flag in the header, the $2r_1$ aperture overlaps the physical boundary of the CCD image. Second, the neighboring galaxy is sufficiently close that R_ℓ measures the edge of the composite profile, and the $2r_1$ aperture radius is thus incorrect. Interactively specifying that $R_\ell = 3$ pixels would correct this problem, but the total magnitude will be slightly overestimated. This illustrates the problem with using aperture photometry to measure companions of larger galaxies. Note that a recalculation of the r_1 moment, which occurs when R_ℓ is modified, will likely eliminate the edge flag.

6. END NOTES: TIPS NOT TOLD ELSEWHERE

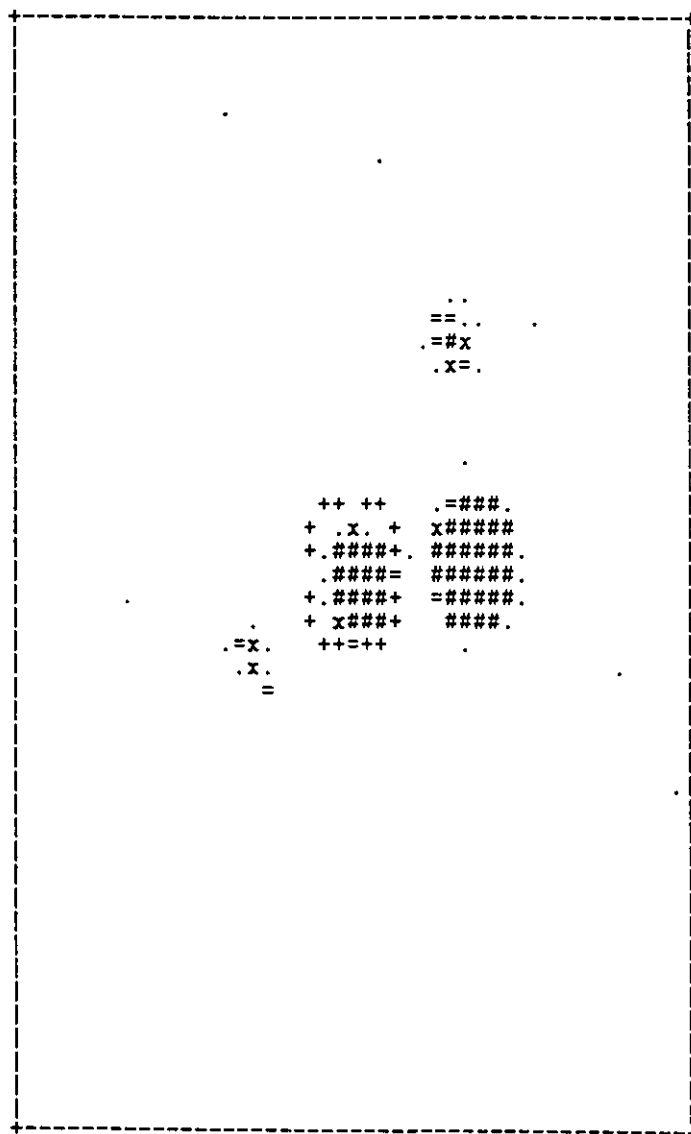
The best way to become familiar with the DYNAMO code and its facilities is to try a test run. Available in a separate TAR file is the artificial CCD image used to generate the figures throughout this text. By using the input parameter file defined above, and running DYNAMO on this image, its output can be verified against the figures included here. The next best way to understand DYNAMO is through the hints provided below.

- Depending on the nature of the CCD image, there may be two or more populations of objects with distinctly different scale sizes (e.g., giant and dwarf galaxies in a galaxy cluster). If both of these object types are to be accurately measured, DYNAMO must be run two or more times on the same image, with different sky annuli specified each time. Simply, for all objects it is imperative that the sky annulus begin after the object's light profile terminates, such that it measures a true sky level.

We have found it useful to select the large scale-size objects by eye, and restrict these to a separate photometry file. For small/faint objects, variations in the local sky level can strongly affect the estimated magnitudes. Therefore it is necessary to properly select the sky annuli specifically for these small objects, and measure them separately from the large objects.

We have found that IRAF's *images.tmark* facility, used in conjunction with an image

ID: 182 Flags: ----- Sky: 1499.28+/- 5.200
 Xcen: 881 Ycen: 322 ell: 0.09 Mtot: 21.828+/- 0.028



Return to accept, d to delete, r for R₁, q to quit ...

Figure A.7: The central galaxy has three nearby neighbors, yet the $2r_1$ radius is computed correctly.

ID: 253 Flags: -e---- Sky: 1499.96+/- 5.170
 Xcen: 1012 Ycen: 271 ell: 0.85 Mtot: 17.623+/- 0.016

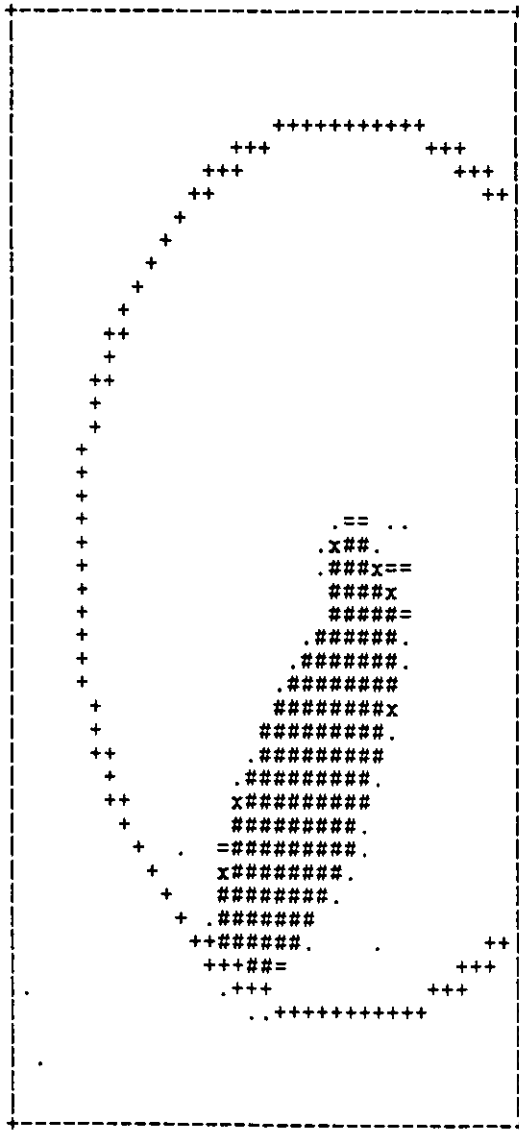


Figure A.9: In this example the small object is almost completely merged with the larger galaxy, illustrating the difficulty of computing meaningful aperture magnitudes in these cases.

display such as SAOIMTOOL or XIMTOOL, provides an effective method to compare the two resulting photometry files.

- Included with the FORTRAN source code is a file named `dynacull.f`. This program facilitates manipulation of DYNAMO photometry files, including the (i) merging of files, (ii) excising of objects based upon a multitude of criteria, (iii) transformation of pixel coordinates, and (iv) application of the full calibration equations. This program is compiled in the usual manner, by typing `f77 -o dynacull dynacull.f` at the UNIX prompt. Comments embedded within the source code provide a fuller description of its use.
- Multiple objects, those for which aperture techniques cannot yield accurate magnitudes, can be separated out based upon their `m` flag in the photometry file. These can be discarded or kept separate for further analysis. As noted above, small companions to large objects are difficult to measure. However, recent advances in isophote-fitting techniques permit these extended objects to be well modelled and subtracted. If these bright galaxies are initially subtracted, the number of multiple objects is greatly decreased, and the resulting object list will not suffer a bias against companion galaxies.
- As implemented, DYNAMO computes the intensity-weighted radial moments τ_1 and τ_2 within a limiting radius R_l defined separately for each object. For crowded fields, this requires visual inspection to ensure that the moments are not affected by their neighbors. However, DYNAMO can be used to perform star/galaxy classification for a list of DAOPHOT object positions, without the need for visual inspection. We suggest this be performed in a parameter space of central surface brightness I_c versus the fixed aperture magnitude. The central surface brightness, by its very definition, depends only upon the object's peak-flux pixel. Likewise, the constant-aperture magnitude is robust to neighboring objects.
- Arrays within the DYNAMO code, as currently specified, are restricted as described below. In order to analyze larger-format images and/or larger scale-size objects, these arrays must be modified. Keep in mind however that changes in array dimensions can drastically increase the internal memory requirements of the program.
 - Only digital images with dimension 2048×2048 pixels and less are permitted. The only location where the physical dimension of the image is specified is the source code file `statistics.f`, where subroutine `globalsky` defines an array `ccd(2048,2048)`.
 - The maximum radius currently allowed is 100 pixels. This applies to the outer radius of the sky annuli, and the $2\tau_1$ aperture radius. The dimension of the array required to hold these pixel values is 40000, which corresponds to 200×200 pixels. Thus in order to analyze larger scale-size objects, these arrays must be appropriately redimensioned.
 - The `find.f` routine is restricted to a total of 80000 pixels above the intensity threshold. A warning is issued if the pixels used for the detection process exceed this number. In order to detect objects on a large-format image without increasing the array dimensions, it is possible to analyze the total image one subsection at a

time, forcing for each subsection the global sky value determined for the image as a whole. Note that the UNIX command line syntax then becomes `dynamo xmin xmax ymin ymax`; the default values for the command line parameters are the physical dimensions of the primary image specified in the parameter file.

- Finally, completeness tests using DYNAMO are trivial in nature. The FIND process is run on an image for which artificial stars and galaxies have been added. Without the need for visual inspection, the resultant object list can be compared to the input list, and the fraction of recovered objects determined as a function of their input magnitude.

Appendix C

Photometry Of The Bright Sample Of Dwarf Elliptical Galaxies

Included here is Table 4-5, which provides the photometry table for the sample of 383 dwarf elliptical galaxy candidates, defined by the limits $15.5 \leq R \leq 20$ mag, and $1.0 \leq (B - R) \leq 1.8$ mag. This and the full photometry tables are available from the author electronically.

TABLE 4.5. Photometry of bright dE candidates in the Coma core.

ID	X px	Y px	R_{2r_1} mag	$(B - R)_{ap}$ mag	r_1 px	I_c mag/arcsec ²
1	186.44	542.22	15.54±0.02	1.53±0.02	2.26	18.76
2	1175.13	1069.89	15.65±0.02	1.62±0.02	5.43	19.92
3	678.92	1795.21	15.69±0.02	1.50±0.02	9.96	20.60
4	1104.51	-233.09	15.75±0.02	1.46±0.02	13.59	21.40
5	270.95	1015.16	15.76±0.02	1.57±0.02	4.83	19.79
6	1419.04	773.03	15.78±0.02	1.62±0.02	7.64	20.38
7	1694.50	-546.33	15.81±0.02	1.37±0.02	12.34	21.72
8	1437.45	146.47	15.82±0.02	1.54±0.02	12.66	21.05
9	2500.49	82.51	15.91±0.02	1.35±0.02	8.28	20.89
10	704.03	1109.88	16.00±0.02	1.46±0.02	6.97	20.74
11	1531.70	-105.50	16.00±0.02	1.53±0.02	6.21	20.41
12	1085.48	100.11	16.03±0.02	1.49±0.02	4.95	19.95
13	1460.98	1784.02	16.03±0.02	1.55±0.02	9.44	21.62
14	1268.82	385.06	16.05±0.02	1.47±0.02	8.11	21.15
15	401.18	390.24	16.07±0.02	1.50±0.02	4.13	20.06
16	3038.23	200.36	16.09±0.02	1.50±0.02	5.15	20.24
17	1044.87	358.84	16.11±0.02	1.49±0.02	6.33	20.83
18	2698.62	563.32	16.19±0.02	1.53±0.02	7.23	21.39
19	408.84	1570.83	16.24±0.02	1.57±0.02	6.82	20.94
20	2007.92	377.30	16.26±0.02	1.56±0.02	10.40	21.53
21	1614.89	1726.03	16.35±0.02	1.40±0.02	7.80	21.75
22	70.09	81.01	16.39±0.02	1.27±0.02	6.22	21.75
23	1119.97	1292.95	16.40±0.02	1.47±0.02	8.46	21.26
24	291.12	1636.15	16.43±0.02	1.48±0.02	7.89	21.47
25	1469.96	1955.03	16.49±0.02	1.55±0.02	6.84	21.35
26	2170.35	214.85	16.50±0.02	1.49±0.02	8.17	21.57
27	840.71	-175.27	16.51±0.02	1.45±0.02	6.99	21.44
28	800.04	843.16	16.53±0.02	1.48±0.02	7.03	20.86
29	2802.43	157.14	16.56±0.02	1.48±0.02	6.69	21.46
30	1953.68	1723.69	16.59±0.02	1.50±0.02	6.72	21.36
31	459.01	1354.87	16.62±0.02	1.52±0.02	6.04	21.27
32	151.92	848.92	16.63±0.02	1.43±0.02	8.06	21.77
33	612.64	-645.13	16.67±0.02	1.43±0.02	5.64	20.89
34	2210.60	589.57	16.73±0.02	1.49±0.02	5.64	21.20
35	2290.45	780.32	16.78±0.02	1.47±0.02	8.47	21.76
36	3068.51	585.03	16.79±0.02	1.48±0.02	9.85	22.26
37	1654.10	878.09	16.80±0.02	1.44±0.02	9.32	22.29
38	326.85	-256.78	16.81±0.02	1.50±0.02	4.33	20.97
39	2145.41	1342.30	16.82±0.02	1.58±0.02	3.09	20.21
40	2140.19	1939.77	16.83±0.02	1.53±0.02	8.01	21.91
41	390.14	595.04	16.83±0.02	1.54±0.02	6.66	21.53
42	796.09	1266.14	16.85±0.02	1.48±0.02	8.05	21.68
43	1280.44	-503.69	16.87±0.02	1.40±0.03	9.03	22.13
44	1219.71	325.05	16.88±0.02	1.57±0.02	4.63	20.93
45	661.91	1109.87	16.93±0.02	1.47±0.02	8.26	21.95
46	965.10	1972.05	16.97±0.02	1.42±0.03	8.86	22.37
47	2531.19	833.75	16.97±0.02	1.47±0.02	8.59	22.16
48	1929.86	1002.45	16.98±0.02	1.43±0.03	6.32	22.03
49	959.83	343.01	17.00±0.02	1.44±0.02	5.29	21.44
50	2704.76	1582.29	17.00±0.02	1.54±0.02	4.62	21.24
51	2556.15	888.60	17.03±0.02	1.44±0.02	7.38	21.98
52	1764.76	1041.94	17.03±0.02	1.49±0.03	5.82	21.78
53	3016.60	1058.58	17.04±0.02	1.39±0.02	7.60	22.26
54	1714.02	-1353.10	17.08±0.02	1.08±0.02	5.39	22.01
55	1282.02	535.16	17.10±0.02	1.48±0.02	5.76	21.57
56	751.07	742.17	17.12±0.02	1.57±0.02	3.43	20.39
57	1046.07	843.07	17.13±0.02	1.39±0.03	9.17	22.21
58	2010.72	1641.94	17.21±0.02	1.17±0.02	9.55	22.41
59	2133.71	1681.99	17.24±0.02	1.26±0.02	5.66	22.07
60	2451.10	2015.04	17.27±0.02	1.54±0.02	6.01	21.85
61	529.17	580.87	17.27±0.02	1.55±0.02	3.45	21.16
62	1420.14	690.02	17.28±0.02	1.47±0.02	5.77	22.39
63	56.54	455.98	17.29±0.02	1.33±0.02	2.26	20.50
64	1343.03	1229.84	17.34±0.02	1.42±0.02	5.76	22.27
65	957.42	-615.10	17.37±0.02	1.45±0.03	8.50	23.02

TABLE 4.5. Continued.

ID	X px	Y px	R_{r_1} mag	$(B - R)_{ap}$ mag	r_1 px	I_c mag/arcsec ²
66	660.15	1073.05	17.38±0.02	1.40±0.03	6.55	22.13
67	1383.99	1167.00	17.38±0.02	1.30±0.03	8.41	22.97
68	272.77	-124.75	17.40±0.02	1.28±0.02	3.18	21.40
69	1369.97	1951.06	17.44±0.02	1.46±0.02	4.93	22.06
70	1811.32	781.45	17.45±0.02	1.16±0.02	6.40	22.52
71	1052.39	647.91	17.48±0.02	1.56±0.02	3.50	21.64
72	68.96	669.23	17.49±0.02	1.72±0.02	5.42	21.58
73	1857.85	996.24	17.49±0.02	1.43±0.03	6.24	22.49
74	968.15	750.93	17.54±0.02	1.46±0.02	6.70	22.48
75	316.96	1773.99	17.55±0.02	1.20±0.02	4.73	22.50
76	1096.15	1412.84	17.59±0.02	1.48±0.02	3.87	21.54
77	1517.00	1082.91	17.62±0.02	1.46±0.02	5.09	22.42
78	823.66	313.88	17.65±0.02	1.41±0.03	5.05	22.12
79	818.06	1842.98	17.66±0.02	1.44±0.03	6.08	22.64
80	1203.36	-594.88	17.68±0.02	1.36±0.03	6.81	22.48
81	2986.57	88.60	17.69±0.02	1.33±0.03	6.17	23.22
82	1847.45	812.23	17.69±0.02	1.47±0.02	3.61	21.44
83	891.58	-27.11	17.69±0.02	1.38±0.03	6.30	22.28
84	1092.79	404.07	17.70±0.02	1.53±0.03	5.65	22.53
85	550.07	1837.74	17.74±0.02	1.59±0.02	2.84	20.90
86	1338.02	1285.06	17.75±0.02	1.39±0.03	6.42	22.99
87	927.89	1429.07	17.75±0.02	1.46±0.02	4.66	22.02
88	1723.36	-682.19	17.80±0.02	1.43±0.03	5.29	22.20
89	929.43	-697.96	17.82±0.02	1.34±0.03	3.25	21.87
90	1064.79	648.19	17.83±0.02	1.47±0.02	3.79	22.04
91	2327.34	1338.65	17.84±0.02	1.43±0.02	5.17	22.48
92	1058.69	-47.02	17.86±0.02	1.41±0.03	7.21	23.09
93	1321.86	1.27	17.88±0.02	1.40±0.03	3.35	21.67
94	883.93	1418.96	17.93±0.02	1.39±0.03	5.33	22.55
95	1004.62	-53.99	17.94±0.02	1.41±0.03	6.25	22.76
96	874.51	-576.04	17.97±0.02	1.33±0.03	4.29	22.19
97	1880.82	973.12	17.97±0.02	1.46±0.02	4.20	22.22
98	577.35	-1220.21	17.98±0.02	1.38±0.03	5.24	22.52
99	576.70	-1199.47	17.99±0.02	1.38±0.03	5.25	22.67
100	2538.42	134.65	18.01±0.02	1.38±0.02	4.00	22.43
101	912.77	102.86	18.02±0.02	1.38±0.03	5.59	22.85
102	763.87	591.91	18.02±0.02	1.24±0.03	5.30	22.48
103	1415.00	666.20	18.09±0.02	1.36±0.02	4.38	22.69
104	2307.38	854.17	18.10±0.02	1.40±0.02	2.86	21.86
105	1047.35	-1410.82	18.10±0.02	1.33±0.03	3.83	22.52
106	1558.95	723.15	18.10±0.02	1.53±0.02	4.33	22.59
107	454.76	44.56	18.11±0.02	1.45±0.03	4.56	22.47
108	553.90	604.90	18.11±0.02	1.41±0.03	5.34	22.94
109	1353.99	1655.00	18.12±0.02	1.35±0.03	7.20	23.89
110	2696.22	187.84	18.14±0.02	1.08±0.02	2.16	21.42
111	334.80	1938.13	18.14±0.02	1.56±0.03	4.20	22.58
112	2878.28	1950.30	18.16±0.02	1.51±0.03	6.19	22.93
113	1633.17	-1417.26	18.16±0.02	1.16±0.03	5.72	23.06
114	2626.35	1203.59	18.18±0.02	1.58±0.03	3.67	22.38
115	1941.56	1219.01	18.21±0.03	1.07±0.03	4.38	22.07
116	2505.61	1143.46	18.22±0.02	1.41±0.03	6.15	23.22
117	548.89	-11.38	18.24±0.02	1.34±0.03	5.08	22.74
118	900.14	895.03	18.24±0.02	1.52±0.02	2.68	21.77
119	2586.46	649.26	18.26±0.02	1.48±0.03	5.27	22.90
120	2580.00	1380.26	18.28±0.02	1.74±0.02	2.93	21.86
121	155.97	1249.00	18.29±0.02	1.33±0.03	5.67	23.35
122	2651.19	1343.35	18.30±0.02	1.04±0.02	4.45	22.75
123	1329.16	-1399.59	18.31±0.02	1.31±0.03	4.82	23.52
124	943.06	1572.05	18.32±0.02	1.35±0.04	3.73	22.96
125	1353.09	1654.09	18.32±0.02	1.34±0.03	6.67	23.93
126	145.05	619.03	18.32±0.02	1.10±0.02	3.02	22.25
127	1027.28	-1152.87	18.35±0.02	1.35±0.03	6.53	23.69
128	566.65	-263.57	18.35±0.02	1.51±0.03	3.28	22.25
129	1715.41	-625.27	18.37±0.02	1.36±0.03	6.15	23.51
130	1644.95	1948.95	18.38±0.02	1.41±0.02	3.71	22.56

TABLE 4.5. Continued.

ID	X px	Y px	R_{2r_1} mag	$(B - R)_{ap}$ mag	r_1 px	I_c mag/arcsec ²
131	2747.64	1641.26	18.40±0.02	1.44±0.03	5.11	23.22
132	183.85	428.88	18.40±0.02	1.30±0.03	4.05	23.17
133	1335.53	53.17	18.41±0.02	1.34±0.04	7.25	23.92
134	1893.42	189.19	18.41±0.02	1.41±0.03	4.85	23.13
135	704.88	52.72	18.47±0.02	1.23±0.03	3.09	22.50
136	142.55	-688.11	18.47±0.02	1.43±0.03	4.34	22.96
137	102.84	1350.13	18.47±0.02	1.33±0.03	3.88	22.99
138	971.70	-246.91	18.47±0.02	1.04±0.03	5.57	23.42
139	2675.55	91.08	18.48±0.02	1.73±0.03	3.39	22.48
140	1812.43	1828.02	18.48±0.02	1.37±0.03	4.60	22.91
141	2324.75	1702.25	18.49±0.02	1.47±0.03	5.26	23.19
142	642.59	-534.30	18.49±0.02	1.72±0.03	3.34	22.52
143	2239.18	244.77	18.49±0.02	1.42±0.03	4.82	23.05
144	2490.67	1675.76	18.53±0.02	1.38±0.03	6.43	23.69
145	828.96	1209.79	18.54±0.02	1.53±0.02	2.56	21.97
146	902.12	-1435.17	18.55±0.02	1.35±0.03	3.42	22.65
147	773.90	1695.05	18.55±0.02	1.38±0.04	7.08	24.58
148	1274.95	1373.83	18.56±0.02	1.37±0.03	3.77	22.73
149	940.47	-644.17	18.56±0.02	1.33±0.03	5.21	23.09
150	319.73	106.35	18.58±0.02	1.52±0.03	3.16	22.34
151	1954.37	669.81	18.59±0.02	1.46±0.03	5.19	23.11
152	694.84	415.65	18.60±0.02	1.70±0.03	3.69	22.97
153	1281.44	-324.79	18.60±0.02	1.23±0.03	5.26	23.64
154	2585.14	809.10	18.61±0.02	1.41±0.03	4.35	22.93
155	198.96	873.03	18.66±0.02	1.46±0.03	3.17	22.74
156	1003.81	1499.91	18.67±0.02	1.67±0.03	5.07	23.69
157	1653.41	324.75	18.67±0.02	1.50±0.03	3.17	22.53
158	324.14	480.96	18.70±0.02	1.31±0.04	6.28	24.28
159	1214.23	500.00	18.70±0.02	1.77±0.03	2.79	22.21
160	2237.91	1042.81	18.71±0.02	1.48±0.03	4.66	23.24
161	2020.49	1588.77	18.71±0.02	1.46±0.03	4.94	23.08
162	558.94	515.84	18.72±0.02	1.42±0.03	4.66	23.36
163	2831.38	1237.99	18.73±0.02	1.72±0.03	3.48	22.74
164	728.51	-593.27	18.73±0.02	1.27±0.03	4.81	23.35
165	2873.35	156.23	18.74±0.02	1.39±0.03	5.15	23.48
166	2211.30	224.03	18.74±0.02	1.38±0.03	3.52	23.00
167	1683.86	347.51	18.74±0.02	1.36±0.03	3.59	22.91
168	2783.73	574.67	18.75±0.02	1.37±0.03	5.62	23.71
169	2876.28	1838.53	18.75±0.02	1.28±0.03	3.62	23.12
170	300.46	-1247.44	18.77±0.02	1.32±0.03	3.66	23.03
171	2364.78	1662.43	18.78±0.02	1.29±0.03	6.07	24.15
172	1182.75	-29.00	18.78±0.02	1.34±0.03	4.65	23.38
173	1039.21	-1466.97	18.80±0.02	1.28±0.03	4.92	23.75
174	248.15	1198.07	18.81±0.02	1.32±0.03	4.24	23.34
175	104.09	1876.02	18.81±0.02	1.36±0.03	5.13	23.94
176	2046.86	552.32	18.81±0.02	1.47±0.03	3.55	23.03
177	34.71	1077.20	18.81±0.02	1.67±0.03	2.89	22.39
178	1773.50	1339.57	18.83±0.02	1.48±0.03	3.79	22.93
179	390.50	-1187.69	18.85±0.02	1.51±0.03	3.70	22.84
180	1803.29	883.17	18.85±0.02	1.37±0.03	3.59	22.98
181	657.34	-1088.73	18.87±0.02	1.33±0.04	6.20	24.13
182	2924.79	560.05	18.87±0.02	1.71±0.03	3.22	22.54
183	1231.02	1509.04	18.88±0.02	1.43±0.03	4.12	23.58
184	361.93	1777.05	18.88±0.02	1.32±0.03	5.20	24.03
185	1427.59	-434.62	18.88±0.02	1.35±0.03	3.09	22.69
186	818.10	1042.06	18.88±0.02	1.34±0.03	4.58	23.58
187	1219.85	898.01	18.91±0.02	1.35±0.03	5.06	23.90
188	2185.51	1758.10	18.91±0.02	1.37±0.03	4.39	23.42
189	118.50	-1431.66	18.91±0.02	1.28±0.03	4.82	23.83
190	711.07	1406.96	18.92±0.02	1.27±0.03	5.15	24.07
191	525.04	1514.96	18.92±0.02	1.00±0.03	3.83	23.25
192	2178.41	1236.63	18.93±0.02	1.38±0.03	4.06	23.29
193	1284.84	335.14	18.94±0.03	1.39±0.05	5.44	24.03
194	1259.48	-463.72	18.95±0.02	1.37±0.04	5.08	23.95
195	1598.89	2024.20	18.95±0.02	1.77±0.03	3.33	23.12

TABLE 4.5. Continued.

ID	X px	Y px	R_{2r_1} mag	$(B - R)_{ap}$ mag	r_1 px	I_c mag/arcsec ²
196	1450.67	123.34	18.95±0.02	1.39±0.04	4.17	23.80
197	468.01	1276.97	18.96±0.02	1.37±0.03	3.34	23.00
198	230.09	1334.02	18.98±0.02	1.39±0.03	3.35	23.09
199	672.81	-125.47	18.99±0.02	1.62±0.03	3.09	22.79
200	202.55	-286.88	19.01±0.02	1.37±0.03	3.61	23.18
201	2287.15	815.32	19.01±0.02	1.64±0.03	3.84	23.21
202	2777.82	1531.35	19.01±0.02	1.37±0.04	5.61	24.16
203	240.90	1121.91	19.01±0.02	1.28±0.03	3.71	23.30
204	1326.14	375.11	19.02±0.02	1.53±0.03	2.43	22.19
205	1336.37	-566.45	19.02±0.02	1.32±0.03	3.84	23.31
206	586.91	1171.97	19.03±0.02	1.48±0.03	2.89	22.63
207	175.75	-854.60	19.04±0.02	1.52±0.03	2.87	22.78
208	748.99	1077.20	19.07±0.02	1.39±0.03	3.26	23.06
209	108.69	-820.66	19.10±0.02	1.33±0.04	5.31	24.33
210	754.23	-1201.98	19.10±0.02	1.71±0.03	3.42	23.34
211	2044.05	1455.14	19.11±0.02	1.73±0.03	3.30	23.32
212	2774.22	312.88	19.11±0.02	1.32±0.03	3.02	22.95
213	163.07	59.90	19.11±0.02	1.24±0.03	3.67	23.42
214	1880.07	1962.13	19.12±0.02	1.50±0.05	5.59	24.48
215	736.65	25.53	19.13±0.02	1.32±0.03	3.56	23.17
216	2029.57	1746.70	19.14±0.02	1.36±0.03	4.32	23.82
217	2484.57	1112.52	19.15±0.02	1.37±0.05	5.50	24.50
218	1168.66	-54.79	19.15±0.02	1.55±0.03	3.18	23.17
219	2163.46	625.30	19.17±0.02	1.57±0.03	3.16	22.98
220	2738.58	1663.33	19.17±0.02	1.43±0.03	3.19	23.17
221	604.74	982.24	19.18±0.02	1.42±0.03	3.34	23.16
222	1313.76	279.06	19.18±0.02	1.27±0.04	3.22	23.57
223	155.69	-513.08	19.18±0.02	1.77±0.03	3.27	23.14
224	158.93	2018.85	19.18±0.02	1.19±0.03	3.35	23.44
225	1457.84	1422.15	19.19±0.02	1.30±0.03	2.77	22.91
226	320.04	1574.88	19.19±0.02	1.28±0.03	4.75	24.01
227	212.52	-1027.82	19.19±0.02	1.41±0.03	2.51	22.64
228	1561.73	58.45	19.20±0.02	1.35±0.03	2.98	23.18
229	263.29	-1379.71	19.20±0.02	1.24±0.03	3.28	23.34
230	254.90	100.19	19.20±0.02	1.64±0.03	3.03	23.11
231	166.44	-1229.96	19.20±0.02	1.27±0.04	5.19	24.33
232	2137.41	737.12	19.21±0.02	1.37±0.03	3.30	23.29
233	2245.99	419.66	19.21±0.02	1.34±0.03	4.46	23.95
234	1090.67	-363.96	19.22±0.02	1.70±0.03	2.70	22.74
235	71.86	586.95	19.22±0.02	1.58±0.03	3.73	23.70
236	457.57	-1042.44	19.22±0.02	1.22±0.03	4.02	23.62
237	1621.87	622.15	19.22±0.02	1.30±0.03	4.32	24.00
238	1244.05	1516.02	19.22±0.02	1.48±0.04	3.88	24.19
239	750.14	1166.02	19.23±0.02	1.38±0.03	4.44	23.76
240	206.06	376.98	19.24±0.02	1.30±0.03	3.75	23.59
241	274.86	211.09	19.24±0.02	1.40±0.03	3.23	23.30
242	523.22	-1479.44	19.24±0.02	1.29±0.03	2.93	23.14
243	349.39	-1135.63	19.26±0.02	1.24±0.03	3.97	23.80
244	445.92	1552.13	19.26±0.02	1.29±0.03	2.86	23.16
245	2261.81	1621.40	19.27±0.02	1.33±0.04	3.36	23.71
246	177.42	-1317.64	19.28±0.02	1.41±0.03	3.93	23.76
247	1291.22	-1356.58	19.29±0.02	1.40±0.03	3.23	23.24
248	1255.13	870.99	19.30±0.02	1.53±0.03	4.13	23.89
249	2369.59	1195.91	19.31±0.02	1.38±0.03	3.83	23.58
250	365.76	-897.33	19.31±0.02	1.27±0.03	2.75	23.10
251	51.05	99.00	19.32±0.02	1.57±0.03	3.33	23.52
252	2181.89	487.45	19.33±0.02	1.33±0.03	3.39	23.99
253	535.41	-1216.61	19.33±0.02	1.28±0.04	4.74	24.32
254	874.41	-627.11	19.33±0.02	1.31±0.04	4.59	24.05
255	1451.46	-70.57	19.33±0.02	1.28±0.03	2.95	23.10
256	1617.44	-234.26	19.33±0.02	1.16±0.03	3.41	23.49
257	2087.21	899.83	19.34±0.02	1.37±0.04	5.25	24.42
258	1984.61	124.38	19.35±0.02	1.34±0.03	4.50	24.14
259	2944.14	338.17	19.35±0.02	1.32±0.03	4.14	24.18
260	1619.82	298.50	19.37±0.02	1.38±0.03	2.28	22.89

TABLE 4.5. Continued.

ID	X px	Y px	R_{2r_1} mag	$(B - R)_{AP}$ mag	r_1 px	I_c mag/arcsec ²
261	2078.15	883.88	19.37±0.02	1.32±0.03	3.97	23.68
262	952.17	-1521.80	19.38±0.02	1.24±0.04	4.46	24.40
263	82.24	185.05	19.39±0.02	1.22±0.04	3.16	23.49
264	2602.40	675.07	19.40±0.02	1.47±0.03	3.80	23.64
265	1617.65	374.29	19.43±0.02	1.04±0.04	4.42	24.40
266	1567.00	1035.08	19.44±0.02	1.35±0.03	3.81	23.90
267	1255.85	-206.85	19.44±0.02	1.25±0.03	1.62	21.95
268	110.89	993.08	19.44±0.02	1.30±0.04	4.26	24.29
269	689.10	1742.03	19.45±0.02	1.64±0.03	2.23	22.70
270	916.24	1800.70	19.46±0.02	1.70±0.05	3.86	23.51
271	1593.52	374.69	19.47±0.02	1.08±0.03	2.52	22.93
272	2491.16	610.91	19.47±0.02	1.71±0.05	5.20	24.14
273	583.50	-1438.28	19.47±0.02	1.23±0.03	1.81	22.38
274	569.59	-1224.33	19.49±0.02	1.65±0.04	2.68	23.16
275	2328.91	1611.28	19.49±0.02	1.14±0.03	3.21	23.45
276	524.92	1039.23	19.50±0.02	1.32±0.04	3.36	23.60
277	1823.23	1845.13	19.51±0.02	1.78±0.03	2.27	22.87
278	1347.67	95.26	19.51±0.02	1.25±0.04	4.65	24.09
279	1048.32	-1261.68	19.51±0.02	1.75±0.03	2.51	22.88
280	2431.97	904.43	19.51±0.02	1.57±0.03	2.92	23.43
281	2092.80	630.89	19.52±0.02	1.28±0.03	3.05	23.21
282	3017.57	1573.84	19.52±0.02	1.36±0.14	4.66	24.96
283	1319.75	132.43	19.52±0.02	1.78±0.03	2.48	22.67
284	901.50	-635.01	19.53±0.02	1.42±0.06	5.22	24.95
285	2725.96	2047.67	19.53±0.02	1.52±0.06	4.71	24.41
286	775.26	648.03	19.53±0.02	1.25±0.04	3.75	23.64
287	562.73	1404.04	19.53±0.02	1.50±0.03	2.30	22.90
288	22.78	1078.75	19.54±0.02	1.71±0.04	2.79	23.29
289	1182.47	-505.73	19.55±0.02	1.18±0.03	2.63	23.02
290	1688.94	-1540.12	19.55±0.02	1.05±0.03	3.31	23.69
291	1454.66	622.13	19.56±0.02	1.24±0.02	1.75	22.27
292	753.47	-515.46	19.57±0.02	1.79±0.03	2.42	22.91
293	560.04	282.54	19.60±0.02	1.56±0.03	3.31	23.67
294	540.52	-288.51	19.60±0.02	1.56±0.05	4.05	23.95
295	866.25	-1557.11	19.60±0.02	1.45±0.03	2.71	23.36
296	1202.59	-505.81	19.61±0.02	1.34±0.03	2.49	23.29
297	829.72	87.87	19.62±0.02	1.38±0.05	4.63	24.69
298	724.91	2003.08	19.63±0.02	1.26±0.03	3.60	24.02
299	835.30	1139.15	19.64±0.02	1.50±0.04	2.68	23.87
300	1231.95	1991.13	19.65±0.02	1.37±0.03	3.66	24.07
301	1696.25	-1137.21	19.65±0.02	1.17±0.04	4.12	24.26
302	2081.40	1171.39	19.65±0.02	1.44±0.03	3.56	23.94
303	182.03	720.96	19.66±0.02	1.29±0.04	3.67	24.08
304	2243.35	741.35	19.66±0.02	1.26±0.04	4.17	24.42
305	2316.22	131.02	19.67±0.02	1.56±0.03	2.73	23.14
306	1971.28	1851.53	19.68±0.02	1.37±0.05	5.09	24.84
307	420.95	1125.22	19.68±0.02	1.25±0.04	3.61	24.08
308	1869.19	1939.20	19.68±0.02	1.36±0.04	3.43	23.88
309	1456.94	1237.08	19.69±0.02	1.34±0.04	3.61	23.99
310	742.59	1034.37	19.70±0.02	1.16±0.03	1.77	22.44
311	2244.40	297.87	19.70±0.02	1.49±0.03	3.42	23.77
312	1021.85	-138.89	19.70±0.02	1.26±0.03	3.03	23.56
313	2492.28	741.98	19.71±0.02	1.35±0.03	2.39	23.28
314	119.04	1454.30	19.72±0.02	1.26±0.03	2.43	23.31
315	1801.79	550.72	19.73±0.02	1.25±0.04	4.96	24.77
316	623.05	538.94	19.73±0.02	1.21±0.04	4.14	24.47
317	2487.06	1506.00	19.74±0.02	1.53±0.03	3.14	23.43
318	864.05	1488.04	19.74±0.02	1.33±0.03	2.45	23.47
319	2078.43	755.05	19.74±0.02	1.24±0.04	4.21	24.50
320	2851.08	831.82	19.75±0.02	1.07±0.03	1.67	22.45
321	2070.00	1943.51	19.75±0.02	1.12±0.03	3.95	24.18
322	1595.37	-1399.23	19.75±0.02	1.09±0.03	1.85	22.69
323	2233.46	60.04	19.76±0.02	1.21±0.03	3.21	23.50
324	1434.59	-58.87	19.76±0.02	1.19±0.03	2.78	23.36
325	1526.19	-570.73	19.76±0.02	1.33±0.03	2.30	23.11

TABLE 4.5. Continued.

ID	X px	Y px	R_{2r_1} mag	$(B - R)_{ap}$ mag	r_1 px	I_c mag/arcsec ²
326	575.79	106.46	19.76±0.02	1.15±0.03	2.71	23.38
327	2274.15	363.84	19.76±0.02	1.42±0.04	4.30	24.57
328	1519.14	556.89	19.76±0.02	1.42±0.03	1.72	22.51
329	1559.30	-497.66	19.77±0.02	1.44±0.04	3.05	23.77
330	282.85	1981.83	19.77±0.02	1.25±0.03	2.25	23.14
331	353.92	1574.28	19.78±0.02	1.40±0.03	1.83	22.62
332	1689.95	1824.89	19.78±0.02	1.30±0.04	3.88	24.40
333	2509.38	613.93	19.79±0.02	1.72±0.03	2.51	23.15
334	1104.47	422.99	19.79±0.02	1.40±0.03	2.44	23.33
335	2219.78	1082.07	19.82±0.02	1.43±0.03	2.26	23.15
336	1150.72	1275.80	19.82±0.02	1.53±0.03	1.78	22.63
337	1273.02	1686.08	19.82±0.02	1.24±0.03	3.73	24.21
338	570.86	551.25	19.83±0.02	1.29±0.04	3.85	24.42
339	1357.81	653.13	19.83±0.02	1.34±0.03	3.23	24.03
340	1597.78	1428.96	19.85±0.02	1.63±0.05	3.11	24.08
341	3092.22	945.84	19.86±0.02	1.47±0.03	2.37	23.26
342	1880.64	692.26	19.86±0.02	1.01±0.03	1.97	22.66
343	3086.46	1769.91	19.86±0.02	1.50±0.03	2.16	23.06
344	2469.91	959.45	19.86±0.02	1.29±0.04	3.79	24.01
345	488.75	-889.76	19.86±0.02	1.14±0.03	2.30	23.08
346	1261.32	-288.85	19.86±0.02	1.27±0.03	3.52	24.07
347	205.53	-564.63	19.86±0.02	1.27±0.04	3.67	24.12
348	729.93	527.07	19.86±0.02	1.31±0.04	3.83	24.45
349	1817.97	1530.50	19.86±0.02	1.37±0.03	3.43	24.05
350	1098.60	346.80	19.87±0.02	1.68±0.03	1.75	22.65
351	296.00	392.22	19.87±0.02	1.03±0.03	2.38	23.23
352	568.40	-1461.99	19.88±0.02	1.44±0.05	4.08	24.49
353	453.87	258.31	19.88±0.02	1.29±0.04	3.30	24.16
354	443.68	-731.43	19.88±0.02	1.34±0.04	3.66	24.26
355	455.51	-758.63	19.88±0.02	1.27±0.04	3.33	24.11
356	1721.07	-1186.37	19.89±0.02	1.34±0.06	4.22	24.82
357	1289.26	-943.53	19.89±0.02	1.36±0.04	3.67	24.31
358	2812.33	715.28	19.89±0.02	1.03±0.03	3.46	23.91
359	111.47	-1444.82	19.89±0.02	1.02±0.05	3.99	24.68
360	990.07	1861.88	19.90±0.03	1.66±0.09	1.77	23.72
361	1453.97	-1149.09	19.91±0.02	1.35±0.03	2.26	23.15
362	341.65	-216.48	19.92±0.03	1.20±0.05	2.94	23.73
363	1407.11	806.06	19.93±0.02	1.32±0.03	2.59	23.57
364	424.04	983.94	19.93±0.02	1.29±0.04	3.39	24.21
365	910.99	1698.24	19.93±0.03	1.56±0.20	2.09	23.45
366	1261.99	466.04	19.95±0.02	1.34±0.04	3.89	24.60
367	1396.64	1121.93	19.95±0.02	1.32±0.04	3.46	24.33
368	656.99	1249.21	19.95±0.02	1.47±0.03	2.54	23.60
369	225.91	1513.95	19.95±0.02	1.63±0.04	2.37	23.43
370	844.06	489.09	19.95±0.02	1.36±0.04	3.36	24.19
371	1377.91	1739.07	19.95±0.02	1.39±0.04	3.53	24.32
372	974.61	270.73	19.95±0.02	1.77±0.03	1.99	23.35
373	593.78	1349.18	19.96±0.02	1.05±0.03	2.26	23.23
374	1691.92	566.91	19.97±0.02	1.49±0.04	3.18	24.17
375	1667.74	1210.12	19.97±0.02	1.56±0.03	1.84	23.02
376	373.55	-1067.25	19.97±0.02	1.52±0.03	2.48	23.57
377	844.90	49.82	19.98±0.02	1.26±0.03	2.96	23.86
378	2750.77	408.88	19.98±0.02	1.29±0.03	2.81	23.75
379	2028.44	1778.69	19.98±0.02	1.67±0.07	3.44	24.10
380	239.32	-1172.64	19.98±0.02	1.41±0.04	2.44	23.55
381	2294.35	1205.94	19.99±0.02	1.38±0.04	3.62	24.25
382	2952.23	767.77	20.00±0.02	1.28±0.05	4.11	24.79
383	225.52	-1317.55	20.00±0.02	1.23±0.04	2.96	23.92